Understanding Radiative Recombination in Two Dimensional Semiconductors

Ali Javey, Ed.

Electrical Engineering and Computer Sciences
University of California, Berkeley

Technical Report No. UCB/EECS-2022-38
http://www2.eecs.berkeley.edu/Pubs/TechRpts/2022/EECS-2022-38.html

May 4, 2022

Understanding Radiative Recombination in Two Dimensional Semiconductors

by

Shiekh Zia Uddin

A dissertation submitted in partial satisfaction of the

requirements for the degree of

Doctor of Philosophy

in

Engineering - Electrical Engineering and Computer Sciences

in the

Graduate Division

of the

University of California, Berkeley

Committee in charge:

Professor Ali Javey, Chair
Professor Eli Yablonovitch
Professor Eran Rabani

Spring 2022

Understanding Radiative Recombination in Two Dimensional Semiconductors

Abstract

Understanding Radiative Recombination in Two Dimensional Semiconductors

by

Shiekh Zia Uddin

Doctor of Philosophy in Engineering - Electrical Engineering and Computer Sciences

University of California, Berkeley

Professor Ali Javey, Chair

Excited carriers relax in semiconductors through various recombination pathways. Some of these processes can be radiative, where photons are created by carrier recombination. It is imperative to understand and increase the efficiency of these radiative processes for the betterment of many optoelectronic devices, such as light emitting diodes, lasers, photodetectors/photovoltaics, and solar cells. Two-dimensional (2D) semiconductors possess van der Waals bonding in the out-of-plane direction and have emerged as a promising material system for high-performance optoelectronic and electronic applications. Due to their reduced Coulomb interaction recombination dynamics of two dimensional semiconductors are significantly different from conventional bulk semiconductors. To achieve their full potential, it is crucial to understand and enhance radiative recombination in 2D semiconductors. Photoluminescence (PL) quantum yield (QY) is the ratio of the number of photons emitted as a fraction of the number of photons absorbed. PL QY governs the ultimate performance of optoelectronic devices and a key indicator of the efficiency of the radiative processes in a semiconductor. The room-temperature PL QY for most as-exfoliated monolayer 2D semiconductors are extremely poor; a prototypical 2D material such as monolayer MoS_2 has a QY of 0.1%. Traditionally, this low QY has been attributed to the large defect density, as defects in conventional semiconductors drastically reduce their PL QY. In the first section of this thesis, I will show how the low QY in monolayer transition metal dichalcogenides (TMDCs) such as MoS_2 is not from defects but from background doping. I will show that the PL QY of as-processed MoS_2 and WS_2 monolayers reaches near-unity when they are made intrinsic through electrostatic or chemical counterdoping, without any chemical passivation. Surprisingly, neutral exciton recombination is entirely radiative even in the presence of a high native defect density. Most optoelectronic devices operate at high photocarrier densities, where all semiconductors suffer from enhanced multiparticle nonradiative recombination and 2D semiconductors are no exception. Although TMDC monolayers exhibit near-unity PL QY at low exciton densities, nonradiative exciton-exciton annihilation (EEA) rapidly degrades their PL QY at high exciton densities and limits their utility in practical applica-

tions. In the next section, we will discuss how by applying small mechanical strain (less than 1%), we can markedly suppressed EEA in monolayer TMDCs, resulting in near-unity PL QY at all exciton densities despite the presence of a high native defect density. Next, I will discuss how these knobs of controlling the photophysics of 2D materials, such as strain and electrostatic doping effect other aspects such as exciton diffusion, electroluminescence and indirect-to-direct transition. As excitonic systems show robust radiative recombination even in the presence of defects, it is desirable to tune the exciton binding energy in the same material system without changing the defect density. However most 2D semiconductors becomes indirect when thickness is increased which obfuscates excitonic radiative recombination. In the final section I will explore exciton to free-carrier transition in black phosphorus (BP), as exceptional system that remains direct at all thicknesses. I will show in the excitonic regime the PL QY decreases with thickness and shows the highest PL QY of $\sim 20\%$ when it is completely excitonic at the monolayer limit. When recombination is dominated by free carriers PL QY increases with thickness, and surface recombination velocity in BP is found to be two orders of magnitude lower than in passivated silicon: the most electrically inactive surface known to the modern semiconductor industry. The rich excitonic photophysics of monolayer 2D semiconductors have already garnered enormous amount of research interest. Even in thick 2D semiconductors where excitonic effects are absent, the recombination can be strikingly different from covalently bonded bulk semiconductors. My findings here will highlight the drastic difference in radiative recombination mechanisms in 2D semiconductors and can enable light-emitting devices that retain high efficiency at all brightness levels despite large defect density.

To the River of My Childhood, Titas

Contents

List of Figures

List of Tables

Acknowledgments

I express my sincere gratitude to Professor Ali Javey for his generous guidance, patient mentorship, and continuous support during this pivotal phase of my life and career the past four and a half years. In hindsight I realize how fortunate I have been to be able to join, learn, and work as a member of his research group. I became a much better scientist because Professor Javey and Professor Eli Yablonovitch always challenged my ideas, for which I am immensely grateful. Eli generously shared his deep understanding of the recombination pathways in semiconductors which has formed the foundation of this work. I thank Professor Eran Rabani for providing critical insights into many of my projects, specially guiding my ideas on auger recombination and exciton-exciton annihilation. I thank Professor Daryl Chrzan for his help with the diffusion project and his anecdotal life advices; especially the one about not trusting John Schrieffer. I also thank Professor Ming Wu for his critical and insightful feedbacks during my qualification exam. Professor Xiang Zhang provided critical guidance in my first semester and always encouraged me during my journey. I thank Professor Alp Sipahighil for many of our informal discussions.

I thank all Javey lab colleagues and mentors who graciously facilitated my growth, corrected my mistakes posthaste, and selflessly propelled me to finish my projects and develop my experimental skills. In particular, Prof. Der-Hsien (Danny) Lien and Dr. Matin Amani played a critical role as great mentors during my initial years as a graduate student. Prof. Hyungjin (Aiden) Kim and Dr. Naoki (Naokisan) Higashitarumizu were instrumental in the success of my research. I will forever cherish working with Aiden in building 2 during the COVID pandemic shutdown and our late nights in molecular foundry. I learned a lot by working with Naokisan and Dr. Jongchan Kim. I appreciate Vivian Wang teaching me Python. Dr. Wenbo Ji's untimely demise prompted me to balance other aspects of my life with work and I dream he is in a better place. I would not have been able to complete this dissertation without the experimental help, discussions, and support of many other brilliant coworkers and friends; including Matt, Peter, Joy, Sharon, Gary, Niharika, Reaz, Monica, Chunsong, James, Sujay, Fahad, Mark, Ed, Alex, Emroz, Mukhlasur, Forsad, Nooruddin and many others to whom I am deeply indebted.

Finally I would like to thank my parents who made tremendous sacrifices to support my choices and invested enthusiastically in my education. My loving, centenarian grandmother passed away during my PhD and I could not say my goodbye in person; she has encouraged me my whole life to excel in my studies. My wife and best friend Saima has always by my side through this journey with encouragements, empathy, and kindness, and I look forward to our coming expeditions together with optimism.

Chapter 1

Introduction

Two-dimensional (2D) materials have shown great promise in various electronic and optoelectronic applications with prospects of improved performance compared to traditional technologies [1]. Some unique advantages include semimetallic properties to having optical bandgaps ranging from mid-infrared to ultraviolet [2], extraordinary defect tolerance [3, 4], the ability to create van der Waals (vdW) heterostructures [5–7], profound quantum properties [8], many-body physics [9, 10], and various approaches to band structure engineering [11, 12]. Unlike the free-carrier characteristics of conventional semiconductors, the photophysics of 2D materials is governed by excitons, which are the primary format of photogenerated carriers at room temperature due to their strong binding energies in 2D materials [13]. Because of this excitonic nature, the recombination pathways can be entirely radiative as long as the photogenerated carriers are in the form of neutral excitons [14]. As a result, the photoluminescence (PL) quantum yield (QY), defined as the ratio of photons emitted to photons absorbed, can approach unity at all generation rates even in the presence of a high native defect density (Fig. 1.1A) [3, 4]. This uniquely robust tolerance to defects presents a key advantage of 2D semiconductors over conventional semiconductors toward developing highly efficient optoelectronics, as stringent growth and fabrication requirements for high-quality crystals can be lowered.

Other advantages of 2D materials are their ease of integration with different substrates and the possibility of fabricating van der Waals (vdW) heterostructures through layer-to-layer integration (Fig. 1.1B) [15]. Traditionally, various growth techniques such as molecular beam epitaxy (MBE) are used to epitaxially create heterostructures. However, because these techniques fundamentally rely on covalent bonding of different materials, undesired lattice mismatch can lead to a high interfacial defect density that consequently degrades device performance [16]. In contrast, vdW heterostructures based on 2D materials can be fabricated with atomic thickness precision, using simple layer transfer techniques to stack selected 2D materials. The 2D heterojunction is based on vdW forces and thus does not suffer from the adverse effects of lattice mismatch. Moreover, because the properties of vdW heterojunctions can be modulated by varying chemical composition, interlayer spacing, and angular alignment, the platform enables new material knobs that could generate extensive device

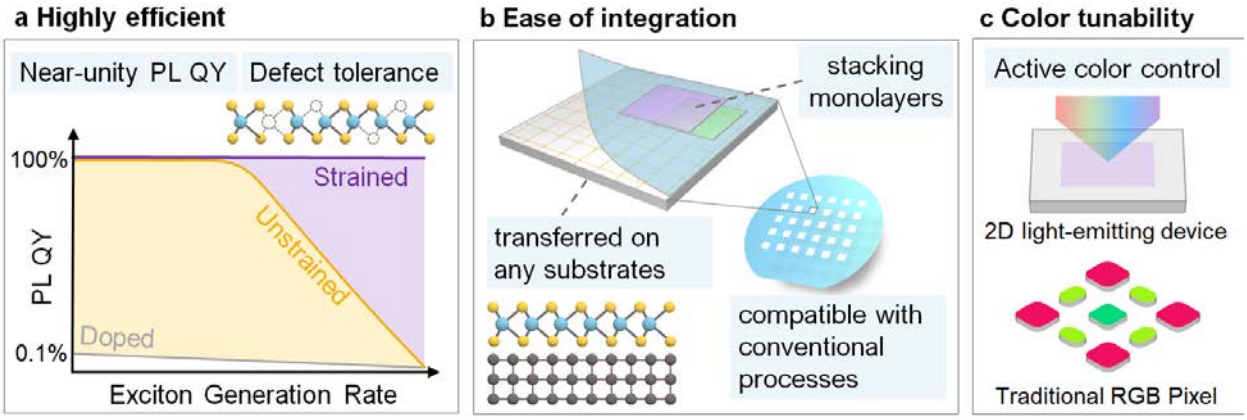

Figure 1.1: **Highlighted merits of semiconducting monolayers for light emitting devices.** (A) Defect tolerance for achieving highly efficient devices. (B) Ease of integration with different substrates without the problem of lattice mismatch, showing a promising compatibility to conventional semiconductor processing. (C) Active control of color in a 2D light-emitting device compared to the traditional display technology.

functionalities. Importantly, the ease of transferring 2D materials to arbitrary substrates enables the integration of 2D materials with existing semiconductor processing and technologies. The capability to engineer the energy band structure in a material is also highly advantageous in modern optoelectronic applications, including light-emitting diodes (LEDs) and lasers. In terms of light-emitting devices, tunability of the emission wavelength is a key feature for scaling current device technology and shrinking pixel size. The advantage of monolayer-based devices is that this tunability can be introduced by strain [17, 18], integrated heterostructures [19, 20], or electrostatic doping [21] (Fig. 1.1C). However, while several potential architectures have been proposed toward this goal, the range of wavelength tunability achieved by those devices still falls short of their theoretical potential.

An excited semiconductor is in a non-equilibrium thermodynamic state and there are multiple recombination processes that facilitate the semiconductor's return to equilibrium. The transition can be radiative, where the excitation energy is radiated away in the form of a photon, or it can be nonradiative, where the energy is released into the crystal lattice as phonons or photochemical changes. PL QY, defined as the ratio of photons emitted to photons absorbed, determines the efficiency of the radiative process and thus limits the efficiency of any light-emitting device [22, 23]. The design of efficient devices thereby requires an in depth understanding of the recombination physics. What happens to electrons and holes after being generated by either optical excitation or electrical injection in a semiconductor depends on how strong the electrostatic Coulomb attraction between them is compared to the average lattice thermal energy. If the energy lowered by forming a bound state of an electron and a hole is larger than the average lattice thermal energy, they will form excitons.

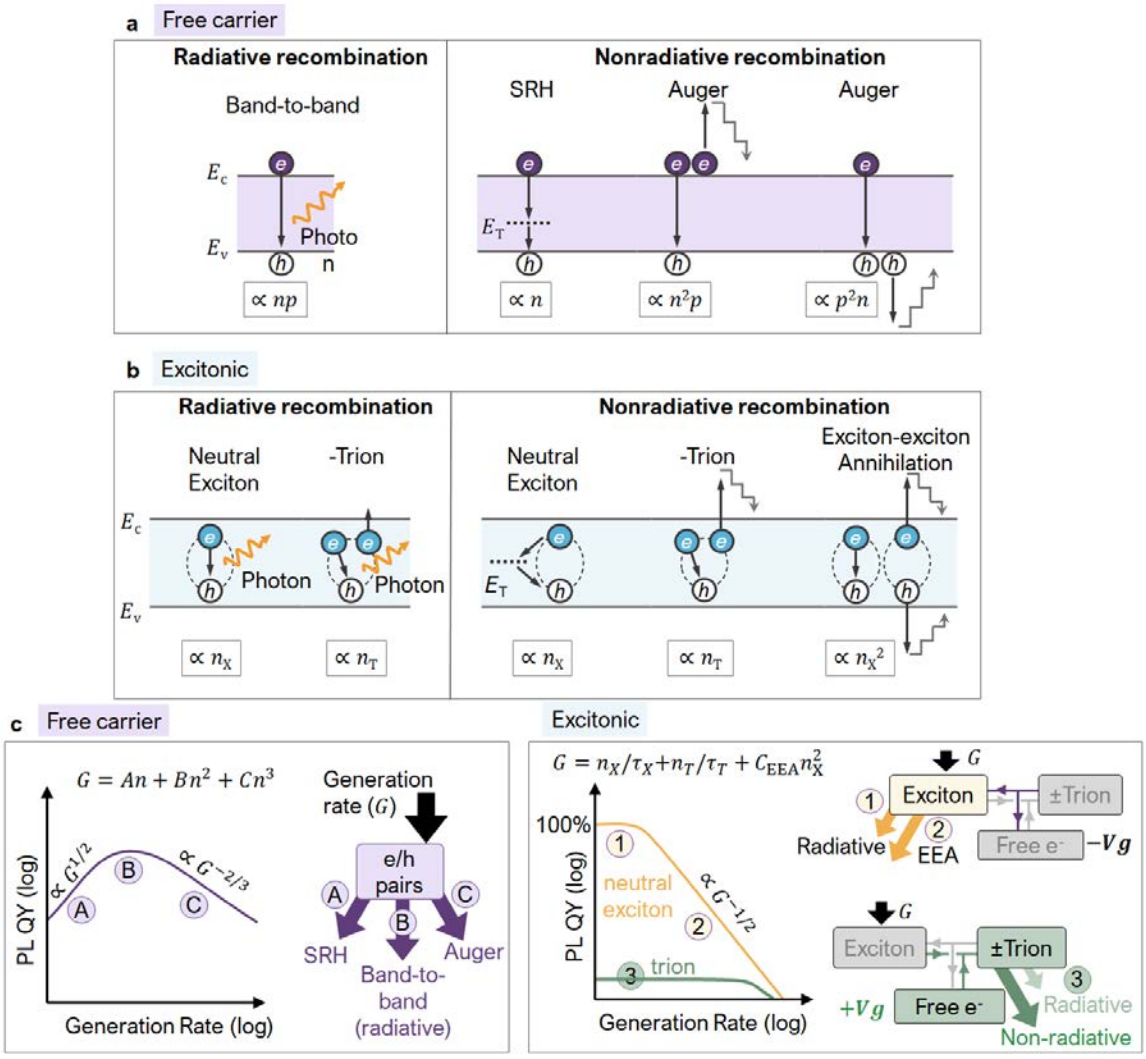

Figure 1.2: **Recombination pathways for free carrier and excitonic systems.** (A) Recombination pathways for a free carrier system. (B) Recombination pathways for an excitonic system. (C) The trends of PL QY versus generation rate for two systems and corresponding recombination pathways.

On the other hand, if the thermal energy is much higher than the binding energy, the electrons and holes will be free and such a semiconductor is called free-carrier semiconductor. Notably, 2D semiconductors in the monolayer limit are found to be excitonic even at room temperature [24, 25]. In contrast, conventional 3D semiconductors such as GaAs and Si are free-carrier systems at room temperature, and will only exhibit excitonic properties at cryogenic temperatures.

Recombination in conventional free-carrier semiconductors can mainly be attributed to three processes (Fig. 1.2A). At room temperature only one process, band-to-band recombination, is generally radiative [26]. In band-to-band recombination, also called direct thermal recombination, a conduction band electron annihilates a valence band hole. As both carrier types need to be available in a band-to-band recombination process, the rate depends on the density of free electrons and holes (n and p), and is generally written as (Bn^2). Defects and interfaces in semiconductors can create allowed energy levels inside the forbidden energy gap. These levels act as an intermediate step for another kind of recombination process: Shockley-Read-Hall (SRH) recombination [27, 28]. The capture of an electron and a hole at the same site by Coulombic attraction results in the annihilation of the electron-hole pair. Also called indirect thermal recombination, this process is characteristically non-radiative. Phonons are produced in this process. With some simplifications, the rate of SRH recombination is proportional to the minority carrier concentration (An) and dominates at low carrier concentrations. At high carrier concentrations, an electron and a hole can directly recombine by transferring their excess energy to another electron or hole. The other electron or hole gains kinetic energy, which is then dissipated through efficient phonon emission. This is the nonradiative Auger recombination process, which limits efficiency in bright light emitting diodes fabricated from conventional semiconductors [29, 30]. The Auger recombination rate depends on the cubic power of carrier concentration (Cn^3). The PL QY of such a free-carrier system is the ratio of the radiative rate and the total generation rate

$$G = An + Bn^2 + Cn^3 \tag{1.1}$$

$$PLQY = \frac{Bn^2}{An + Bn^2 + Cn^3} \tag{1.2}$$

At low pump, SRH recombination dominates and PL QY increases with G; at high pump Auger recombination dominates and PL QY decreases with G (Fig. 1.2C).

In Chapter two, I will outline primary recombination channels in an excitonic semiconductor (Fig. 1.2B) where photogenerated electron hole pairs form excitons which either recombine radiatively by emitting a photon or transfer their energy nonradiatively to trap states. The recombination rate is proportional to the exciton density (n_X). At low pump, neutral excitons recombine mostly radiatively. At high exciton densities, exciton-exciton annihilation (EEA) occurs, where one exciton nonradiatively recombines and transfers its energy to ionize or increase the center-of-mass kinetic energy of another nearby exciton ($C_{EEA}n_X^2$). When excitons are the dominant photoactive quasiparticle, PL QY is initially flat and then decreases with generation rate (Fig. 1.2C). Depending on the background carrier concentration and the strength of Coulomb interaction in the semiconductor, photogenerated excitons bind with background carriers and create three-body quasiparticles known as trions [31]. The recombination rate of trions is proportional to the trion concentration (n_T). For trions, the recombination is dominated by the non-radiative Auger process, in which the electron and hole recombine and excess energy is transferred to the third particle. Therefore, if there are background carriers present in an excitonic semiconductor, mainly

trions are photogenerated and PL QY is low. In general, the PL QY of such an excitonic system is the ratio of radiative rate and the total generation rate

$$G = \frac{n_X}{\tau_X} + \frac{n_T}{\tau_T} + C_{EEA} n_X^2 \tag{1.3}$$

$$PLQY = \frac{n_X/\tau_{Xr} + n_T/\tau_{Tr}}{G} \tag{1.4}$$

where τ_X and τ_T are exciton and trion lifetime, and τ_{Xr} and τ_{Tr} are exciton and trion radiative lifetime, respectively. The ratio of exciton to trion population density is determined by the concentration of background carriers in the system. I will show how the excitonic nature of 2D semiconductors greatly affects how their PL QY changes as a function of background doping (Fig. 1.2C). The ratio of exciton to trion population in these semiconductors is controlled by the Fermi level position. When the Fermi level is mid-bandgap in monolayer MoS_2, a prototypical 2D semiconductor, the PL QY reaches near unity at low generation rates. In contrast, when the Fermi level is close to the conduction band, the PL QY is $\sim 0.1\%$. This is because excitons recombine completely radiatively whereas trions recombine mostly non-radiatively. When these semiconductors are made intrinsic, either by chemical or electrostatic doping (Fig. 1.3A), the dominant recombining quasiparticle is the neutral exciton. Therefore, even in the presence of defects near-unity PL QY can be observed in monolayer excitonic semiconductors provided the Fermi level is moved to the middle of the bandgap [14, 3]. Thus, light-emitting devices based on excitonic semiconductors must have the emitting layer charge-free for them to achieve maximum efficiency.

At high-injection levels, EEA starts to dominate the overall recombination process and PL QY decreases [32–34]. In light-emitting devices, this efficiency droop is a notorious source of deteriorating device performance because: 1) the current required to increase brightness increases disproportionately at higher intensities, and 2) excess power turns into heat, which compromises the lifetime of the devices. This effect limits the brightness at device-relevant exciton densities, especially for high power applications such as lighting and lasers. For an excitonic system, the droop is a bimolecular recombination process which follows $QY \propto \sqrt{G}$. Efficiency drops from $\sim$ 100% to less than 10% as the carrier concentration grows higher than 10^{17} cm^2 for the mostly studied transition-metal dichalcogenide monolayers (Fig. 1.3A). This is more severe than the three-particle Auger recombination in conventional semiconductors, where $QY \propto G^{-2/3}$, and presents a major drawback of semiconducting monolayers. During EEA, one exciton nonradiatively transfers its energy to another nearby exciton. The final state of the energetic exciton depends on the detailed band structure. The density of states in a two dimensional (2D) periodic crystal are topologically constrained to exhibit logarithmic van Hove singularities (VHSs) arising from saddle points in the energy dispersion [35, 36]. When the energy of a transition is near the VHS, weak interactions are often intensified by the enhanced density of states (DOS). Counterdoped TMDC monolayers exhibit enhanced EEA because the final energy of EEA coincides with inherent VHS. In Chapter three, I will discuss how Strain drives the final energy away from the VHS resonance and substantially reduces EEA in both sulfur- and selenide-based TMDCs. Care must be

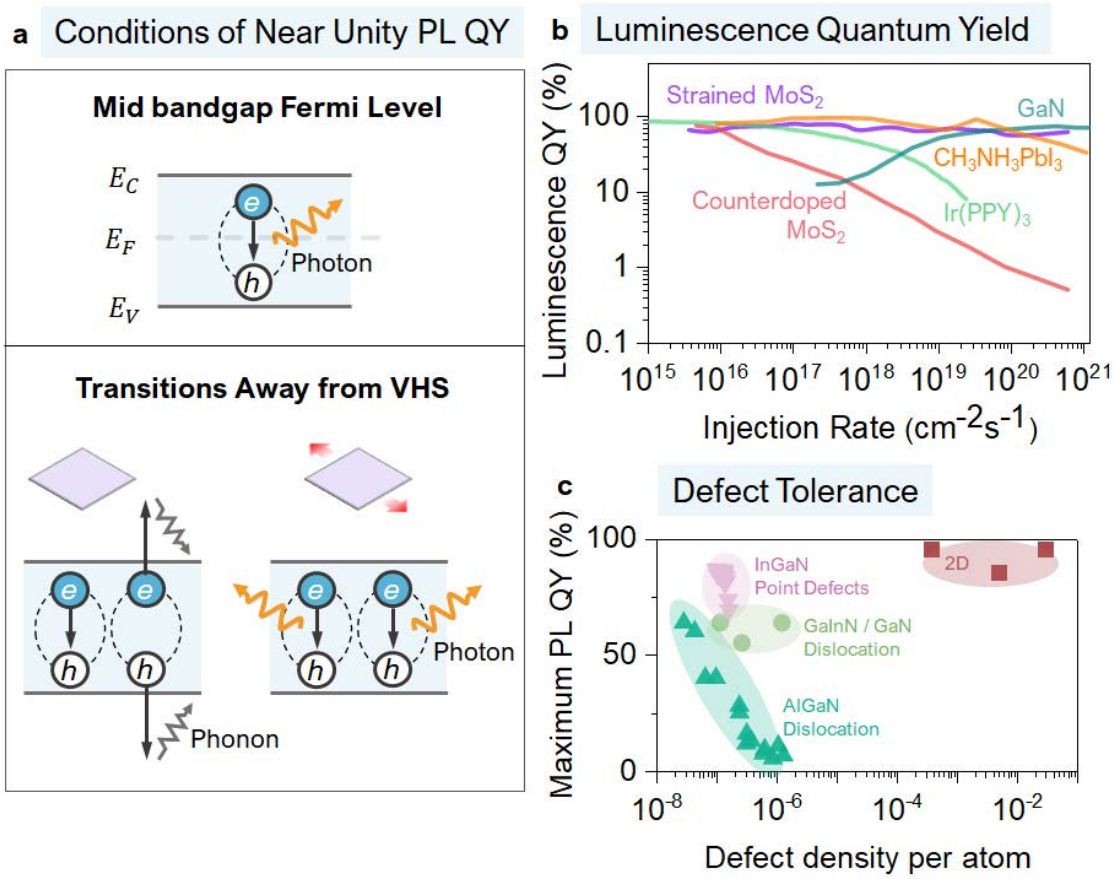

Figure 1.3: **Near-Unity QY in semiconducting monolayers.** (A) PL QY of MoS_2 monolayer reaches near unity when it is intrinsic and EEA is not in resonance with VHS. (B) QY of counterdoped MoS_2 compared to pervoskite ($CH_3NH_3PbI_3$), organic dye ($Ir(PPY)_3$), and inorganic semiconductor (single crystalline GaN). (C) Maximum PL QY with defects in bulk and monolayer semiconductors.

taken while selecting tensile or compressive strain, so that recombination only occurs through direct excitons. The room temperature QY of strained monolayer MoS_2 is compared to high-quality perovskite ($CH_3NH_3PbI_3$), organic dye ($Ir(PPY)_3$), and inorganic semiconductor (single crystalline GaN) in Fig. 1.3C [37–40]. Free-carrier semiconductors such as GaN lose efficiency at low pump due to SRH, whereas organic semiconductors suffer from EEA at high generation rate. 2D TMDC semiconductors have near-unity QY at all generation rates and compared to perovskites are thermodynamically more stable. This high PL QY is achieved even in the presence of extraordinarily high defect density, one in every thousand atoms (Fig. 1.3C). QY in conventional semiconductors approaches zero when one defect is present for every million atoms. This unique property makes monolayer excitonic semiconductors an attractive material system for efficient optoelectronics, since in conventional free-carrier semiconductors the presence of even a small concentration of defects drastically reduces PL QY. The conditions which lead to near unity PL QY in 2D monolayers at all generation rates are summarized in Fig. 1.3.

I will then discuss the how these knobs that control the photophysics of 2D materials, such as strain and electrostatic doping, effect other aspects of carrier recombination. The exciton diffusion length is a critical parameter that reflects the quality of exciton transport in monolayer TMDCs and limits the performance of many excitonic devices. Although diffusion lengths of a few hundred nanometers have been reported in the literature for as-exfoliated monolayers, these measurements are convoluted by neutral and charged excitons (trions) that coexist at room temperature due to natural background doping. Untangling the diffusion of neutral excitons and trions is paramount to understand the fundamental limits and potential of new optoelectronic device architectures made possible using TMDCs.

In Chapter four, I will first present the diffusion lengths of pure neutral excitons and trions in monolayer MoS_2 by tuning the background carrier concentration using a gate voltage and utilizing both steady state and transient spectroscopy. I will then explore the effect of strain on exciton diffusion and show how EEA also enhances diffusion in monolayer semiconductors. EEA degrades luminescence efficiency at high exciton densities and causes efficiency roll-off in light-emitting devices. Transition metal dichalcogenides (TMDCs), such as WSe_2 monolayer, have been demonstrated to exhibit a near-unity photoluminescence (PL) quantum yield (QY) even at the high exciton densities when the band structure is optimally modified by mechanical strain. In Chapter five, I will demonstrate roll-off free electroluminescence (EL) device composed of TMDC monolayers tunable by strain. I will show two order of magnitude EL enhancement from WSe_2 monolayer by applying a relatively small strain of 0.5%. An internal quantum efficiency of 8% are obtained at all injection rates. I also demonstrate transient EL turn-on voltages as small as the bandgap. Our approach will contribute to practical applications of roll-off free optoelectronic devices based on excitonic materials.

In Chapter six, I will discuss how the EEA suppression evolves alongside an indirect to direct transition. In counterdoped monolayer transition metal dichalcogenides (TMDCs) the PL QY monotonously approaches unity with strain at all generation rates. In contrast, in bilayers (2L) of tungsten diselenide (WSe_2) we observe a nonmonotonic change in EEA rate at high generation rates accompanied by a drastic enhancement in their PL QY at low gen-

eration rates. EEA is suppressed both at 0% and 1% strain, but activated at intermediate strains. By strain and electrostatic counterdoping, we attain $\sim 50\%$ PL QY at all generation rates in 2L WSe_2, originally an indirect semiconductor. We demonstrate transient electroluminescence from 2L WSe_2 with $\sim 1.5\%$ internal quantum efficiency for a broad range of carrier densities by applying strain, which is ~ 50 times higher than without strain.

Carrier recombination in a van der Waals (vdW) semiconductor is expected to transition from excitonic to free-carrier in nature as the number of layers is increased. However, in most vdW semiconductors this transition is obscured by the lack of direct bandgap in the bulk state. Black phosphorus (BP) in an exception which maintains a direct bandgap at all thicknesses. In Chapter seven, I will explore the excitonic to free-carrier transition in BP across a wide range of thicknesses. In the excitonic regime the PL QY decreases with thickness and shows the highest PL QY of $\sim 20\%$ when it is completely excitonic at the monolayer limit. On the other hand, when recombination is dominated by free carriers PL QY increases with thickness, and we observe the surface recombination velocity in BP to be two orders of magnitude lower than in passivated silicon: the most electrically inactive surface known to the modern semiconductor industry.

1.1 References

[1] Manish Chhowalla, Debdeep Jena, and Hua Zhang. Two-dimensional semiconductors for transistors. *Nature Reviews Materials*, 1(11):1–15, 2016.

[2] A Chaves, JG Azadani, Hussain Alsalman, DR Da Costa, R Frisenda, AJ Chaves, Seung Hyun Song, YD Kim, Daowei He, Jiadong Zhou, et al. Bandgap engineering of two-dimensional semiconductor materials. *npj 2D Materials and Applications*, 4(1):1–21, 2020.

[3] Der-Hsien Lien, Shiekh Zia Uddin, Matthew Yeh, Matin Amani, Hyungjin Kim, Joel W Ager, Eli Yablonovitch, and Ali Javey. Electrical suppression of all nonradiative recombination pathways in monolayer semiconductors. *Science*, 364(6439):468–471, 2019.

[4] Hyungjin Kim, Shiekh Zia Uddin, Naoki Higashitarumizu, Eran Rabani, and Ali Javey. Inhibited nonradiative decay at all exciton densities in monolayer semiconductors. *Science*, 373(6553):448–452, 2021.

[5] Andre K Geim and Irina V Grigorieva. Van der Waals heterostructures. *Nature*, 499(7459):419–425, 2013.

[6] KS Novoselov, o A Mishchenko, o A Carvalho, and AH Castro Neto. 2D materials and van der Waals heterostructures. *Science*, 353(6298):aac9439, 2016.

[7] Yuan Liu, Nathan O Weiss, Xidong Duan, Hung-Chieh Cheng, Yu Huang, and Xiangfeng Duan. Van der Waals heterostructures and devices. *Nature Reviews Materials*, 1(9):1–17, 2016.

[8] Justin CW Song and Nathaniel M Gabor. Electron quantum metamaterials in van der Waals heterostructures. *Nature Nanotechnology*, 13(11):986–993, 2018.

[9] Alexander Kerelsky, Leo J McGilly, Dante M Kennes, Lede Xian, Matthew Yankowitz, Shaowen Chen, K Watanabe, T Taniguchi, James Hone, Cory Dean, et al. Maximized electron interactions at the magic angle in twisted bilayer graphene. *Nature*, 572(7767):95–100, 2019.

[10] Matthew Yankowitz, Shaowen Chen, Hryhoriy Polshyn, Yuxuan Zhang, K Watanabe, T Taniguchi, David Graf, Andrea F Young, and Cory R Dean. Tuning superconductivity in twisted bilayer graphene. *Science*, 363(6431):1059–1064, 2019.

[11] Zhaohe Dai, Luqi Liu, and Zhong Zhang. Strain engineering of 2D materials: issues and opportunities at the interface. *Advanced Materials*, 31(45):1805417, 2019.

[12] Rafael Roldán, Andrés Castellanos-Gomez, Emmanuele Cappelluti, and Francisco Guinea. Strain engineering in semiconducting two-dimensional crystals. *Journal of Physics: Condensed Matter*, 27(31):313201, 2015.

[13] Hannu-Pekka Komsa and Arkady V Krasheninnikov. Effects of confinement and environment on the electronic structure and exciton binding energy of MoS_2 from first principles. *Physical Review B*, 86(24):241201, 2012.

[14] Matin Amani, Der-Hsien Lien, Daisuke Kiriya, Jun Xiao, Angelica Azcatl, Jiyoung Noh, Surabhi R Madhvapathy, Rafik Addou, KC Santosh, Madan Dubey, et al. Near-unity photoluminescence quantum yield in MoS_2. *Science*, 350(6264):1065–1068, 2015.

[15] Hui Fang, Corsin Battaglia, Carlo Carraro, Slavomir Nemsak, Burak Ozdol, Jeong Seuk Kang, Hans A Bechtel, Sujay B Desai, Florian Kronast, Ahmet A Unal, et al. Strong interlayer coupling in van der Waals heterostructures built from single-layer chalcogenides. *Proceedings of the National Academy of Sciences*, 111(17):6198–6202, 2014.

[16] Geun Ho Ahn, Matin Amani, Haider Rasool, Der-Hsien Lien, James P Mastandrea, Joel W Ager III, Madan Dubey, Daryl C Chrzan, Andrew M Minor, and Ali Javey. Strain-engineered growth of two-dimensional materials. *Nature Communications*, 8(1):1–8, 2017.

[17] Sujay B Desai, Gyungseon Seol, Jeong Seuk Kang, Hui Fang, Corsin Battaglia, Rehan Kapadia, Joel W Ager, Jing Guo, and Ali Javey. Strain-induced indirect to direct bandgap transition in multilayer WSe_2. *Nano Letters*, 14(8):4592–4597, 2014.

[18] Yang Li, Tianmeng Wang, Meng Wu, Ting Cao, Yanwen Chen, Raman Sankar, Rajesh K Ulaganathan, Fangcheng Chou, Christian Wetzel, Cheng-Yan Xu, et al. Ultrasensitive tunability of the direct bandgap of 2D InSe flakes via strain engineering. *2D Materials*, 5(2):021002, 2018.

[19] Ouri Karni, Elyse Barré, Sze Cheung Lau, Roland Gillen, Eric Yue Ma, Bumho Kim, Kenji Watanabe, Takashi Taniguchi, Janina Maultzsch, Katayun Barmak, et al. Infrared interlayer exciton emission in MoS_2/WSe_2 heterostructures. *Physical Review Letters*, 123(24):247402, 2019.

[20] Pasqual Rivera, John R Schaibley, Aaron M Jones, Jason S Ross, Sanfeng Wu, Grant Aivazian, Philip Klement, Kyle Seyler, Genevieve Clark, Nirmal J Ghimire, et al. Observation of long-lived interlayer excitons in monolayer $MoSe_2$–WSe_2 heterostructures. *Nature Communications*, 6(1):1–6, 2015.

[21] Jason S Ross, Sanfeng Wu, Hongyi Yu, Nirmal J Ghimire, Aaron M Jones, Grant Aivazian, Jiaqiang Yan, David G Mandrus, Di Xiao, Wang Yao, et al. Electrical control of neutral and charged excitons in a monolayer semiconductor. *Nature Communications*, 4(1):1–6, 2013.

[22] G Bemski. Recombination in semiconductors. *Proceedings of the IRE*, 46(6):990–1004, 1958.

[23] VN Abakumov, Vladimir Idelevich Perel, and IN Yassievich. *Nonradiative Recombination in Semiconductors*. Elsevier, 1991.

[24] Xiaomu Wang, Aaron M Jones, Kyle L Seyler, Vy Tran, Yichen Jia, Huan Zhao, Han Wang, Li Yang, Xiaodong Xu, and Fengnian Xia. Highly anisotropic and robust excitons in monolayer black phosphorus. *Nature Nanotechnology*, 10(6):517–521, 2015.

[25] Keliang He, Nardeep Kumar, Liang Zhao, Zefang Wang, Kin Fai Mak, Hui Zhao, and Jie Shan. Tightly bound excitons in monolayer WSe_2. *Physical Review Letters*, 113(2):026803, 2014.

[26] William P Dumke. Spontaneous radiative recombination in semiconductors. *Physical Review*, 105(1):139, 1957.

[27] Re N Hall. Electron-hole recombination in germanium. *Physical Review*, 87(2):387, 1952.

[28] WTRW Shockley and WT Read Jr. Statistics of the recombinations of holes and electrons. *Physical Review*, 87(5):835, 1952.

[29] A Haug. Auger recombination in direct-gap semiconductors: band-structure effects. *Journal of Physics C: Solid State Physics*, 16(21):4159, 1983.

[30] AR Beattie and PT Landsberg. Auger effect in semiconductors. *Proceedings of the Royal Society of London. Series A. Mathematical and Physical Sciences*, 249(1256):16–29, 1959.

[31] Timothy C Berkelbach, Mark S Hybertsen, and David R Reichman. Theory of neutral and charged excitons in monolayer transition metal dichalcogenides. *Physical Review B*, 88(4):045318, 2013.

[32] Shiekh Zia Uddin, Eran Rabani, and Ali Javey. Universal inverse scaling of exciton–exciton annihilation coefficient with exciton lifetime. *Nano Letters*, 21(1):424–429, 2020.

[33] Feng Wang, Yang Wu, Mark S Hybertsen, and Tony F Heinz. Auger recombination of excitons in one-dimensional systems. *Physical Review B*, 73(24):245424, 2006.

[34] KE O'hara, JR Gullingsrud, and JP Wolfe. Auger decay of excitons in Cu_2O. *Physical Review B*, 60(15):10872, 1999.

[35] Noah FQ Yuan, Hiroki Isobe, and Liang Fu. Magic of high-order van hove singularity. *Nature Communications*, 10(1):1–7, 2019.

[36] Léon Van Hove. The occurrence of singularities in the elastic frequency distribution of a crystal. *Physical Review*, 89(6):1189, 1953.

[37] Ian L Braly, Dane W DeQuilettes, Luis M Pazos-Outón, Sven Burke, Mark E Ziffer, David S Ginger, and Hugh W Hillhouse. Hybrid perovskite films approaching the radiative limit with over 90% photoluminescence quantum efficiency. *Nature Photonics*, 12(6):355–361, 2018.

[38] Kwon-Hyeon Kim, Chang-Ki Moon, Jeong-Hwan Lee, Sei-Yong Kim, and Jang-Joo Kim. Highly efficient organic light-emitting diodes with phosphorescent emitters having high quantum yield and horizontal orientation of transition dipole moments. *Advanced Materials*, 26(23):3844–3847, 2014.

[39] MA Reshchikov, M Foussekis, JD McNamara, A Behrends, A Bakin, and A Waag. Determination of the absolute internal quantum efficiency of photoluminescence in GaN co-doped with Si and Zn. *Journal of Applied Physics*, 111(7):073106, 2012.

[40] Jong-In Shim and Dong-Soo Shin. Measuring the internal quantum efficiency of light-emitting diodes: towards accurate and reliable room-temperature characterization. *Nanophotonics*, 7(10):1601–1615, 2018.

Chapter 2

Quantum Yield at Low Generation Rates

2.1 Introduction

[1]Defects in conventional semiconductors substantially lower the photoluminescence (PL) quantum yield (QY), a key metric of optoelectronic performance that directly dictates the maximum device efficiency. Two-dimensional (2D) transition metal dichalcogenides (TMDCs), such as monolayer MoS_2, often exhibit low PL QY for as-processed samples, which has typically been attributed to a large defect density. Here, we show that the PL QY of as-processed MoS_2 and WS_2 monolayers reaches near-unity when they are made intrinsic by electrostatic doping, without any chemical passivation. Surprisingly, neutral exciton recombination is entirely radiative even in the presence of a high defect density. This work highlights a unique feature of TMDC monolayers for practical device applications, as the stringent requirement of low defect density for high optoelectronic performance is eased.

2.2 Electrical Suppression of Nonradiative Recombination

Multiparticle Coulomb interactions are particularly pronounced in transition metal dichalcogenide (TMDC) monolayers, leading to a multitude of recombination pathways, each associated with the different quasiparticles produced by these interactions [1]. Excitons formed by photogenerated carriers are the basic particles in this system [2, 3], and their recombination rate depends nonlinearly on the concentration. Because excitons interact with background charge to form trions [4–8], the Fermi level also controls the dominant recombination path-

[1]The following section was published in a similar form in Science. (Lien, D.H.*, Uddin, S.Z.*, Yeh, M., Amani, M., Kim, H., Ager, J.W., Yablonovitch, E. and Javey, A., Electrical suppression of all nonradiative recombination pathways in monolayer semiconductors, *Science*, 364(6439), pp.468-471, 2019.)

way. Therefore, both the background carrier concentration and the generation rate must be tuned to investigate the complete effect of multiparticle interactions on TMDC photoluminescence (PL) quantum yield (QY). In this work, we simultaneously alter the photocarrier generation rate (G) by varying the incident pump power, and the total charge concentration (electron and hole population densities; N and P) by varying the back-gate voltage (V_g) in a capacitor structure (Fig. 2.1A). Surprisingly, we find that all neutral excitons recombine radiatively in as-processed monolayers of MoS_2, resulting in near-unity QY at low generation rates. This is despite a reported high defect density of $10^{10} - 10^{13}$ cm^{-2} determined by microscopy techniques [9], in stark contrast to conventional inorganic semiconductors, where even a small number of defects has detrimental effects on the PL QY [10]. To gain additional insight into the photophysics, we also present introduce a simple kinetic model involving excitons, trions, exciton-exciton annihilation and free carriers for both sulfur- and selenide-based TMDCs.

We first present data from a MoS_2 device, which contains a monolayer of MoS_2 encapsulated in PMMA, along with a transferred gold electrical contact [11]. Notably, PMMA reduces V_g hysteresis [12, 13], thus enabling more stable and accurate measurements (Fig. 2.2).

[Device fabrication details are below]. The V_g-dependence of the PL spectra of a MoS_2 monolayer measured at a high generation rate of $G = 10^{18}$ cm^{-2}s^{-1} is shown in Fig. 2.2B. The peak PL intensity at $V_g = -20$ V shows a $\sim$ 300-fold enhancement compared to $V_g = 0$ V (Fig. 2.1B). A peak energy shift of 30 meV is also observed (inset of Fig. 2.1B), which has been attributed to the trion binding energy [14]. PL images of a monolayer device show that the enhancement of PL intensity by electrostatic doping is spatially uniform (Fig. 2.1 C, D, and E). Calibrated PL measurements at room temperature were performed to quantitatively extract the QY as a function of V_g and G (Fig. 2.3A and B). At $V_g = 0$ V and $G = 6 \times 10^{17}$ cm^{-2}s^{-1}, a QY of 0.1% is measured (Fig. 2.3B), consistent with the pristine MoS_2 in previous reports [15, 16]. The QY increases as V_g decreases. At $V_g = -20$ V and a low generation rate of $G = 6 \times 10^{15}$ cm^{-2}s^{-1}, the QY increases by 3 orders of magnitude and reaches a peak value of 75% (PL QY vs V_g shown in the Fig. S2). Through application of V_g, the QY of a chemically-untreated MoS_2 monolayer approaches unity, matching the behavior previously observed in MoS_2 monolayers treated with bis(trifluoromethane) sulfonimide (TFSI) [11].

In the traditional ABC-model [17] of carrier recombination in semiconductors, defect-mediated Shockley-Read-Hall (SRH) recombination dominates at low generation rates, while Auger recombination dominates at high generation. In the SRH regime, it is known that QY increases linearly with G. In the Auger regime, QY decreases with a slope of $-2/3$ in a log-log plot [18, 19]. Neither of these power-laws are present in the pump-dependent QY behavior of MoS_2. Instead, the observed behavior can be understood by considering the interaction of excitons, trions, and free carriers and their subsequent recombination channels (shown schematically in Fig. 2.3C). Depending on the type of carriers present, the behavior of an exciton formed by photogenerated carriers varies dramatically. If the semiconductor is intrinsic, the exciton stays neutral; if the majority charge carriers are holes or electrons, the exciton may become a positive or negative trion, respectively. For the case with negative

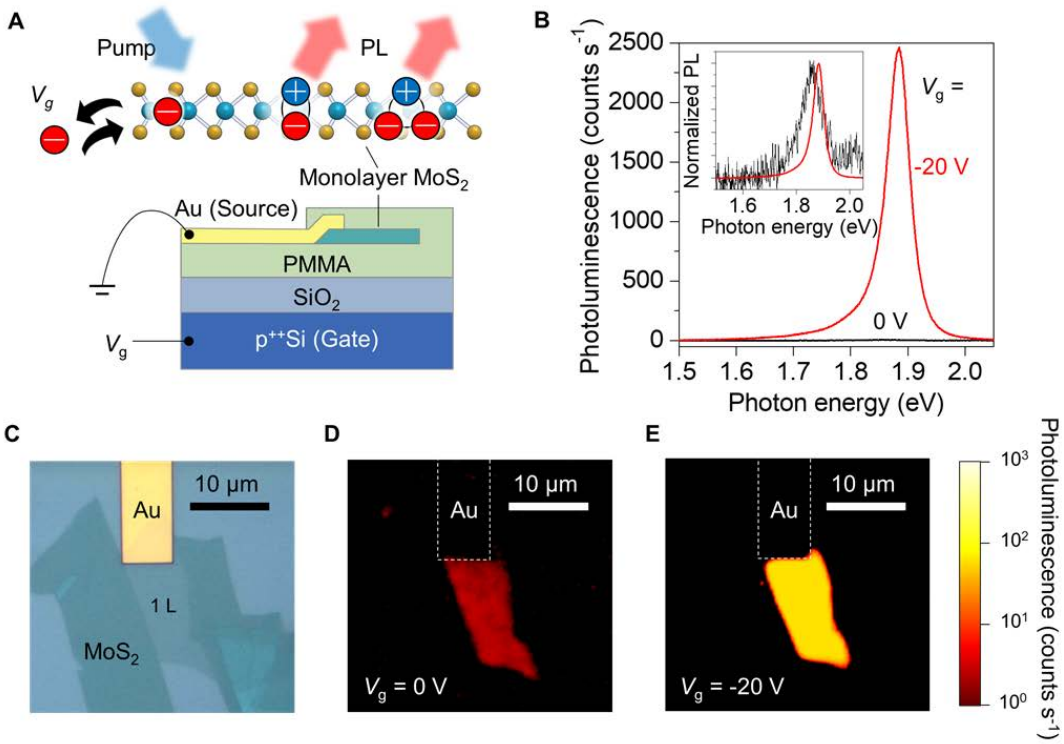

Figure 2.1: **Schematics of the device and the gate dependence of photoluminescence in MoS_2.** (A) Schematic showing control of different quasiparticles by gate voltage V_g and generation rate G. (B) PL spectra of the MoS_2 monolayer device under gate voltages $V_g = -20$ V and 0 V at generation rate $G = 10^{18}$ cm^{-2}s^{-1}. Inset is the normalized PL spectra depicting the spectral shift. (C) Top-view optical micrograph of a MoS_2 device. (D) PL imaging of the device at $V_g = 0$ V, and (E) $V_g = -20$ V.

trions, the generation rate G in steady state is balanced by the rates of all the recombination channels

$$G = \frac{n_X}{\tau_X} + \frac{n_T^-}{\tau_T^-} + C_{EEA} n_X^2 \tag{2.1}$$

where n_X, and n_T^- (τ_X, and τ_T^-) are the neutral exciton, and negative trion population densities (lifetimes), respectively, and C_{EEA} is the exciton-exciton annihilation coefficient [20, 21]. The exciton and trion lifetimes have radiative (τ_{Xr}, τ_{Tr}) and nonradiative (τ_{Xnr}, τ_{Tnr}) components

$$\frac{1}{\tau_X} = \frac{1}{\tau_{Xr}} + \frac{1}{\tau_{Xnr}} \tag{2.2}$$

$$\frac{1}{\tau_T^-} = \frac{1}{\tau_{Tr}^-} + \frac{1}{\tau_{Tnr}^-} \tag{2.3}$$

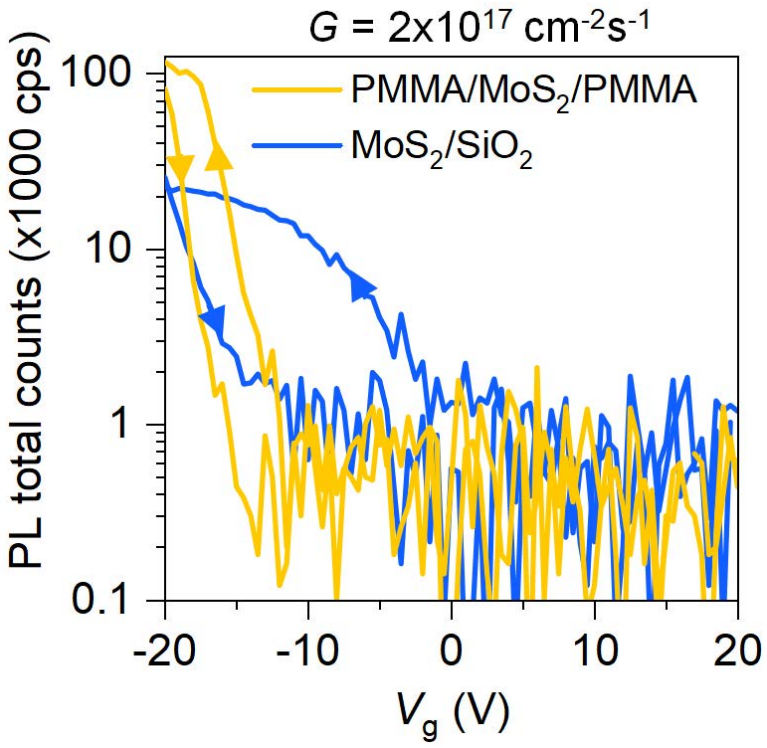

Figure 2.2: V_g **hysteresis for different substrates.** A comparison of the effect of V_g hysteresis between a PMMA/MoS_2/PMMA device and a MoS_2/SiO_2 device. The PMMA device exhibits significantly lower hysteresis, thus allowing for more stable and accurate gated PL measurements.

The QY is then given by the ratio of the radiative recombination rate of both trions and excitons to total generation rate G.

$$QY = \frac{1}{G}\left(\frac{n_X}{\tau_{Xr}} + \frac{n_T^-}{\tau_{Tr}^-}\right) \tag{2.4}$$

The total negative charge concentration in the monolayer is given by $N = C_{ox}(V_g - V_{th})/q$, where C_{ox} is the gate-oxide capacitance, q is the electronic charge and V_{th} is the threshold voltage. $N = n_e + n_T^-$, as this negative charge density arises from negative trions (n_T^-) or free electrons (n_e). The trion formation and dissociation rates balance in steady state and yield a law of mass-action $n_T = T n_X n_e$, where T is the trion formation coefficient [22]. Combining these equations, the trion concentration can be written as a function of exciton concentration n_X

$$n_T = \frac{T n_X}{(1 + T n_X)N} \tag{2.5}$$

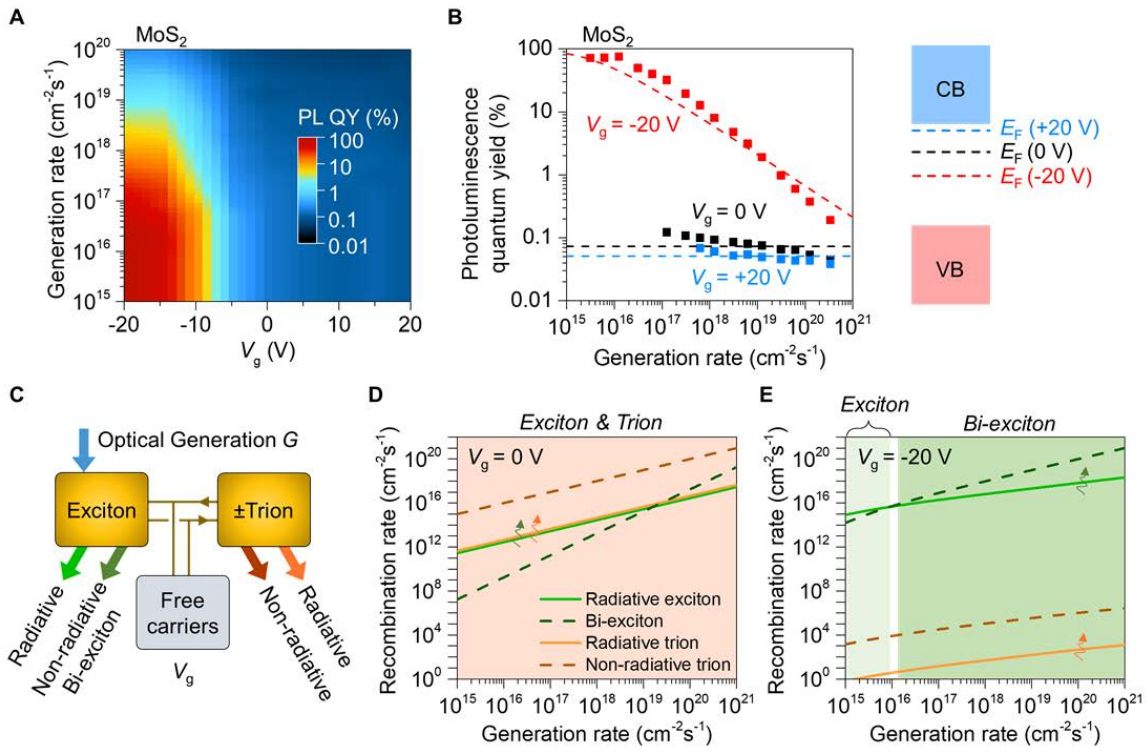

Figure 2.3: **Near-unity PL QY in MoS_2 by electrostatic doping compensation.** (A) A color plot of MoS_2 PL QY vs G and V_g. (B) The MoS_2 PL QY vs G at $V_g = +20$ V (negative trions), 0 V (negative trions) and -20 V (no trions). Points, experimental data; dashed lines, model. Illustration of Fermi level position for different V_g on the right side of the panel. (C) Exciton and trion recombination pathways in TMDC materials. (D) Calculated radiative and nonradiative recombination rates of excitons and trions in MoS_2 at $V_g = 0$ V, and (E) -20 V.

At low exciton density ($Tn_X << 1$), the trion and exciton densities are mutually proportional ($n_T \approx TNn_X$), but at high exciton density ($Tn_X >> 1$), the trion concentration asymptotically approaches the background electron concentration ($n_T \approx N$). Numerically solving equations (1) and (3) provides exciton and trion densities for any generation rate G and gate voltage V_g. This model well-describes the MoS_2 QY data shown in Fig. 2.3B. By fitting the experimental data to the model, we extract $\tau_{Tr}^{-} = 110$ ns; $\tau_{Tnr}^{-} = 50$ ps; $\tau_{Xr} = 8$ ns; $C_{EEA} = 3.5$ cm^{2}s^{-1}. Excitons are radiative, while trions and exciton-exciton annihilation are nonradiative. Specifically, the extracted trion nonradiative lifetime is almost three orders of magnitude lower than the radiative lifetime of trions, implying that the dominant trion recombination pathway is nonradiative. This could be the result of a geminate Auger-like process where the electron provides the third particle required for momentum conservation.

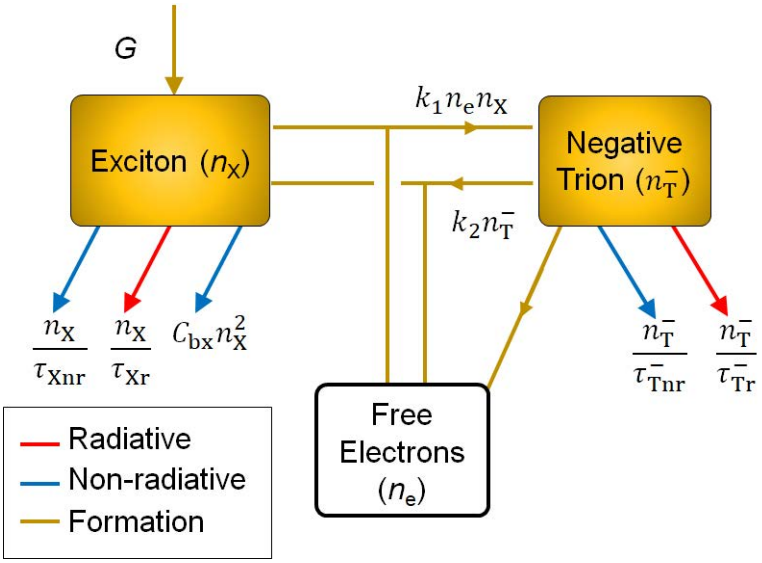

Figure 2.4: **Components of the kinetic model.** Exciton and trion recombination pathways in TMDC materials.

Nonradiative Auger-like recombination of trions has also been identified in doped quantum dots [23]. On the other hand, the model does not require an exciton nonradiative lifetime to fit the data, highlighting that pure exciton recombination is entirely radiative. At high exciton densities (i.e., high generation rates), nonradiative exciton-exciton annihilation dominates. At a specific generation rate G, the gate voltage changes the relative populations of excitons and trions, resulting in different recombination pathways dominating (Fig. 2.3D and E). As-exfoliated monolayer MoS_2 is electron-rich due to donor-like chalcogenide vacancies, placing the Fermi level close to the conduction band [24]. Thus, for $V_g \geq 0$ V, the trion nonradiative recombination rate dominates for all G, resulting in the low observed QY (Fig. 2.3D). On the other hand, by applying negative V_g the background electron concentration reduces and the majority of the quasiparticles are neutral excitons (Fig. 2.4). This is validated by the spectral shift in Fig. 2.1B. In this regime, the exciton radiative recombination rate dominates (Fig. 2.3E) and the observed QY is near-unity at low generation rates. At high generation rates, the exciton recombination rate changes as $G^{-0.5}$ due to exciton-exciton annihilation (Fig. 2.3E). This causes a droop in the QY (Fig. 2.3B).

We also studied the V_g and G dependence of PL QY for monolayers of WS_2, WSe_2, and $MoSe_2$. We find that the same model accurately describes these TMDCs (table 2.1). Similar to MoS_2, WS_2 monolayers are inherently n-doped due to sulfur vacancies and reach near-unity QY at $V_g = -20$ V (Fig. 2.7) [25].

In contrast, WSe_2 and $MoSe_2$ are nearly intrinsic at $V_g = 0$ V (Fig. 2.5A and B, $MoSe_2$ data in Fig. 2.6).Thus, exciton radiative recombination dominates at near-zero V_g and low G, resulting in the highest measured QY of $\sim 8\%$ (Fig. 2.5C). Positive and negative V_g move

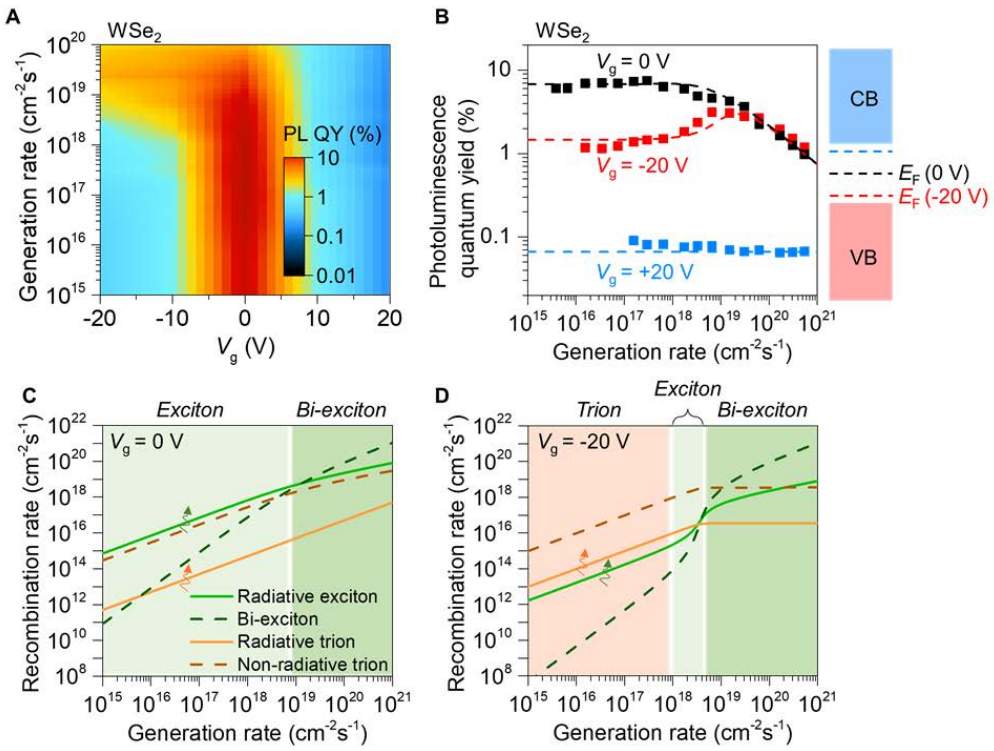

Figure 2.5: **PL QY versus generation rate in WSe_2 monolayers.** (A) A color plot of PL QY vs G and V_g in WSe_2. (B) The PL QY vs G at $V_g = +20$ V (negative trions), 0 V (no trions) and -20 V (positive trions). Points, experimental data; dashed lines, model. Illustration of Fermi level position for different V_g on the right side of the panel. (C) Radiative and nonradiative recombination rates of excitons and trions in WSe_2 at $V_g = 0$ V, and (D) -20 V. At $V_g = -20$ V, recombination rate shows the effect of positive trion saturation leading to the observed bump in (B).

the Fermi level closer to the conduction band and the valence band, respectively (Fig. 2.5B). At $V_g = +20$ V and -20 V, the negative and positive trion nonradiative recombination rates dominate, respectively, lowering the QY. Notably, at $V_g = -20$ V the QY increases with G from $10^{18} < G < 10^{19}$ cm^{-2}s^{-1}. This perplexing behavior is also well captured by our model. Specifically, at $G = 10^{18}$ cm^{-2}s^{-1}, the trion concentration saturates to the total charge concentration, beyond which excess excitons cannot form trions (Fig. 2.6). The neutral exciton recombination pathway then dominates, increasing the QY until exciton-exciton annihilation takes over (Fig. 2.5D). Finally, unlike sulfur-based TMDCs, selenide-based TMDCs do not achieve near-unity QY even when their Fermi levels are near mid-gap. The reason could either be the presence of an indirect bandgap near the direct bandgap [26, 27], or dark excitons [28].

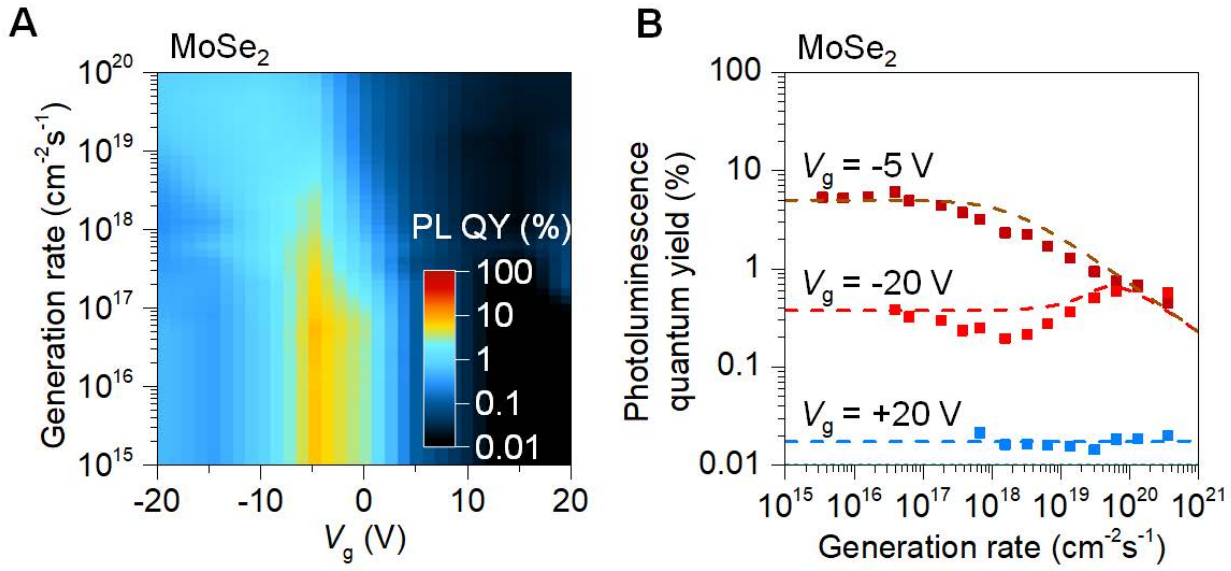

Figure 2.6: **PL QY versus generation rate in $MoSe_2$ monolayers.** (A) A color plot of PL QY vs G and V_g in $MoSe_2$. (B) The PL QY vs G at $V_g = +20$ V, -5 V and -20 V. Points, experimental data; dashed lines, model. Illustration of Fermi level position for different V_g on the right side of the panel.

TFSI-treated monolayer MoS_2 was previously shown to exhibit near-unity PL QY, but the underlying enhancement mechanism was unclear. Here we show that the effect of the treatment is electron counterdoping, justified by both PL QY and time resolved PL (TRPL) measurements. TFSI-treated MoS_2 and an untreated sample at $V_g = -20$ V have similar PL QY over five orders of magnitude variation in G (Fig. 2.5A). They also have comparable TRPL decay at a low pump fluence of 5 nJcm^{-2}, with respective lifetimes of 10.2 ns and 6.9 ns (Fig. 2.8B). Additionally, their TRPL lifetimes match closely for all fluence (Fig. 2.8C, Fig. 2.9). The Lewis acid nature of TFSI is well-established in organic chemistry [29]. Our results depict that TFSI acts as a Lewis acid by withdrawing electrons from (i.e., hole doping) TMDCs via surface charge transfer. This is further validated by the observation of a threshold voltage shift in TMDC transistors after TFSI treatment, consistent with hole doping (Fig. 2.10). Finally, the reduction of PL QY in selenide-based TMDCs after TFSI treatment [16] is also consistent with the gated PL measurements, and the fact that these materials are initially close to intrinsic.

A generic question arises whether the photophysics observed here is generic to all excitonic materials. If excitons are less susceptible to defect assisted nonradiative recombination, perhaps other low dimensional semiconductors such as quantum dots, nanowires and platelets, molecular systems such as C_{60} can reach high QY by removing excess carriers from them.

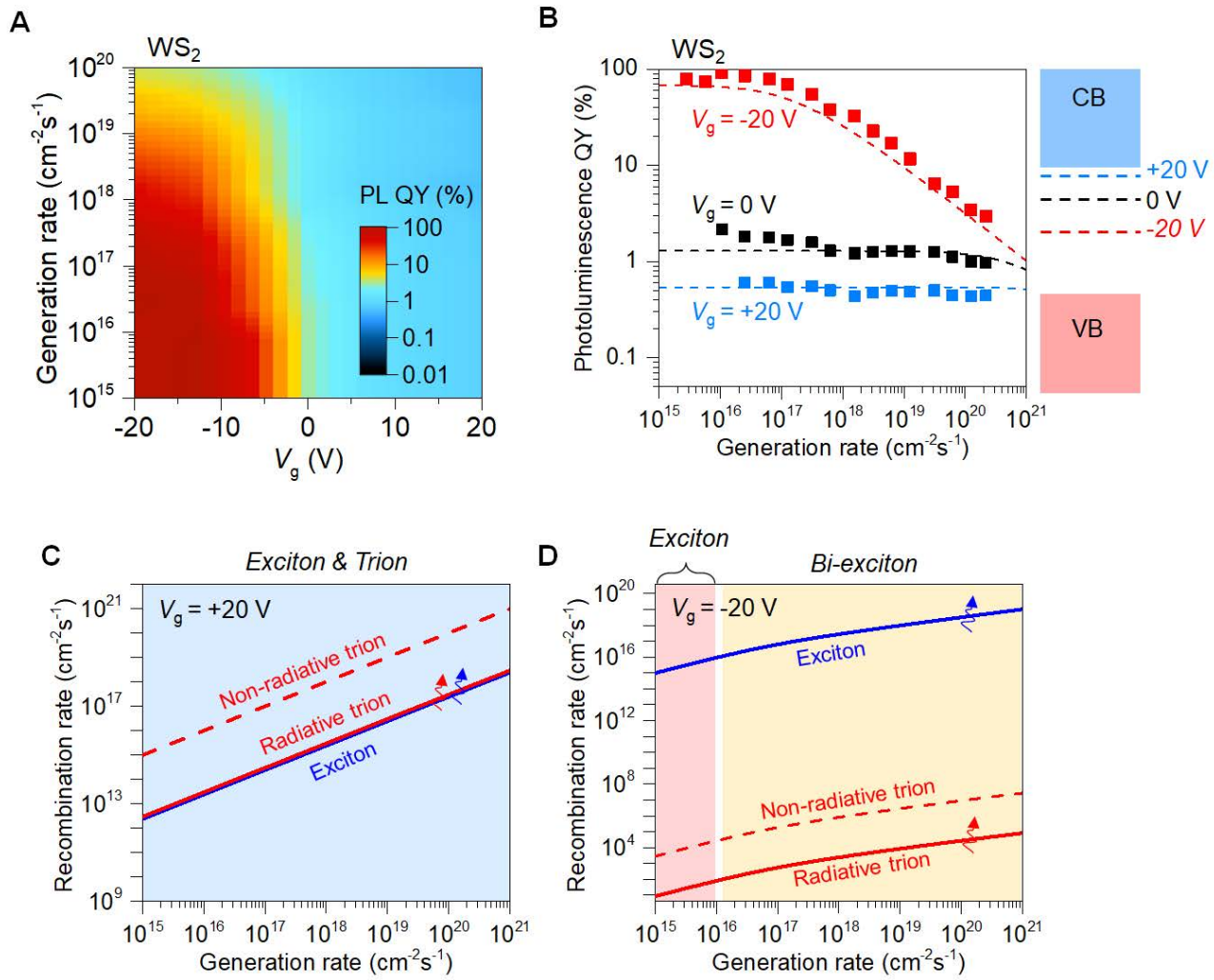

Figure 2.7: **PL QY versus generation rate in WS_2 monolayers.** (A) A color plot of WS_2 PL QY vs G and V_g. (B) The WS_2 PL QY vs G at $V_g = +20$ V (negative trions), 0 V (negative trions), and -20 V (no trions). Points, experimental data; dashed lines, model. Illustration of Fermi level position for different V_g on the right side of the panel. (C) Radiative and nonradiative recombination rates of excitons and trions in WSe_2 at $V_g = 0$ V, and (D) -20 V.

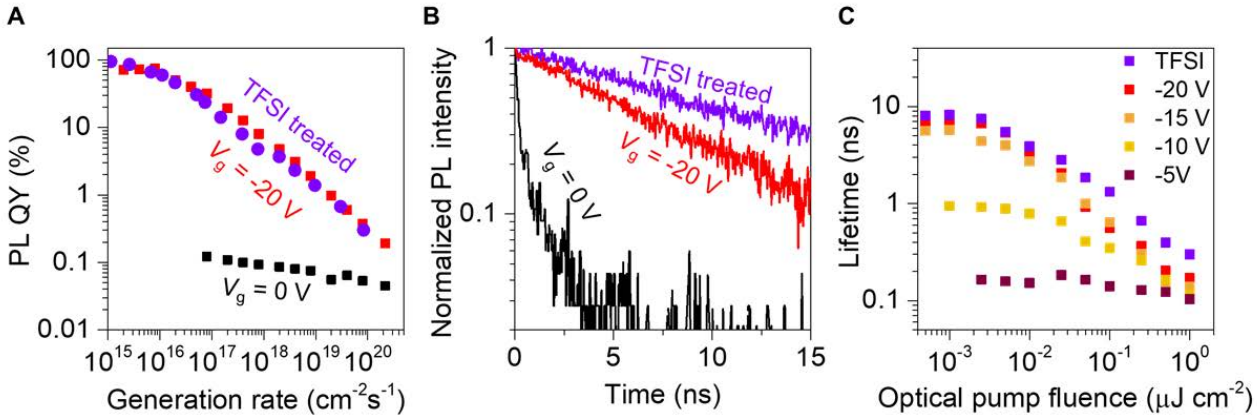

Figure 2.8: **Comparison of electrostatic doping and TFSI treatment.** (A) QY vs G for TFSI-treated and electrostatically-doped monolayer MoS_2. (B) TRPL of a TFSI-treated MoS_2 (purple), and a MoS_2 device under $V_g = 0$ V (black), $V_g = -20$ V (red) at pump fluence of 5 nJcm^{-2}. (C) PL lifetime vs optical pump fluence for TFSI-treated MoS_2 and a MoS_2 device under various gate voltages V_g. Increasing V_g decreases TRPL lifetime since trions have a significantly shorter lifetime than excitons. Increasing fluence decreases the lifetime due to exciton-exciton annihilation.

Semiconducting quantum dots (QD) are important for a number of practical applications and can be excitonic due to confinement. Ligand chemistry plays a big role in achieving high efficiency in colloidal QDs, but their role is not well understood. Often the improvement by ligands is attributed to the passivation of the surface dangling bonds, however ligands has also been shown to dope the semiconductor nanocrystals by surface charge transfer. Preliminary measurements in Fig. 2.11 show electrostatic counterdoping can improve PL intensity of QD.

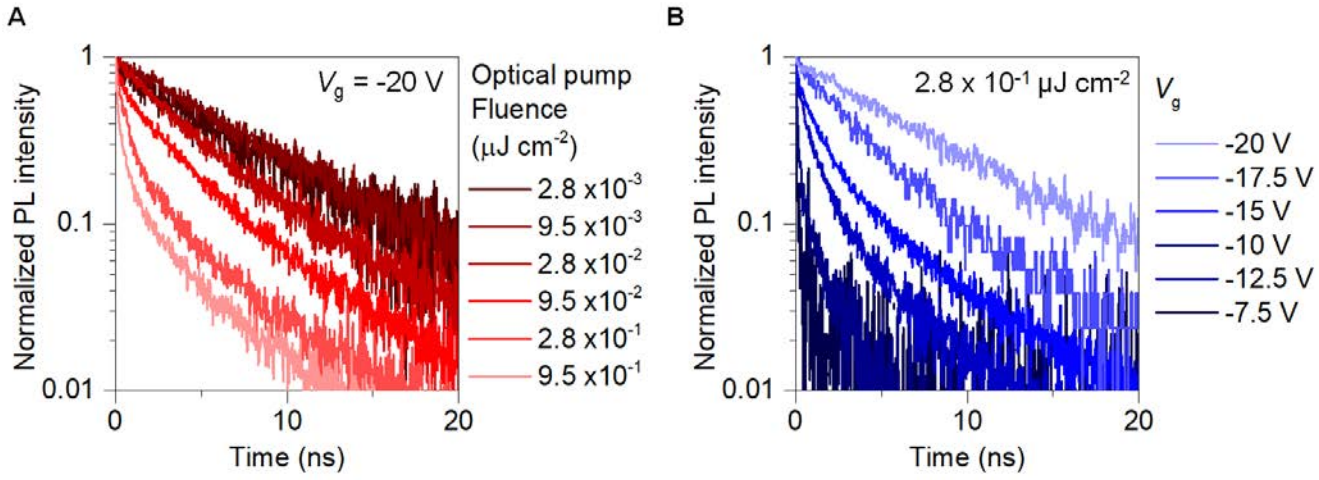

Figure 2.9: **Time-Resolved PL of the MoS_2 under different optical pump fluence and V_g.** (A) Time-resolved PL emission under different optical pump fluence at $V_g = -20$ V. (B) Time-resolved PL of the MoS_2 monolayer under different V_g at an optical pump fluence of 2.8×10^{-1} μJcm^{-2}. Note that the lifetime for V_g greater than -7.5 V is shorter than the instrument response function width.

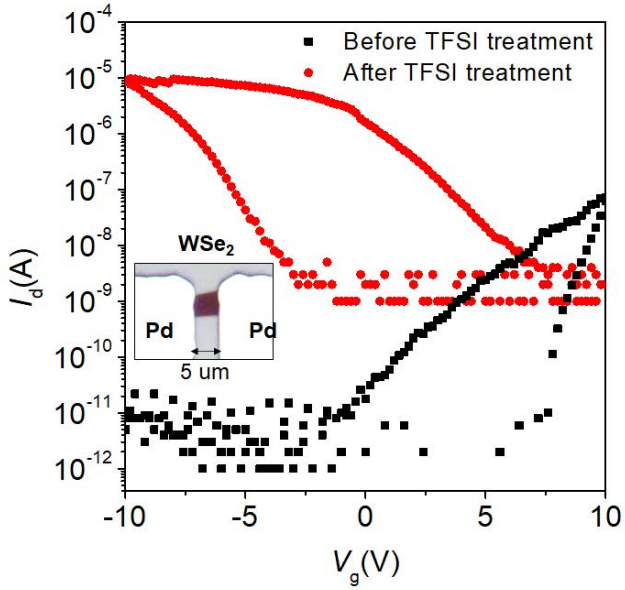

Figure 2.10: **The effect of TFSI treatment on a WSe_2 transistor.** $I_d - V_g$ characteristics of a 3 layer$-WSe_2$ transistor contacted by Pd before and after TFSI treatment.

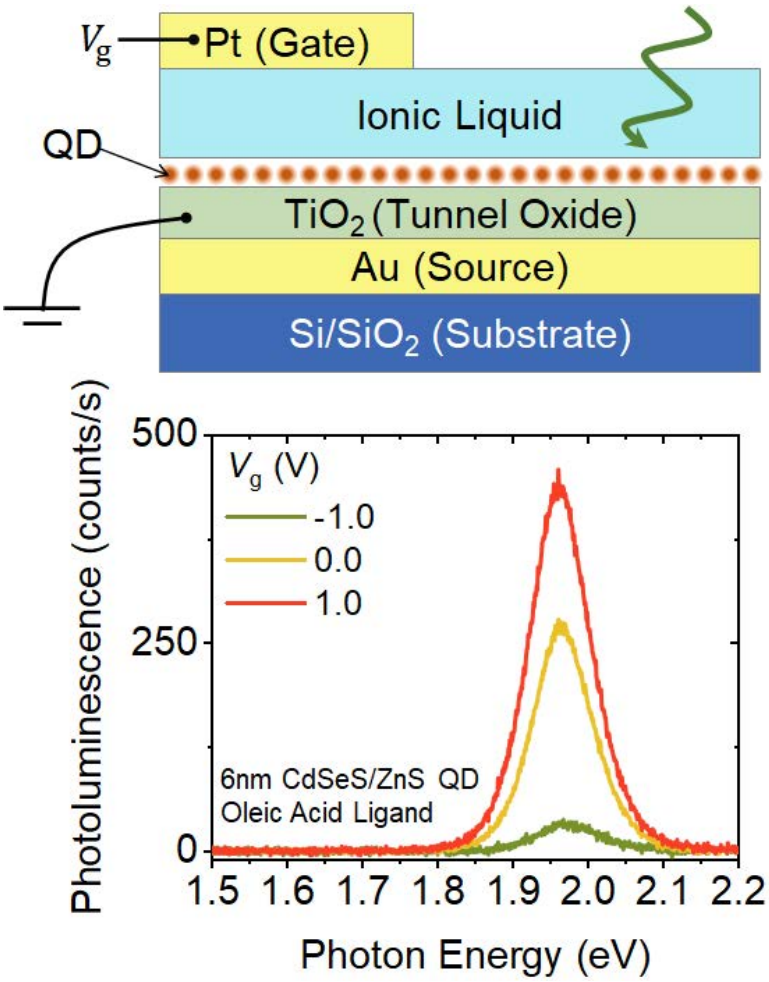

Figure 2.11: **QD gated PL.** Device structure and PL spectra at different gate voltages for a QD monolayer film.

	$\mathbf{MoS_2}$	$\mathbf{WS_2}$	$\mathbf{MoSe_2}$	$\mathbf{WSe_2}$
τ_{Xr} (ns)	8	2	80	16.7
τ_{Xnr} (ns)			26.7	1.9
τ_{Tr}^{-} (μs)	0.11	0.032	4.4	0.33
τ_{Tnr}^{-} (ns)	0.05	0.1	0.066	0.033
τ_{Tr}^{+} (μs)			50	1
τ_{Tnr}^{+} (ns)			50	1
T^{-} (cm^2)	2×10^{-11}	5×10^{-12}	3×10^{-12}	2.5×10^{-11}
T^{+} (cm^2)			1×10^{-10}	3.5×10^{-10}
C_{EEA} ($\mathrm{cm}^2\mathrm{s}^{-1}$)	3.5	2.4	0.03	0.06

Table 2.1: **Kinetic Model parameters.** Parameters used in the model at room temperature.

2.3 Summary

We have achieved near-unity PL QY in chemically-untreated sulfur-based TMDCs at room temperature using only electrostatic doping. The QY is highest when the monolayers are intrinsic, implying that all neutral excitons radiatively recombine even in the presence of defects. While near-unity QY is commonly observed in organic dye molecules, it is uncommon in conventional inorganic semiconductors. This work establishes TMDC monolayers as a unique choice for optoelectronics as they exhibit near-unity PL QY without the stringent requirement for low defect density. This electrostatic PL enhancement scheme is simple and general enough to be applied to other excitonic systems without the need for material-specific passivation techniques.

2.4 Experimental and Theoretical Details

Device Fabrication

MoS_2 (SPI supplies), WS_2 (HQ Graphene), WSe_2 (HQ Graphene) and $MoSe_2$ (HQ Graphene) were mechanically exfoliated on top of poly(methyl methacrylate) (PMMA, 100 nm), which was spin-coated on SiO_2 (50 nm)/ p^{++} Si substrate. Monolayers were identified by optical contrast. 40 nm thick Au contacts were evaporated on a sacrificial 280 nm $SiO_2/p^{++}Si$, and then picked up and placed on the monolayer by a pick-and-place dry transfer method, using PMMA as the transfer medium. A window in the top PMMA was opened by electron-beam lithography to expose the Au contact pad for electrical probing. The monolayers were electrically grounded by the Au source contact, and the back-gate voltage was applied to the $p^{++}Si$ substrate.

Electrical and Optical Characterization

Voltage was applied on the device gate electrode from a Keithley 2410 Source Meter, while the Au source contact was grounded. The PL QY was measured using a customized micro-PL instrument described in detail in previous studies [11]. An Ar ion laser with a 514.5 nm line was used as the excitation source. Time-resolved PL measurements were collected using a time-correlated single photon counting (TCSPC) module. A monochromated 514 nm line from a supercontinuum laser was used as the excitation source. PL images were taken in a florescence microscopy setup using a 470 nm LED as the excitation source and an Andor Luca CCD as the detector. All measurements reported in this paper were taken at room temperature, in an ambient lab environment. Transistor I_d-V_g characteristics were measured using an Agilent B1500A semiconductor parameter analyzer.

Measurement Accuracy and Precision

A detailed overview of the calibration method used to confirm the accuracy of the setup is provided in our previous work [11]. The optical interference from SiO_2/Si substrates was quantitatively studied in our previous work [11] and has been taken into account when PL QY is calculated. The interference alters both the light absorption of the monolayers and their PL emission. The coupling factor F depends on the thickness of SiO_2 (Fig. 2.12A). Two control experiments have been performed to quantitatively confirm the factors:

i) The coupling factors are extracted by PL and Raman spectroscopy of the same monolayer WSe_2 on SiO_2/Si substrates with different SiO_2 thicknesses. The values acquired from experimental results agree with the theory and simulations [30].

ii) The factors are also confirmed using TFSI-treated MoS_2 as a reference. Monolayer MoS_2 with near-unity PL QY has a TRPL lifetime of 10 ns, independent of SiO_2 thickness and choice of substrate. TRPL of TFSI-treated MoS_2 monolayers on 50 nm, 90 nm and 260 nm SiO_2/Si substrates shows 10 ns PL decay time (Fig. 2.12B). Even though these monolayers have near-unity PL QY, they show varied PL intensities corresponding to the varying coupling factor for different substrates (Fig. 2.12C). Therefore, the coupling factor can be extracted from the integrated PL counts (Fig. 2.12D), which matches with the transfer matrix simulation (Fig. 2.12A).

We now elaborate on the precision of the measurement. The QY is calculated by dividing the CCD counts (N) by the product of pump power (P) and coupling factor (F), i.e.

$$QY = \frac{N}{F * P} \tag{2.6}$$

. The uncertainty or standard deviation of PL QY can be written as

$$\sigma_{QY} = QY\sqrt{\frac{\sigma_P^2}{P^2} + \frac{\sigma_N^2}{N^2} - \frac{2\sigma_{PN}}{NP} + \frac{\sigma_F^2}{F^2}} \tag{2.7}$$

where P and σ_P is the measured laser power and the corresponding uncertainty, N and σ_N is the measured CCD counts and corresponding uncertainty, and F and σ_F is the light coupling

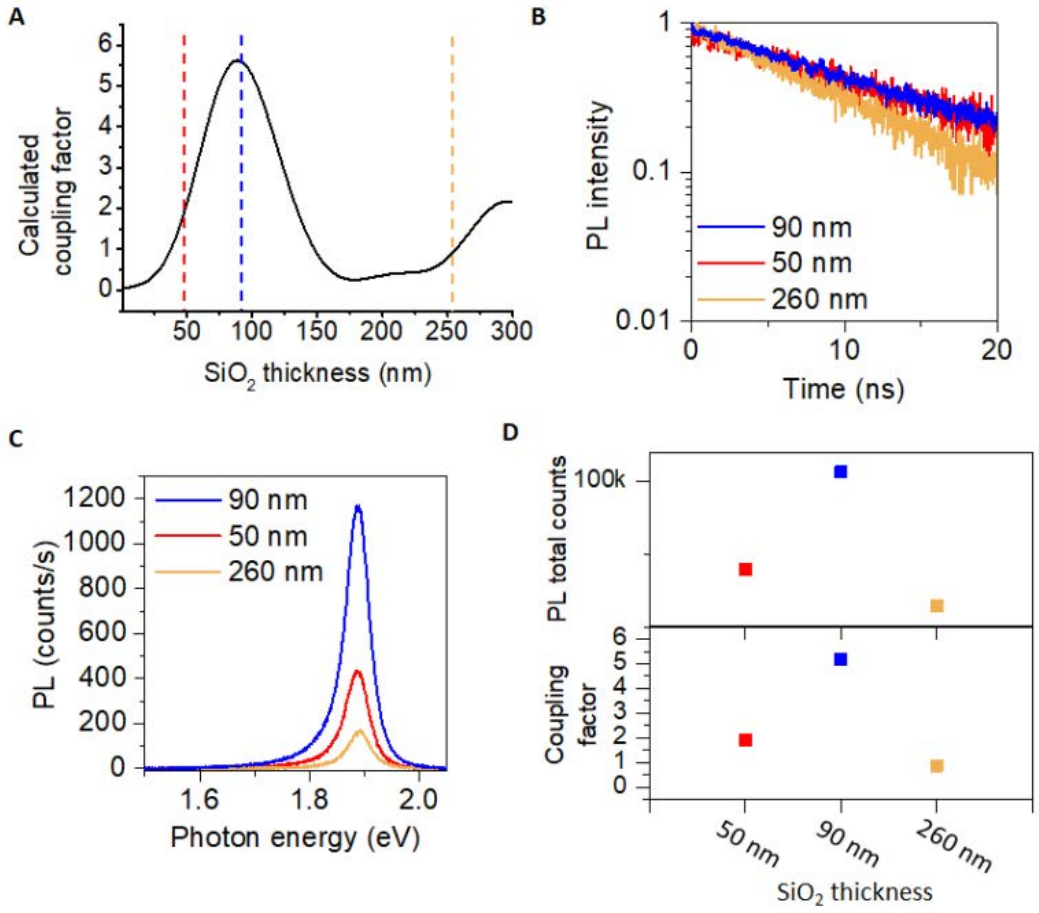

Figure 2.12: **. Calibration for optical interference from SiO_2/Si substrate.** (A) Calculated coupling factor as a function of the SiO_2 thickness. (B) TRPL of the MoS_2 monolayers prepared on 50 nm, 90 nm and 260 nm SiO_2/Si substrates and (C) the corresponding PL spectra. (D) Extracted coupling factor from the measured PL total counts.

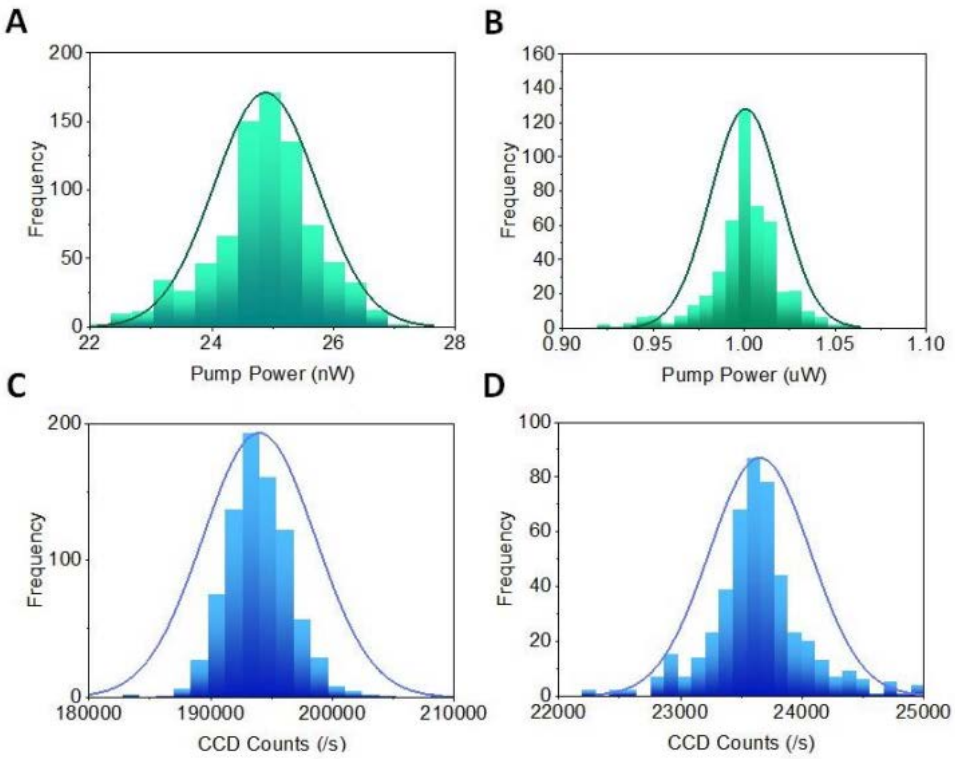

Figure 2.13: **Distribution of laser power and CCD counts.** (A,B) Distribution of laser power with repeated measurements when set to 25 nW and 1 μW. (C, D) Distribution of the corresponding CCD counts.

coefficient and the corresponding uncertainty [31]. Note that the laser power and the CCD counts are correlated, so their covariance must be considered. We show the distribution of laser power and corresponding distribution of CCD counts in Fig. 2.13 when the power was set to 25 nW and 1 μW, respectively. The variances σ_N, σ_P and covariance σ_{PN} can be can be calculated from this measurement. Furthermore, there is a 5% variation in the dielectric thickness, which leads to a relative error of $\sigma_F/F = 11\%$ in the coupling factor. Combining all the components described above, the relative error in PL QY of a MoS_2 flake at -20 V at low pump has been calculated to be $\sigma_{QY}/QY = 13\%$.

Reproducibility

To ensure the reproducibility of our results, over 30 MoS_2 devices were measured. All of them show similar results with maximum QYs over 40%. Note that all the data presented in the manuscript is acquired from the same device (the image of this device is shown in Fig. 2.1C). Results obtained from multiple MoS_2 devices are shown in Fig. 2.14D.

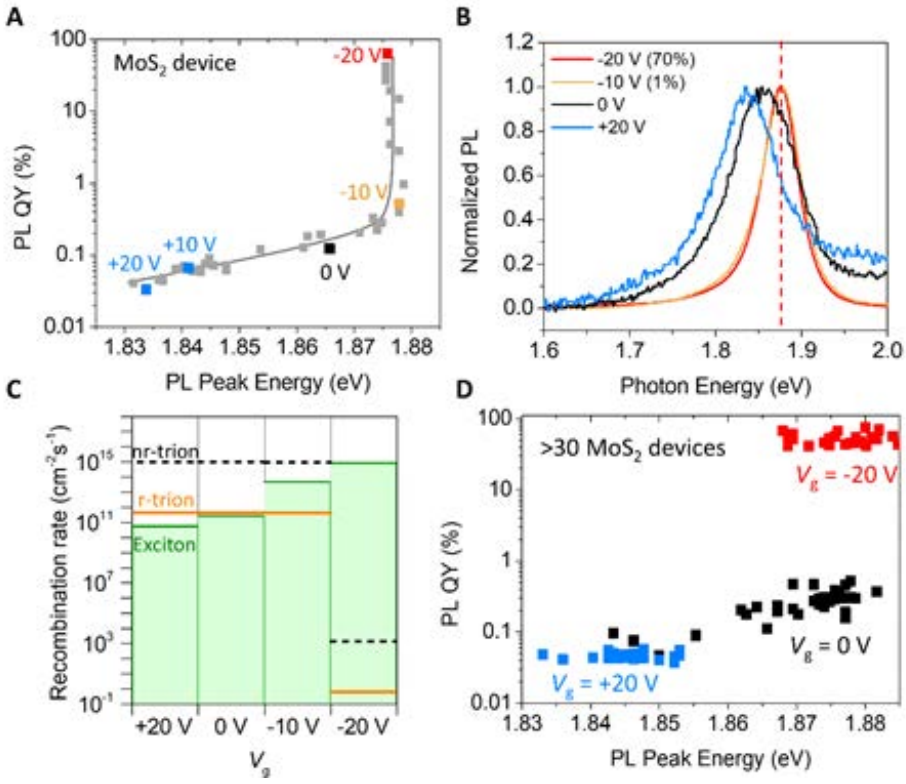

Figure 2.14: **PL QY and PL peak energy as a function of V_g.** (A) PL QY and PL peak energy for a MoS_2 device under various V_g. (B) Normalized PL profiles for V_g = +20 V, 0 V, -10 V and -20 V. (C) Radiative and nonradiative recombination rates of excitons and trions in MoS_2 at V_g = +20 V, 0 V, -10 V and -20 V. (D) PL QY and corresponding PL peak energy obtained from multiple MoS_2 devices.

Kinetic Model

Due to strong Coulomb interaction, electrons and holes generated from above-bandgap photo-excitation create neutral excitons in monolayer TMDC semiconductors. Some of these excitons bind to additional electrons or holes present in the material and form charged excitons, or trions. At higher densities, two excitons interact such that one of them recombines, transferring its energy to the other and sending the constituent carriers to higher energies. This Auger-like process is known as exciton-exciton annihilation. The photoluminescence (PL) of a TMDC semiconductor thus contains a mixed signature of all the quasiparticles present. To determine the PL QY at different generation rates and voltages, we developed a kinetic model combining all quasiparticles in our system.

Prior to light excitation, the total charge in the system comes from electrostatic doping by back-gate voltage application. Ignoring the effects of quantum capacitance, if the total

number of negative and positive charges (i.e., total background electrons and holes) per unit area present in the system are N and P, respectively, then the net charged carrier density in the channel is:

$$N - P = C_{OX}\left(\frac{V_g - V_{th}}{q}\right) \tag{2.8}$$

where C_{OX} is the gate oxide capacitance, V_g is the gate voltage, q is the electronic charge and V_{th} is the threshold voltage. The electron and hole densities are related by

$$\left[\exp\left(\frac{N}{g_{2D}^{c} k_B T}\right) - 1\right]\left[\exp\left(\frac{P}{g_{2D}^{v} k_B T}\right) - 1\right] = \exp\left(-\frac{E_g}{k_B T}\right) \tag{2.9}$$

where $g_{2D}^{c,v}$ is the two-dimensional density of states in the conduction and valence bands, respectively, k_B is the Boltzmann constant, T is the absolute temperature and E_g is the single-electron bandgap. At moderate carrier concentration, this relation simplifies to the more familiar $NP = n_i^2$, where n_i is the intrinsic carrier concentration. Solving these two equations simultaneously gives the background electron and hole densities at a specific gate voltage. As the single electron bandgaps of the monolayer TMDC semiconductors are greater than 2 eV, $\exp\left(-E_g/(k_B T)\right)$ is very small, which at moderate doping conditions implies either $N \approx 0$ or $P \approx 0$. Hence, we can ignore excess electrons (holes) if $V_g < V_{th} (V_g > V_{th})$.

Let us consider the case where electrons are dominant in concentration ($P \approx 0$). We denote the concentrations of neutral excitons, negative trions, and free electrons as n_X,n_T^-, and n_e, respectively. The total negative charge arises from either trions or free electrons:

$$N = n_e + n_T^- \tag{2.10}$$

A kinetic model accounting for exciton and trion formation and recombination, trion disassociation, and exciton-exciton annihilation arises from writing a continuity equation for each type of quasi-particle shown in Fig. 2.10. It is given by the following equations:

$$\frac{dn_X}{dt} = G - \left(\frac{1}{\tau_{Xr}} + \frac{1}{\tau_{Xnr}}\right) n_X - C_{EEA} n_X^2 - k_1 n_X n_e + k_2 n_T^- \tag{2.11}$$

$$\frac{dn_T^-}{dt} = -\frac{dn_e}{dt} = -k_2 n_T^- + k_1 n_X n_e - \left(\frac{1}{\tau_{Tr}^-} + \frac{1}{\tau_{Tnr}^-}\right) n_T^- \tag{2.12}$$

At steady state (i.e., when the generation rate G is time-independent) by setting $d/dt = 0$, this equation gives a Saha equation relating the concentrations of free electron, trion and exciton

$$n_T^- = \frac{k_1}{(k_2 + 1/\tau_{Tr}^- + 1/\tau_{Tnr}^-} n_X n_e = T^- n_e n_X \tag{2.13}$$

This is expected as trion formation is similar to a reversible reaction: electron+ neutral exciton⇌trion. Here the negative trion formation coefficient is given by

$$T^- = \frac{2(2m_e^* + m_h^*)}{4 k_B T m_e^* (m_e^* + m_h^*)} \exp\left(\frac{E_T}{k_B T}\right) = \frac{k_1}{(k_2 + 1/\tau_{Tr}^- + 1/\tau_{Tnr}^-} \tag{2.14}$$

E_T is the trion binding energy, and $m^*_{e,h}$ are the electron and hole effective masses, respectively. Combining these equations we get

$$n_e = \frac{N}{1 + T^- n_X} \tag{2.15}$$

$$n_T^- = \frac{T^- n_X}{1 + T^- n_X) N} \tag{2.16}$$

At low exciton concentration ($T^- n_X << 1$), $n_e \approx N$ and $n_{T^-} \approx T^- N n_X$, so almost all electrons are free and trion concentration increases linearly with exciton concentration. At high exciton concentration ($T^- n_X >> 1$), $n_{T^-} \approx N$, so almost all background electrons become trions and the number of free electrons is very low. This saturation of the number of trions has an experimentally measurable consequence on the PL QY of selenide-based TMDC monolayers. At steady state we get

$$G = \left(\frac{1}{\tau_{Xr}} + \frac{1}{\tau_{Xnr}}\right) n_X + \left(\frac{1}{\tau_{Tr}^-} + \frac{1}{\tau_{Tnr}^-}\right) n_T^- + C_{EEA} n_X^2 = \frac{n_X}{\tau_X} + \frac{n_T^-}{\tau_T^-} + C_{EEA} n_X^2 \tag{2.17}$$

where $\frac{1}{\tau_X} \equiv \frac{1}{\tau_{Xr}} + \frac{1}{\tau_{Xnr}}$ and $\frac{1}{\tau_T^-} \equiv \frac{1}{\tau_{Tr}^-} + \frac{1}{\tau_{Tnr}^-}$, and subscript 'r' and 'nr' indicate the radiative and nonradiative lifetime components, respectively. By using these equations we get

$$G = \frac{n_X}{\tau_X} + \frac{N T^- n_X}{\tau_T^- (1 + T^- n_X)} + C_{EEA} n_X^2 \tag{2.18}$$

$$C_{EEA} T^- n_X^3 + \left(C_{EEA} + \frac{T^-}{\tau_X}\right) n_X^2 + \left(\frac{1}{\tau_X} + \frac{N T^-}{\tau_T^-} - G T^-\right) - G = 0 \tag{2.19}$$

This is a third order polynomial of n_X. This fact, in addition to the form of the equation, ensures one real positive solution of n_X for any positive value of generation rate G. They yield n_T^- and n_e. If there are positive trions, similar equations with different constants τ_{Tr}^+,T^+ can be written for the positive trion density n_T^+, and the steady state rate equation becomes

$$G = \frac{n_X}{\tau_X} + \frac{N T^- n_X}{\tau_T^- (1 + T^- n_X)} + \frac{P T^+ n_X}{\tau_T^+ (1 + T^+ n_X)} + C_{EEA} n_X^2 \tag{2.20}$$

which is a fifth order polynomial of n_X and can be solved given N,P, and G. PL from the TMDC monolayer combines emission from neutral, positive and negative trions. The quantum yield is the ratio of the total radiative recombination rate of all quasiparticles to the generation rate

$$QY = \frac{1}{G}\left(\frac{n_X}{\tau_{Xr}} + \frac{n_T^-}{\tau_{Tr}^-} + \frac{n_T^+}{\tau_{Tr}^+}\right) \tag{2.21}$$

Parameter Extraction Procedure

We use both steady state PL QY and gate dependent time resolved PL experimental data to fit the previous model.

Low Generation Rate, $Vg \approx V_{th}$

At gate voltage near threshold $Vg \approx V_{th}$, the background carrier concentration is very low $N = n_i \approx 0$. As the number of trions is limited by the number of electrons or holes, there will be almost no trions. In this condition, at low generation the rate equation can be simplified to

$$\frac{dn_X}{dt} \approx G - \left(\frac{1}{\tau_{Xr}} + \frac{1}{\tau_{Xnr}}\right) n_X \tag{2.22}$$

where the EEA and trion terms are ignored. If an impulse generation (pulsed laser source) is used, then

$$G = n_0 \delta(t) \tag{2.23}$$

$$\Rightarrow n_X(t) = n_0 \exp -t \left(\frac{1}{\tau_{Xr}} + \frac{1}{\tau_{Xnr}}\right) \tag{2.24}$$

Therefore, under conditions of low generation and $Vg \approx V_{th}$ the lifetime from a time resolved photoluminescence measurement is the effective lifetime $\frac{1}{\tau_{Xr}} + \frac{1}{\tau_{Xnr}}$. The PL at this condition is solely from neutral excitons, and so the steady state PL QY becomes

$$QY = \frac{n_X \tau_{Xr}}{n_X(1/\tau_{Xr} + 1/\tau_{Xnr})} = \frac{\tau_{Xnr}}{\tau_{Xr} + \tau_{Xnr}} \tag{2.25}$$

From this we get separate values of τ_{Xr} and τ_{Xnr}. For sulfide-based TMDCs $1/\tau_{Xnr} \sim 0$, leading to near unity PL QY.

High Generation Rate, $Vg \approx V_{th}$

At high generation rates exciton-exciton annihilation occurs, the effects of which clearly show up in both TRPL and steady state PL QY data. In the steady state PL QY data, the generation rate at which the droop starts to occur gives us the value of exciton-exciton annihilation coefficient C_{EEA}. If G_0 is the generation rate at which PL QY becomes half of low pump PL QY at $Vg \approx V_{th}$, then

$$C_{EEA} n_X^2 = \left(\frac{1}{\tau_{Xr}} + \frac{1}{\tau_{Xnr}}\right) n_X \tag{2.26}$$

$$\Rightarrow n_X = \frac{1}{C_{EEA}} \left(\frac{1}{\tau_{Xr}} + \frac{1}{\tau_{Xnr}}\right) = \frac{1}{C_{EEA}\tau_X} \tag{2.27}$$

$$\Rightarrow G = \frac{1}{\tau_X} \frac{1}{C_{EEA}\tau_X} + C_{EEA} \left(\frac{1}{C_{EEA}\tau_X}\right)^2 \tag{2.28}$$

$$\Rightarrow C_{EEA} = \frac{2}{\tau_X^2 G_0} \tag{2.29}$$

Extracting G_0 from steady state PL QY and using previously estimated lifetimes, we can now calculate C_{EEA}. All neutral exciton related parameter values ($\tau_{Xr}, \tau_{Xnr}, C_{EEA}$) are now known.

Low Generation Rate, $V_g >> V_{th}$

In this condition, there is a considerable amount of background electrons in the system. At low generation rates almost all the excitons become trions, as the number of excitons is orders of magnitude lower than the number of background electrons. Therefore, the emission from the material in this case mostly comes from trions (Fig. 2.1B). In this case, the steady state PL QY gives the ratio of trion lifetimes, whereas the TRPL lifetime provides the trion effective lifetime. Similar to the analysis of section I, we can now calculate τ_{Tr}^{-} and τ_{Tnr}^{-} from TRPL and steady state PL QY data in this condition.

Low Generation Rate, $V_g << V_{th}$

The same analysis as the previous section at low generation and $V_g << V_{th}$ gives τ_{Tr}^{+} and τ_{Tnr}^{+}.

2.5 References

[1] Ashwin Ramasubramaniam. Large excitonic effects in monolayers of molybdenum and tungsten dichalcogenides. *Physical Review B*, 86(11):115409, 2012.

[2] Kin Fai Mak, Changgu Lee, James Hone, Jie Shan, and Tony F Heinz. Atomically thin MoS_2: a new direct-gap semiconductor. *Physical Review Letters*, 105(13):136805, 2010.

[3] Andrea Splendiani, Liang Sun, Yuanbo Zhang, Tianshu Li, Jonghwan Kim, Chi-Yung Chim, Giulia Galli, and Feng Wang. Emerging photoluminescence in monolayer MoS_2. *Nano Letters*, 10(4):1271–1275, 2010.

[4] Freddie Withers, O Del Pozo-Zamudio, A Mishchenko, AP Rooney, Ali Gholinia, K Watanabe, T Taniguchi, Sarah J Haigh, AK Geim, AI Tartakovskii, et al. Light-emitting diodes by band-structure engineering in van der Waals heterostructures. *Nature Materials*, 14(3):301–306, 2015.

[5] Long Ju, Lei Wang, Ting Cao, Takashi Taniguchi, Kenji Watanabe, Steven G Louie, Farhan Rana, Jiwoong Park, James Hone, Feng Wang, et al. Tunable excitons in bilayer graphene. *Science*, 358(6365):907–910, 2017.

[6] Jason S Ross, Sanfeng Wu, Hongyi Yu, Nirmal J Ghimire, Aaron M Jones, Grant Aivazian, Jiaqiang Yan, David G Mandrus, Di Xiao, Wang Yao, et al. Electrical control of neutral and charged excitons in a monolayer semiconductor. *Nature Communications*, 4(1):1–6, 2013.

[7] Pasqual Rivera, Kyle L Seyler, Hongyi Yu, John R Schaibley, Jiaqiang Yan, David G Mandrus, Wang Yao, and Xiaodong Xu. Valley-polarized exciton dynamics in a 2D semiconductor heterostructure. *Science*, 351(6274):688–691, 2016.

[8] Kin Fai Mak, Keliang He, Changgu Lee, Gwan Hyoung Lee, James Hone, Tony F Heinz, and Jie Shan. Tightly bound trions in monolayer MoS_2. *Nature Materials*, 12(3):207–211, 2013.

[9] Rafik Addou, Luigi Colombo, and Robert M Wallace. Surface defects on natural MoS_2. *ACS Applied Materials & Interfaces*, 7(22):11921–11929, 2015.

[10] Hans J Queisser and Eugene E Haller. Defects in semiconductors: some fatal, some vital. *Science*, 281(5379):945–950, 1998.

[11] Matin Amani, Der-Hsien Lien, Daisuke Kiriya, Jun Xiao, Angelica Azcatl, Jiyoung Noh, Surabhi R Madhvapathy, Rafik Addou, KC Santosh, Madan Dubey, et al. Near-unity photoluminescence quantum yield in MoS_2. *Science*, 350(6264):1065–1068, 2015.

[12] Hui Fang, Corsin Battaglia, Carlo Carraro, Slavomir Nemsak, Burak Ozdol, Jeong Seuk Kang, Hans A Bechtel, Sujay B Desai, Florian Kronast, Ahmet A Unal, et al. Strong interlayer coupling in van der Waals heterostructures built from single-layer chalcogenides. *Proceedings of the National Academy of Sciences*, 111(17):6198–6202, 2014.

[13] Woong Kim, Ali Javey, Ophir Vermesh, Qian Wang, Yiming Li, and Hongjie Dai. Hysteresis caused by water molecules in carbon nanotube field-effect transistors. *Nano Letters*, 3(2):193–198, 2003.

[14] Yuan Liu, Jian Guo, Enbo Zhu, Lei Liao, Sung-Joon Lee, Mengning Ding, Imran Shakir, Vincent Gambin, Yu Huang, and Xiangfeng Duan. Approaching the schottky–mott limit in van der Waals metal–semiconductor junctions. *Nature*, 557(7707):696–700, 2018.

[15] Bo Liu, Weijie Zhao, Zijing Ding, Ivan Verzhbitskiy, Linjun Li, Junpeng Lu, Jianyi Chen, Goki Eda, and Kian Ping Loh. Engineering bandgaps of monolayer MoS_2 and WS_2 on fluoropolymer substrates by electrostatically tuned many-body effects. *Advanced Materials*, 28(30):6457–6464, 2016.

[16] Matin Amani, Peyman Taheri, Rafik Addou, Geun Ho Ahn, Daisuke Kiriya, Der-Hsien Lien, Joel W Ager III, Robert M Wallace, and Ali Javey. Recombination kinetics and effects of superacid treatment in sulfur-and selenium-based transition metal dichalcogenides. *Nano Letters*, 16(4):2786–2791, 2016.

[17] Shun Lien Chuang. *Physics of photonic devices*, volume 80. John Wiley & Sons, 2012.

[18] WTRW Shockley and WT Read Jr. Statistics of the recombinations of holes and electrons. *Physical Review*, 87(5):835, 1952.

[19] AR Beattie and PT Landsberg. Auger effect in semiconductors. *Proceedings of the Royal Society of London. Series A. Mathematical and Physical Sciences*, 249(1256):16–29, 1959.

[20] Yumeng You, Xiao-Xiao Zhang, Timothy C Berkelbach, Mark S Hybertsen, David R Reichman, and Tony F Heinz. Observation of biexcitons in monolayer WSe_2. *Nature Physics*, 11(6):477–481, 2015.

[21] Marvin Kulig, Jonas Zipfel, Philipp Nagler, Sofia Blanter, Christian Schüller, Tobias Korn, Nicola Paradiso, Mikhail M Glazov, and Alexey Chernikov. Exciton diffusion and halo effects in monolayer semiconductors. *Physical Review Letters*, 120(20):207401, 2018.

[22] J Siviniant, D Scalbert, AV Kavokin, D Coquillat, and JP Lascaray. Chemical equilibrium between excitons, electrons, and negatively charged excitons in semiconductor quantum wells. *Physical Review B*, 59(3):1602, 1999.

[23] Annika Kurzmann, Arne Ludwig, Andreas D Wieck, Axel Lorke, and Martin Geller. Auger recombination in self-assembled quantum dots: quenching and broadening of the charged exciton transition. *Nano Letters*, 16(5):3367–3372, 2016.

[24] Branimir Radisavljevic, Aleksandra Radenovic, Jacopo Brivio, Valentina Giacometti, and Andras Kis. Single-layer MoS_2 transistors. *Nature Nanotechnology*, 6(3):147–150, 2011.

[25] Lingming Yang, Kausik Majumdar, Han Liu, Yuchen Du, Heng Wu, Michael Hatzistergos, PY Hung, Robert Tieckelmann, Wilman Tsai, Chris Hobbs, et al. Chloride molecular doping technique on 2D materials: WS_2 and MoS_2. *Nano Letters*, 14(11):6275–6280, 2014.

[26] Chendong Zhang, Yuxuan Chen, Amber Johnson, Ming-Yang Li, Lain-Jong Li, Patrick C Mende, Randall M Feenstra, and Chih-Kang Shih. Probing critical point energies of transition metal dichalcogenides: surprising indirect gap of single layer WSe_2. *Nano Letters*, 15(10):6494–6500, 2015.

[27] Sujay B Desai, Gyungseon Seol, Jeong Seuk Kang, Hui Fang, Corsin Battaglia, Rehan Kapadia, Joel W Ager, Jing Guo, and Ali Javey. Strain-induced indirect to direct bandgap transition in multilayer WSe_2. *Nano Letters*, 14(8):4592–4597, 2014.

[28] Xiao-Xiao Zhang, Yumeng You, Shu Yang Frank Zhao, and Tony F Heinz. Experimental evidence for dark excitons in monolayer WSe_2. *Physical Review Letters*, 115(25):257403, 2015.

[29] Wanxiang Zhao and Jianwei Sun. Triflimide ($HNTf_2$) in organic synthesis. *Chemical Reviews*, 118(20):10349–10392, 2018.

[30] Der-Hsien Lien, Jeong Seuk Kang, Matin Amani, Kevin Chen, Mahmut Tosun, Hsin-Ping Wang, Tania Roy, Michael S Eggleston, Ming C Wu, Madan Dubey, et al. Engineering light outcoupling in 2D materials. *Nano Letters*, 15(2):1356–1361, 2015.

[31] Leo A Goodman. On the exact variance of products. *Journal of the American statistical association*, 55(292):708–713, 1960.

Chapter 3

Quantum Yield at High Generation Rates

3.1 Introduction

[1]Most optoelectronic devices operate at high photocarrier densities, where all semiconductors suffer from enhanced nonradiative recombination. Nonradiative processes proportionately reduce photoluminescence (PL) quantum yield (QY), a performance metric that directly dictates the maximum device efficiency. Although transition-metal dichalcogenide (TMDC) monolayers exhibit near-unity PL QY at low exciton densities, nonradiative exciton-exciton annihilation (EEA) enhanced by van-Hove singularity (VHS) rapidly degrades their PL QY at high exciton densities and limits their utility in practical applications. Here, by applying small mechanical strain ($< 1\%$), we circumvent VHS resonance and drastically suppress EEA in monolayer TMDCs, resulting in near-unity PL QY at all exciton densities despite the presence of a high native defect density. Our findings can enable light-emitting devices that retain high efficiency at all brightnesses.

3.2 Inhibited Nonradiative Recombination at All Generation Rates

Exciton recombination in TMDC monolayers depends on exciton generation rate, background carrier concentration, and electronic band structure. The combined effect of the first two factors has been studied thoroughly [1], where the photocarrier generation rate (G) and background carrier concentration were tuned by varying the incident pump power and the gate voltage (V_g), respectively, in a capacitor structure. Given pronounced Coulomb interac-

[1]The following section was published in a similar form in Science. (Kim, H.*, Uddin, S.Z.*, Higashitarumizu, N., Rabani, E. and Javey, A., Inhibited nonradiative decay at all exciton densities in monolayer semiconductors, *Science*, 373(6553), pp.448-452, 2021.)

tions, background carriers turn photogenerated excitons into charged trions [2] that mostly recombine nonradiatively [3]. In the absence of background carriers, at low exciton densities, neutral excitons in intrinsic monolayers can recombine completely radiatively even in the presence of defects [4]. However, at high exciton densities, recombination of neutral excitons is dominated by exciton-exciton annihilation (EEA), where an exciton nonradiatively recombines while colliding with another exciton [5, 6]. All excitonic materials found in nature [7] exhibit EEA, which is the primary cause of efficiency roll-off observed in all organic [8] and some inorganic [9, 10] light-emitting devices. The EEA effect has similarities to Auger recombination, which is commonly observed in conventional free-carrier systems and also a prominent cause of efficiency roll-off observed in light-emitting diodes and solar cells [11, 12]. Through the conservation of momentum and energy the participating quasiparticles, EEA depends on the aforementioned third factor: detailed band structure [13, 14].

In this work, we modulate these three factors simultaneously. Along with V_g and pump power, we altered the electronic band structure by applying a uniaxial strain (ϵ). With appropriate strain, all neutral excitons recombined radiatively even at high concentrations in monolayers of WS_2, WSe_2, and MoS_2, resulting in near-unity quantum yield (QY) at all measured generation rates. The density of states of electrons in a two-dimensional (2D) periodic crystal are topologically constrained to exhibit logarithmic van Hove singularities (VHSs) arising from saddle points in the energy dispersion [15]. When the energy of a transition is near the VHS, weak interactions are often intensified by the enhanced density of states (DOS) [16]. From energy and momentum conservation, we showed that as-exfoliated TMDC monolayers exhibited enhanced EEA because the final energy of this process coincided with inherent VHS. Strain drove the final energy away from the VHS resonance and drastically reduced EEA in both sulfur- and selenide based TMDCs. We could uniformly suppress all nonradiative recombination in a centimeter-scale CVD-grown WS_2 monolayer at all generation rates. Monolayer field effect transistor (FET) devices were fabricated on plastic flexible substrate enabling simultaneous modulation of carrier concentration and strain while performing quantitative photoluminescence (PL) QY measurements (device fabrication details are available in the supplementary materials). Fig. 3.1A shows the schematic and optical micrograph of such a device using WS_2 monolayers. Mechanically exfoliated monolayers were transferred to a polyvinyl alcohol (PVA) layer attached to polyethylene terephthalate (PET) handling substrate, a combination selected for its superior strain transfer efficiency [17]. Exfoliated hexagonal boron nitride (hBN; 70 to 100 nm in thickness) and graphene (2 to 5 nm in thickness) were transferred sequentially on the monolayer WS_2 to serve as a gate insulator and gate electrode, respectively. The WS_2 monolayer was electrically grounded and V_g was applied to the top graphene. Bending the PET substrate with positive curvature applied tensile strain to the monolayer in the direction of bending [18]. Applied strain is calculated from geometrical considerations. Generation rate G is the number of excitons created or the number of photons absorbed per-unit area per unit time, which can be tuned by changing the laser intensity.

As-exfoliated monolayer WS_2 is known to be electron-rich. Application of a negative $V_g = -30$ V electrostatically compensated for that unintentional electron doping and ensured

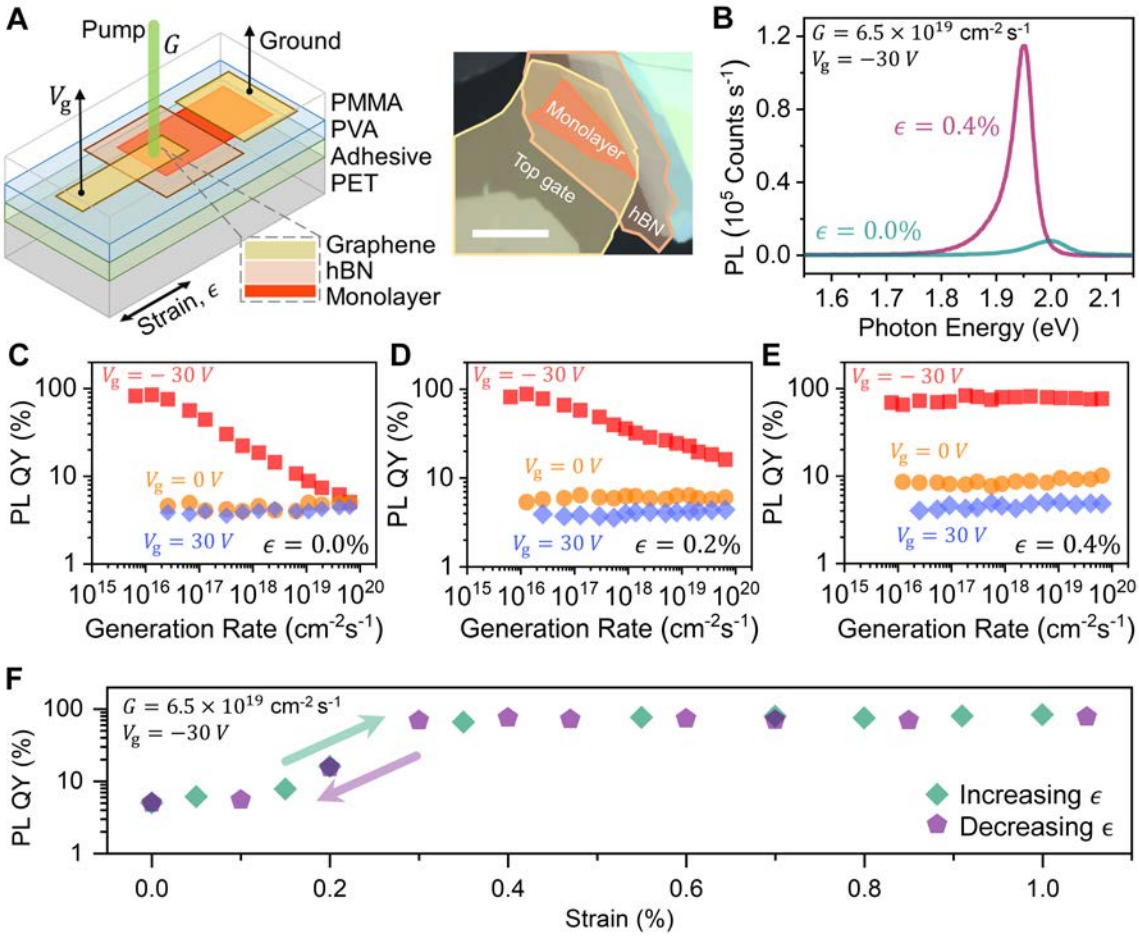

Figure 3.1: **Near-unity PL QY in WS_2 at all generation rates.** (A) Schematic and optical micrograph of the device structure, scale bar is 20 μm. A two-terminal MOS capacitor structure with graphene as source and gate, and hBN as insulator is fabricated on a flexible polymer substrate. (B) Comparison of PL spectra of unstrained and 0.4% strained monolayer WS_2 at a high generation rate of $G = 6.5 \times 10^{19} cm^{-2} s^{-1}$ and a gate voltage of $V_g = -30$ V. (C, D, E) PL QY of monolayer WS_2 as a function of gate voltage, generation rate and strain. (F) PL QY approaching unity with the application of strain at a high generation rate of $G = 6.5 \times 10^{19}$ cm^{-2}s^{-1}.

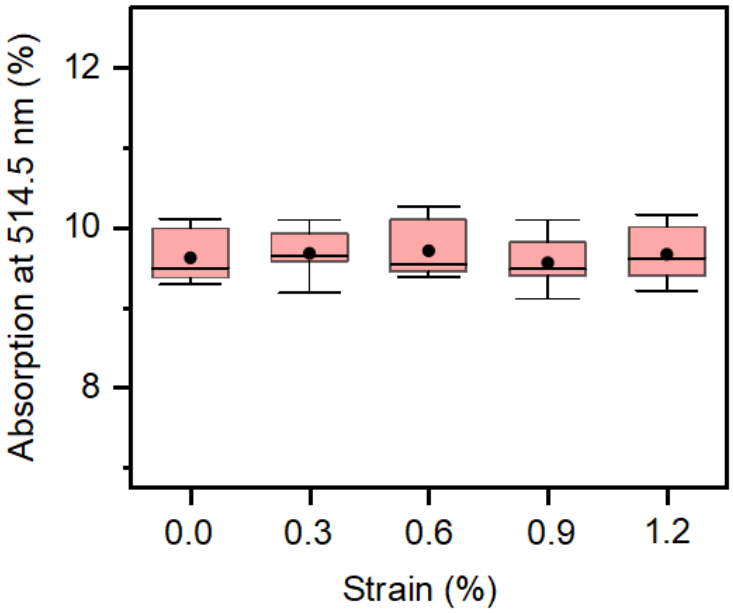

Figure 3.2: **Absorption at excitation wavelength under applied strain.** Absorption of monolayer WS_2 as a function of applied strain at pump laser wavelength ($\lambda = 514.5$ nm).

that the recombination process was dominated by neutral excitons [1]. At this biasing condition, we compared PL spectra of an unstrained and strained WS_2 monolayer at a high generation rate of $G = 6.5 \times 10^{19} cm^{-2} s^{-1}$ (Fig. 3.1B). We observed both a redshift of PL spectra and ~ 15 times enhancement in PL intensity with the application of $\epsilon = 0.4\%$ tensile strain at this high generation rate. Note that, G is independent of strain since absorption at pump wavelength does not change with strain (Fig. 3.2).

Calibrated PL measurements at room temperature were performed to quantitatively extract the QY as a function of ϵ, V_g and G (Fig. 3.1C to F, Fig. 3.3), and Fig. 3.1C shows PL QY as a function of the gate voltage, V_g and the generation rate, G when no strain is applied. At zero and positive gate voltages, background electron concentration of monolayer WS_2 was large and led to formation of negative trions that predominantly recombined nonradiatively, thus yielding a low PL QY. At negative V_g the background electrons were removed, and recombination of neutral excitons dominated. At low generation rates, neutral excitons recombined completely radiatively despite native defect density.

At high generation rates, PL QY rolled off because of EEA. These same results were observed previously for other substrates, such as PMMA and SiO_2 and are quantitatively the same as the results here [1]. With the application of 0.2% tensile strain, the PL QY drop-off at high exciton generation rate was notably reduced for negative V_g. (Fig. 3.1D). For a tensile strain of 0.4% , no PL QY drop-off at high generation rate was observed (Fig. 3.1E). Thus, all nonradiative recombination processes in as-exfoliated monolayer WS_2 were

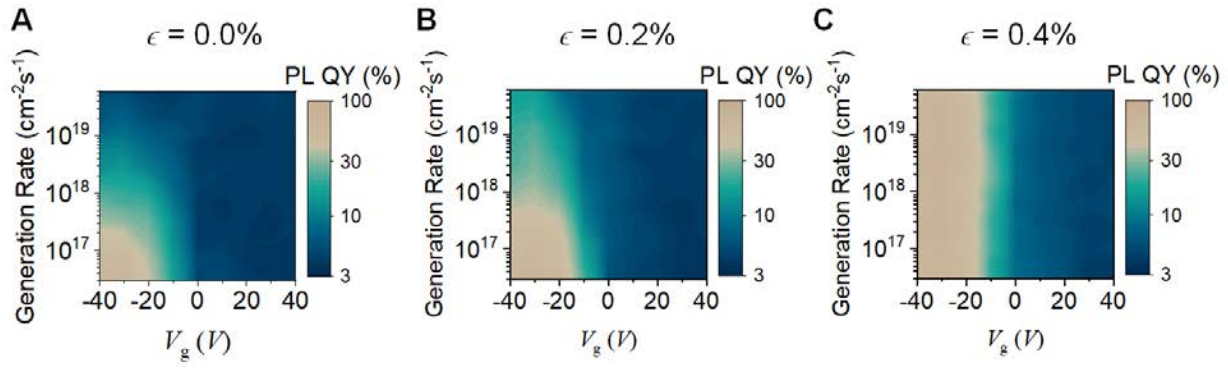

Figure 3.3: **PL QY versus G and V_g in WS_2 at different strains.** A color plot of PL QY in monolayer WS_2 as a function of gate voltages and generation rate with applied strains.

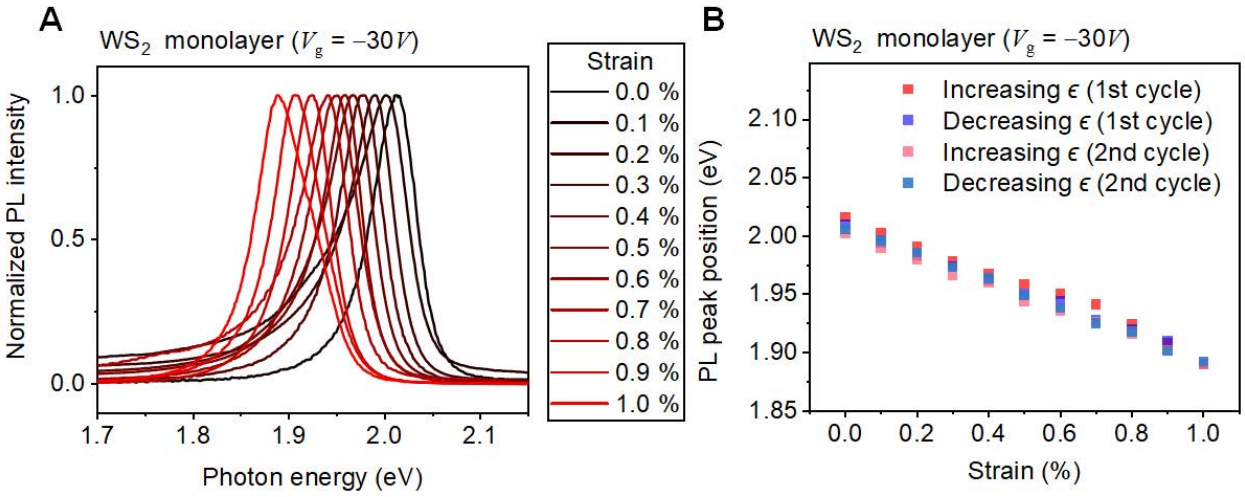

Figure 3.4: **PL peak position shift of monolayer WS_2.** (A) Normalized PL intensity of monolayer WS_2 at $V_g = -30$ V as a function of applied strains. (B) PL peak position during multiple bending and release cycles.

suppressed by applying tensile strain and V_g.

Suppression of EEA is further elucidated in Fig. 3.1F, where we show PL QY as a function of strain at $V_g = -30V$ and at a high generation rate $G = 6.5 \times 10^{19} cm^{-2} s^{-1}$. For no applied strain, PL QY was low at this generation rate, but for a threshold strain of 0.3% PL QY increased sharply and asymptotically approached unity. This PL QY enhancement by strain was also reversible and repeatable, as PL QY traces for increasing and decreasing strain fully overlapped (Fig. 3.4). Such reversibility and repeatability indicates absence of

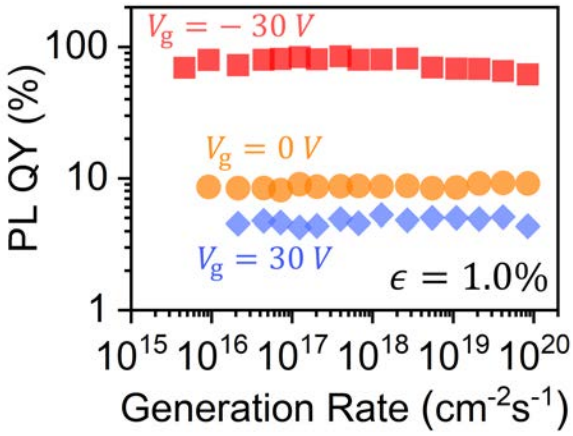

Figure 3.5: **Near-unity PL QY in WS_2 at all generation rates.** PL QY of monolayer WS_2 as a function of gate voltage and generation rate at 1.0% strain.

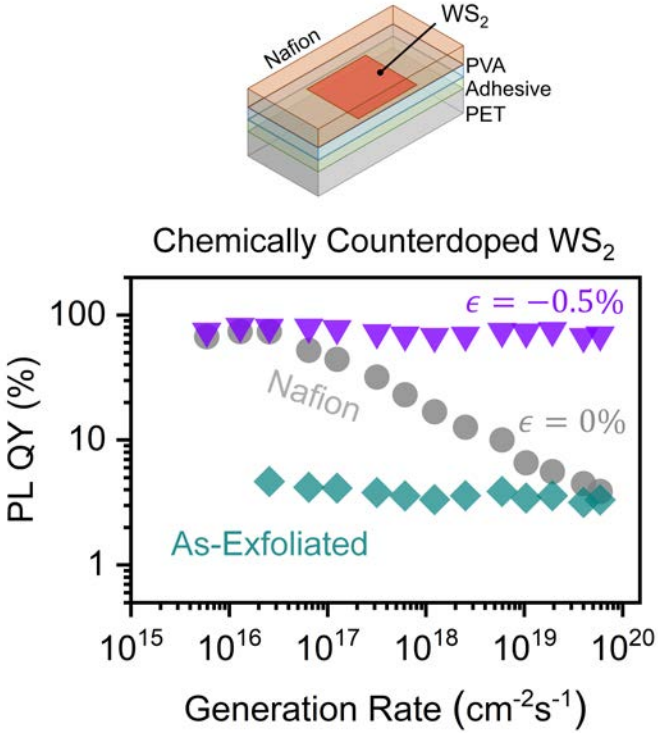

Figure 3.6: **Near-unity PL QY in chemically counterdoped WS_2 under strain.** PL QY of as-exfoliated and chemically counterdoped monolayer WS_2 as a function of strain.

slippage, so applied strain is equal to the actual strain transferred to the monolayer. High PL QY at all pump powers persisted even for a tensile strain of $\epsilon = 1.0\%$ (Fig 3.1F, Fig. 3.5). In addition to electrostatic counter-doping, high PL QY was achieved by applying tensile strain in monolayer WS_2 chemically counter-doped by Nafion, a known hole-dopant (Fig. 3.6).

The PL QY for neutral excitons ($V_g = -30V$) can be written as the ratio of radiative recombination rate of to the total recombination rate

$$QY = \frac{R_r}{R_r + R_{nr}} \tag{3.1}$$

where R_r and R_{nr} are the exciton radiative and nonradiative recombination rates, respectively. Nonradiative recombination for neutral excitons are predominantly through the EEA process. Therefore, $R_{nr} = R_{EEA}$ where R_EEA is the nonradiative EEA rate. Even with application of strain, the semiconductor remained strongly excitonic, so strain did not change the PL QY versus G response at low generation rates, and R_r was independent of strain (Fig. 3.1, D to F). However, because strain changed the QY at high pump powers, R_{EEA} must depend strongly on the strain. Using the experimentally measured PL QYs at a high generation rate of $G = 6.5 \times 10^{19} cm^{-2} s^{-1}$, we found that

$$\frac{R_{EEA}(\epsilon = 0.4\%)}{R_{EEA}(\epsilon = 0.0\%)} \approx 7 \times 10^{-3} \tag{3.2}$$

which would indicate roughly two orders of magnitude decrease in EEA rate at the highest generation rate. Although the EEA rate was not rigorously zero, it was decreased by the application of strain such $R_r >> R_{EEA}$, and the radiative relaxation dominated the total recombination.

The photophysics of these monolayer semiconductors as a function of V_g and generation rate arises from the quasiparticle interaction and can be captured by a simple kinetic model described elsewhere [1]. The exciton-to-trion ratio can be tuned with V_g, activating their respective recombination routes, whereas high densities of neutral excitons activate the EEA process. However, the mechanism by which strain suppresses EEA at high pump necessitated a closer look at the EEA process itself. EEA occurs when one exciton ionizes another exciton by nonradiatively transferring its energy (Fig. 3.7A). The initial state consists of two excitons, with center-of-mass momenta $\mathbf{K_1}$ and $\mathbf{K_2}$ and energies E_1 and E_2, respectively. The exciton energy and momentum are related by (13)

$$E_1 = E_G - E_B + \frac{\hbar^2 |\mathbf{K_1}|^2}{2M_X} \tag{3.3}$$

$$E_2 = E_G - E_B + \frac{\hbar^2 |\mathbf{K_2}|^2}{2M_X}. \tag{3.4}$$

In the above relations, E_G is the fundamental bandgap, E_B is the exciton binding energy and M_X is the exciton mass. The final state consists of a high energy electron and hole,

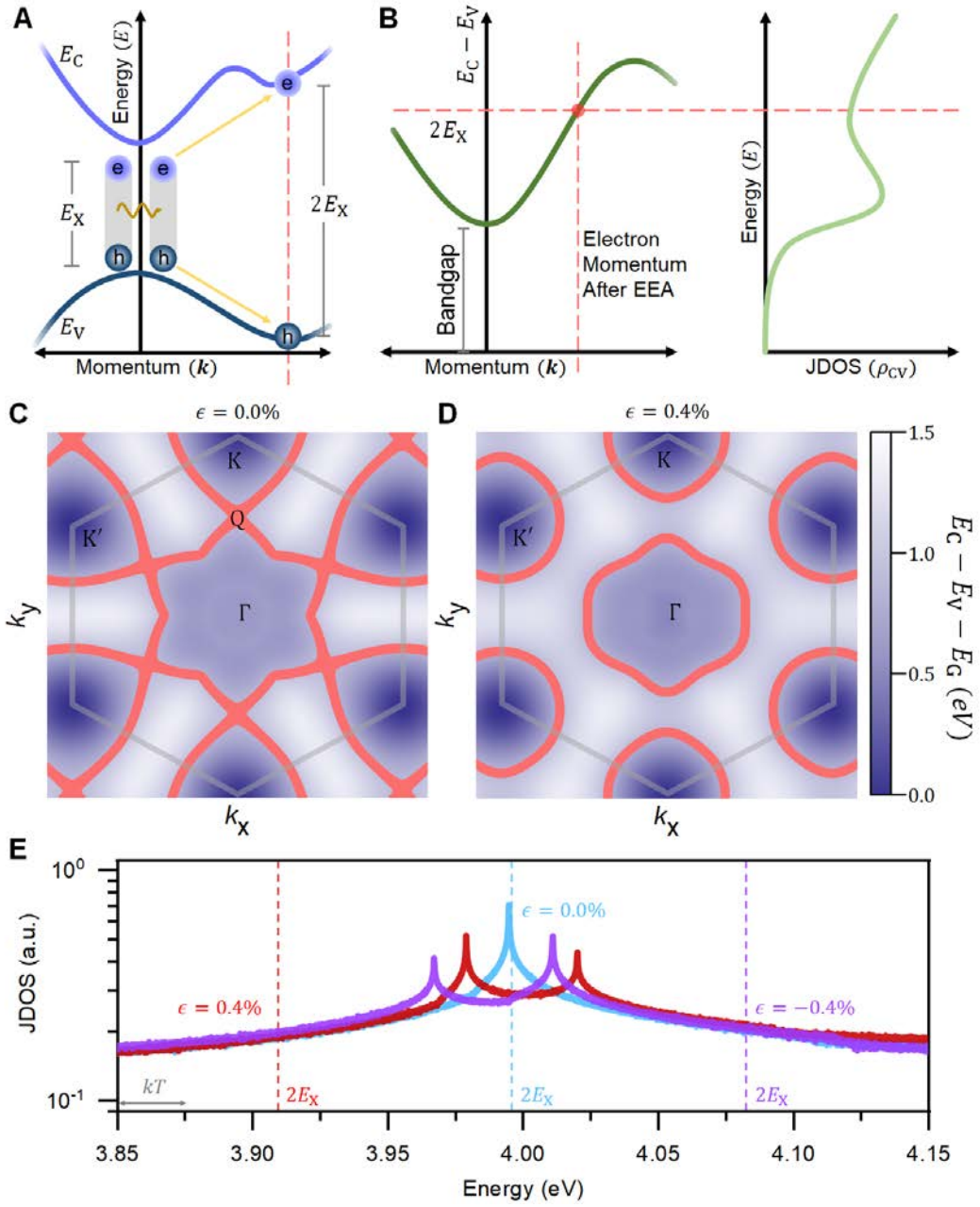

Figure 3.7: **EEA suppression by strain.** (A) Microscopic mechanism of EEA. (B) From momentum and energy conservation, the electron from the ionized exciton ends up at a wavevector where the energy difference between the conduction and valance band is twice the exciton transition energy. The Joint density of states (JDOS) at $E = E_C - E_V = 2E_X$ determines EEA rate. (C, D) Energy difference between the conduction and valance band for unstrained and 0.4% strained monolayer WS_2, respectively. Grey hexagon with 19.946 nm^{-1} sides denotes the first Brillouin zone. Possible final wavevectors (highlighted in red) in unstrained WS_2 include the saddle points Q, where there are VHSs; but strained samples do not. (E) Calculated JDOS for monolayer WS_2

with crystal momenta $\mathbf{k_e}$ and $\mathbf{k_h}$ and energies E_e and E_h, respectively. Irrespective of the details of the interaction potential, two quantities are conserved in the EEA process: total momentum and energy [19, 20]. The condition for conservation of crystal momentum yields

$$\mathbf{k_e} + \mathbf{k_h} = \mathbf{K_1} + \mathbf{K_2}. \tag{3.5}$$

Because K_1 and K_2 are determined by the thermal motion of excitons, they are negligible compared to k_e and k_h, implying that the electron and the hole momentum in the final state should be almost opposite to each other.

$$\mathbf{k_e} \approx -\mathbf{k_h}, \tag{3.6}$$

Therefore, momentum conservation dictates the electron and hole from the ionized exciton have opposing crystal wavevectors (on top of each other in the energy dispersion, shown with the red dashed line in Fig. 3.7A). The condition for conservation of crystal momentum yields

$$E_e + E_h = E_1 + E_2. \tag{3.7}$$

Because the exciton center of mass wavevector is negligible, $E_1 \approx E_2 \approx E_G - E_B = E_X$, where E_X is the exciton transition energy. Therefore, energy conservation stipulates that the energy difference between the electron and hole must be $2E_X$

$$E_e + E_h \approx 2E_X \tag{3.8}$$

If we denote the conduction and valance band of the semiconductor as E_C and E_V, then combined momentum and energy conservation can be written as

$$E_e + E_h = E_C(\mathbf{k_e}) - E_V(-\mathbf{k_h}) = E_C(\mathbf{k_e}) - E_V(\mathbf{k_e}) = 2E_X. \tag{3.9}$$

Therefore, any wavevector where the energy difference between the conduction and valance band is equal to twice the exciton transition energy can be the final wavevector of the electron from the ionized exciton (Fig. 3.7B). Note that the exciton transition energy is different from the fundamental bandgap because of enhanced electron-hole interaction in TMDC monolayers. By Fermi's golden rule, the joint density of states (JDOS) at twice the exciton transition energy determines the strength of EEA process.

Typically, the effective mass approximation is invoked to determine the energy of the ionized electron. However, the ionized electron and hole have high energy so this is no longer a valid approximation. We first calculated the band structure of monolayer TMDC with an 11-band tight binding theory based on Wannier transformation of ab-initio density functional theory calculations [21, 22]. We then calculated the energy difference between the conduction and valance band ($E_C - E_V$) for unstrained and strained monolayer WS_2, respectively. The first Brillouin zone is indicated by a gray hexagon (Fig. 3.7 C and D). Red areas are the final states of the electron from the ionized exciton where the conservation laws are satisfied.

We note that possible final wavevectors in unstrained monolayer WS_2 include the saddle points Q (Fig. 3.7C), but in 0.4% strained WS_2 they do not include the saddle points (Fig. 3.7D). Saddle points in the band structure of a 2D semiconductor create VHS and result in a logarithmically diverging JDOS [23, 24]. The JDOS for monolayer WS_2 $\rho_{CV}(E)$ at $E = E_C - E_V = 2E_X$ determines the strength of EEA. We show the JDOS of 0.4% strained and unstrained WS_2 in Fig 3.7E. In unstrained samples, there was a VHS at twice the exciton transition energy, resulting in an expedited EEA. Strain shifted the exciton transition energy E_X such that $2E_X$ did not overlap VHS resonance and reduced EEA. We also show the JDOS of a 0.4% compressively strained WS_2 monolayer in Fig. 3.7E. We note that compressive strain also drove the EEA process off VHS resonance by changing the exciton transition energy, both for uniaxial strain applied in any direction or biaxial strain (Fig. 3.8, 3.9, 3.10). The choice of tensile versus compressive strain to suppress all nonradiative recombination should ensure that the system remains direct bandgap with the application of strain to avoid nonradiative recombination through momentum-dark indirect excitons [25]. Compressive strain can make some TMDC monolayers such as WS_2 indirect.

Strain has also been used to reduce traditional Auger recombination in conventional 3D semiconductors, but the mechanism is different [26]. In 3D semiconductors, bandgap renormalization and effective mass equalization by applied strain can lead to one order of magnitude reduction of conventional Auger rate [27]. However, in the case of 2D TMDCs EEA is inhibited by shifting the exciton transition energy E_X such that $2E_X$ did not overlap VHS resonance. Because the existence of saddle points, logarithmic VHS always characteristically appeared in 2D semiconductors and were not found in three dimensions, leading to a much stronger response to strain in monolayer TMDCs [28].

These principles applied equally to other TMDC semiconductors. Like WS_2, exfoliated monolayer WSe_2 also exhibited near-unity PL QY at all generation rates when it was made intrinsic by electrostatic counterdoping and tensile strain was being applied (Fig. 3.11A and Fig 3.12). As-exfoliated monolayer MoS_2 has PL QY in the range of 0.1 to 1.0%, which drastically increased at low pump after chemical counterdoping by Nafion (Fig. 3.11B). Unlike WS_2 and WS_2, monolayer MoS_2 became an indirect-gap material when tensile strain was applied and remained direct-gap when compressive strain was applied. We found that, rather than creating compressive strain, downward bending of flexible substrate with negative curvature resulted in buckling of monolayer TMDC. Instead, we used the thermal coefficient of expansion mismatch between the glycol-modified polyethylene terephthalate (PETG) substrate and MoS_2 to apply compressive strain. A chemically counterdoped, 0.5% compressively strained monolayer MoS_2 also exhibited roll-off free PL QY at all generation rates.

The optoelectronic quality of large-area 2D TMDCs must be improved for their use as next-generation devices. The principles of suppressing all nonradiative recombination can also be applied to achieve high PL QY on centimeter-scale WS_2 monolayer grown by chemical vapor deposition (CVD). We first transfer a large-area CVD grown WS_2 [29] onto a flexible substrate and spin-coated it with Nafion (Fig. 3.13A). The normalized PL spectra redshifted with applied tensile strain (Fig. 3.13B). Nafion counterdoping led to a strain-independent PL

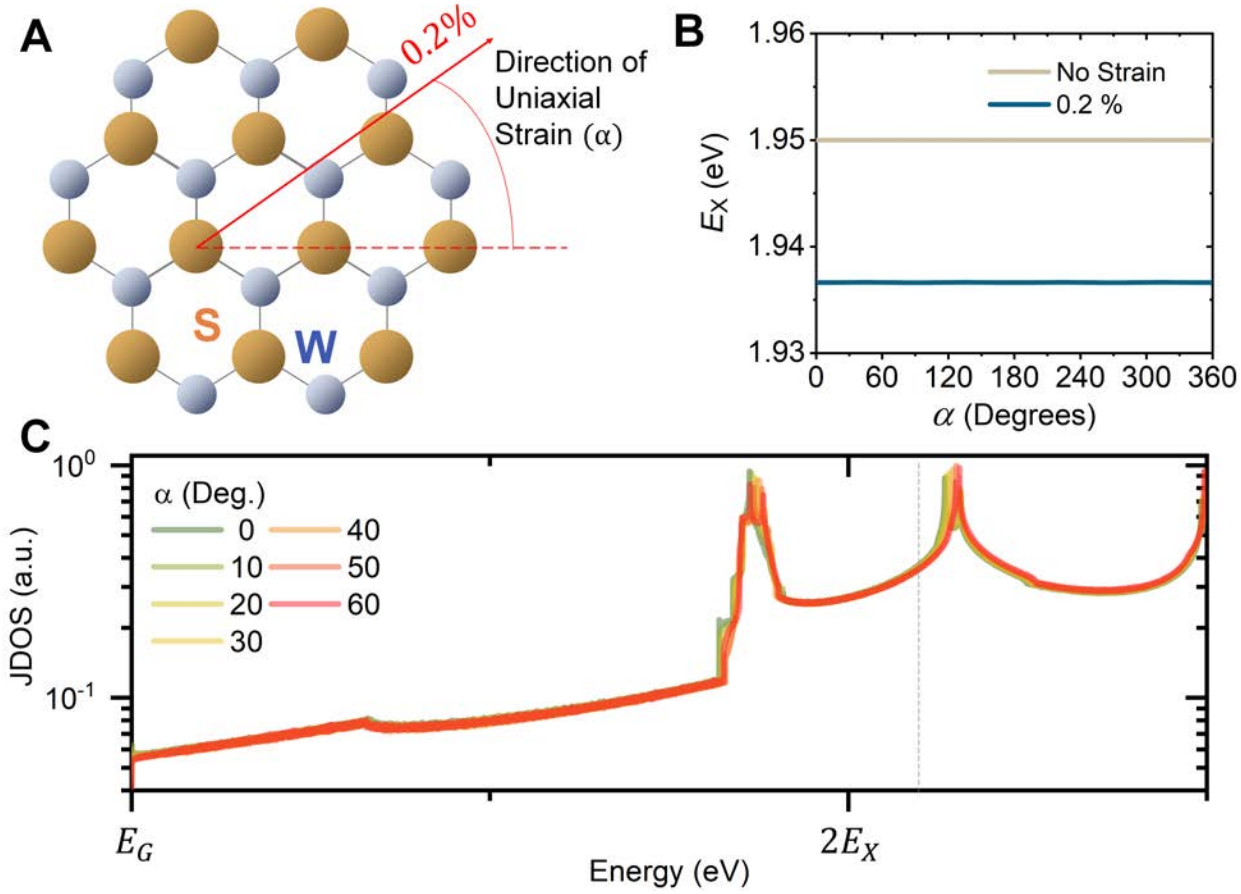

Figure 3.8: **Direction independence of EEA suppression.** (A) Direction of uniaxial strain (B) Exciton transition energy as a function of strain direction (C) VHS is shifted from twice of exciton transition energy independent of tensile strain direction.

QY of 70±10 % (mean ± standard deviation) at low pump powers, as can be seen in a spatial map of the PL QY of a 2 mm × 2 cm area taken at a generation rate of $G = 10^{16} cm^{-2} s^{-1}$ (Fig. 3.13C). At a high generation rate of $G = 10^{16} cm^{-2} s^{-1}$, if no strain was applied, a low PL QY of 1.6 ± 0.8 % was observed uniformly, consistent with as-exfoliated monolayer WS_2. (Fig. 3.13D). However, at 0.4% applied tensile strain, PL QY of the same area reaches $59 \pm 10\%$, indicating a ~ 38 times uniform enhancement of PL QY for a large-scale grown sample at a high generation rate of $G = 10^{20} cm^{-2} s^{-1}$. This demonstration showcases that ideal optoelectronic quality can be achieved in large-area grown monolayers by relatively simple and scalable application of counterdoping and strain.

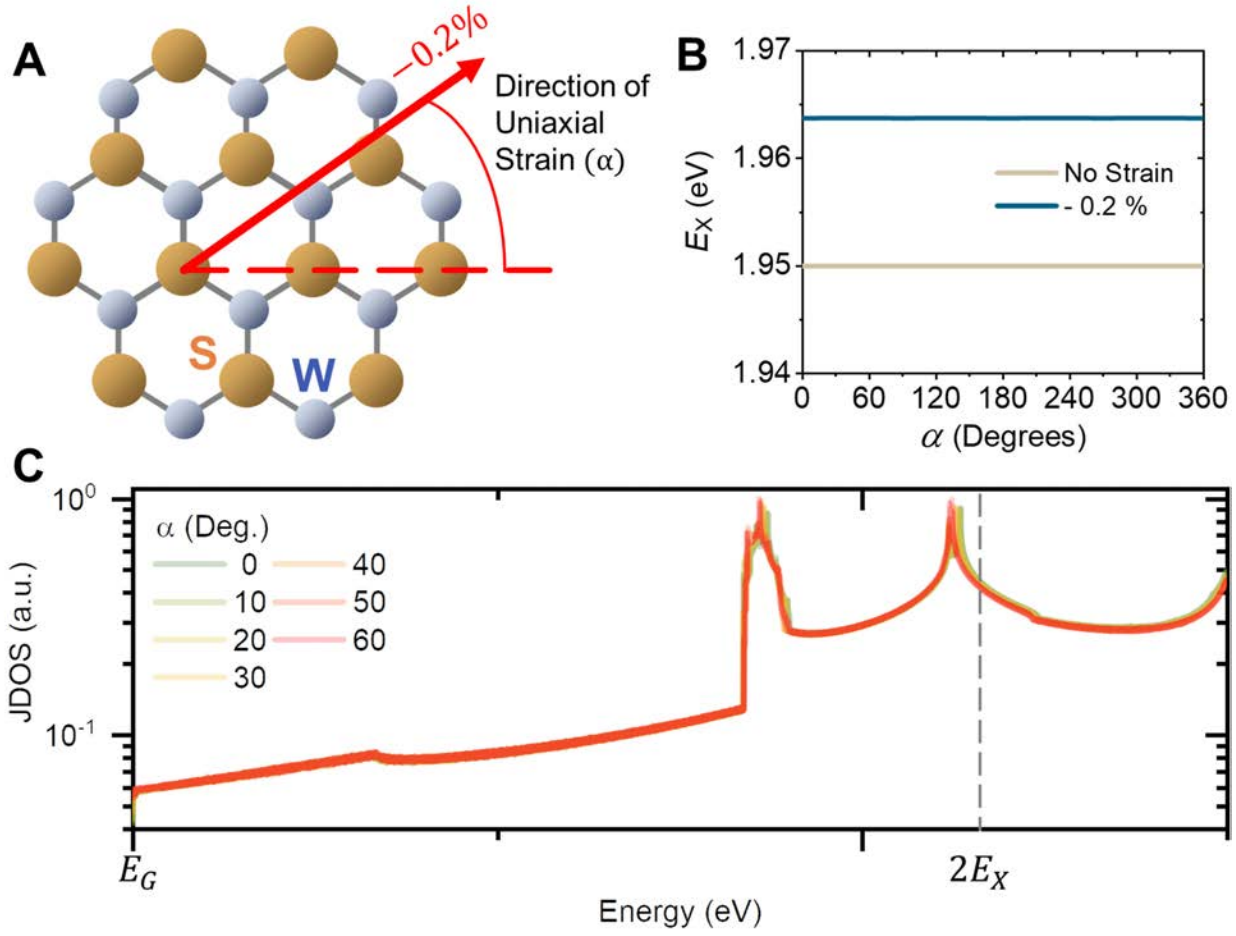

Figure 3.9: **Direction independence of EEA suppression.** (A) Direction of uniaxial strain (B) Exciton transition energy as a function of strain direction (C) VHS is shifted from twice of exciton transition energy independent of compressive strain direction.

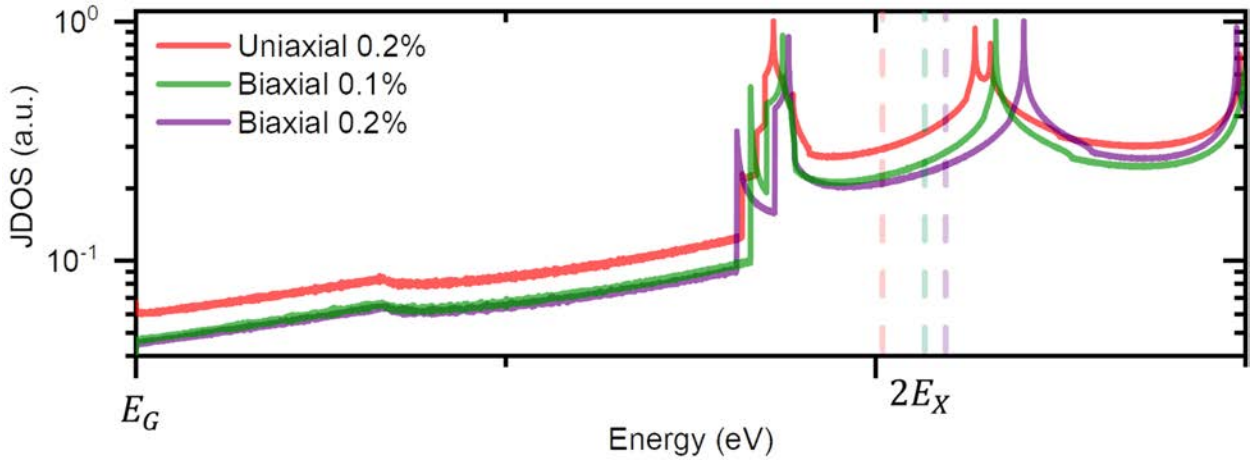

Figure 3.10: **EEA Suppression with Biaxial Strain.** VHS is also shifted from twice of exciton transition energy with biaxial compressive strain.

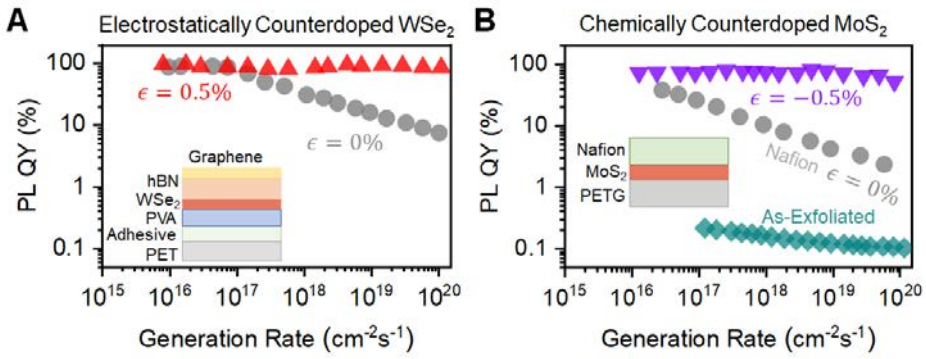

Figure 3.11: **Universal nature of EEA suppresion.** (A, B) Near-unity PL QY at all generation rates in electrostatically counterdoped WSe_2 and chemically counterdoped MoS_2 by tensile and compressive strain, respectively, demonstrates the universality of the conditions that suppress nonradiative recombination.

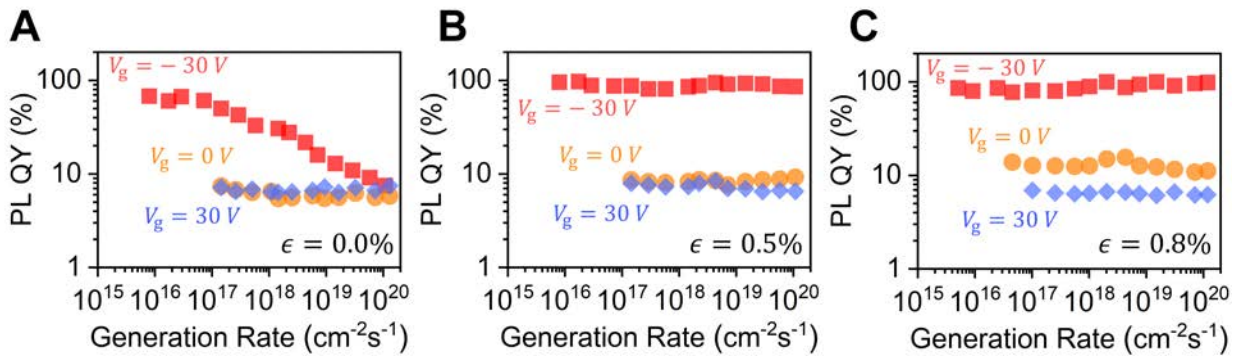

Figure 3.12: **Near-unity PL QY in WSe_2 at all generation rates.** (A, B, C), PL QY of monolayer WSe_2 as a function of gate voltage, generation rate and strain.

3.3 Exciton-Exciton Annihilation in Different Semiconductors

[2]Be it for essential everyday applications such as bright light emitting devices or to achieve quasiparticle Bose-Einstein condensation, materials in which high densities of excitons recombine radiatively are of crucial importance. However, in all excitonic materials exciton-exciton annihilation (EEA) becomes the dominant loss mechanism at high densities, where an exciton nonradiatively recombines in the course of colliding with another exciton. This recombination channel drastically reduces the observed effective lifetime and luminescence quantum efficiency of excitons. EEA has been experimentally observed in numerous materials and typically, a macroscopic parameter named EEA coefficient is used to compare rates of EEA between different materials at the same density; the higher the EEA coefficient the higher the rate of EEA. Here we examine the reported values of EEA coefficient for 140 different materials and find that it is inversely related to the lifetime of single exciton. We explain this trend with the quantum theory of interacting excitons; since during EEA one exciton must relax to ground state, EEA coefficient is proportional to the single-exciton recombination rate. Surprisingly, this leads to a counterintuitive observation that, the exciton recombination rate at which EEA starts to dominate is inversely correlated to EEA coefficient. Materials with highest EEA coefficient also have highest EEA-onset recombination rate. These results broaden our understanding of EEA across different material systems and provide a point of reference to future excitonic materials and devices.

Excitons can be formed by direct photoexcitation or by association of free electrons and holes due to their attractive coulombic interaction. Excitons dominate the photophysics of

[2]The following section was published in a similar form in *Nano Letters*. (Uddin, S.Z., Rabani, E. and Javey, A., Universal inverse scaling of exciton–exciton annihilation coefficient with exciton lifetime. *Nano Letters*, 21(1), pp.424-429, 2020.)

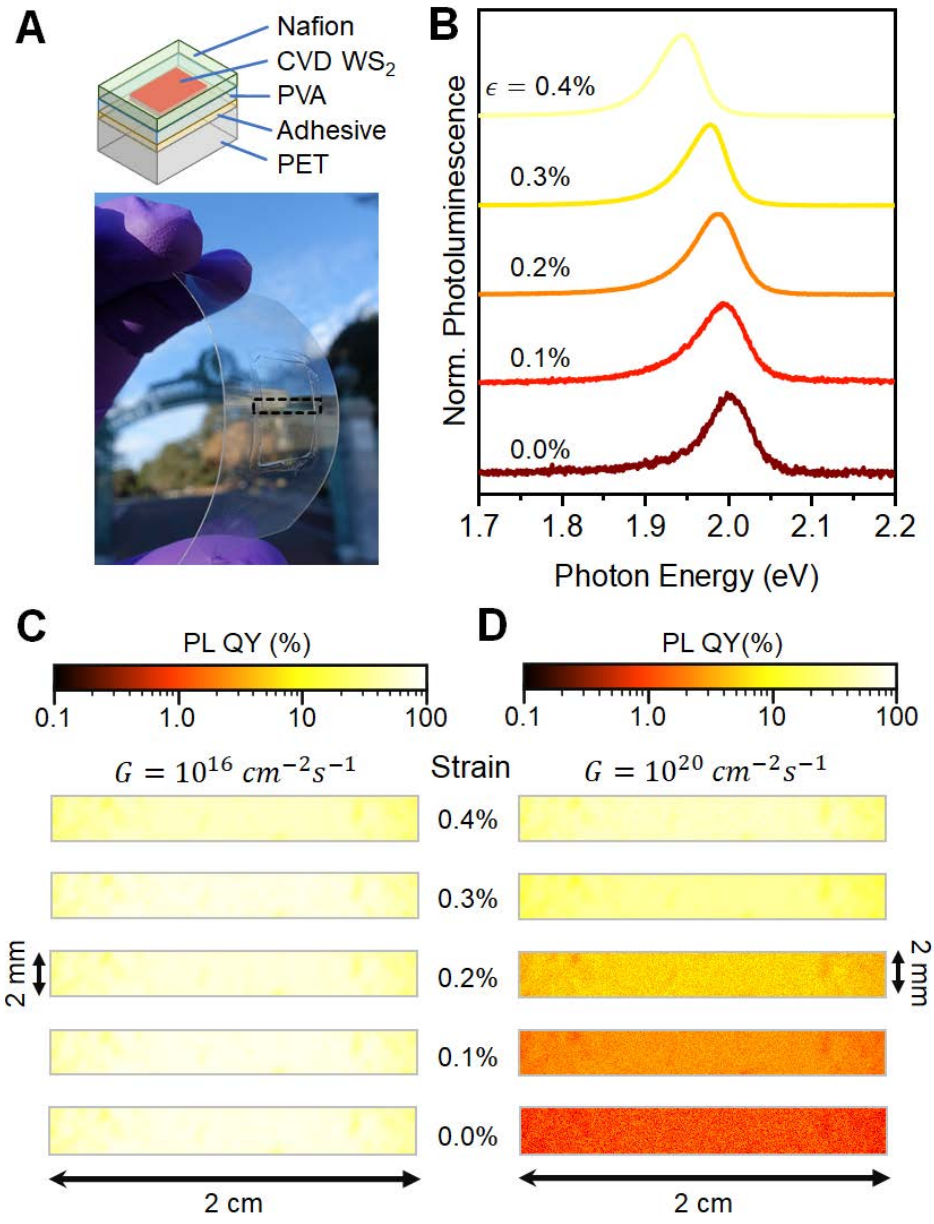

Figure 3.13: **High PL QY on large-area CVD-grown WS_2.** (A) Schematic (top) and photograph (bottom) of the flexible substrate used to strain CVD grown, centimeter-scale WS_2. (B) Normalized PL spectra of a typical spot at different strains. (C, D) Spatial mapping of PL QY of a 2 mm X 2 cm area of grown WS_2 at a low generation rate of $G = 10^{16} cm^{-2} s^{-1}$ and a high generation rate of $G = 10^{20} cm^{-2} s^{-1}$, respectively, shows high PL QY is uniformly achieved by strain at the highest generation rate, while maintaining high PL QY at low pump.

many different classes of material systems; from nanoscale complexes [30] such as molecules, molecular aggregates [31], quantum dots [32], nanotubes [33], two dimensional semiconductors [34] at room temperature to bulk semiconductors [35] at cryogenic temperatures. At low exciton densities, many of these excitonic materials have high luminescence efficiency and this property has been leveraged in commercial light-emitting device technologies [36]. However, at high exciton concentrations the recombination is dominated by exciton-exciton annihilation (EEA), where an exciton nonradiatively recombines in the course of colliding with another exciton [37]. This nonradiative process drastically reduces the luminesce efficiency and is the leading efficiency-limiting factor in numerous applications. Although EEA is ubiquitously observed and extensively studied in excitonic materials, a clear and systematic comparison of EEA rate across different materials systems is lacking. Generally, EEA is characterized by a macroscopic parameter named exciton-exciton annihilation coefficient C_{EEA}. High values of C_{EEA} implies high EEA rates for a given exciton density.

Here, we investigate EEA across 140 different material systems (see table 3.1,3.2,3.3,3.4) collected from published literature. They represent different classes of materials, such as two-dimensional (2D) and bulk semiconductors, chloroplasts, solid phase of noble gas atoms, crystalline ionic compounds, scintillators, molecular crystals and films, fluorophores, covalent organic frameworks, quantum dots array, nanotubes and nanowires, thus providing a broad basis for characterizing general patterns in EEA. The observed values of EEA coefficient and exciton lifetime in these materials spans ten orders of magnitude. We find that across different material systems, contrary to intuition, EEA coefficient C_{EEA} is linearly correlated with the single-exciton lifetime τ_X. We explain the observed trend with a microscopic quantum theory of EEA. This trend sets a universal limiting exciton concentration of $\sim 10^{20}$ cm^{-3} at which EEA starts to dominate single-exciton recombination in different materials, despite having drastically different EEA coefficients. More importantly, this trend shows that the recombination rate at the onset of EEA is linearly correlated to EEA coefficient, which is a paradigm shifting insight. These results advance our ability to recognize existing materials which can support large densities of excitons without compromising luminescence efficiency, provides a point of reference against which new materials can be benchmarked and shed new light on the microscopic mechanism of exciton-exciton annihilation.

Exciton, a bound state of an electron and a hole due to their attractive electrostatic Coulomb force, is often discussed in the two limiting cases depending of the size of the exciton. Small Frenkel excitons have similar size as lattice spacing and are typically found in organic molecular crystals [38], whereas Wannier-Mott excitons are larger than lattice spacing and are typically found in inorganic crystals [39]. Both types of excitons show EEA at high densities. Energy level diagram demonstrating EEA of localized Frenkel excitons with discrete energy levels are shown in Fig. 3.14A. Initially two molecules are in their first excited state, where they each have one exciton. EEA occurs when the exciton in the right molecule moves to the ground state and sends the exciton in the left molecule to a higher energy state through energy transfer. Internal conversion by phonon emission leads to a rapid relaxation of the left molecule into its first excited state, leaving only one exciton after EEA. The energy of large and mobile Wannier-Mott excitons in semiconductor crystals

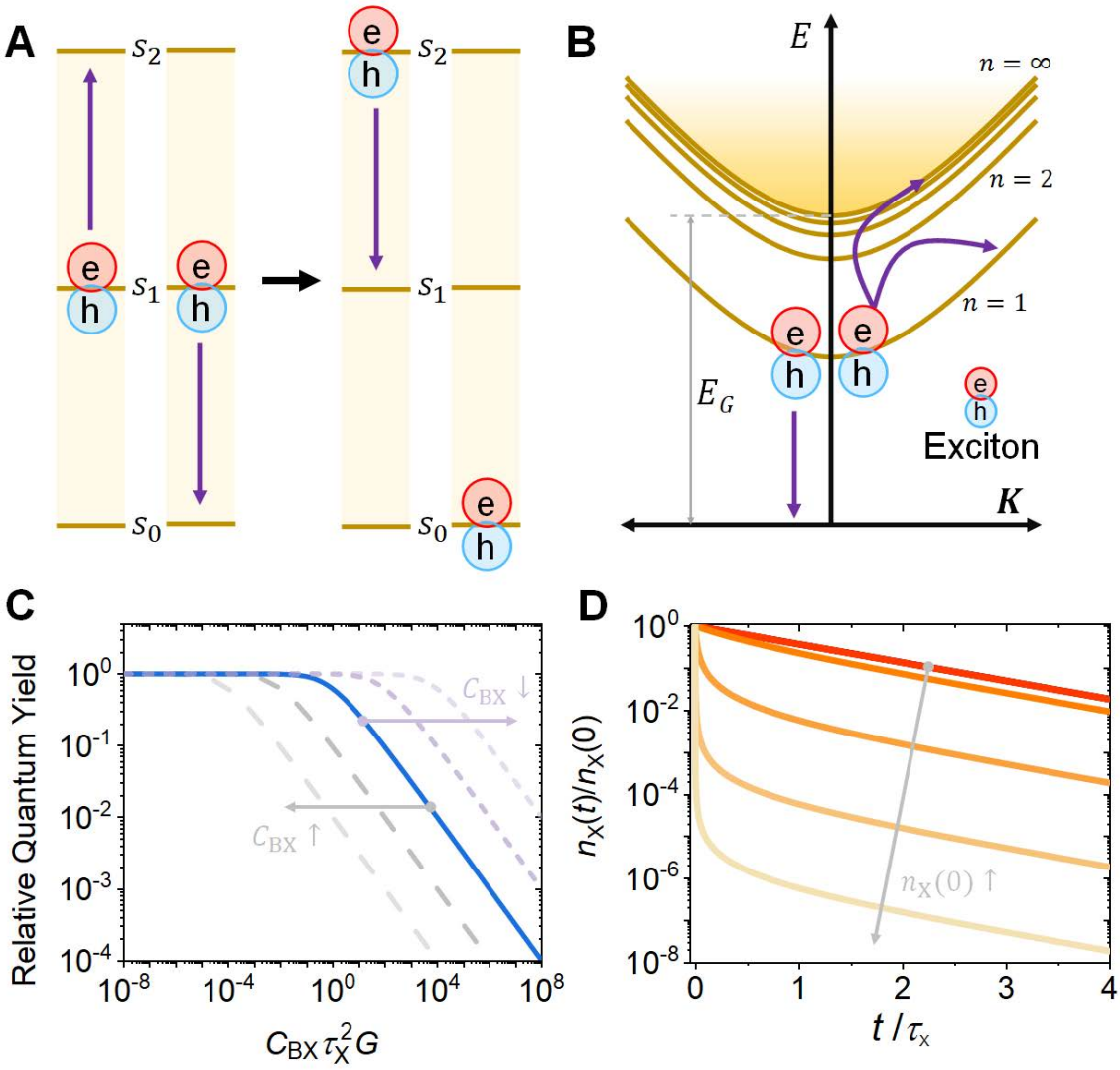

Figure 3.14: **Mechanism and Signatures of Exciton-exciton annihilation.** Schematic representation of the EEA process in (A) adjacent discrete molecules and (B) crystalline semiconductors with energy dispersion. Effect of EEA on (C) quantum yield measured by continuous excitation and (D) time resolved exciton concentration following pulsed excitation.

depends on their center-of-mass momentum. Schematic representation of EEA for Wannier-Mott excitons along with their energy dispersion is shown in Fig. 3.14B, where one exciton nonradiatively transfers its energy to ionize and/or increase the center-of-mass kinetic energy of another nearby exciton, conserving total momentum.

The two principal evidences that identify EEA are that (i) the luminescence quantum

yield decreases sublinearly with increasing excitation power and (ii) the observed lifetime of excitons shortens substantially at high exciton densities [1]. For both Frankel and Wannier-Mott excitons, the experimental observations can be captured by a phenomenological macroscopic rate equation[40] for the exciton density $n_X(r,t)$ containing an annihilation term proportional to the square of this density,

$$\frac{\partial n_X(r,t)}{\partial t} = G(r,t) + D\nabla^2 n_X(r,t) - \frac{n_X(r,t)}{\tau_X} - C_{EEA} n_X^2(r,t) \tag{3.10}$$

where r is position, t is time, $G(r,t)$ is the exciton generation rate, D is the exciton diffusion coefficient, τ_X is the single-exciton lifetime and C_{EEA} is the EEA coefficient. In case of spatially uniform generation $G(r,t) = G(t)$, the diffusion term vanishes, and the previous equation simplifies to

$$\frac{\partial n_X(r,t)}{\partial t} = G(t) - \frac{n_X(t)}{\tau_X} - C_{EEA} n_X^2 \tag{3.11}$$

which is widely used to describe photophysics of excitonic systems. In case of steady state excitation, the time derivative vanishes and

$$G(t) = G = \frac{n_X}{\tau_X} + C_{EEA} n_X^2 \tag{3.12}$$

. The radiative recombination of rate is proportional to the exciton concentration. Therefore, the relative quantum yield (QY) can be written as

$$QY \propto \frac{n_X}{G} = \frac{n_X}{n_X/\tau_X + C_{EEA} n_X^2}, \tag{3.13}$$

which is constant at low exciton density and decreases with increasing exciton density. This is one of the primary evidences of EEA (Fig. 3.14C). We define the exciton density and generation rate, at which relative quantum yield drops to half of the low pump value, as the onset exciton density and onset recombination rate

$$n_{1/2} = \frac{1}{C_{EEA}\tau_X} \tag{3.14}$$

$$G_{1/2} = \frac{2}{C_{EEA}\tau_X^2} \tag{3.15}$$

For the same lifetime the onset exciton concentration decreases with increasing C_{EEA} (Fig. 3.14C). In the case of pulsed excitation, $G(t) = n_X(0)\delta(t)$, where $\delta(t)$ is the Dirac delta function, time varying exciton concentration can be written as

$$n_X(t) = \frac{n_X(0)\exp\left(-t/\tau_X\right)}{1 + n_X(0) C_{EEA}\tau_X \left[1 - \exp\left(-t/\tau_X\right)\right]}. \tag{3.16}$$

We note, at increased exciton concentration, the initial decay of the excitation population becomes faster, leading to an observation of reduced effective lifetime. This is another primary evidence of EEA (Fig. 3.14D).

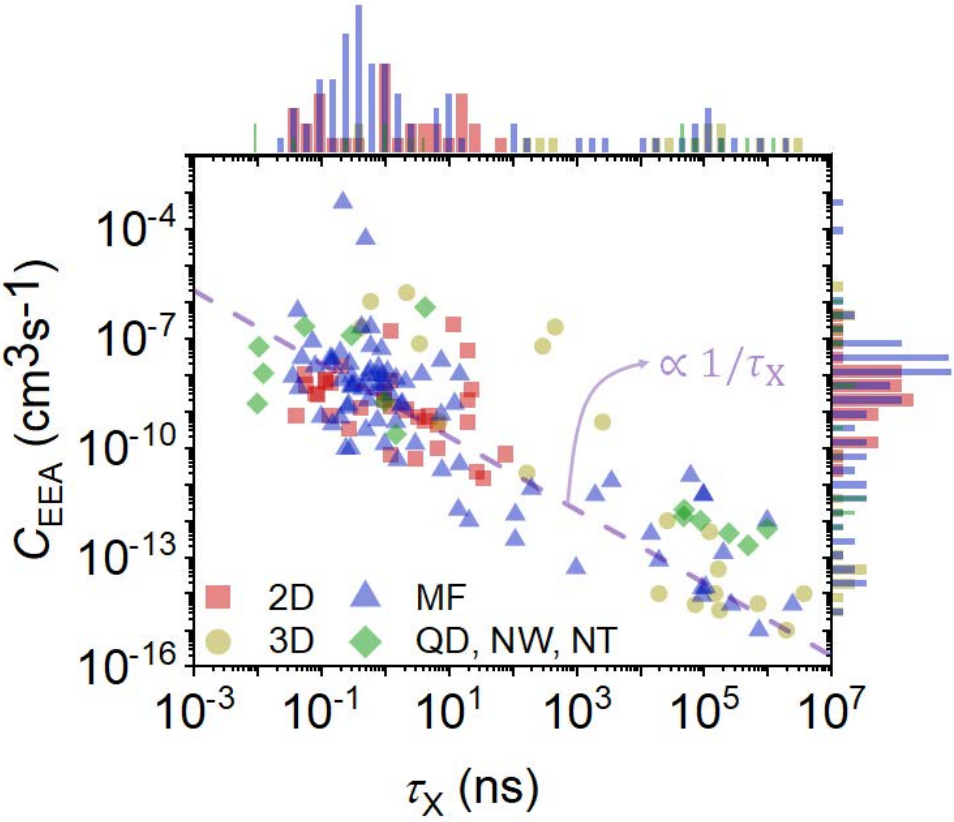

Figure 3.15: **Exciton-exciton annihilation coefficient vs exciton lifetime.** Exciton-exciton annihilation coefficient decreases with increasing single exciton lifetime in different excitonic materials. 2D, MF, 3D, QD, NW, and NT are abbreviations of two-dimensional, molecular films, three-dimensional, quantum dot, nanowire, and nanotube, respectively. The relative histogram of C_{EEA} and τ_X is shown on right and top, respectively and has the same color coding as the main figure. Each decade is divided into two bins, the height of the bars represents how many values fall into each interval. The bars on the histogram have different widths for distinguishability and carries no numerical significance.

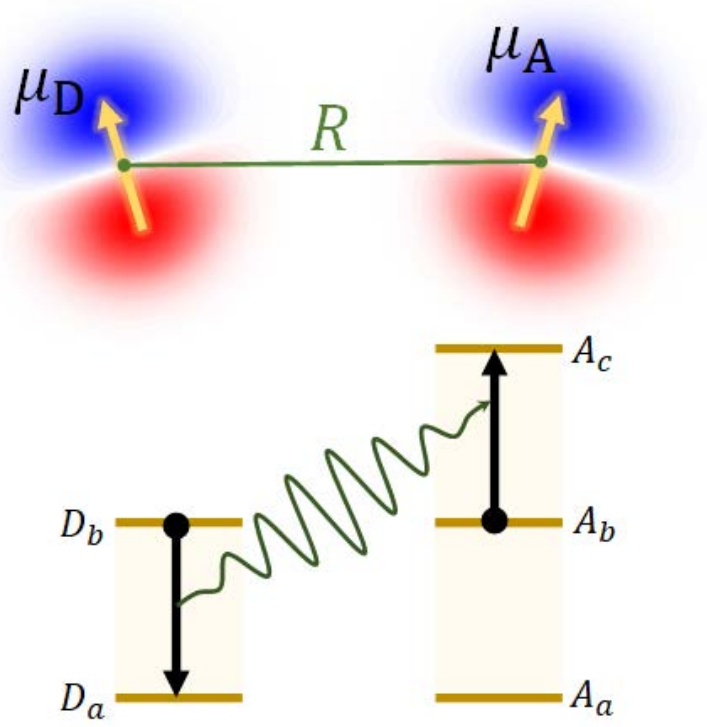

Figure 3.16: **Interaction between excitons.** Nonradiative energy transfer between two excitons either in molecular systems or crystalline semiconductors. The transition rate depends on the relative orientation of the transition dipole moments and the distance R between them.

EEA has been extensively studied in many different material systems. EEA coefficient (C_{EEA}) as a function of exciton lifetime (τ_X) for different materials along with their relative histograms are shown in Fig. 3.15. To be present in our data, a material must have been characterized in literature either by experimental techniques that track time-resolved exciton density after pulsed excitation or by steady state measurement of luminescence efficiency as a function of exciton density. The observed values of τ_X and C_{EEA} in nature spans ten orders of magnitude. We note from the histogram that, 2D semiconductors have relatively short exciton lifetime ($0.1 - 10$ ns), but large EEA coefficient ($10^{-10} - 10^{-7}$ cm^3/s). In contrast, bulk semiconductors exhibit relatively long exciton lifetime ($10^4 - 10^7$ ns), but small EEA coefficient ($10^{-15} - 10^{-12}$ cm^3/s). Molecular films however cover the entire range of lifetime and EEA coefficient. Over the whole range, we observe a general trend of decreasing C_{EEA} with increasing exciton lifetime τ_X for all material classes.

We now present a quantum theory of interacting dipoles that provides an intuitive understanding of the crucial mechanism that leads to the inverse relationship between EEA coefficient and single-exciton lifetime. We first explore the microscopic EEA rate at the limit

where excitons do not diffuse. Then we introduce exciton diffusion and relate the macroscopic EEA coefficient C_{EEA} with the microscopic rate. Let us consider the non-radiative transfer of energy from a donor exciton to an acceptor exciton that are very close to each other and fixed at nearby sites, as shown in Fig. 3.16. This is similar to fluorescence resonance energy transfer (FRET), however unlike FRET the acceptor site is at an excited state. Energy levels that are relevant to exciton-exciton annihilation (EEA) is also shown in Fig. 3.16. The ground-state (a), the first excited state (b), and higher excited state (c) energies of a pair of excitons are labelled. These energy levels could be the discrete levels of Frenkel excitons discussed in Fig. 3.14A or relevant k-states of Wannier-Mott excitons in Fig. 3.14B. At the beginning, both donor and acceptor excitons are in their ground excited state, b. After EEA, the donor exciton is annihilated, and the acceptor is excited to higher energy state c. If the wavefunctions are denoted by ψ, the initial and final state can be written as $|\psi_b^A \psi_b^D >$ and $|\psi_c^A \psi_a^D >$, respectively. Therefore, from Fermi's golden rule, the rate of non-radiative energy transfer can be written as

$$B = \frac{2\pi}{\hbar} \left| < \psi_c^A \psi_a^D | V | \psi_b^A \psi_b^D > \right|^2 \rho_F \tag{3.17}$$

where V is the dipole-dipole interaction potential, and ρ_F is the density of states at the energy of the final states. The electrostatic potential between two dipoles that have transition dipole moments of μ_A and μ_D and are distance R apart can be approximated as

$$V \propto \frac{\mu_A \mu_D}{R^3} \tag{3.18}$$

where angular dependence is ignored for simplicity. Substituting the potential on the rate equation and using the fact that the coordinates of donor and acceptor excitons are independent, we can write

$$B \propto \frac{1}{R^6} \left| < \psi_a^D | \mu_D | \psi_b^D > \right)\Big|^2 \left| < \psi_c^A | \mu_A | \psi_b^A > \right|^2 . \tag{3.19}$$

The first matrix element of the product is proportional to the rate of transition of the donor exciton to the ground state, independent of the presence of any other excitons, which is inversely related to the single exciton lifetime (τ_X). The second matrix element of the product is proportional to the rate of transition of the acceptor exciton to a higher excited state, which is related to the relative absorptivity of these two levels and is independent of the single exciton lifetime (τ_X). Therefore, the microscopic EEA coefficient, B is inversely proportional to τ_X,($B \propto 1/\tau_X$).

Now let us consider the case where the excitons can move on a lattice of points in a crystal or among molecules in a film, denoted by a vector $\mathbf{q}$ which as the same dimensionality as the material. The time evolution of the probability $f_{\mathbf{q}}(t)$ of finding an exciton at point $\mathbf{q}$ can be written as [40–42]

$$\frac{df_{\mathbf{q}}(t)}{dt} = \frac{f_{\mathbf{q}}(t)}{\tau_X} + F \left[\sum_{\mathbf{q}', \mathbf{q}' \neq \mathbf{q}} f_{\mathbf{q}'}(t) - f_{\mathbf{q}}(t) \right] - \int_0^t dt' \Gamma(t - t') f_{\mathbf{q}}^2(t') \tag{3.20}$$

where F is the rate of diffusion between two adjacent points, and $\Gamma(t)$ is a memory function that takes into account of the movement of excitons prior to annihilation and depends on both the microscopic EEA coefficient, B and the diffusion rate, F. Dividing the probabilities with unit cell volume V gives us the mean-field rate equation [43]. The diffusion coefficient D is related to the diffusion rate as $D = FA$, where A is the average unit-cell side area. The macroscopic EEA rate coefficient C_{EEA} results from the integration of the memory function term. Detail derivation of the memory function gives the following expression in one dimension14

$$C_{EEA} = V\frac{B\sqrt{1+4F\tau_X}}{B\tau_X+\sqrt{1+4F\tau_X}} \tag{3.21}$$

relating macroscopic EEA rate coefficient C_{EEA} to the microscopic EEA rate and diffusion coefficient. We have already derived that $B \propto 1/\tau_X$, therefore

$$C_{EEA} \propto \frac{1}{\tau_X}\frac{\sqrt{1+4F\tau_X}}{B\tau_X+\sqrt{1+4F\tau_X}} \tag{3.22}$$

In an excitonic semiconductor two limiting cases of transport are often distinguished [44, 45]. In hopping transport, the Frenkel exciton is almost localized, and they can transfer from one site to another. In molecular crystals where hopping is the main mechanism of diffusion, it is known from Smoluchowski–Einstein theory of random walks that [46–49] $F \propto 1/\tau_X$. Therefore for hopping dominated diffusion, we get $C_{EEA} \propto 1/\tau_X$.

In band transport, phonons scatter the Wannier-Mott excitons in a crystalline semiconductor from one wavevector state to another. The transport is then governed by the scattering times of the wavevector states. The dependence of diffusion constant on the exciton lifetime at the band limit is complex, but it decreases with increasing lifetime [50, 51]. Combination of these relationships still leads to decreasing C_{EEA} with increasing τ_X. If the diffusion rate is large $\sqrt{1+4F\tau_X} >> B\tau_X$) then also $C_{EEA} \propto 1/\tau_X$. Therefore, for both types of transport, we observe decreasing EEA coefficient with increasing lifetime. The relationship between macroscopic and microscopic EEA coefficients are convoluted in higher dimensions, but in all dimensions C_{EEA} decreases with increasing exciton lifetime [40, 42].

The onset exciton density and recombination rate at which relative quantum yield drops to half of the low pump value can be written as

$$n_{1/2} = \frac{1}{C_{EEA}\tau_X} \tag{3.23}$$

$$G_{1/2} = \frac{2}{C_{EEA}\tau_X^2} \tag{3.24}$$

Both quantities have a more direct impact on practical applications than either lifetime or EEA coefficient. For light emitting devices, higher onset recombination rate $G_{1/2}$ would imply higher photon emission rate without dropping efficiency due to EEA. In case of Bose-Einstein condensation or excitonic lasing, larger onset exciton concentration $n_{1/2}$ would imply large number of quasiparticles can be amassed in that material without sacrificing lifetime.

We show $G_{1/2}$ and $n_{1/2}$ in Fig. 3.17 as a function of τ_X in different materials. If C_{EEA} and τ_X were independent, above equations would suggest that $G_{1/2}$ is inversely proportional to τ_X^2. However, as a consequence of the trend between EEA coefficient and lifetime, $G_{1/2}$ scales inversely with τ_X, independent of the type of exciton, material or diffusion involved (Fig. 3.17A). Therefore, materials with very short lifetimes such as 2D semiconductors are suitable for bright light emitting devices. Since materials with short lifetimes have the largest C_{EEA}, materials with the largest C_{EEA} also has the largest onset recombination rate for EEA.

$$C_{EEA} \propto \frac{1}{\tau_X} \Rightarrow G_{1/2} = \frac{2}{C_{EEA}\tau_X} \propto C_{EEA} \tag{3.25}$$

Similarly, if C_{EEA} and τ_X were independent, Eq. 6 would suggest that $n_{1/2}$ is inversely proportional to τ_X. However, due to the inverse scaling of EEA coefficient with lifetime, onset exciton concentration shows no strong dependence on τ_X (Fig. 3.17B). In all excitonic materials characterized in literature, EEA begins to dominate the recombination process below an exciton concentration of 10^{20} cm^{-3}, corresponding to an interexciton distance of just 2.7 nm. This is a very important number to gauge the potential of future excitonic materials compared to the existing library of materials. The inverse scaling of EEA coefficient with single-exciton lifetime leads to strikingly different scaling of onset recombination rate and onset exciton concentration with lifetime, which is not evident from Eq. 6. We also show the EEA coefficient and lifetime with corresponding exciton emission energy for different materials in Fig. 3.18. We do not observe any general correlation among them. Optical bandgap of 90% of the materials, in which EEA has been characterized, lies between 1.5 eV to 2.5 eV.

3.4 Summary

Inorganic or organic, defective or unblemished, excitonic or free-carrier system, irrespective of which classification any semiconductor belongs to, nonradiative recombination has always been observed in all semiconductors at high photocarrier concentrations. Here we show that in both exfoliated and grown two dimensional semiconductors nonradiative recombination processes can be suppressed at all generation rates as long as the material is chemically intrinsic by electrostatic or chemical counterdoping, and EEA process is not in resonance with VHS as achieved by strain. Considering how common van Hove singularities are in low dimensional semiconductors these concepts in principle could apply to other systems. Our findings here present a strong case for the use of 2D materials for optoelectronic devices, although a number of challenges still need to be overcome in terms of the device design and implementation.

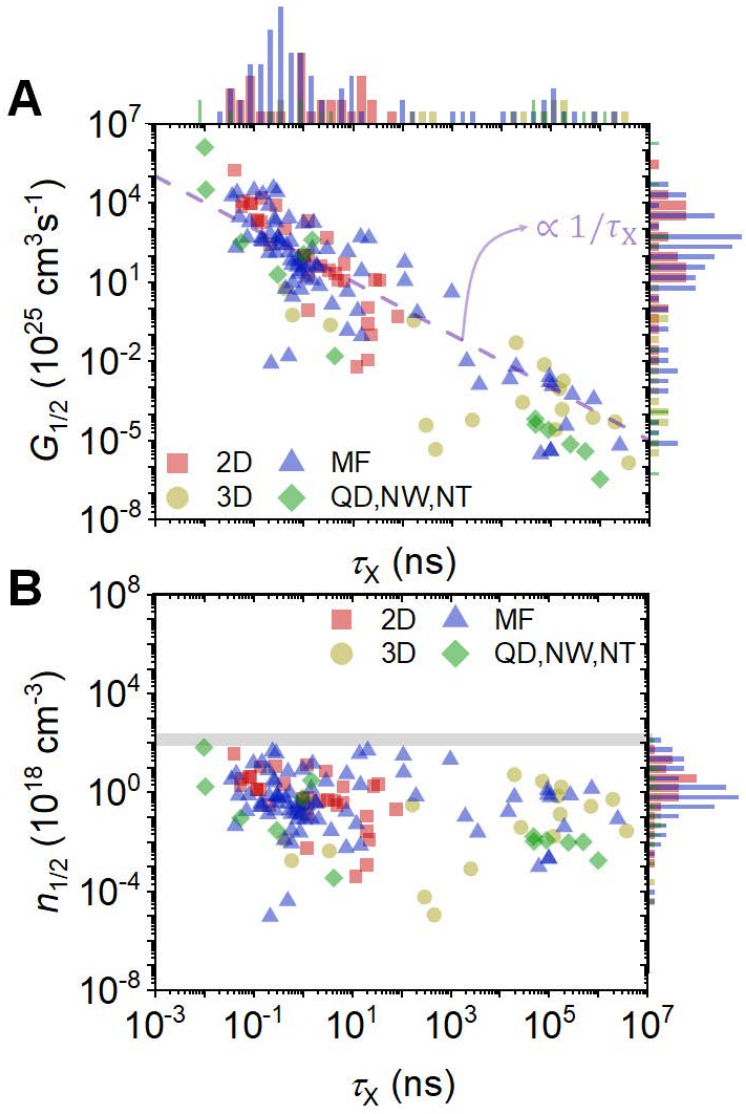

Figure 3.17: **Onset of exciton-exciton annihilation.** (A) Generation rate and (B) exciton concentration at the onset of exciton-exciton annihilation. 2D, MF, 3D, QD, NW, and NT are abbreviations of two-dimensional, molecular films, three-dimensional, quantum dot, nanowire, and nanotube, respectively. Histograms of onset generation rate and exciton concentration are shown on the left.

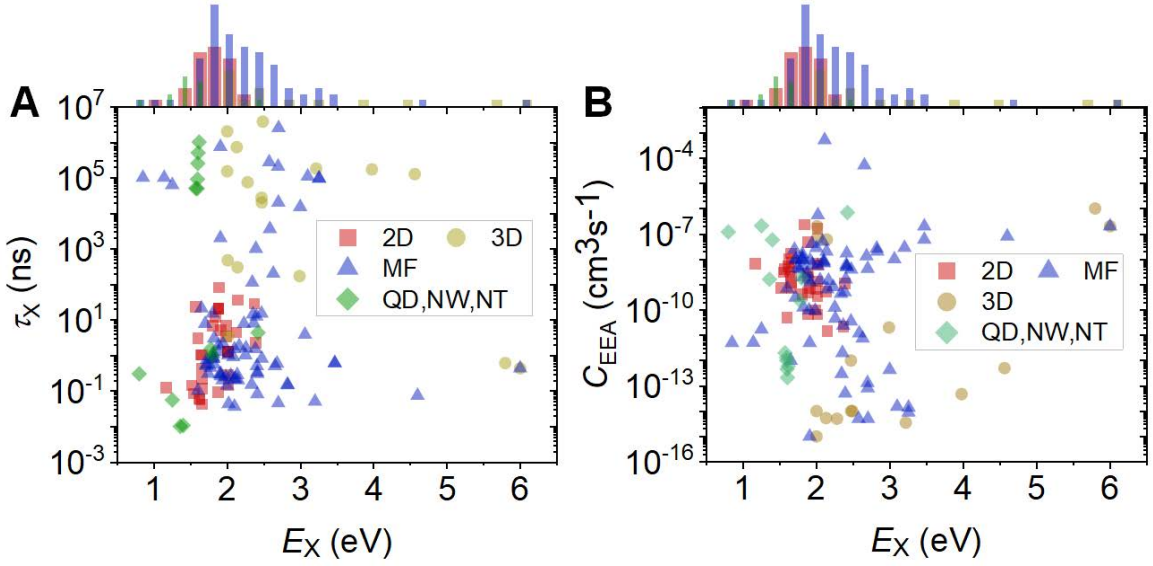

Figure 3.18: **EEA coefficient and exciton lifetime with exciton transition energy.** (A), EEA coefficient and (B) single exciton lifetime as a function of exciton emission energy E_X. 2D, MF, 3D, QD, NW, and NT are abbreviations of two-dimensional, molecular films, three-dimensional, quantum dot, nanowire, and nanotube, respectively. Relative histogram of exciton transition energy is shown on the top.

3.5 Experimental and Theoretical Details

Device Fabrication

TMDC monolayers (WS_2 and WSe_2 from HQ Graphene, MoS_2 from SPI supplies) were mechanically exfoliated on top of 50 nm SiO_2/Si p^{++} substrates and were identified by optical contrast. 10 wt% polyvinyl alcohol (PVA, Alfa Aesar, $98-99$ % hydrolyzed, molecular weight $130,000$ g/mol) solution were spin-coated at 1000 rpm for 40 seconds on the substrate with TMDC monolayer, and baked at 70° C for 3 minutes to remove water solvent. Subsequently, a polyethylene terephthalate (PET, 125 μm thick) film is attached on top of the PVA film using adhesive (Super glue, Gorilla Glue Company) for ease of handling. Next, the entire flexible substrate (PVA/adhesive/PET) with the encapsulated monolayer TMDC is slowly peeled off from SiO_2 substrate using tweezer and resized so that the monolayer is at the center. Hexagonal boron-nitride (hBN, HQ Graphene) is mechanically exfoliated onto a 1×1 cm polydimethylsiloxane (PDMS) substrate. The flexible substrate is put on a sample stage under a modified optical microscope (bh2, Olympus) at room temperature and the hBN-exfoliated PDMS stamp was positioned upside down and aligned with the monolayer on the flexible substrate. The stamp was slowly brought into contact with the monolayer and peeled off rapidly, leading to transferred hBN on top of TMDC monolayer forming

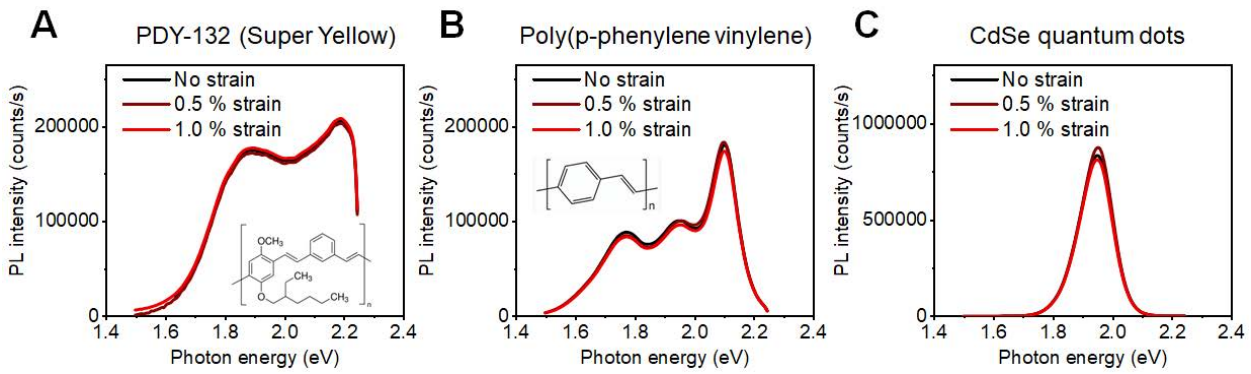

Figure 3.19: **Negligible change in PL by bending of substrates.** PL spectra of (A) PDY-132, (B) Poly(p-phenylene vinylene) (PPV), (C) CdSe quantum dots on PVA-PET flexible substrates as a function of applied strains.

the insulator. In a similar fashion, Graphene (Graphenium, NGS Naturgraphit) is subsequently stamp-transferred on top of the TMDC monolayer/hBN stack to from source and top gate. Contacts are formed to the source and gate by applying silver conductive paste (EMS #12640, Electron Microscopy Sciences) to the graphene with a sharpened wooden tip under a Nikon stereomicroscope. Lastly, the device is encapsulated with poly(methyl methacrylate) (PMMA; 950 A11, Microchem) prior to measurement by dropcasting and subsequent soft-baking at 70° C for 5 minutes. To prepare compressively strained monolayer MoS_2, first MoS_2 was exfoliated on PDMS and then stamp was slowly brought into contact with the center of a piece of glycol-modified Polyethylene terephthalate (PETG, 2.54 mm thick, 3 cm length) at 90° C and peeled off, followed by rapid quenching of the MoS_2-transferred PETG down to room temperature. The coefficients of thermal expansion (CTEs) of PETG and monolayer MoS_2 over the range of $20-90°$ C were experimentally measured to be 80.5 ± 2.5 ppm/°C and 7 ppm/°C, respectively [52]. The biaxial compressive strain applied in the monolayer MoS_2 due to the CTE mismatch can thus be calculated as

$$\epsilon(T_{tr}) = \int_{20°C}^{T_{tr}} \alpha_{PETG}(T)dT - \int_{20°C}^{T_{tr}} \alpha_{MoS_2}(T)dT \tag{3.26}$$

where T_{tr} is the transfer temperature of monolayer onto the PETG, α_{PETG} is the CTE of the PETG substrate, and α_{MoS_2} is the CTE of the monolayer MoS_2. Since we are using the transfer temperature of 90° C, the biaxial compressive strain in the monolayer MoS_2 resulting from this quenching process was 0.51 After the transfer, 3% Nafion perfluorinated resin solution (5 wt% in lower aliphatic alcohols and water, contains $15-20\%$ water, Sigma Aldrich) diluted by ethanol was spin coated at 4000 rpm on the prepared MoS_2 sample with biaxial compressive strain.

Electrical and Optical Characterization

Devices were charged from an Keithley 2410 Source Meter Unit connected to the gate electrode, while the graphene source contact was grounded. The PL QY was measured using a customized micro-PL instrument which was calibrated as following procedure. The PL QY measurement calibration is also described in detail in previous study [4]. The wavelength of spectrometer was verified with Ar lamps (Newport) and the wavelength-dependent instrument response function was measured by a virtual Lambertian blackbody source, which was created with a stabilized lamp (Thorlabs SLS201) and a spectralon reflection standard (Labsphere). The collection efficiency was then acquired by measuring the laser response which was focused on the spectralon relfection standard. Because the emission profile of the monolayer semiconductors has been known to be Lambertian, this gives the reasonable approximation of the source of PL emission from the monolayers. For calibration measurements taken from the spectralon reflection standard, the fraction of generated photons which escape from the sample was calculated using $1/4n^2$, where n is the refractive index of the medium [53]. Because the calibration was performed based on quartz substrates, the possibility of the errors from light leakage through transparent substrates was excluded. Independent approach was also used to verify the system calibration using a sample which has been known to have $QY \sim 100\%$ (rhodamine 6G in methanol). In order to ensure that there is no change in light outcoupling factors or collection efficiency, we measured the samples that have PL QY independent of strain, as shown in the Fig. S9. All of the samples show no change in PL spectra with applied strains, indicating that substrate-bending does not affect the PL QY and the same calibration approach can be used due to no change in light outcoupling and collection efficiency of the system. An Ar ion laser with a 514.5 nm line was used as the excitation source. All measurements reported in this paper are taken at room temperature, in an ambient lab conditions under nitrogen flow. The applied strain on the flexible substrate were calculated using the equation $\epsilon = t/R$, where $2t$ and R are the substrate thickness and curvature radius. The thickness 2t of the entire flexible substrate is measured through the cross-section optical image. The curvature radius R were measured through the side-view photograph. All theory calculations are carried out in MATLAB.

EEA Coefficient in Different Materials

Material/ Substrate (Reference)	EEA Coefficient (cm^2s)	Exciton Lifetime (ns)	Optical Bandgap (eV)
MoS_2/PMMA [1]	3.5	12.0	1.84
MoS_2/SiO_2 [54]	$(4.3 \pm 1.1) \times 10^{-2}$	0.09	1.88
MoS_2/Quartz [55]	$0.62 - 0.81$	20.0	1.89
MoS_2/sapphire [55]	$0.02 - 0.04$	20.0	1.89
MoS_2/STO [55]	$0.0049 - 0.0098$	20.0	1.89
WS_2/PMMA [1]	2.4	1.25	2.01
WS_2/hBN [56]	$(6.3 \pm 1.7) \times 10^{-3}$	0.06	1.99
WS_2/Quartz [55]	$0.0888 - 0.1171$	1.00	2.01
WS_2/sapphire [55]	$0.01752 - 0.02311$	1.00	2.01
WS_2/STO [55]	$0.000864 - 0.001126$	1.00	2.01
WS_2/SiO_2 [57]	0.089 ± 0.001	0.14 ± 0.001	2.01
WSe_2/SiO_2 [58]	0.03	1.00	1.66
WSe_2/SiO_2 [59]	0.05	1.00	1.64
WSe_2/SiO_2/Si 10K [60]	0.26 ± 0.02	0.21 ± 0.005	1.66
WSe_2/sapphire 10K [60]	0.011 ± 0.002	0.041 ± 0.002	1.66
CVD WSe_2/sapphire 10K [60]	0.15 ± 0.02	0.055 ± 0.002	1.63
WSe_2/MgF_2 10K [60]	0.018 ± 0.002	0.418 ± 0.010	1.65
WSe_2/hBN/Si_3N_4/Si 10K [60]	0.11 ± 0.02	0.116 ± 0.05	1.66
WSe_2/SiO_2 50K [61]	1.1	0.027	1.74
$MoSe_2$/SiO_2 [62]	0.06	23.0	1.57
$MoTe_2$/SiO_2 [63]	0.1	0.12	1.17
Black Phosphorus 4K [64]	$(5.0 \pm 0.2) \times 10^{-3}$	0.28	2.01
RP perovskite [65] ($n = 1$)	$(3.35 \pm 0.15) \times 10^{-4}$	28 ± 7	2.37
($n = 2$)	$(1.1 \pm 0.35) \times 10^{-4}$	35 ± 4	2.15
($n = 3$)	$(4.9 \pm 0.12) \times 10^{-4}$	6.7 ± 0.8	1.99
($n = 4$)	$(2.5 \pm 0.5) \times 10^{-4}$	8 ± 10	1.89
SnS (1.10 nm) [66]	4.34×10^{-4}	3.00	1.60
2D perovskite [67] 1L	$(17 \pm 5) \times 10^{-3}$	2.22	2.39
2L	$(4.1 \pm 1.0) \times 10^{-3}$	4.3478	2.13
3L	$(3.5 \pm 0.6) \times 10^{-3}$	3.3333	1.99
4L	$(2.8 \pm 0.6) \times 10^{-3}$	5.00	1.91
5L	$(1.3 \pm 0.3) \times 10^{-3}$	6.6667	1.81
ReS_2 [68] 1L	0.078 ± 0.015	0.059 ± 0.003	1.62
2L	0.047 ± 0.016	0.083 ± 0.007	1.55
3L	0.011 ± 0.005	0.139 ± 0.010	1.52

Table 3.1: EEA Coefficient and exciton lifetime of 2D materials. (RP = Ruddlesden–Popper)

Material/ Substrate (Reference)	EEA Coefficient (cm^2s)	Exciton Lifetime (ns)	Optical Bandgap (eV)
Hexagonal Boron Nitride [69]	2×10^{-7}	0.43	6.00
Bulk hBN 8K [70, 71]	1×10^{-6}	0.6	5.79
bulk CuO_2 11K [72]	$(0.5 - 4) \times 10^{-7}$	470 ± 12	2.01
CuO_2 2K [73]	7×10^{-8}	3.50	2.01
CuO_2 30K [74]	1×10^{-15}	2^6	2.00
CuO_2 2K [74]	1×10^{-14}	150×10^3	2.00
CuO_2 70K [75]	6×10^{-8}	300	2.14
Terbium Phosphate 300K [76, 77]	5×10^{-15}	73.9×10^3	2.28
Terbium Fluoride 3.95K [78, 79]	3.5×10^{-15}	179×10^3	3.22
MnF_2 1.7K [80]	5×10^{-13}	0.125×10^6	4.56
5 at.% Cm_4:CeF_4 2K [81]	$(1 \pm 0.25) \times 10^{-14}$	20×10^3	2.47
$Cm_{0.05}Ce_{0.95}F_4$ 4.2K [82]	1×10^{-12}	27.78×10^3	2.47
$Cs_2UO_2C_4$ Crystal 12.5K [83]	$(1 - 10) \times 10^{-14}$	3.7736×10^3	2.49
$CsMnF_3$ 3.5K [84]	$(5.3 \pm 2.5) \times 10^{-15}$	$(0.72 \pm 0.05) \times 10^6$	2.13
$GdCI_3$ 4.4K [85]	4.7×10^{-14}	170×10^3	3.98
NaI:TI [86]	2×10^{-11}	169.5	2.99
Intrinsic Silicon 4K [87]	0.5×10^{-9}	2600	1.20
DMABI [88]	5×10^{-10}	7.1429	2.39
Solid Xe crystal 20K [89]	1.75×10^{-6}	2.2	8.37

Table 3.2: EEA Coefficient and exciton lifetime of bulk materials.

Material/ Substrate (Reference)	EEA Coefficient (cm^2s)	Exciton Lifetime (ns)	Optical Bandgap (eV)
(6, 5) SW CNT [90]	$(2.0814 \pm 1.2050) \times 10^{-7}$	0.055	1.25
Semiconducting SW CNT [91]	1.1831×10^{-6}	0.3	0.80
CdSe Nanowires [92]	2.3025×10^{-10}	1.5	1.78
Ti-catalyzed Si NW [93] 4K	$(6 \pm 2.8) \times 10^{-13}$	10^6	1.62
50K	$(2.1 \pm 0.5) \times 10^{-13}$	500×10^3	1.61
100K	$(4.5 \pm 0.15) \times 10^{-13}$	250×10^3	1.59
300K	$(1.3 \pm 0.2) \times 10^{-12}$	49×10^3	1.59
Si nanocrystal [94]	$(0.8 - 2) \times 10^{-9}$	0.01	1.36
Si NW [95] 100K	1×10^{-12}	90×10^3	1.59
300K	2×10^{-12}	50×10^3	1.57
(6,4) single walled CNT [96]	$(5.79 \pm 2.43) \times 10^{-8}$	0.0106	1.40
CdSe nanorods [97]	1.8×10^{-9}	1	1.79
$CsPbBr_3$ Quantum Dots [98]	7×10^{-7}	4.3	2.42
COF-5 [99]	1.09×10^{-8}	0.0125	2.64

Table 3.3: EEA Coefficient and exciton lifetime of one, and zero dimensional, and molecular systems (SW = Single wall, CNT = Carbon nano tube, NW = Nanowire, COF = Covalent organic framework).

Material/ Substrate (Reference)	EEA Coefficient (cm^2s)	Exciton Lifetime (ns)	Optical Bandgap (eV)
MEH-PPV [100, 101]	$(2.8 \pm 0.5) \times 10^{-8}$	0.140	2.00
MEH-PPV [102]	1.2403×10^{-9}	0.260	1.91
MEH-DSB [103]	4.3274×10^{-10}	0.150	2.33
PPV 259K [104]	4×10^{-8}	0.200	1.94
PPV 77K [105]	2×10^{-8}	0.280	2.14
2CzPN [106]	5×10^{-15}	273×10^3	2.57
Chlorelia pyrenoidosa [107, 108]	1×10^{-8}	15	1.80
PDHS [109, 109]	2×10^{-7}	0.600	3.47
TMMC [110]	1×10^{-15}	740×10^3	1.91
Polyfluorene [111]	$(1.5 - 3.8) \times 10^{-8}$	0.150	2.82
$\beta-$Phase Polyfluorene [112]	2×10^{-8}	0.144	2.83
J-Cyanine [113]	0.55×10^{-6}	0.043	2.02
J-pseudoisocyanine [114]	$(2.6 \pm 0.5) \times 10^{-3}$	$0.071 - 0.167$	2.16
F8−PDA [115, 116]	1.2×10^{-11}	3.6×10^3	2.58
Anthracene [117–120]	$(1 \pm 0.5) \times 10^{-8}$	$3.5 - 4.1$	3.06
Tetracene [121]	5×10^{-9}	0.3	2.41
Tetracene [122]	$(1.70 \pm 0.08) \times 10^{-8}$	0.08 ± 0.003	2.41
P3HT/PCBM blend [123]	4×10^{-9}	0.450	1.77
TTBC adsorbed silica [124]	5×10^{-8}	0.889	2.09
Alq_3 [125, 126]	$(3.5 \pm 2.5) \times 10^{-11}$	$14 - 16$	2.47
$Eu(tta)_4N(Et)_4$ [127]	5.5×10^{-9}	1	2.02
solid C60 [128]	$(7 \pm 1) \times 10^{-10}$	0.1	1.60
β-hydrogen phthalocyanine [129]	9.376×10^{-11}	0.2459512	1.98
J-cyanine chloride [130]	6.5×10^{-10}	0.2	2.15
J-BTHC [131]	0.5150×10^{-4}	0.500 ± 0.020	2.65
TDBC−1 [132]	0.5115×10^{-3}	0.220	2.11
Pyrene [133]	$(7.5 \pm 4.0) \times 10^{-12}$	200	2.63
Spinach chloroplasts [134]	$(5.2 \pm 1.6) \times 10^{-9}$	0.8	1.81
	$(15.6 \pm 4.0) \times 10^{-9}$	0.8	1.81
	$(9.6 \pm 4.8) \times 10^{-9}$	0.9	1.81
	$(12 \pm 4) \times 10^{-9}$	1.1	1.81
x-benzophenone [135]	$(5 \pm 1.2) \times 10^{-15}$	2.5×10^3	2.70
a-benzophenone [135]	$(1.3 \pm 0.7) \times 10^{-13}$	205×10^3	2.69

DCB 4K [136]	$(4.3 \pm 2.0) \times 10^{-13}$	15×10^3	2.99
α-sexithienyl [137]	2.83×10^{-8}	0.050	3.20
P3HT [138]	3.0386×10^{-10}	0.5063	1.71
α-Fe_2O_3 Hematite [139]	$(7.60 \pm 0.02) \times 10^{-9}$	1.5	2.10
4% CBP:PtOEP [140, 141]	1.5×10^{-14}	108×10^3	3.10
8% PtOEP:Alq_3 [140, 141]	8.0×10^{-14}	20×10^3	2.70
C_{60} [142]	7×10^{-9}	0.010	2.09
$C_{60}-O_2$ [142]	8.75×10^{-9}	0.036	2.09
Region-random P3HT [143]	1.23×10^{-10}	1	2.25
Regio-regular P3HT [144]	$(0.9 \pm 0.8) \times 10^{-8}$	0.3 ± 0.1	1.91
LPPP [145]	4.2×10^{-9}	0.045	2.69
poly thiophene [146]	$(1.5 \pm 0.2) \times 10^{-9}$	0.270 ± 0.020	2.05
Oligothiophene dioxide [147]	$(2.4 \pm 0.2) \times 10^{-11}$	7.9	2.37
	$(4.5 \pm 0.5) \times 10^{-11}$	1.6	2.26
	$(9.5 \pm 0.5) \times 10^{-11}$	0.29	1.90
P3HT [148]	4.5×10^{-9}	0.3049	1.74
Polyparaphenylene [149]	1.3×10^{-8}	0.59 ± 0.020	2.68
FALPc [150]	9.33×10^{-9}	0.75 ± 0.05 ps	1.72
DPT [151]	3.9×10^{-9}	0.0008	2.47
Chlorophyl A [152]	1.25×10^{-10}	3	1.82
1:1 F8BT:PFB [153]	5×10^{-12}	2×10^3	1.91
DPOP-PPV [154]	5×10^{-10}	1.5	2.38
c-Phycoerythrin [155]	1.44×10^{-9}	1.8349	2.16
c-Phycocyanin [155]	6.3×10^{-9}	2.1097	1.94
Allophycocyanin [155]	1.6×10^{-9}	1.8657	1.89
poly(phenyl methyl silane) [156]	8×10^{-8}	0.073	4.60
poly(di-n-hexyl silane) [156]	6×10^{-8}	0.6	3.47
platinum-octaethylporphyrin [157]	$1.39 \times 10 - 14$	95×10^3	3.25
N719 dye [158]	1×10^{-12}	21	1.65
D149 dye [158]	2×10^{-9}	0.55	1.82
MK2 dye [158]	1×10^{-8}	0.55	1.72
$Ir(ppy)_3$ G1 [159]	200×10^{-14}	14.2857	2.35
$Ir(ppy)_3$ carb [159]	30×10^{-14}	111.1111	2.34
$Ir(ppy)_3$ G2 [159]	5×10^{-14}	1000	2.39
CBP PtOEP [160]	$(8.5 - 9) \times 10 - 15$	95×10^3	3.25
IrG1:CBP [161]	$(6 \pm 1) \times 10^{-9}$	0.5	2.41

Tetracene [162]	1.6×10^{-9}	12.5	2.40
	1.7×10^{-11}	62.5×10^{3}	1.25
Rubrene [162]	8×10^{-10}	7.6923	2.23
	5.1×10^{-12}	100×10^{3}	1.14
TIPS-pentacene [162]	2.4×10^{-8}	7.6923	1.70
TIPS-pentacene [162]	5×10^{-12}	10^{5}	0.85
Chlorophyll a/b [163]	2.75×10^{-9}	1.25	1.88
ACRXTN [164]	1.46×10^{-12}	112.4859	2.39
CBP [165, 166]	1×10^{-14}	15×10^{6}	1.91
Bisfluorene-cored dendrimer [167]	5.5×10^{-10}	0.7692	2.95
Trans-stilbene [168]	1×10^{-12}	10^{7}	2.15

Table 3.4: EEA Coefficient and exciton lifetime of molecular films. (MEH-PPV = Poly[2-methoxy-5-(2-ethylhexyloxy)-1,4-phenylenevinylene], MEH-DSB = 2-methoxy-5-(2'-ethylhexyloxy)-distyryl benzene, PPV = Poly(p-phenylene vinylene), 2CzPN = 4,5-di (9H-carbazol-9-yl) 30 phthalonitrile), PDHS = poly(din-hexylsilane), = Tetramethylammonium manganese trichloride, PFO = polyfluorene, poly(3−hexylthiophene = P3HT), TTBC = tetrachlorobenzimidazolocarbocyanine, Alq_3 = tris (8-hydroxyquinoline), $Eu(tta)_4N(Et)_4$ = tetraethylammonium tetrakis4,4,4,- trifluoro-1-2-thienyl-1,3-butadionoeuropiumIII, DCB = Dichlorobenzophenone , LPPP = ladder-type poly p-phenylene, FAlPc = fluoroaluminum phthalocyanine, DPT = 5,12-diphenyl tetracene , PtOEP = platinum-octaethylporphyrin , $Ir(ppy)_3$ = fac-tris(2-phenylpyridine) iridium(III)

3.6 References

[1] Der-Hsien Lien, Shiekh Zia Uddin, Matthew Yeh, Matin Amani, Hyungjin Kim, Joel W Ager, Eli Yablonovitch, and Ali Javey. Electrical suppression of all nonradiative recombination pathways in monolayer semiconductors. *Science*, 364(6439):468–471, 2019.

[2] Jason S Ross, Sanfeng Wu, Hongyi Yu, Nirmal J Ghimire, Aaron M Jones, Grant Aivazian, Jiaqiang Yan, David G Mandrus, Di Xiao, Wang Yao, et al. Electrical control of neutral and charged excitons in a monolayer semiconductor. *Nature Communications*, 4(1):1–6, 2013.

[3] Freddie Withers, O Del Pozo-Zamudio, A Mishchenko, AP Rooney, Ali Gholinia, K Watanabe, T Taniguchi, Sarah J Haigh, AK Geim, AI Tartakovskii, et al. Light-emitting diodes by band-structure engineering in van der Waals heterostructures. *Nature Materials*, 14(3):301–306, 2015.

[4] Matin Amani, Der-Hsien Lien, Daisuke Kiriya, Jun Xiao, Angelica Azcatl, Jiyoung Noh, Surabhi R Madhvapathy, Rafik Addou, KC Santosh, Madan Dubey, et al. Near-unity photoluminescence quantum yield in MoS_2. *Science*, 350(6264):1065–1068, 2015.

[5] Yiling Yu, Yifei Yu, Chao Xu, Andy Barrette, Kenan Gundogdu, and Linyou Cao. Fundamental limits of exciton-exciton annihilation for light emission in transition metal dichalcogenide monolayers. *Physical Review B*, 93(20):201111, 2016.

[6] Feng Wang, Yang Wu, Mark S Hybertsen, and Tony F Heinz. Auger recombination of excitons in one-dimensional systems. *Physical Review B*, 73(24):245424, 2006.

[7] Shiekh Zia Uddin, Eran Rabani, and Ali Javey. Universal inverse scaling of exciton–exciton annihilation coefficient with exciton lifetime. *Nano Letters*, 21(1):424–429, 2020.

[8] Caroline Murawski, Karl Leo, and Malte C Gather. Efficiency roll-off in organic light-emitting diodes. *Advanced Materials*, 25(47):6801–6827, 2013.

[9] Wei Zou, Renzhi Li, Shuting Zhang, Yunlong Liu, Nana Wang, Yu Cao, Yanfeng Miao, Mengmeng Xu, Qiang Guo, Dawei Di, et al. Minimising efficiency roll-off in high-brightness perovskite light-emitting diodes. *Nature Communications*, 9(1):1–7, 2018.

[10] Wan Ki Bae, Young-Shin Park, Jaehoon Lim, Donggu Lee, Lazaro A Padilha, Hunter McDaniel, Istvan Robel, Changhee Lee, Jeffrey M Pietryga, and Victor I Klimov. Controlling the influence of auger recombination on the performance of quantum-dot light-emitting diodes. *Nature Communications*, 4(1):1–8, 2013.

[11] Justin Iveland, Lucio Martinelli, Jacques Peretti, James S Speck, and Claude Weisbuch. Direct measurement of auger electrons emitted from a semiconductor light-emitting diode under electrical injection: identification of the dominant mechanism for efficiency droop. *Physical Review Letters*, 110(17):177406, 2013.

[12] Martin A Green. Limits on the open-circuit voltage and efficiency of silicon solar cells imposed by intrinsic auger processes. *IEEE Transactions on electron devices*, 31(5):671–678, 1984.

[13] Georgios M Kavoulakis and Gordon Baym. Auger decay of degenerate and bose-condensed excitons in Cu_2O. *Physical Review B*, 54(23):16625, 1996.

[14] Ozgur Burak Aslan, Minda Deng, and Tony F Heinz. Strain tuning of excitons in monolayer WSe_2. *Physical Review B*, 98(11):115308, 2018.

[15] Léon Van Hove. The occurrence of singularities in the elastic frequency distribution of a crystal. *Physical Review*, 89(6):1189, 1953.

[16] JE Hirsch and DJ Scalapino. Enhanced superconductivity in quasi two-dimensional systems. *Physical Review Letters*, 56(25):2732, 1986.

[17] Zhiwei Li, Yawei Lv, Liwang Ren, Jia Li, Lingan Kong, Yujia Zeng, Quanyang Tao, Ruixia Wu, Huifang Ma, Bei Zhao, et al. Efficient strain modulation of 2D materials via polymer encapsulation. *Nature Communications*, 11(1):1–8, 2020.

[18] Sujay B Desai, Gyungseon Seol, Jeong Seuk Kang, Hui Fang, Corsin Battaglia, Rehan Kapadia, Joel W Ager, Jing Guo, and Ali Javey. Strain-induced indirect to direct bandgap transition in multilayer WSe_2. *Nano Letters*, 14(8):4592–4597, 2014.

[19] G Bemski. Recombination in semiconductors. *Proceedings of the IRE*, 46(6):990–1004, 1958.

[20] VN Abakumov, Vladimir Idelevich Perel, and IN Yassievich. *Nonradiative Recombination in Semiconductors*. Elsevier, 1991.

[21] Shiang Fang, Stephen Carr, Miguel A Cazalilla, and Efthimios Kaxiras. Electronic structure theory of strained two-dimensional materials with hexagonal symmetry. *Physical Review B*, 98(7):075106, 2018.

[22] Shiang Fang, Rodrick Kuate Defo, Sharmila N Shirodkar, Simon Lieu, Georgios A Tritsaris, and Efthimios Kaxiras. Ab initio tight-binding hamiltonian for transition metal dichalcogenides. *Physical Review B*, 92(20):205108, 2015.

[23] Franco Bassani, Giuseppe Pastori Parravicini, Raymond A Ballinger, and Joseph L Birman. Electronic states and optical transitions in solids. *Physics Today*, 29(3):58, 1976.

[24] Manuel Cardona and Y Yu Peter. *Fundamentals of semiconductors*, volume 619. Springer, 2005.

[25] Julien Madéo, Michael KL Man, Chakradhar Sahoo, Marshall Campbell, Vivek Pareek, E Laine Wong, Abdullah Al-Mahboob, Nicholas S Chan, Arka Karmakar, Bala Murali Krishna Mariserla, et al. Directly visualizing the momentum-forbidden dark excitons and their dynamics in atomically thin semiconductors. *Science*, 370(6521):1199–1204, 2020.

[26] Mark Silver, EP O'reilly, and AR Adams. Determination of the wavelength dependence of auger recombination in long-wavelength quantum-well semiconductor lasers using hydrostatic pressure. *IEEE journal of Quantum Electronics*, 33(9):1557–1566, 1997.

[27] A Haug. Auger recombination in direct-gap semiconductors: band-structure effects. *Journal of Physics C: Solid State Physics*, 16(21):4159, 1983.

[28] Xie Zhang, Jimmy-Xuan Shen, and Chris G Van de Walle. Anomalous auger recombination in PbSe. *Physical Review Letters*, 125(3):037401, 2020.

[29] Joy Cho, Matin Amani, Der-Hsien Lien, Hyungjin Kim, Matthew Yeh, Vivian Wang, Chaoliang Tan, and Ali Javey. Centimeter-scale and visible wavelength monolayer light-emitting devices. *Advanced Functional Materials*, 30(6):1907941, 2020.

[30] Gregory D Scholes. Insights into excitons confined to nanoscale systems: electron–hole interaction, binding energy, and photodissociation. *ACS Nano*, 2(3):523–537, 2008.

[31] Aleksandr Sergeevich Davydov. The theory of molecular excitons. *Soviet Physics Uspekhi*, 7(2):145, 1964.

[32] Louis Brus. Zero-dimensional 'excitons' in semiconductor clusters. *IEEE Journal of Quantum Electronics*, 22(9):1909–1914, 1986.

[33] Feng Wang, Gordana Dukovic, Louis E Brus, and Tony F Heinz. The optical resonances in carbon nanotubes arise from excitons. *Science*, 308(5723):838–841, 2005.

[34] Andrea Splendiani, Liang Sun, Yuanbo Zhang, Tianshu Li, Jonghwan Kim, Chi-Yung Chim, Giulia Galli, and Feng Wang. Emerging photoluminescence in monolayer MoS_2. *Nano Letters*, 10(4):1271–1275, 2010.

[35] SW Koch, M Kira, G Khitrova, and HM Gibbs. Semiconductor excitons in new light. *Nature Materials*, 5(7):523–531, 2006.

[36] Chihaya Adachi, Marc A Baldo, Mark E Thompson, and Stephen R Forrest. Nearly 100% internal phosphorescence efficiency in an organic light-emitting device. *Journal of Applied Physics*, 90(10):5048–5051, 2001.

[37] A Suna. Kinematics of exciton-exciton annihilation in molecular crystals. *Physical Review B*, 1(4):1716, 1970.

[38] Volkhard May. Kinetic theory of exciton–exciton annihilation. *The Journal of Chemical Physics*, 140(5):054103, 2014.

[39] DT Nguyen, C Voisin, Ph Roussignol, C Roquelet, Jean-Sébastien Lauret, and Guillaume Cassabois. Elastic exciton-exciton scattering in photoexcited carbon nanotubes. *Physical Review Letters*, 107(12):127401, 2011.

[40] VM Kenkre. Validity of the bilinear rate equation for exciton annihilation and expressions for the annihilation constant. *Zeitschrift für Physik B Condensed Matter*, 43(3):221–227, 1981.

[41] Luxia Wang and Volkhard May. Theory of multiexciton dynamics in molecular chains. *Physical Review B*, 94(19):195413, 2016.

[42] Florian Katsch, Malte Selig, Alexander Carmele, and Andreas Knorr. Theory of exciton–exciton interactions in monolayer transition metal dichalcogenides. *Physica Status Solidi (b)*, 255(12):1800185, 2018.

[43] Peter Reineker. *Exciton dynamics in molecular crystals and aggregates*, volume 94. Springer, 1982.

[44] VM Kenkre. Theory of exciton annihilation in molecular crystals. *Physical Review B*, 22(4):2089, 1980.

[45] RW Munn and R Silbey. Remarks on exciton—phonon coupling and exciton transport. *Molecular Crystals and Liquid Crystals*, 57(1):131–144, 1980.

[46] Jan A Freund and Thorsten Pöschel. *Stochastic processes in physics, chemistry, and biology*, volume 557. Springer Science & Business Media, 2000.

[47] Oleksandr V Mikhnenko, Paul WM Blom, and Thuc-Quyen Nguyen. Exciton diffusion in organic semiconductors. *Energy & Environmental Science*, 8(7):1867–1888, 2015.

[48] Conor Madigan and Vladimir Bulović. Modeling of exciton diffusion in amorphous organic thin films. *Physical Review Letters*, 96(4):046404, 2006.

[49] Franziska Fennel and Stefan Lochbrunner. Exciton-exciton annihilation in a disordered molecular system by direct and multistep förster transfer. *Physical Review B*, 92(14):140301, 2015.

[50] J Erland, BS Razbirin, K-H Pantke, VG Lyssenko, and JM Hvam. Exciton diffusion in CdSe. *Physical Review B*, 47(7):3582, 1993.

[51] V Čápek and RW Munn. Exciton transport in the band limit. *The Journal of Chemical Physics*, 76(9):4674–4675, 1982.

[52] Lenan Zhang, Zhengmao Lu, Youngsup Song, Lin Zhao, Bikram Bhatia, Kevin R Bagnall, and Evelyn N Wang. Thermal expansion coefficient of monolayer molybdenum disulfide using micro-raman spectroscopy. *Nano Letters*, 19(7):4745–4751, 2019.

[53] Eli Yablonovitch and George D Cody. Intensity enhancement in textured optical sheets for solar cells. *IEEE Transactions on Electron Devices*, 29(2):300–305, 1982.

[54] Dezheng Sun, Yi Rao, Georg A Reider, Gugang Chen, Yumeng You, Louis Brézin, Avetik R Harutyunyan, and Tony F Heinz. Observation of rapid exciton–exciton annihilation in monolayer molybdenum disulfide. *Nano Letters*, 14(10):5625–5629, 2014.

[55] AJ Goodman, D-H Lien, GH Ahn, LL Spiegel, M Amani, AP Willard, A Javey, and WA Tisdale. Substrate-dependent exciton diffusion and annihilation in chemically treated MoS_2 and WS_2. *The Journal of Physical Chemistry C*, 124(22):12175–12184, 2020.

[56] Yusuke Hoshi, Takashi Kuroda, Mitsuhiro Okada, Rai Moriya, Satoru Masubuchi, Kenji Watanabe, Takashi Taniguchi, Ryo Kitaura, and Tomoki Machida. Suppression of exciton-exciton annihilation in tungsten disulfide monolayers encapsulated by hexagonal boron nitrides. *Physical Review B*, 95(24):241403, 2017.

[57] Paul D Cunningham, Kathleen M McCreary, and Berend T Jonker. Auger recombination in chemical vapor deposition-grown monolayer WS_2. *The Journal of Physical Chemistry Letters*, 7(24):5242–5246, 2016.

[58] AT Hanbicki, M Currie, G Kioseoglou, AL Friedman, and BT Jonker. Measurement of high exciton binding energy in the monolayer transition-metal dichalcogenides WS_2 and WSe_2. *Solid State Communications*, 203:16–20, 2015.

[59] Mathieu Massicotte, Fabien Vialla, Peter Schmidt, Mark B Lundeberg, Simone Latini, Sten Haastrup, Mark Danovich, Diana Davydovskaya, Kenji Watanabe, Takashi Taniguchi, et al. Dissociation of two-dimensional excitons in monolayer WSe_2. *Nature communications*, 9(1):1–7, 2018.

[60] Sina Lippert, Lorenz Maximilian Schneider, Dylan Renaud, Kyung Nam Kang, Obafunso Ajayi, Jan Kuhnert, Marc-Uwe Halbich, Oday M Abdulmunem, Xing Lin, Khaleel Hassoon, et al. Influence of the substrate material on the optical properties of tungsten diselenide monolayers. *2D Materials*, 4(2):025045, 2017.

[61] Yumeng You, Xiao-Xiao Zhang, Timothy C Berkelbach, Mark S Hybertsen, David R Reichman, and Tony F Heinz. Observation of biexcitons in monolayer WSe_2. *Nature Physics*, 11(6):477–481, 2015.

[62] Nardeep Kumar, Qiannan Cui, Frank Ceballos, Dawei He, Yongsheng Wang, and Hui Zhao. Exciton diffusion in monolayer and bulk $MoSe_2$. *Nanoscale*, 6(9):4915–4919, 2014.

[63] Guillaume Froehlicher, Etienne Lorchat, and Stéphane Berciaud. Direct versus indirect band gap emission and exciton-exciton annihilation in atomically thin molybdenum ditelluride ($MoTe_2$). *Physical Review B*, 94(8):085429, 2016.

[64] Alessandro Surrente, AA Mitioglu, Krzysztof Galkowski, L Klopotowski, Wojciech Tabis, Baptiste Vignolle, Duncan Kennedy Maude, and Paulina Plochocka. Onset of exciton-exciton annihilation in single-layer black phosphorus. *Physical Review B*, 94(7):075425, 2016.

[65] Géraud Delport, Gabriel Chehade, Ferdinand Lédée, Hiba Diab, Cosme Milesi-Brault, Gaelle Trippe-Allard, Jacky Even, Jean-Sébastien Lauret, Emmanuelle Deleporte, and Damien Garrot. Exciton–exciton annihilation in two-dimensional halide perovskites at room temperature. *The Journal of Physical Chemistry Letters*, 10(17):5153–5159, 2019.

[66] Abdus Salam Sarkar, Aamir Mushtaq, Dushyant Kushavah, and Suman Kalyan Pal. Strong many-body interactions in ultrathin anisotropic tin (II) monosulfide. *arXiv preprint arXiv:1811.00209*, 2018.

[67] Shibin Deng, Enzheng Shi, Long Yuan, Linrui Jin, Letian Dou, and Libai Huang. Long-range exciton transport and slow annihilation in two-dimensional hybrid perovskites. *Nature Communications*, 11(1):1–8, 2020.

[68] Sangwan Sim, Doeon Lee, Jekwan Lee, Myungjun Cha, Soonyoung Cha, Wonhyeok Heo, Sungjun Cho, Wooyoung Shim, Kyusang Lee, Jinkyoung Yoo, et al. Role of weak interlayer coupling in ultrafast exciton-exciton annihilation in two-dimensional rhenium dichalcogenides. *Physical Review B*, 101(17):174309, 2020.

[69] Ioannis Chatzakis, Roderick B Davidson, Adam D Dunkelberger, Song Liu, Jaime Freitas, James Culbertson, JH Edgar, Daniel C Ratchford, Chase T Ellis, Andrea B Grafton, et al. Rapid bimolecular and defect-assisted carrier recombination in hexagonal Boron Nitride. *The Journal of Physical Chemistry C*, 123(23):14689–14695, 2019.

[70] Alexandre Plaud, Léonard Schué, Kenji Watanabe, Takashi Taniguchi, F Fossard, F Ducastelle, A Loiseau, and J Barjon. Exciton-exciton annihilation in hBN. *Applied Physics Letters*, 114(23):232103, 2019.

[71] Léonard Schué, Lorenzo Sponza, Alexandre Plaud, Hakima Bensalah, Kenji Watanabe, Takashi Taniguchi, François Ducastelle, Annick Loiseau, and Julien Barjon. Bright luminescence from indirect and strongly bound excitons in h-BN. *Physical review letters*, 122(6):067401, 2019.

[72] David Snoke and GM Kavoulakis. Bose–einstein condensation of excitons in Cu_2O: progress over 30 years. *Reports on Progress in Physics*, 77(11):116501, 2014.

[73] KE O'hara, JR Gullingsrud, and JP Wolfe. Auger decay of excitons in Cu_2O. *Physical Review B*, 60(15):10872, 1999.

[74] A Jolk, M Jörger, and C Klingshirn. Exciton lifetime, auger recombination, and exciton transport by calibrated differential absorption spectroscopy in Cu_2O. *Physical Review B*, 65(24):245209, 2002.

[75] JT Warren, KE O'Hara, and JP Wolfe. Two-body decay of thermalized excitons in Cu_2O. *Physical Review B*, 61(12):8215, 2000.

[76] PC Diggle, KA Gehring, and RM Macfarlane. Exciton-exciton annihilation in $TbPO_4$. *Solid State Communications*, 18(3):391–394, 1976.

[77] Weihua Di, Jie Li, Naoto Shirahata, Yoshio Sakka, Marc-Georg Willinger, and Nicola Pinna. Photoluminescence, cytotoxicity and in vitro imaging of hexagonal terbium phosphate nanoparticles doped with europium. *Nanoscale*, 3(3):1263–1269, 2011.

[78] MF Joubert, B Jacquier, and R Moncorgé. Exciton-exciton annihilation and saturation effect in TbF_3. *Physical Review B*, 28(7):3725, 1983.

[79] V Vasyliev, EG Víllora, Y Sugahara, and K Shimamura. Judd-ofelt analysis and emission quantum efficiency of tb-fluoride single crystals: $LiTbF_4$ and $Tb_{0.81}Ca_{0.19}F_{2.81}$. *Journal of Applied Physics*, 113(20):203508, 2013.

[80] BA Wilson, J Hegarty, and WM Yen. Biexciton decay in MnF_2. *Physical Review Letters*, 41(4):268, 1978.

[81] GK Liu and James V Beitz. Excited-state dynamics and energy transfer of+ 4 curium in cerium tetrafluoride. *Physical Review B*, 41(10):6201, 1990.

[82] GK Liu and James V Beitz. Fluorescence dynamics and cross relaxation of 4+ curium in cerium tetrafluoride. *Journal of Luminescence*, 45(1-6):254–257, 1990.

[83] DM Krol. Energy transfer and biexciton decay in $Cs_2UO_2C_4$ crystals. *Chemical Physics Letters*, 74(3):515–518, 1980.

[84] R Moncorgé, B Jacquier, C Madej, M Blanchard, and LC Brunel. Exciton dynamics and energy transfers in pure $CsMnF_3$. *Journal de Physique*, 43(8):1267–1281, 1982.

[85] R Mahiou, B Jacquier, and C Madej. One-dimensional energy transfer in $GdCl_3$. *The Journal of Chemical Physics*, 89(9):5931–5942, 1988.

[86] Jai Singh and Alexander Koblov. Excitonic processes and their contribution to non-proportionality observed in the light yield of inorganic scintillators. *The European Physical Journal B*, 86(2):1–6, 2013.

[87] JD Cuthbert. Recombination kinetics of excitonic molecules and free excitons in intrinsic silicon. *Physical Review B*, 1(4):1552, 1970.

[88] G Kodis, V Gulbinas, L Valkūnas, and S Juršėnas. Non-linear luminescence of dimethylaminobenzylidene-1, 3-indandione solids. *Advanced Materials for Optics and Electronics*, 6(5-6):391–394, 1996.

[89] T Kessler, R Markus, H Nahme, and N Schwentner. Nonlinear excitation of pure and doped rare gas crystals. *Physica Status Solidi (b)*, 139(2):619–625, 1987.

[90] Xuedan Ma, Oleskiy Roslyak, Juan G Duque, Xiaoying Pang, Stephen K Doorn, Andrei Piryatinski, David H Dunlap, and Han Htoon. Influences of exciton diffusion

and exciton-exciton annihilation on photon emission statistics of carbon nanotubes. *Physical Review Letters*, 115(1):017401, 2015.

[91] Dac-Trung Nguyen, Christophe Voisin, Ph Roussignol, Cyrielle Roquelet, Jean-Sébastien Lauret, and Guillaume Cassabois. Excitonic nonlinearities in single-wall carbon nanotubes. *Physica Status Solidi (b)*, 249(5):907–913, 2012.

[92] István Robel, Bruce A Bunker, Prashant V Kamat, and Masaru Kuno. Exciton recombination dynamics in CdSe nanowires: bimolecular to three-carrier auger kinetics. *Nano Letters*, 6(7):1344–1349, 2006.

[93] Alex R Guichard, Rohan D Kekatpure, Mark L Brongersma, and Theodore I Kamins. Temperature-dependent auger recombination dynamics in luminescent silicon nanowires. *Physical Review B*, 78(23):235422, 2008.

[94] Miroslav Kořínek, František Trojánek, Daniel Hiller, Sebastian Gutsch, Margit Zacharias, Christian Kübel, and Petr Malỳ. Picosecond dynamics of photoexcited carriers in interacting silicon nanocrystals. *Applied Surface Science*, 377:238–243, 2016.

[95] Alex R Guichard, Rohan D Kekatpure, and Mark L Brongersma. Auger recombination in luminescent, CMOS-compatible Si nanowires. In *2007 4th IEEE International Conference on Group IV Photonics*, pages 1–3. IEEE, 2007.

[96] Takeshi Koyama, Yasumitsu Miyata, Hideo Kishida, Hisanori Shinohara, and Arao Nakamura. Photophysics in single-walled carbon nanotubes with (6, 4) chirality at high excitation densities: Bimolecular auger recombination and phase-space filling of excitons. *The Journal of Physical Chemistry C*, 117(4):1974–1981, 2013.

[97] H Htoon, JA Hollingsworth, R Dickerson, and VI Klimov. Effect of zero-to one-dimensional transformation on multiparticle auger recombination in semiconductor quantum rods. *Physical Review Letters*, 91(22):227401, 2003.

[98] Ke Wei, Xin Zheng, Xiangai Cheng, Chao Shen, and Tian Jiang. Observation of ultrafast exciton–exciton annihilation in $CsPbBr_3$ quantum dots. *Advanced Optical Materials*, 4(12):1993–1997, 2016.

[99] Nathan C Flanders, Matthew S Kirschner, Pyosang Kim, Thomas Fauvell, Austin Evans, Waleed Helweh, Austin P Spencer, Richard D Schaller, William Dichtel, and Lin X Chen. Ultrafast exciton dynamics in two dimensional covalent organic frameworks reveals size dependence to exciton diffusion. *chemrxiv*, 2020.

[100] AJ Lewis, A Ruseckas, OPM Gaudin, GR Webster, PL Burn, and IDW Samuel. Singlet exciton diffusion in MEH-PPV films studied by exciton-exciton annihilation. *Organic Electronics*, 7(6):452–456, 2006.

[101] IH Campbell, TW Hagler, DL Smith, and JP Ferraris. Direct measurement of conjugated polymer electronic excitation energies using metal/polymer/metal structures. *Physical Review Letters*, 76(11):1900, 1996.

[102] Arthur Dogariu, Dan Vacar, and Alan J Heeger. Picosecond time-resolved spectroscopy of the excited state in a soluble derivative of poly (phenylene vinylene): Origin of the bimolecular decay. *Physical Review B*, 58(16):10218, 1998.

[103] ES Maniloff, VI Klimov, and DW McBranch. Intensity-dependent relaxation dynamics and the nature of the excited-state species in solid-state conducting polymers. *Physical Review B*, 56(4):1876, 1997.

[104] RG Kepler, VS Valencia, SJ Jacobs, and JJ McNamara. Exciton-exciton annihilation in poly (p-phenylenevinylene) films. *Synthetic Metals*, 78(3):227–230, 1996.

[105] Michels MA Bassler H Van der Horst JW, Bobbert PA. Calculation of excitonic properties of conjugated polymers using the Bethe–Salpeter equation. *The Journal of Chemical Physics*, 15(114):6950–7, 2001.

[106] Kensuke Masui, Hajime Nakanotani, and Chihaya Adachi. Analysis of exciton annihilation in high-efficiency sky-blue organic light-emitting diodes with thermally activated delayed fluorescence. *Organic Electronics*, 14(11):2721–2726, 2013.

[107] AJ Campillo, SL Shapiro, VH Kollman, KR Winn, and RC Hyer. Picosecond exciton annihilation in photosynthetic systems. *Biophysical Journal*, 16(1):93, 1976.

[108] CE Swenberg, NE Geacintov, and M Pope. Bimolecular quenching of excitons and fluorescence in the photosynthetic unit. *Biophysical Journal*, 16(12):1447–1452, 1976.

[109] RG Kepler, ZG Soos, and JRG Thorne. Exciton kinetics in poly (di-n-hexylsilane). *Synthetic Metals*, 54(1-3):391–397, 1993.

[110] Ron Kroon, Hilde Fleurent, and Rudolf Sprik. Diffusion-limited exciton fusion reaction in one-dimensional tetramethylammonium manganese trichloride (TMMC). *Physical Review E*, 47(4):2462, 1993.

[111] Paul E Shaw, Arvydas Ruseckas, Jeffrey Peet, Guillermo C Bazan, and Ifor DW Samuel. Exciton–exciton annihilation in mixed-phase polyfluorene films. *Advanced Functional Materials*, 20(1):155–161, 2010.

[112] Francisco Montilla, Arvydas Ruseckas, and Ifor DW Samuel. Exciton–polaron interactions in polyfluorene films with β-phase. *The Journal of Physical Chemistry C*, 122(18):9766–9772, 2018.

[113] Gleb M Akselrod, YR Tischler, Elizabeth R Young, Daniel G Nocera, and Vladimir Bulovic. Exciton-exciton annihilation in organic polariton microcavities. *Physical Review B*, 82(11):113106, 2010.

[114] V Sundström, T Gillbro, RA Gadonas, and A Piskarskas. Annihilation of singlet excitons in J aggregates of pseudoisocyanine (PIC) studied by pico-and subpicosecond spectroscopy. *The Journal of Chemical Physics*, 89(5):2754–2762, 1988.

[115] Yasunari Tamai, Hideo Ohkita, Hiroaki Benten, and Shinzaburo Ito. Triplet exciton dynamics in fluorene- amine copolymer films. *Chemistry of Materials*, 26(8):2733–2742, 2014.

[116] A Horvath, G Weiser, C Lapersonne-Meyer, M Schott, and S Spagnoli. Wannier excitons and franz-keldysh effect of polydiacetylene chains diluted in their single crystal monomer matrix. *Physical Review B*, 53(20):13507, 1996.

[117] SD Babenko, VA Benderskii, VI Goldanskii, AG Lavrushko, and VP Tychinskii. Singlet exciton annihilation in anthracene crystals. *Physica Status Solidi (b)*, 45(1):91–97, 1971.

[118] B Schweitzer and H Bässler. Excitons in conjugated polymers. *Synthetic Metals*, 109(1-3):1–6, 2000.

[119] Pabitra K Nayak. Exciton binding energy in small organic conjugated molecule. *Synthetic Metals*, 174:42–45, 2013.

[120] Martin Pope and José Burgos. Autoionization and exciton annihilation in anthracene. *Molecular Crystals and Liquid Crystals*, 3(2):215–226, 1967.

[121] Graham R Fleming, David P Millar, Graeme C Morris, John M Morris, and GW Robinson. Exciton fission and annihilation in crystalline tetracene. *Australian Journal of Chemistry*, 30(11):2353–2359, 1977.

[122] Murad JY Tayebjee, Raphaël GCR Clady, and Timothy W Schmidt. The exciton dynamics in tetracene thin films. *Physical Chemistry Chemical Physics*, 15(35):14797–14805, 2013.

[123] Hai Wang, Hai-Yu Wang, Bing-Rong Gao, Lei Wang, Zhi-Yong Yang, Xiao-Bo Du, Qi-Dai Chen, Jun-Feng Song, and Hong-Bo Sun. Exciton diffusion and charge transfer dynamics in nano phase-separated P3HT/PCBM blend films. *Nanoscale*, 3(5):2280–2285, 2011.

[124] Serdar Oezcelik and Daniel L Akins. Nature of exciton- exciton annihilation in an aggregated cyanine dye. *The Journal of Physical Chemistry B*, 101(16):3021–3024, 1997.

[125] I Sokolik, Richard Priestley, Ardie D Walser, Roger Dorsinville, and Ching Wan Tang. Bimolecular reactions of singlet excitons in tris (8-hydroxyquinoline) aluminum. *Applied Physics Letters*, 69(27):4168–4170, 1996.

[126] IG Hill, A Kahn, ZG Soos, and RA Pascal Jr. Charge-separation energy in films of π-conjugated organic molecules. *Chemical Physics Letters*, 327(3-4):181–188, 2000.

[127] J Mezyk, D Di Nuzzo, A Mech, R Tubino, and F Meinardi. Exciton-exciton annihilation in organic lanthanide complexes. *The Journal of Chemical Physics*, 132(2):024504, 2010.

[128] SL Dexheimer, WA Vareka, D Mittleman, A Zettl, and CV Shank. Nonexponential relaxation in solid c60 via time-dependent singlet exciton annihilation. *Chemical Physics Letters*, 235(5-6):552–557, 1995.

[129] BI Greene and RR Millard. Singlet-exciton fusion in molecular solids: A direct subpicosecond determination of time-dependent annihilation rates. *Physical Review Letters*, 55(12):1331, 1985.

[130] Donald V Brumbaugh, Annabel A Muenter, Wayne Knox, Gerard Mourou, and Bruce Wittmershaus. Singlet exciton annihilation in the picosecond fluorescence decay of 1, 1'-diethyl-2, 2'-cyanine chloride dye j-aggregate. *Journal of Luminescence*, 31:783–785, 1984.

[131] Johannes Moll, William J Harrison, Donald V Brumbaugh, and Annabel A Muenter. Exciton annihilation in J-aggregates probed by femtosecond fluorescence upconversion. *The Journal of Physical Chemistry A*, 104(39):8847–8854, 2000.

[132] Mirjam van Burgel, Douwe A Wiersma, and Koos Duppen. The dynamics of one-dimensional excitons in liquids. *The Journal of Chemical Physics*, 102(1):20–33, 1995.

[133] V Ern, H Bouchriha, M Bisceglia, S Arnold, and M Schott. Total and radiative triplet-triplet exciton-annihilation rate constant in pyrene crystals. *Physical Review B*, 8(12):6038, 1973.

[134] Nicholas E Geacintov, Jacques Breton, Charles E Swenberg, and Guy Paillotin. A single pulse picosecond laser study of exciton dynamics in chloroplasts, 1977.

[135] AN Faidysh and AS Gaevsky. Influence of triplet exciton annihilation on quantum efficiency and phosphorescence decay law in benzophenone crystals. *Molecular Crystals and Liquid Crystals*, 19(1):13–24, 1972.

[136] AA Avdeenko, TL Dobrovolskaya, VA Kultchitskii, and Yu V Naboikin. Mutual annihilation of triplet excitons in 4, 4'-dichlorobenzophenone single crystals at low temperatures. *Physica Status Solidi (b)*, 99(1):409–415, 1980.

[137] Guglielmo Lanzani, Mauro Nisoli, Sandro De Silvestri, and F Abbate. Exciton dynamics in α-sexithienyl films. *Chemical Physics Letters*, 264(6):667–672, 1997.

[138] Yasunari Tamai, Yuu Matsuura, Hideo Ohkita, Hiroaki Benten, and Shinzaburo Ito. One-dimensional singlet exciton diffusion in poly (3-hexylthiophene) crystalline domains. *The Journal of Physical Chemistry Letters*, 5(2):399–403, 2014.

[139] Alexander T Paradzah, Kelebogile D Maabong, Huzifa MAM Elnour, Asmita Singh, Mmantsae Diale, and Tjaart PJ Kruger. Identification of exciton–exciton annihilation in hematite thin films. *The Journal of Physical Chemistry C*, 123(30):18676–18684, 2019.

[140] Marc A Baldo and Stephen R Forrest. Transient analysis of organic electrophosphorescence: I. transient analysis of triplet energy transfer. *Physical Review B*, 62(16):10958, 2000.

[141] Marc A Baldo, Chihaya Adachi, and Stephen R Forrest. Transient analysis of organic electrophosphorescence. ii. transient analysis of triplet-triplet annihilation. *Physical Review B*, 62(16):10967, 2000.

[142] SR Flom, FJ Bartoli, HW Sarkas, CD Merritt, and ZH Kafafi. Resonant nonlinear optical properties and excited-state dynamics of pristine, oxygen-doped, and photopolymerized c60 in the solid state. *Physical Review B*, 51(17):11376, 1995.

[143] A Pivrikas, G Juška, R Österbacka, M Westerling, M Viliūnas, K Arlauskas, and H Stubb. Langevin recombination and space-charge-perturbed current transients in regiorandom poly (3-hexylthiophene). *Physical Review B*, 71(12):125205, 2005.

[144] Gerald Dicker, Matthijs P de Haas, and Laurens DA Siebbeles. Signature of exciton annihilation in the photoconductance of regioregular poly (3-hexylthiophene). *Physical Review B*, 71(15):155204, 2005.

[145] A Haugeneder, M Neges, C Kallinger, W Spirkl, U Lemmer, J Feldmann, M-C Amann, and Ullrich Scherf. Nonlinear emission and recombination in conjugated polymer waveguides. *Journal of Applied Physics*, 85(2):1124–1130, 1999.

[146] Yuri Zaushitsyn, Kim G Jespersen, Leonas Valkunas, Villy Sundström, and Arkady Yartsev. Ultrafast dynamics of singlet-singlet and singlet-triplet exciton annihilation in poly (3-2'-methoxy-5' octylphenyl) thiophene films. *Physical Review B*, 75(19):195201, 2007.

[147] S Lattante, M De Giorgi, G Barbarella, L Favaretto, G Gigli, R Cingolani, and M Anni. Interplay between stimulated emission and singlet-singlet annihilation in oligothiophene dioxide thin films. *Journal of Applied Physics*, 100(2):023530, 2006.

[148] Andrew J Ferguson, Nikos Kopidakis, Sean E Shaheen, and Garry Rumbles. Quenching of excitons by holes in poly (3-hexylthiophene) films. *The Journal of Physical Chemistry C*, 112(26):9865–9871, 2008.

[149] V Gulbinas, I Minevičiūtė, D Hertel, R Wellander, Arkady Yartsev, and Villy Sundström. Exciton diffusion and relaxation in methyl-substituted polyparaphenylene polymer films. *The Journal of chemical physics*, 127(14):144907, 2007.

[150] VS Williams, S Mazumdar, NR Armstrong, ZZ Ho, and N Peyghambarian. Femtosecond excited-state dynamics in fluoro-and chloroaluminum phthalocyanine thin films. *The Journal of Physical Chemistry*, 96(11):4500–4505, 1992.

[151] Sean T Roberts, R Eric McAnally, Joseph N Mastron, David H Webber, Matthew T Whited, Richard L Brutchey, Mark E Thompson, and Stephen E Bradforth. Efficient singlet fission discovered in a disordered acene film. *Journal of the American Chemical Society*, 134(14):6388–6400, 2012.

[152] Thomas Bittner, Klaus-Dieter Irrgang, Gernot Renger, and Michael R Wasielewski. Ultrafast excitation energy transfer and exciton-exciton annihilation processes in isolated light harvesting complexes of photosystem ii (lhc ii) from spinach. *The Journal of Physical Chemistry*, 98(46):11821–11826, 1994.

[153] Ian A Howard, Justin M Hodgkiss, Xinping Zhang, Kiril R Kirov, Hugo A Bronstein, Charlotte K Williams, Richard H Friend, Sebastian Westenhoff, and Neil C Greenham. Charge recombination and exciton annihilation reactions in conjugated polymer blends. *Journal of the American Chemical Society*, 132(1):328–335, 2010.

[154] W Holzer, Alfons Penzkofer, R Stockmann, H Meysel, H Liebegott, and HH Hörhold. Energy density dependent fluorescence quenching of diphenyl substituted phenylene-vinylene and diphenylene-vinylene polymers by exciton–exciton annihilation. *Synthetic Metals*, 125(3):343–357, 2001.

[155] AG Doukas, V Stefancic, J Buchert, R Alfano, and BA Zilinskas. Exciton annihilation in the isolated phycobiliproteins from the blue-green alga nostoc sp. using picosecond absorption spectroscopy. *Photochemistry and Photobiology*, 34(4):505–510, 1981.

[156] RG Kepler and JM Zeigler. Mutual annihilation of singlet excitons in [sgrave]-conjugated polysilanes. *Molecular Crystals and Liquid Crystals*, 175(1):85–91, 1989.

[157] Toshiya Yonehara, Kenichi Goushi, Tomoaki Sawabe, Isao Takasu, and Chihaya Adachi. Comparison of transient state and steady state exciton–exciton annihilation rates based on förster-type energy transfer. *Japanese Journal of Applied Physics*, 54(7):071601, 2015.

[158] Akihiro Namekawa and Ryuzi Katoh. Exciton annihilation in dye-sensitized nanocrystalline semiconductor films. *Chemical Physics Letters*, 659:154–158, 2016.

[159] Ebinazar B Namdas, Arvydas Ruseckas, Ifor DW Samuel, Shih-Chun Lo, and Paul L Burn. Triplet exciton diffusion in fac-tris (2-phenylpyridine) iridium (III)-cored electroluminescent dendrimers. *Applied Physics Letters*, 86(9):091104, 2005.

[160] W Staroske, M Pfeiffer, K Leo, and M Hoffmann. Single-step triplet-triplet annihilation: An intrinsic limit for the high brightness efficiency of phosphorescent organic light emitting diodes. *Physical Review Letters*, 98(19):197402, 2007.

[161] A Ruseckas, JC Ribierre, PE Shaw, SV Staton, PL Burn, and IDW Samuel. Singlet energy transfer and singlet-singlet annihilation in light-emitting blends of organic semiconductors. *Applied Physics Letters*, 95(18):286, 2009.

[162] Tong Zhu, Yan Wan, Zhi Guo, Justin Johnson, and Libai Huang. Two birds with one stone: tailoring singlet fission for both triplet yield and exciton diffusion length. *Advanced Materials*, 28(34):7539–7547, 2016.

[163] TM Nordlund and WH Knox. Lifetime of fluorescence from light-harvesting chlorophyll a/b proteins. excitation intensity dependence. *Biophysical Journal*, 36(1):193–201, 1981.

[164] Monirul Hasan, Atul Shukla, Viqar Ahmad, Jan Sobus, Fatima Bencheikh, Sarah KM McGregor, Masashi Mamada, Chihaya Adachi, Shih-Chun Lo, and Ebinazar B Namdas. Exciton–exciton annihilation in thermally activated delayed fluorescence emitter. *Advanced Functional Materials*, 30(30):2000580, 2020.

[165] M Lebental, H Choukri, S Chenais, S Forget, A Siove, B Geffroy, and E Tutiš. Diffusion of triplet excitons in an operational organic light-emitting diode. *Physical Review B*, 79(16):165318, 2009.

[166] Hiroshi Kanno, Yiru Sun, and Stephen R Forrest. White organic light-emitting device based on a compound fluorescent-phosphor-sensitized-fluorescent emission layer. *Applied Physics Letters*, 89(14):143516, 2006.

[167] JC Ribierre, A Ruseckas, OPM Gaudin, IDW Samuel, H Barcena, SV Staton, and PL Burn. Effects of thermal annealing on the photophysical properties of bisfluorene-cored dendrimer films. *Organic Electronics*, 10(5):803–808, 2009.

[168] JP Aimé, V Ern, JL Fave, and M Schott. Triplet excitions in crystalline trans-stilbene i. spectroscopy of the $s_0 \rightarrow t_1$ transition. *Molecular Crystals and Liquid Crystals*, 46(3-4):169–180, 1978.

Chapter 4

Exciton Transport in Two Dimensional Semiconductors

4.1 Introduction

Monolayer transition metal dichalcogenides (TMDCs) are promising materials for next generation optoelectronic devices. Exciton diffusion is the primary channel of energy transport in excitonic semiconductors. The exciton diffusion length is a critical design parameter that reflects the quality of exciton transport in monolayer TMDCs and limits the performance of many excitonic devices. Although diffusion lengths of a few hundred nanometers have been reported in the literature for as-exfoliated monolayers, these measurements are convoluted by neutral and charged excitons (trions) that coexist at room temperature due to natural background doping. Untangling the diffusion of neutral excitons and trions is paramount to understand the fundamental limits and potential of new optoelectronic device architectures made possible using TMDCs. So at first we measure the diffusion lengths of neutral excitons and trions in monolayer MoS_2 by tuning the background carrier concentration using a gate voltage and utilizing both steady state and transient spectroscopy. We observe diffusion lengths of 1.5 μm and 300 nm for neutral excitons and trions, respectively, at an optical power density of 0.6 Wcm^{-2}.

Once we examine the diffusion of pure neutral excitons in MoS_2 and WS_2, we find that surprisingly increasing generation rate shortens the exciton lifetime but increases the diffusion length in unstrained monolayers of transition metal dichalcogenides (TMDCs). This is in direct contrast to the standard semiconductor paradigm, which predicts a shorter carrier recombination lifetime should lead to a smaller diffusion length. This increase in diffusion length with pump has also been observed in other experiments in the literature, but the exact mechanism has not been understood. Neutral excitons recombine completely radiatively at low generation rates. Nonradiative exciton-exciton annihilation (EEA) reduces the photoluminescence quantum yield (PL QY) at high generation rates. Since the enhanced diffusion occurs at high generation rates, EEA might play a role. Strain has been shown to

suppress EEA in monolayer TMDCs, resulting in near-unity PL QY at all exciton densities. When we suppressed EEA by strain, both lifetime and diffusion length became independent of generation rate. EEA therefore enhances diffusion length but decreases exciton lifetime. During EEA one exciton nonradiatively recombines and kinetically energizes another exciton, which then diffuses fast. Our kinetic model predicts diffusion coefficient and PL QY are inversely related, which we observe in our experiments. These results elucidate how strain controls exciton transport and many-body interactions in TMDC monolayers.

4.2 Neutral Exciton Diffusion in Monolayer MoS_2

[1]Due to strong Coulomb interaction, photogenerated carriers in TMDC monolayers form excitons with binding energy over an order of magnitude larger than in conventional semiconductors [1, 2]. These excitons can turn into positive or negative trions in the presence of background holes or electrons, respectively [3]. Energy transport in monolayer semiconductors occurs mainly by the diffusion of these tightly bound quasiparticles. Therefore, the operation of a wide array of optoelectronic devices such as light-emitting diodes [4, 5], solar cells [6] and excitonic switches [7] that utilize monolayer semiconductors is governed by exciton and trion diffusion. Understanding and manipulating the exciton diffusion in these monolayers can improve device performance and lead to the development of next-generation room-temperature excitonic technologies.

While diffusion in monolayer semiconductors has been studied extensively [8–17], the effect of background carriers has been largely overlooked. Since almost all as-exfoliated monolayer semiconductors have some amount of unintentional doping [18], a mixture of excitons and trions are created after photoexcitation and previous approaches have produced an averaged diffusion length of both excitons and trions. In this work, we electrostatically tune the background carrier concentration of monolayer molybdenum disulfide (MoS_2), a prototypical monolayer semiconductor, to retrieve the separated exciton and trion diffusion length. Our findings demonstrate that excitons and trions in monolayer MoS_2 have very different diffusion lengths (1.5 μm and 300 nm at a power density of 0.6 Wcm^{-2}, respectively). This finding has wide implications for the design of excitonic devices utilizing monolayer semiconductors.

We tune the background carrier concentration (electron and hole population densities) of the monolayer MoS_2 by varying the back-gate voltage (V_g) in a capacitor structure (Fig. 4.1A). The schematic of the device is shown in Fig. 4.1A, and an optical micrograph of a device is shown in the inset of Fig. 4.1A. We also tune the photocarrier generation rate by varying the incident pump power. MoS_2 monolayers are mechanically exfoliated on top of poly(methyl methacrylate) (PMMA, 100 nm), which is spin-coated on SiO_2 (50 nm)/Si substrate. The Au contacts (thickness 30 nm) are then transferred on the monolayer using a

[1]The following section was published in a similar form in ACS Nano. (S. Z. Uddin*, H. Kim*, M. Lorenzon, M. Yeh, D.-H. Lien, E. S. Barnard, H. Htoon, A. Weber-Bargioni, A. Javey, "Neutral Exciton Diffusion in Monolayer MoS_2", *ACS Nano*, 14, 13433–13440, 2020.)

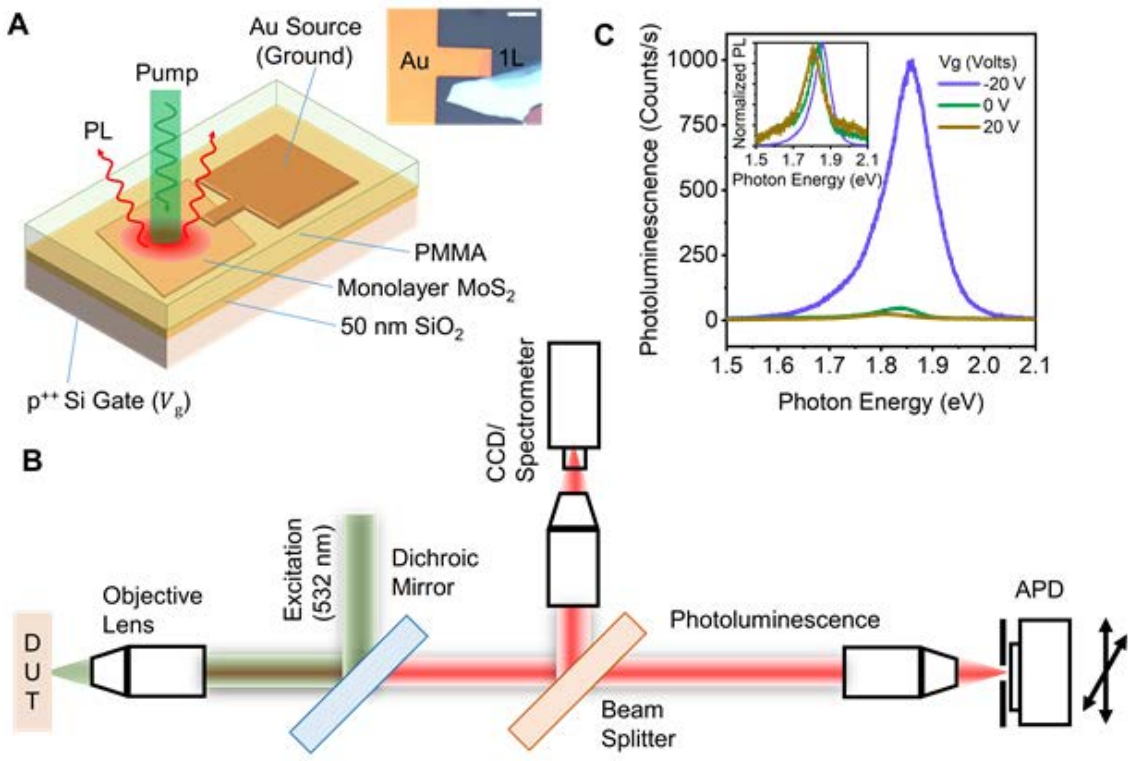

Figure 4.1: **Neutral exciton transport in monolayer MoS_2.** (A) Schematic of the device, inset shows optical micrograph of the device (Scale bar 10 μm). (B) Schematic of the exciton diffusion imaging setup. Photoluminescence excited by either pulsed or continuous wave excitation can be sent to a camera for imaging, a spectrometer for PL spectra or an APD for time-resolved single photon counting. The time resolved APD can be scanned across the emission spot to obtain a map of emission intensity as a function of position and time. (C) PL spectra of the MoS_2 monolayer device under gate voltages $V_g = -20$ V, 0 V and 20 V at the pump density of 10^2 Wcm^{-2}.

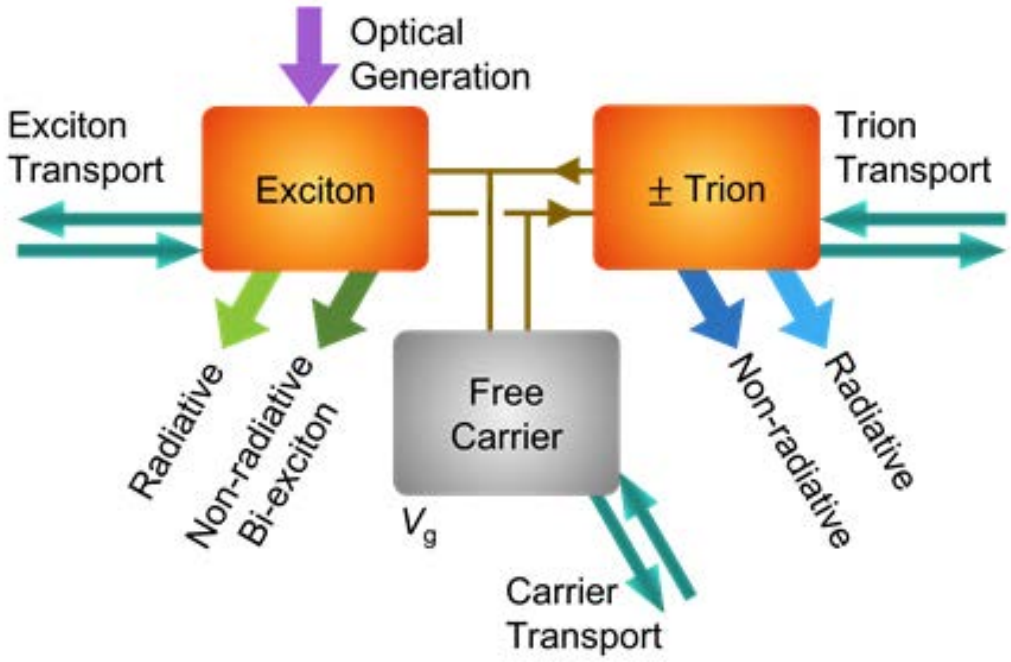

Figure 4.2: **Local balance of various quasiparticles in monolayer MoS_2.** In a differential area, exciton concentration increases by 1. generation upon absorption of a photon, 2. exciton transport into the area resulting from concentration or potential gradients, and 3. ionization of trions. Exciton concentration decreases by 1. trion formation, 2. radiative recombination and 3. exciton-exciton annihilation. Similar generation and recombination processes occur for trions. The ratio of excitons and trions are controlled by the background carrier concentration, which also can drift and diffuse.

dry transfer technique [18]. Exciton recombination in monolayer MoS_2 was probed spatially, spectrally and temporally in an inverted fluorescence microscope (Fig. 4.1B). Photoluminescence (PL) was excited at $\lambda = 532$ nm wavelength by either a continuous wave (CW) laser or a 100 fs pulsed laser focused to a near-diffraction-limited spot with a full width at half maximum (FWHM) of $w_0 = 287$ nm. When excited by the CW laser, the resulting PL is either imaged or sent to a spectrometer. When excited by the pulsed laser, the PL is sent to a time-resolved single photon counting detector, which is then scanned across the image to obtain a map of the time-dependent exciton density as a function of position. All measurements reported in this paper are taken at room temperature, in an ambient lab environment.

We first discuss the results of CW excitation. The PL spectra (Fig. 4.1C) of a MoS_2 monolayer measured at $V_g = -20$ V and 0 V show a $\sim$ 20-fold difference in the PL peak intensity at a pump power of 10^2 Wcm^{-2}, with a peak energy shift of 30 meV. This difference

in PL intensity and spectra has been attributed to the different photo-emitting quasiparticles in the monolayer[3] (Fig. 4.2). The time-dependent concentrations of excitons, trions and background carriers in a monolayer semiconductor are locally determined by three dynamic processes: generation, recombination and transport (Fig. 4.2). At a specific location, exciton concentration increases if they are generated from a photon-absorption event or a trion-ionization at that location, or if excitons diffuse in from surrounding points. Concurrently, exciton concentration decreases through trion formation, radiative recombination and biexciton annihilation. Similar generation, recombination and transport processes also occur for trions. The ratio of exciton and trion concentration is determined by the local background carrier concentration, which can be controlled by the gate voltage.18 As-exfoliated monolayer MoS_2 is electron-rich due to substrate-induced doping and intrinsic chalcogenide vacancies[19]. At $V_g = -20$ V, the background electrons are removed from the monolayer MoS_2 and it is close to intrinsic (Fermi level is at mid-bandgap). In this case, emission is observed primarily from neutral excitons which show high PL intensity. Positive V_g moves the Fermi level closer to the conduction band, introducing a large number of background electrons that turn photogenerated excitons into trions. These negative trions show low PL intensity. As both neutral excitons and negative trions coexist at $V_g = 0$ V, previously reported diffusion lengths of as-exfoliated MoS_2 monolayers are a result of combined diffusion from both excitons and trions and do not reflect the true neutral exciton diffusion length in MoS_2.

PL images of a MoS_2 monolayer excited by a diffraction-limited CW laser at different V_g and different pump powers are shown in Fig. 4.3. In the figure, images in the same row are captured at the same pump power, while images in the same column are captured at the same V_g. For the lowest pump power, we note that PL at $V_g = -20$ V is bright, while at $V_g = 20$ V it is below the noise floor, indicating neutral excitons are much brighter than the negative trions. For neutral excitons, ($V_g = -20$ V column) slight power dependence is observed in the measured diffusion map. Also, for all powers, neutral excitons diffuse much further than the negative trions. This is related to the difference in their effective lifetime. As neutral excitons have longer effective lifetime ($\sim$ 10 ns) compared to trions ($\sim$ 50 ps) [18], they also diffuse to a larger distance compared to trions.

Photoluminescence quantum yield (PL QY) is defined as the ratio of the number of photons the material radiates to the number of absorbed photons. We first present the PL QY of monolayer MoS_2 in Fig. 4.4A as a function of pump power and V_g. The details of calibrated PL QY measurement and quantitative recombination kinetics at different V_g and pump have been discussed elsewhere [18]. At $V_g = -20$ V all photogenerated carriers create neutral excitons, as there are no excess background carriers. We note that the PL QY vs. pump profile at $V_g = -20$ V has two distinct regions, indicated by different background colors in Fig. 4.4A. At low pump the PL QY does not change with pump. PL QY reaches near unity in this linear regime. At high pump the PL QY decreases with pump power. This nonlinear droop has been attributed to the bi-exciton annihilation process at high exciton densities [20]. At $V_g = 20$ V a large concentration of excess electrons accumulates in the monolayer, and almost all photogenerated carriers turn into negative trions (Fig. 4.4B). Trions can

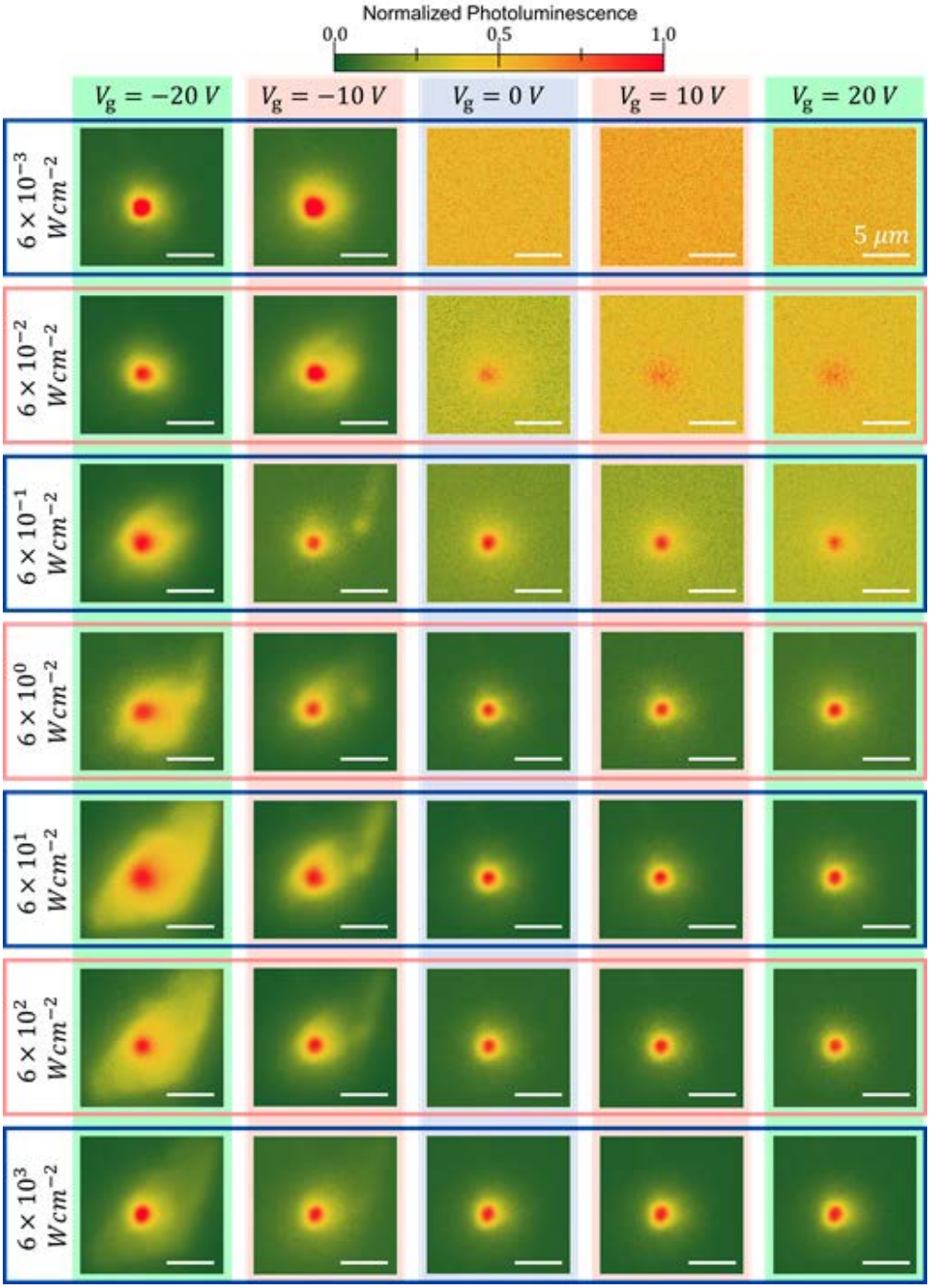

Figure 4.3: **PL images at various pump powers and gate voltages.** PL excited by a CW laser focused on a diffraction-limited spot for various pump powers and gate voltages. Images in the same row have the same pump power, and in the same column have the same gate voltage. Scale bar is 5 μm. Radial anisotropy arises from the finite size of the monolayer.

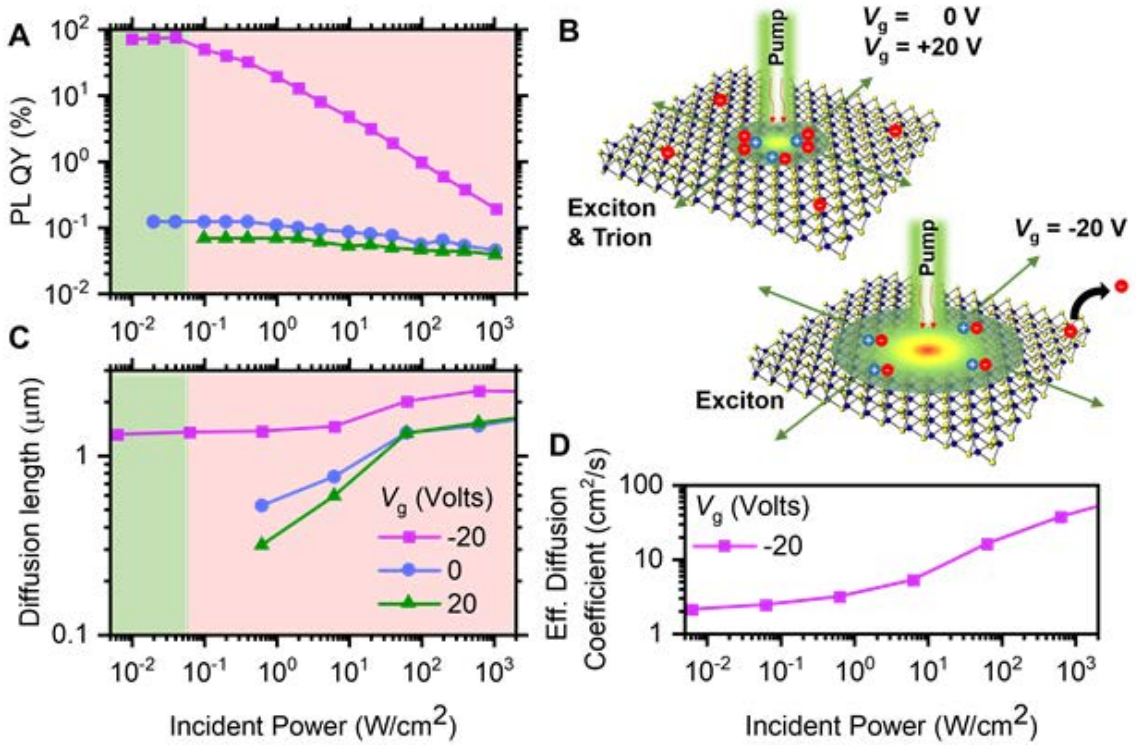

Figure 4.4: **Diffusion of neutral excitons.** (A) Pump-power dependence of the PL QY for electrostatically-doped MoS_2. (B) Exciton and trion diffusion in MoS_2. (C) Diffusion length of a MoS_2 device under $V_g = 0$ V, $V_g = -20$ V and $V_g = 20$ V. (D) Effective diffusion coefficient for neutral excitons in MoS_2 at different pump power.

non-radiatively recombine by transferring their excess energy into secondary electrons in an Auger-like process [21], so the PL QY is low.

We now present the diffusion length of monolayer MoS_2 in Fig. 4.4C as a function of pump power and V_g. Throughout the manuscript, we define the squared width of the diffusion pattern as

$$w^2(t) = \frac{\int |\mathbf{r}|^2 I(\mathbf{r}, r) d^2\mathbf{r}}{\int I(\mathbf{r}, r) d^2\mathbf{r}} \tag{4.1}$$

where $I(\mathbf{r}, t)$ is PL intensity, $\mathbf{r}$ is the radial coordinate, t is time and the integrations are limited to the area of the monolayer. The steady state diffusion length (L_D) is then defined as the mean-square radius of the diffusion map deconvoluted by the laser spot size. At low pump we observe diffusion lengths of 1.5 μm and 300 nm at $V_g = -20$ V and 20 V, respectively. At $V_g = -20$ V, the diffusion length shows a slight increase over six orders of magnitude of pump power, while at $V_g = 20$ V the diffusion length is low at moderate pumps and increases by $\sim$ 5X at high pump. The reason for increase of diffusion length with

pump has been discussed in detail in the next section in this chapter. Note that we could not measure the diffusion length of trions at very low pumps due to low PL signal intensity.

To extract the diffusion coefficient of neutral excitons, we extend the kinetic model of exciton recombination to incorporate diffusion. Considering only neutral excitons (at $V_g = -20$ V), we can write the time-dependent continuity equation as:

$$\frac{\partial n_X(\mathbf{r},t)}{\partial t} = \nabla \cdot [D_X(n_X,t)\nabla n_X] + G(\mathbf{r},t) - \frac{n_X}{\tau_X} - C_{EEA} n_X^2 \tag{4.2}$$

where n_X and τ_X are the neutral exciton population density and lifetime, respectively, and C_{EEA} is the exciton-exciton annihilation coefficient. Both the exciton lifetime ($\tau_X \sim 10$ ns) and exciton-exciton annihilation coefficient ($C_{EEA} \sim 3.5$ cm^{2}s^{-1}) have been experimentally measured previously and are known [22]. At steady state, $\frac{\partial n_X}{\partial t} = 0$. We consider a Gaussian generation rate given by

$$G(\mathbf{r}) = G_0 \exp\left(\frac{-2|\mathbf{r}|^2}{w_0^2}\right) \tag{4.3}$$

where the peak G_0 is determined by pump intensity. The only unknown parameter in the continuity equation is D_X. We extract an effective diffusion coefficient D_X at different pump intensity that gives the experimentally measured diffusion length shown in Fig. 4.4C. This extraction process is done by assuming a constant diffusion coefficient and numerically solving the continuity equation for exciton concentration n_X. The extracted effective diffusion coefficient at different powers is shown in Fig. 4.4D. We note that the effective diffusion coefficient increases with pump power. This increase in effective diffusion coefficient has been observed in other excitonic systems such as 2D heterostructures and as-exfoliated WS_2 monolayers and is attributed to correlation driven diffusion [23]. At the lowest pump density where neutral excitons recombine completely radiatively, a diffusion length of 1.5 μm and a diffusion coefficient of 2.1 cm^{2}s^{-1} has been observed for neutral excitons.

Unlike the case of neutral excitons, extracting the trion diffusion coefficient is more complex due to its charged nature. Diffusion of trions would perturb the local charge neutrality, and the free carriers will respond to the resultant lateral electric field. Furthermore, the observed PL is a result of radiative recombination of both excitons and trions. Thus, we calculate an effective diffusion coefficient (L_D^2/τ_T^-) at $V_g = 20$ V using the known trion effective lifetime of $\tau_T^- = 50$ ps. At a pump power density of 0.6 Wcm^{-2}, we observe a trion diffusion length of 300 nm (Fig. 4.4C), which corresponds to an effective diffusion coefficient of 18 cm^{2}s^{-1}. This large diffusion coefficient could be a result of strong Coulomb interaction between charged trions. We also note that, at very high pump, the diffusion length at any V_g will converge to the neutral exciton diffusion length. This is because the number of trions cannot be larger than the number of background carriers, and thus once the trion population saturates, recombination and diffusion must be dominated by excitons. This explains the increase of diffusion length with pump at $V_g = 20$ V and 0 V.

Now we discuss the results of pulsed excitation. Figure 4.5A, B, and C show the spatial and temporal evolution of the emission intensity distribution $I(\mathbf{r},t)$ after pulsed excitation

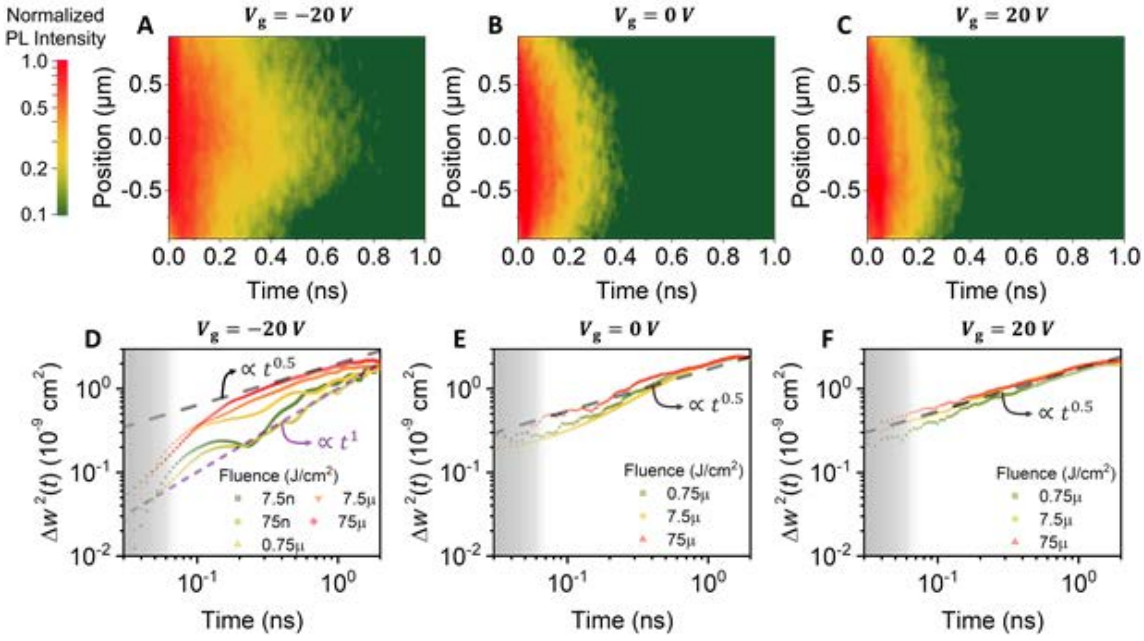

Figure 4.5: **Temporal and spatial imaging of exciton transport in MoS_2** (A, B, C) Map of emission intensity as it evolves in space and time at $V_g = -20$ V, 0 V, and 20 V, respectively at a pump fluence of 75 μJcm^{-2}. (D, E, F) Time evolution of differential squared width for various pump fluence at $V_g = -20$ V, 0 V and 20 V, respectively. The instrument response function (IRF) has a FWHM of ~ 50 ps, which is shown as a shaded region.

at $t = 0$ at $V_g = -20$ V, 0 V, and 20 V, respectively at a pump fluence of 75 μJcm^{-2}. We can see the neutral excitons spread further in time due to their considerably longer lifetime. The neutral exciton distribution variance can be obtained directly from the measured intensity distribution variance $\Delta w^2(t) = w^2(t) - w^2(0)$, which is shown in Fig. 4.5D, E and F for different optical pump fluences at $V_g = -20$ V, 0 V and 20 V, respectively. $\Delta w^2(t)$ does not depend on the width of the initial distribution created by the laser pulse. In general, the variance can be written as

$$\Delta w^2(t) = At^{\alpha} \tag{4.4}$$

The exponent α characterizes the type of diffusion and A is the empirically observed proportionality factor which has fractional time units. For $\alpha = 1$, we get linear diffusion. In the case of $\alpha > 1$ and $\alpha < 1$ the transport is called superdiffusive and subdiffusive, respectively, which results from the concentration dependence of the effective diffusion coefficient [24, 25]. We note that in monolayer MoS_2 the nature of diffusion changes from linearly diffusive at low pump to subdiffusive at high pump (Fig. 4.5D). This could be because of exciton-exciton interaction at high pump densities. At low fluence excitons recombine completely radiatively and diffuse linearly with $\alpha = 1$. For linear diffusion, the halved slope of $\Delta w^2(t)$ gives the

diffusion coefficient. An effective diffusion coefficient of ~ 1.2 cm^{2}s^{-1} has been found at low fluence, which matches well with the steady state measurements. At high fluence, biexciton recombination dominates the recombination kinetics and subdiffusive ($\alpha < 1$) behavior is observed, indicative of a reaction-diffusion process. This could also be related to the relaxation of nonresonantly excited hot exciton gas by losing its excess kinetic energy [26] and further careful study is required to shed light on these mechanisms. At $V_g = 0$ V and 20 V, subdiffusive behavior ($\alpha < 1$) is observed (Fig. 4.5E, F). As previously discussed, this is a result of diffusion of both excitons and trions at high fluence [27]. The PL signal of trions is too low to measure diffusion at low pump.

Exciton diffusion length is not only of essential importance for understanding the energy transport physics in excitonic semiconductors, but also an imperative design consideration for optoelectronic applications [28–32]. The physical process of exciton-exciton annihilation involves the diffusion of excitons and the rate of exciton-exciton annihilation increases with diffusivity. In light emitting devices, the emission region must be located at least a diffusion length away from the injection region to avoid quenching. On the contrary, in energy harvesting devices the contacts must be closer to the absorption region to collect excitons. Materials with different diffusion coefficients can therefore be suitable for different applications. Some examples of different classes of excitonic materials with their diffusion lengths are shown in Table 4.1. Generally, quasi-0D systems such as molecular films and quantum dot films have very low diffusion lengths (1 nm – 50 nm) at room temperature, as the diffusion mainly occurs by site hopping [33]. One dimensional excitonic semiconductors, such as semiconducting single wall carbon nanotube (SWCNT) have larger (~ 300 nm) diffusion lengths [34–36], depending on the chirality and dielectric environment. A two-dimensional excitonic semiconductor, such as the monolayer MoS_2 discussed here can have an exciton diffusion length of ~ 1500 nm and a trion diffusion length of 300 nm at room temperature. In a three-dimensional bulk semiconductor, strong dielectric screening generally leads to low exciton binding energy, so excitons exist only at cryogenic temperatures. At those low temperatures they show the largest diffusion length ($10 - 1000$ μm), however the required operating temperature limits their practical usability. Therefore, among the classes of excitonic semiconductors discussed here, two dimensional materials such as monolayer MoS_2 achieve the highest diffusion lengths at room temperature and are particularly suitable for applications that require a large diffusion length. Furthermore, excitons in MoS_2 achieve near-unity PL QY at room-temperature, even in the presence of defects. Exciton transport in MoS_2 can also be tuned by electrostatic doping, strain and dielectric environment, further adding to their appeal. These qualities make two-dimensional semiconductors an ideal candidate for future room-temperature excitonic devices.

Dimension	Material	Diffusion Length (μm)	Diffusion Coefficient cm^2s^{-1}
0	Tris(8-hydroxyquinolinato) aluminum, Alq_3 [33, 37]	0.003-0.025	$(3 - 2000) \times 10^{-6}$
0	Spin-coated poly (p-phenylene vinylene) [38]	0.004-0.006	6×10^{-6}
0	CdSe/CdS core/shell QD [39]	0.019-0.024	2×10^{-4}
0	Cesium Lead Bromide perovskite nanocrystal [40]	0.2	0.5
1	Air suspended (9,8) SWCNT [34]	0.29-0.61	44
1	Micelle encapsulated SWCNT [35]	0.08-0.12	2.5-10
1	(6,5) SWCNT [36]	0.095-0.145	10.7
1	GaAs quantum wire (15 K) [41]	4	-
2	AlAs/GaAs QW (200 K) [42]	5	3×10^5
2	AlAs/GaAs QW (200 K) [42]	5	3×10^5
2	As-exfoliated monolayer WSe_2 [9]	0.55-1.8	0.6-1.2
2	As-exfoliated monolayer WS_2 [43]	0.36-0.75	0.41
2	As-exfoliated monolayer $MoSe_2$ [44]	0.4	9-15
2	Monolayer 2D perovskite [45]	0.16	0.06
3	Undoped Si (11 K) [46]	25	100
3	Doped Silicon (11 K) [47]	24	11
3	Germanium (4.2 K) [48]	900	10^3
3	Cu_2O (1.2 K) [49]	70	10^3

Table 4.1: **Exciton diffusion in various materials.** Exciton diffusion length and diffusion coefficient of various materials. All measurements are at room temperature unless specified. (Quantum Well = QW, single-wall carbon nano tube = SWCNT)

4.3 Exction-Exciton Annihilation Enhanced Diffusion in Monolayer WS_2

[2]Near-unity photoluminescence (PL) quantum yield (QY) is observed in monolayers of transition metal dichalcogenides (TMDCs) at low generation rates when neutral exciton recombination is made the dominant pathway by electrostatic or chemical counterdoping [20, 18]. However, neutral excitons nonradiatively recombine through exciton-exciton annihilation (EEA) at high generation rates, which drastically reduces the PL QY [50]. EEA in monolayer TMDCs can be suppressed by favorably altering the band-structure through strain, resulting in near-unity PL QY at all generation rates [51]. Neutral excitons must be the dominant photocarrier in any efficient optoelectronic device, since PL QY fundamentally limits the maximum attainable device efficiency. The primary mechanism of exciton transport is diffusion and the diffusion length is an imperative design consideration for most optoelectronic applications [8, 9, 16, 10, 52]. In this work, we measure the temporal decay and spatial diffusion of pure neutral excitons under various applied strains and generation rates. We find that in an unstrained monolayer WS_2 while the exciton lifetime decreases with exciton density, the diffusion length increases with generation rate. This is highly incongruous to the conventional semiconductors in which carrier diffusion length decreases with carrier lifetime [53]. This anomalous behavior is a result of the underlying excitonic photophysics. During EEA one exciton nonradiatively transfers its energy to another exciton [54, 55] and reduces both PL QY and observed lifetime. However, the energized hot excitons produced by EEA have large center-of-mass kinetic energy that thermalizes while undergoing rapid diffusion. Therefore, the average diffusion length increases with the generation rate when EEA is active. But diffusion is dominated by cold excitons when strain suppresses EEA process, and both exciton lifetime and diffusion length become independent of generation rate. Our EEA enhanced diffusion model considers the population of hot and cold excitons and predicts an inversely proportional relationship between exciton diffusion coefficient and PL QY; which is observed in our experiments. Strain now provides another knob to control exciton diffusion in monolayer semiconductors, along with electrostatic or chemical doping. Increased diffusion with pump has also been observed in other excitonic semiconductors [55, 45], however our results concentrate solely on neutral excitons and establish EEA as the primary reason behind this observed enhancement. These findings uncover EEA enhanced exciton diffusion in monolayer TMDCs, and open up further engineering of neutral exciton transport in monolayer semiconductors through strain.

Figure 4.6A shows a schematic of the device used to explore the diffusion of neutral excitons in monolayer WS_2. We used 1.5 mm thick polyimide substrate as the strain platform for its flexibility and thermal stability, on which 10 nm Titanium, 100 nm gold, and 10 nm titanium films were sequentially deposited. A 50 nm thick Al_2O_3 gate oxide was deposited

[2]The following section was published in a similar form in ACS Nano. (S. Z. Uddin, N, Higashitarumizu, H. Kim, J. Yi, X. Zhang, D. Chrzan, and A. Javey, "Enhanced neutral exciton diffusion in monolayer WS_2 by exciton-exciton annihilation", *ACS Nano*, 2022.)

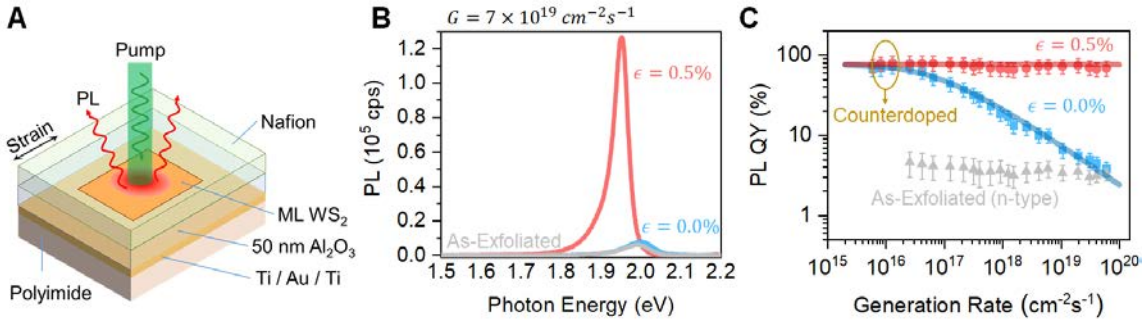

Figure 4.6: **Strain-Induced Changes in Photoluminescence in Monolayer WS_2.** (A) Schematic of the device used to explore the diffusion of excitons in monolayer WS_2. (B) PL spectra of monolayer WS_2: as-exfoliated and chemically counterdoped monolayer WS_2 at $\epsilon = 0\%$,0.5%. (C) PL QY of monolayer WS_2 as a function of generation rate. Points, experimental data; dashed lines, model.

on top of the metal mirror through an atomic layer deposition process. Exfoliated monolayer WS_2 was dry-transferred onto the Al_2O_3 gate oxide. As-exfoliated WS_2 is known to be n-type due to native sulfur vacancies, which generates negative trions resulting in large nonradiative recombination [18]. Measured diffusion of as-exfoliated WS_2 is convoluted by coexisting neutral and charged excitons (trions). It is therefore paramount to untangle the diffusion of neutral excitons and trions to fully understand the underlying photophysics and energy transfer. Electrostatic and chemically counterdoping can compensate for the background electron concentration and suppress the nonradiative recombination. As a hole dopant, Nafion was spin-coated on top of the monolayer to counterdope and move the Fermi level to the middle of the bandgap. Calibrated PL measurements were performed to quantitatively extract the QY as a function of generation rate and strain. Figure 4.6B shows PL spectra of as-exfoliated and counterdoped WS_2 flakes under different uniaxial tensile strains at a generation rate of $G = 7.0 \times 10^{19}$ cm^{-2}s^{-1}. At this high generation rate, PL intensity does not change significantly after Nafion treatment. But when 0.5% uniaxial tensile strain is applied, PL intensity increases by more than an order of magnitude. Figure 4.6C shows PL QY as a function of generation rate (G) for as-exfoliated and counterdoped monolayer with a different strain. Although PL QY droops at the high generation rate for counterdoped unstrained sample, constant PL QY of $\sim 73\%$ on average was observed at all the generation rates for the strained sample owing to suppressed EEA [45, 43].

Time-resolved (TR) PL measurements were performed on the unstrained and strained samples to investigate the effect of strain on the temporal decay of excitons. Figure 4.7(A and B) shows TR PL of counterdoped monolayer WS_2 under different initial exciton concentration at different strains of $\epsilon = 0\%$, 0.5%, respectively. We note that the unstrained sample shows an initial fast decay and then a slow decay tail, which is indicative of a density

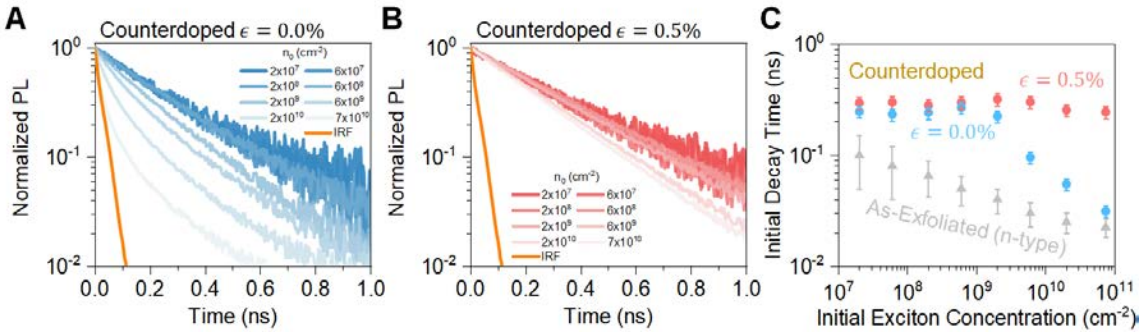

Figure 4.7: **Time-resolved photoluminescence.** (A, B) Radiative decay of chemically counterdoped monolayer WS_2 with tensile strain at different initial exciton concentration at $\epsilon = 0\%$,0.5%, as well as the instrument response function (IRF). (C) Effective PL lifetime as a function of initial exciton concentration: as-exfoliated and counterdoped monolayer at $\epsilon = 0\%$, 0.5%.

dependent recombination channel previously attributed to EEA [43, 56, 57]. Whereas, the strained sample shows a monoexponential decay, indicating only one recombination channel is dominant. The extracted initial decay time or lifetime for as-exfoliated and counterdoped samples are shown in Fig. 4.7C. The trend in lifetime with initial exciton density is consistent with PL QY changes with generation rate. The lifetime of the unstrained sample shows a decrease at high initial concentration from EEA, whereas for 0.5% strained sample it is independent of initial exciton concentrations indicating suppression of EEA. The detailed mechanism of EEA suppression by strain is discussed in Ref. [51].

PL imaging is an effective tool for probing steady-state exciton diffusion in two dimensions. PL images of a WS_2 monolayer excited by a diffraction-limited 514.5 nm continuous-wave laser at different generation rate and strain is measured to explore steady state exciton propagation. Figure 4.8 shows PL images of as-exfoliated and counterdopoed monolayer WS_2 under different generation rates at tensile strain of $\epsilon = 0\%$, 0.5%. Strained monolayer shows a shorter spread compared to unstrained monolayer. To further investigate, we redefine the squared width of the diffusion pattern as

$$w^2(t) = \frac{\int |\mathbf{r}|^2 I(\mathbf{r}, r) d^2\mathbf{r}}{\int I(\mathbf{r}, r) d^2\mathbf{r}} \tag{4.5}$$

where $I(\mathbf{r})$ is the steady-state PL intensity, $\mathbf{r}$ is the radial coordinate, and the integrations are limited to the area of the monolayer. The steady-state effective diffusion length (L_D) is then defined as the mean-square radius of the diffusion map deconvoluted by the laser spot size [57]. We show the measured diffusion length as a function of generation rate and strain in Fig. 4.11A. For as-exfoliated monolayer WS_2, we observe a diffusion length of $\sim$ 200 nm, consistent with previously reported values [8, 57, 58, 15]. In the unstrained

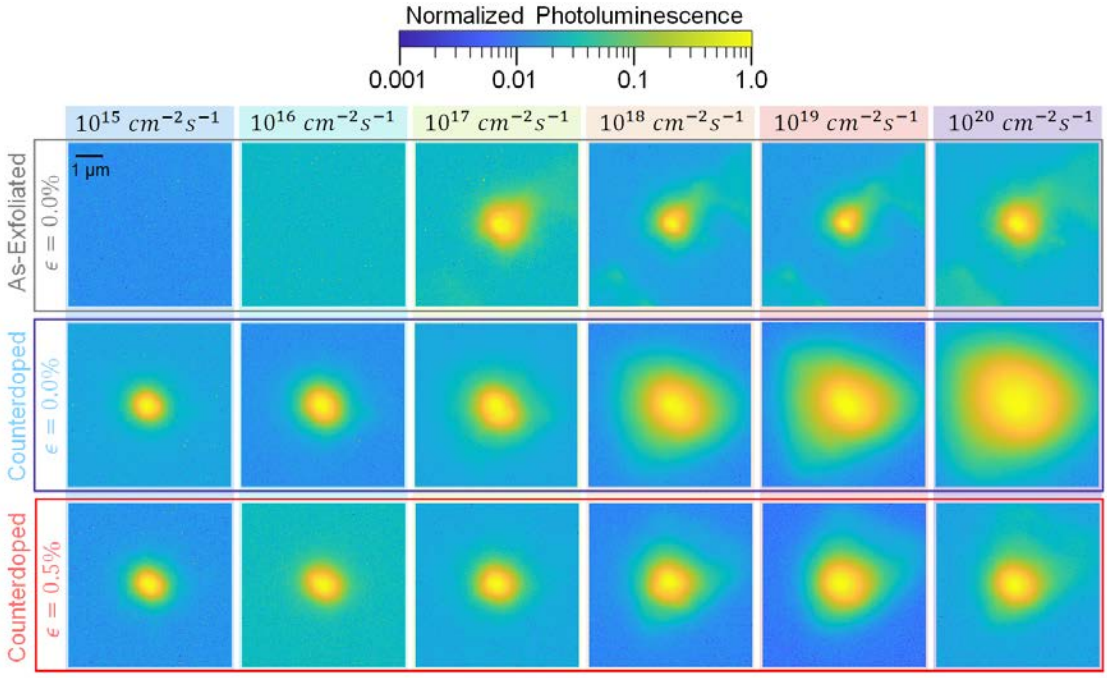

Figure 4.8: **Neutral exciton diffusion.** PL images of as-exfoliated and counterdoped monolayer WS_2 with tensile strain at $\epsilon = 0\%$, 0.5% excited by a CW laser focused on a diffraction limited spot at different generation rates G. Scale bar is 1 μm.

counterdoped WS_2, the diffusion length increases monotonically with generation rate from $G \approx 10^{17}$ cm^{-2}s^{-1}. We emphasize that, although such increase has been observed before [8, 58, 15, 59], our result reflects the diffusion of purely neutral excitons as we have employed chemical counterdoping, whereas previous results represent convoluted diffusion of both neutral and charged excitons (trions) that coexist at room temperature due to natural background doping. The diffusion length of a counterdoped WS_2 monolayer is ~ 2 times higher than that of an unstrained monolayer at low generation rates [60]. Moreover, the diffusion length is independent of generation rate (Fig. 4.11A). Comparing how the generation rate dependence of diffusion length and PL QY changes with strain, we conclude EEA is the primary driving mechanism behind enhanced diffusion in unstrained counterdoped samples. To extract the diffusion coefficient of neutral excitons, we use the time-dependent continuity equation for neutral excitons:

$$\frac{\partial n_X(\mathbf{r},t)}{\partial t} = \nabla \cdot [D_X(n_X,t)\nabla n_X] + G(\mathbf{r},t) - \frac{n_X}{\tau_X} - C_{EEA}n_X^2 \tag{4.6}$$

where n_X and τ_X are the neutral exciton population density and lifetime, respectively. $D(n_x)$ is the concentration and time dependent diffusion coefficient for the excitons that reflects

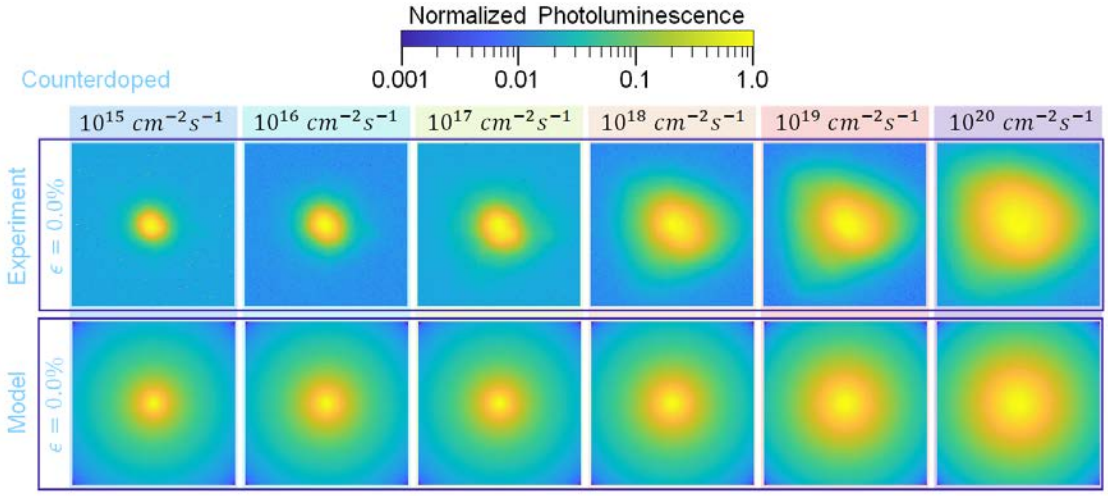

Figure 4.9: **Neutral exciton diffusion.** Comparison of experimental PL images and simulated model for unstrained counterdoped WS_2 monolayer at different generation rates.

both the normal diffusion of excitons as well as the random faster events triggered by EAA. C_{EEA} is the EEA coefficient. Both the single-exciton lifetime and EEA coefficient are known from the PL QY and lifetime measurements in Fig. 4.6 and 4.7. At steady state, $\frac{\partial n_X}{\partial t} = 0$. We assume a Gaussian generation rate given by

$$G(\mathbf{r}) = G_0 \exp\left(\frac{-2|\mathbf{r}|^2}{w_0^2}\right) \tag{4.7}$$

where the peak G_0 is determined by pump intensity and w_0 the pump spot size. To simplify the analysis of each experimental result, we assume that the concentration dependent diffusion coefficient can be replaced by a constant effective diffusion coefficient, D_{eff}. We numerically solve the differential equation for different generation rates and find effective diffusion coefficient, D_{eff} that yields the experimentally measured PL map.

The extracted D_{eff} is shown in Fig. 4.11B. For unstrained monolayer, the effective diffusion coefficient increases with generation rate. However, for strained monolayer D_{eff} is independent of generation rate for six orders of magnitude change in pump intensity. At low generation rates D_{eff} increases with strain, possibly due to effective mass change with strain [60]. The effective diffusion coefficient as a function of corresponding PL QY is shown in Fig. 4.11C. An inversely proportional relationship of diffusion coefficient and PL QY is observed for unstrained monolayer WS_2.

The Boltzmann transport equation (BTE) provides a complete description of diffusing excitons while they are recombining through multiple channels releasing photons and phonons [61]. The momentum and spatial probability distribution of the nonequilibrium exciton gas found by solving BTE has previously been used to explain the interplay between exciton

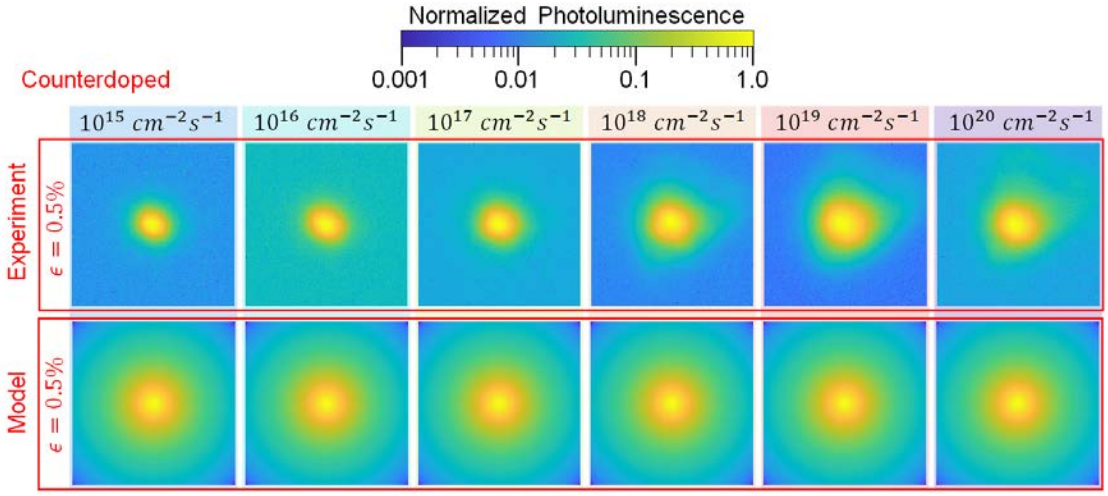

Figure 4.10: **Neutral exciton diffusion.** Comparison of experimental PL images and simulated model for 0.5% strained counterdoped WS_2 monolayer at different generation rates.

propagation and many-particle interactions in monolayer TMDCs [27, 62]. To explain our results, here we distill the whole probability distribution into two baths of excitons: hot and cold, that interact with and transform into each other (Fig. 4.11D). Upon absorption of photons and thermalization cold excitons are created at generation rage G. At low generation rates, all excitons decay radiatively. At high generation rates, excitons could decay nonradiately through exciton-exciton annihilation (EEA). Excitons are generated at rate G. Since the generation and recombination rates must balance, at steady state

$$G = \frac{n_X}{\tau_X} + C_{EEA} n_X^2 \tag{4.8}$$

$$\frac{G}{n_X} = \frac{1}{\tau_X} + C_{EEA} n_X \tag{4.9}$$

where n_X and τ_X are the neutral exciton population density and lifetime, and C_{EEA} is the EEA coefficient, respectively. The exciton lifetime in general can have radiative and nonradiatve components.

$$\frac{1}{\tau_X} = \frac{1}{\tau_{Xr}} + \frac{1}{\tau_{Xnr}}. \tag{4.10}$$

Quantum yield is the ratio of emitted photons to all generated excitons can be written as

$$QY = \frac{n_X/\tau_{Xr}}{n_X/\tau_X + C_{EEA} n_X^2} \tag{4.11}$$

$$\Rightarrow \frac{1}{QY * \tau_{Xr}} = \frac{1}{\tau_X} + C_{EEA} n_X \tag{4.12}$$

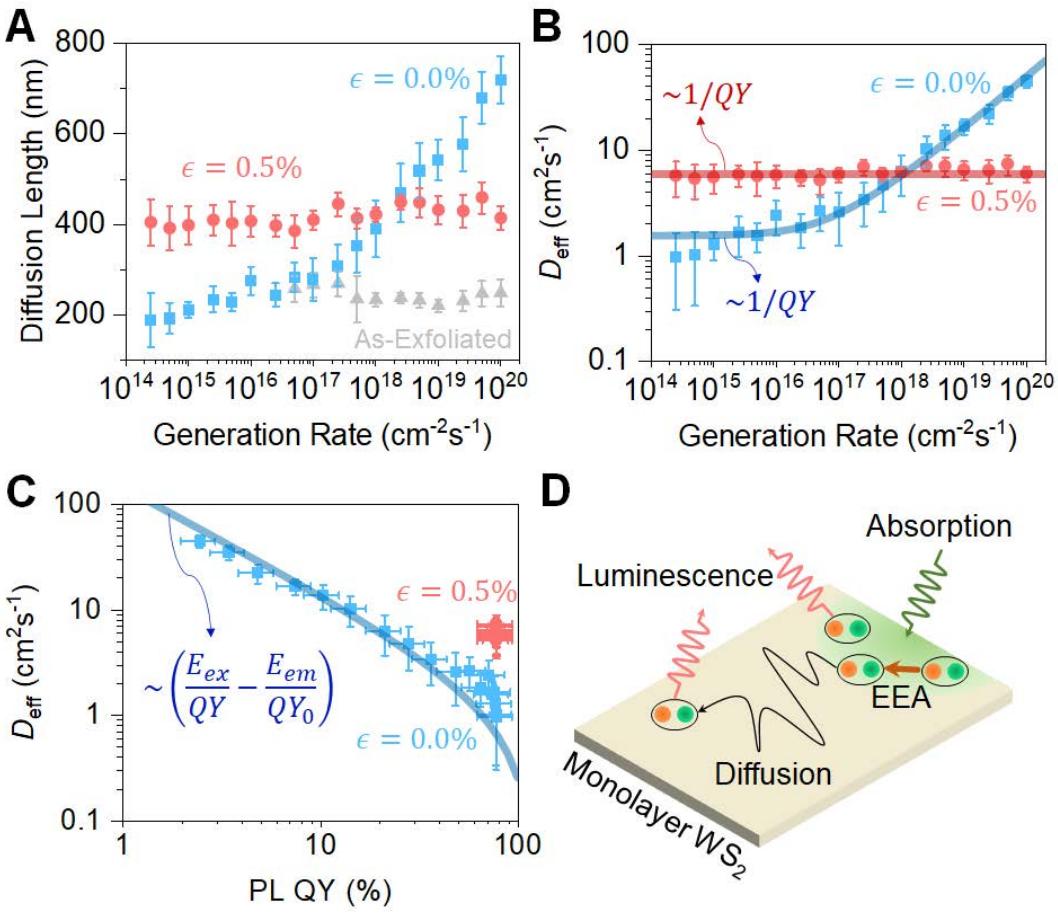

Figure 4.11: **Exciton-exciton annihilation enhanced diffusion.** (A) Diffusion length of neutral excitons in monolayer WS_2 at different generation rates and strains. (B) Effective diffusion coefficient Deff versus generation rate for monolayer WS_2 with different strains at $\epsilon = 0\%$,0.5%. (C) Inversely proportional relationship between D_{eff} and PL QY, which can be switched by strain. (D) Annihilation of an exciton provides additional kinetic energy to another nearby exciton to traverse further and then emit light, resulting in a large diffusion pattern.

The maximum quantum yield QY_0 is achieved when exciton concentration is very low

$$QY_0 = \frac{1/\tau_{Xr}}{1/\tau_X} \tag{4.13}$$

The excess energy available to a single cold exciton is $E_{ex} - E_{em}$, where E_{ex} is the excitation photon energy and, E_{em} is the emission photon energy. In case the EEA channel is active, some excitons relax to the ground state transferring all its energy (E_{em}) to a nearby exciton. This hot energetic exciton loses its large kinetic energy by diffusing very fast in the crystal in a random direction while emitting phonons. By losing its energy a hot exciton turns into a cold exciton, which can then luminesce. However, if the EEA channel is suppressed, no hot excitons are created. Hot electrons are generated at a rate of $C_{EEA}n_X^2$, and each hot electron has an average kinetic energy of E_{em}. The average kinetic energy per exciton (KE) provided to the exciton population in steady state is

$$KE \sim \frac{(E_{ex} - E_{em})G + E_{em}C_{EEA}n_X^2}{n_X} \tag{4.14}$$

$$= (E_{ex} - E_{em})\frac{G}{n_X} + E_{em}C_{EEA}n_X \tag{4.15}$$

where the first term indicates the thermal energy from the excitation laser and the second term indicates the energy from the nonradiative recombination of EEA. Using above equations

$$= (E_{ex} - E_{em})\left(\frac{1}{\tau_X} + C_{EEA}n_X\right) + E_{em}C_{EEA}n_X \tag{4.16}$$

$$= E_{ex}\left(\frac{1}{\tau_X} + C_{EEA}n_X\right) - E_{em}\frac{1}{\tau_X} \tag{4.17}$$

Using above equations

$$= \frac{E_{ex}}{\tau_{Xr} * QY} - \frac{E_{em}}{\tau_X} \tag{4.18}$$

$$= \frac{1}{\tau_{Xr}}\left(\frac{E_{ex}}{QY} - \frac{E_{em} * \tau_{Xr}}{\tau_X}\right) \tag{4.19}$$

$$= \frac{1}{\tau_{Xr}}\left(\frac{E_{ex}}{QY} - \frac{E_{em}}{QY_0}\right) \tag{4.20}$$

According to the semiclassical description [63, 64], the diffusion coefficient is determined by the exciton mass M_X and the scattering time τ_s

$$D_{eff} = \frac{\tau_s KE}{M_X}. \tag{4.21}$$

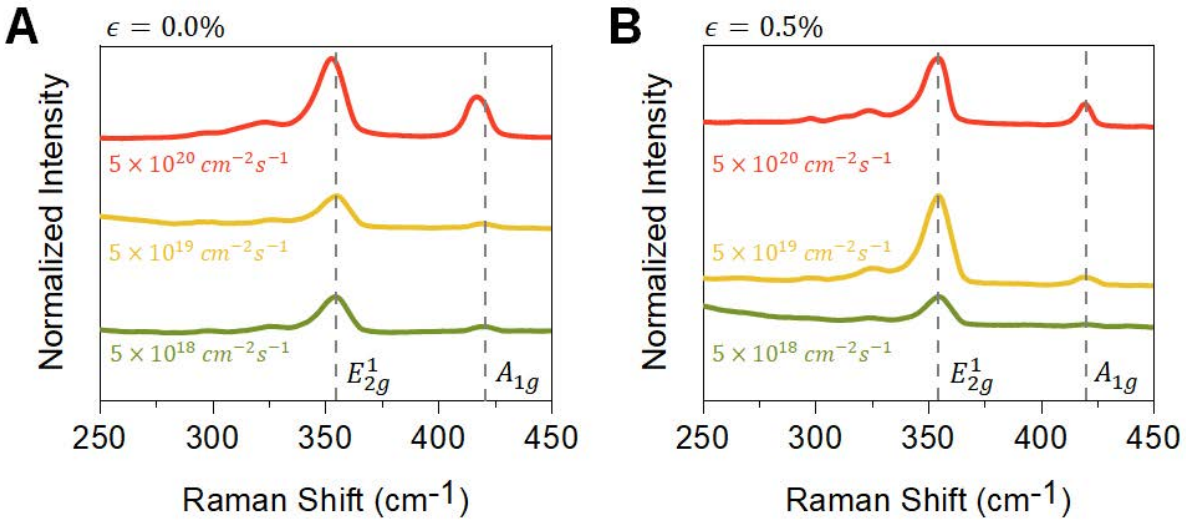

Figure 4.12: **Raman spectra of monolayer WS_2.** (A, B) Generation rate dependent Raman spectra of monolayer WS_2 with variant uniaxial strains of $\epsilon = 0\%$, 0.5%.

Now by using the expression of average kinetic energy as a function of quantum yield we find that

$$D_{eff} \sim \frac{E_{ex}}{QY} - \frac{E_{em}}{QY_0}. \tag{4.22}$$

whereas QY is the quantum yield at any generation rate and QY_0 is the maximum quantum yield at low generation rate. We note that, in Fig. 4.11B and C, these simple expressions fit the experimental value very well with only one proportionality factor.

If EEA is active, excitons gain kinetic energy from the nonradiative expense of another exciton (Fig. 4.11D). These hot excitons diffuse fast but lose their energy by releasing phonons. This in turn heats up the lattice, which can be observed in the pump-dependent Raman spectra of monolayer WS_2 (Fig. 4.12). Both E^1_{2g} and A_{1g} peaks of unstrained counterdoped monolayer WS_2 red-shifted with increasing generation rate, whereas strained monolayer does not show any shift. The lattice temperature of unstrained monolayer at $G = 5 \times 10^{10}$ cm^{-2}s^{-1} is estimated to increase by $260°C$ from the linear temperature dependence of Raman modes with temperature coefficients of -1.25×10^{-2} and -1.49×10^{-2} cm^{-1}K^{-1} for the E^1_{2g} and A_{1g} modes, respectively [65]. Note that, changing the crystal temperature in monolayers by heating the substrate does not have the same effect on exciton diffusion as this process does not create hot excitons at same energy as EEA (Fig. 4.13).

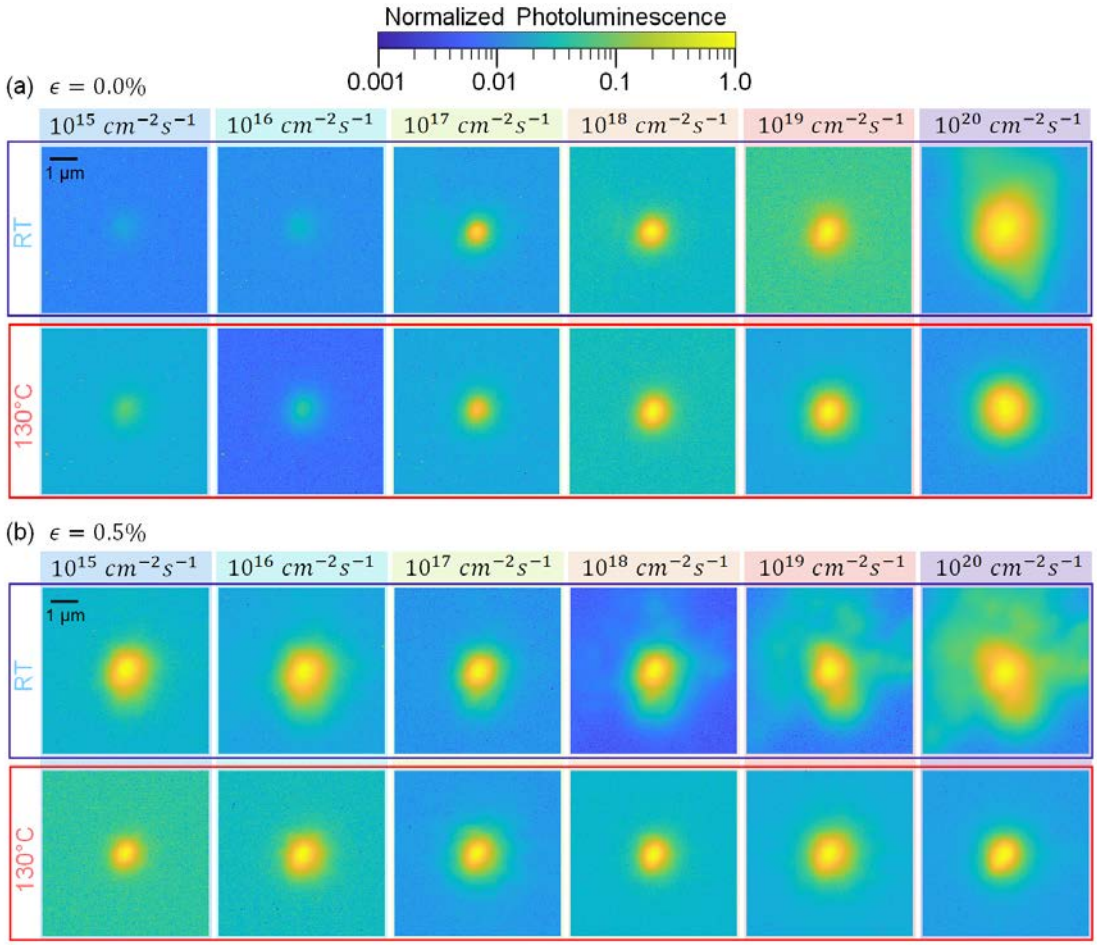

Figure 4.13: **Exciton diffusion on heated monolayer** (A,B) PL images of counterdoped monolayer WS_2 as a function of generation rate and strain at different substrate temperature. Scale bar is 1 μm. No significant enhancement was observed in the exciton diffusion when the substrate temperature was changed from room temperature to 130°C.

4.4 Summary

In summary, we have measured the diffusion length of neutral excitons in monolayer MoS_2. The steady state exciton diffusion length is found to be between 1.5-4 μm depending on the pump intensity. Our measurements demonstrate that with increasing exciton concentration the diffusion coefficient increases and transport of neutral excitons in MoS_2 changes from linear diffusion to subdiffusive. The diffusion coefficient of neutral excitons measured by steady state measurements and time resolved measurements are found to be in excellent agreement. These results are direct spatial and temporal observation of isolated neutral exciton diffusion in a monolayer semiconductor, which will be invaluable for the design and characterization of systems that rely on neutral and charged exciton diffusion at room-temperature. We further explored neutral exciton transport in monolayer semiconductors at room temperatures as a function of strain and generation rate. EEA is shown to have a profound effect on exciton propagation, resulting in strong pump-dependence of the measured diffusion drastically different from conventional semiconductors. Our results reveal strain as a unique tuning knob for mobile optical excitations in 2D materials, and show EEA is relevant for the design of optoelectronic devices not only because it affects PL QY but also it enhances exciton diffusion.

4.5 Experimental and Theoretical Details

Device Fabrication

TMDC monolayers are mechanically exfoliated on top of poly(methyl methacrylate) (PMMA, 100 nm), which is spin-coated on SiO_2 (50 nm)/Si substrate. MoS_2 (SPI supplies), WS_2 (HQ Graphene), WSe_2 (HQ Graphene) and $MoSe_2$ (HQ Graphene) were mechanically exfoliated onto 50 nm SiO_2/Si p^{++} substrates. Monolayers were identified by optical contrast. 40 nm thick Au contacts were evaporated on 280 nm SiO_2/Si, and then picked up and placed on the monolayer by a dry transfer method, using PMMA as the transfer medium. Electron-beam lithography was used to open a window in the transferred PMMA, allowing probe tip contact.

The flexible devices for optical measurements were fabricated on polyimide substrate (Kapton, Dupont, 1.5 mm thick). To prevent the background PL from polyimide substrate, a metal mirror of Ti (10 nm)/Au (100 nm)/Ti (10 nm) was fabricated using standard photolithography and thermal evaporation, and 50 nm Al_2O_3 was deposited via atomic layer deposition (ALD) at 200°C. WS_2 (HQ Graphene) was mechanically exfoliated on a 50 nm SiO_2/Si substrate. Monolayer WS_2 flakes were picked up with poly(methyl methacrylate) (PMMA) and transferred onto the ALD oxide, followed by a post-baking at 180°C for 5 minutes and dichloromethane (DCM) treatment to remove PMMA. As a chemical counterdoping, 3% Nafion perfluorinated resin solution (Sigma Aldrich) diluted by ethanol was spin-coated on the prepared monolayer WS_2.

Electrical and Optical Characterization

Devices were charged from a Keithley 2410 Source Meter applied to the gate electrode, while the Au source contact was grounded. The PL QY was measured using a customized micro-PL instrument described in detail in previous study.18,20 For steady state measurements, a green diode laser was used as the excitation source. Laser source was collimated and then focused to a diffraction-limited spot by a 100×0.95 NA objective lens. The back aperture of the objective was overfilled to assure diffraction-limited performance. Emission from the sample was collected by the same objective and additionally magnified 5.3× for a total magnification of 530× and imaged on a camera (Andor Neo sCMOS 5.5, sensor size 16.6×14 mm, 2560×2160 pixels) with pixel size 6.5 μm, which provided an effective imaging pixel size of 8.63 nm. A long-pass dichroic filter and two long-pass edge filters (Semrock) were used to remove the excitation laser beam from the PL signal. To ensure no Fresnel broadening of the PL by the top PMMA, we compared the reflected laser profile from a thick reflective MoS_2 with and without top PMMA and found no significant broadening.

For time-resolved measurements, a Ti-Sapphire laser along with an OPO was used as the excitation source. The laser beam was collimated and focused by a 100×0.95 NA objective lens. The back aperture of the objective was overfilled to assure diffraction-limited performance. Emission from the sample was collected by the same objective and imaged on a single-mode fiber (P1-405P-FC-2, Thorlabs) attached to a translation stage (Attocube ECS series) that scanned the emission focal plane. The stage was moved in 5 μm steps corresponding to 50 nm at the sample. The signal was detected by a single-photon counting avalanche photodiode (MPD PDM-series) connected to a time-correlated single-photon counting unit (Picoharp 300). The temporal resolution was approximately 50 ps, as determined by the FWHM of the instrument response function.

We simulated the processes of exciton generation and recombination by discretizing and solving the continuity equation in MATLAB. The spatial grid was sampled at 5 nm distances. Time was nonuniformly sampled, denser sampling points when concentration is higher to ensure convergence.

PL spectra and QY were measured using a customized micro-PL instrument described in detail in the previous study (26). An Ar ion laser with a 514.5 nm line was used as the excitation source. The calibrated PL QY measurement is also described in detail in previous studies [20]. A two-point bending method was used to apply a tensile strain in the monolayer WS_2 [66]. The nominal applied strain was calculated using the equation $\epsilon = t/R$, where $2t$ and R are the substrate thickness and curvature radius measured through the cross-section optical image. TRPL measurements were collected using a time-correlated single-photon counting (TCSPC) module. A monochromated line of 514 nm from a supercontinuum laser was used as the excitation source. Exciton diffusion images were measured with taken in a fluorescence microscopy setup using the green laser same as the excitation source for PL measurement, and a CCD detector (Andor Luca) to acquire images. The samples were excited with a 514.5 nm wavelength laser focused to a diffraction-limited spot. Raman spectra were measured by a Raman microscopic system (Horiba Labram HR Evolution)

using an excitation laser of 532 nm.

4.6 References

[1] Ashwin Ramasubramaniam. Large excitonic effects in monolayers of molybdenum and tungsten dichalcogenides. *Physical Review B*, 86(11):115409, 2012.

[2] Bairen Zhu, Xi Chen, and Xiaodong Cui. Exciton binding energy of monolayer WS_2. *Scientific Reports*, 5(1):1–5, 2015.

[3] Jason S Ross, Sanfeng Wu, Hongyi Yu, Nirmal J Ghimire, Aaron M Jones, Grant Aivazian, Jiaqiang Yan, David G Mandrus, Di Xiao, Wang Yao, et al. Electrical control of neutral and charged excitons in a monolayer semiconductor. *Nature Communications*, 4(1):1–6, 2013.

[4] Jason S Ross, Philip Klement, Aaron M Jones, Nirmal J Ghimire, Jiaqiang Yan, DG Mandrus, Takashi Taniguchi, Kenji Watanabe, Kenji Kitamura, Wang Yao, et al. Electrically tunable excitonic light-emitting diodes based on monolayer WSe_2 p–n junctions. *Nature Nanotechnology*, 9(4):268–272, 2014.

[5] Der-Hsien Lien, Matin Amani, Sujay B Desai, Geun Ho Ahn, Kevin Han, Jr-Hau He, Joel W Ager, Ming C Wu, and Ali Javey. Large-area and bright pulsed electroluminescence in monolayer semiconductors. *Nature Communications*, 9(1):1–7, 2018.

[6] Yuan Liu, Jian Guo, Enbo Zhu, Lei Liao, Sung-Joon Lee, Mengning Ding, Imran Shakir, Vincent Gambin, Yu Huang, and Xiangfeng Duan. Approaching the schottky–mott limit in van der Waals metal–semiconductor junctions. *Nature*, 557(7707):696–700, 2018.

[7] Dmitrii Unuchek, Alberto Ciarrocchi, Ahmet Avsar, Kenji Watanabe, Takashi Taniguchi, and Andras Kis. Room-temperature electrical control of exciton flux in a van der Waals heterostructure. *Nature*, 560(7718):340–344, 2018.

[8] Marvin Kulig, Jonas Zipfel, Philipp Nagler, Sofia Blanter, Christian Schüller, Tobias Korn, Nicola Paradiso, Mikhail M Glazov, and Alexey Chernikov. Exciton diffusion and halo effects in monolayer semiconductors. *Physical Review Letters*, 120(20):207401, 2018.

[9] F Cadiz, Cédric Robert, E Courtade, M Manca, L Martinelli, T Taniguchi, K Watanabe, Thierry Amand, ACH Rowe, D Paget, et al. Exciton diffusion in WSe_2 monolayers embedded in a van der Waals heterostructure. *Applied Physics Letters*, 112(15):152106, 2018.

[10] Jonas Zipfel, Marvin Kulig, Raül Perea-Causín, Samuel Brem, Jonas D Ziegler, Roberto Rosati, Takashi Taniguchi, Kenji Watanabe, Mikhail M Glazov, Ermin Malic, et al. Exciton diffusion in monolayer semiconductors with suppressed disorder. *Physical Review B*, 101(11):115430, 2020.

[11] Darwin F Cordovilla Leon, Zidong Li, Sung Woon Jang, Che-Hsuan Cheng, and Parag B Deotare. Exciton transport in strained monolayer WSe_2. *Applied Physics Letters*, 113(25):252101, 2018.

[12] Jing Wang, Yang Guo, Yuan Huang, Hailan Luo, Xingjiang Zhou, Changzhi Gu, and Baoli Liu. Diffusion dynamics of valley excitons by transient grating spectroscopy in monolayer WSe_2. *Applied Physics Letters*, 115(13):131902, 2019.

[13] MM Glazov. Phonon wind and drag of excitons in monolayer semiconductors. *Physical Review B*, 100(4):045426, 2019.

[14] Shengcai Hao, Matthew Z Bellus, Dawei He, Yongsheng Wang, and Hui Zhao. Controlling exciton transport in monolayer $MoSe_2$ by dielectric screening. *Nanoscale Horizons*, 5(1):139–143, 2020.

[15] Raul Perea-Causin, Samuel Brem, Roberto Rosati, Roland Jago, Marvin Kulig, Jonas D Ziegler, Jonas Zipfel, Alexey Chernikov, and Ermin Malic. Exciton propagation and halo formation in two-dimensional materials. *Nano Letters*, 19(10):7317–7323, 2019.

[16] Yang Fu, Dawei He, Jiaqi He, Ang Bian, Lu Zhang, Shuangyan Liu, Yongsheng Wang, and Hui Zhao. Effect of dielectric environment on excitonic dynamics in monolayer WS_2. *Advanced Materials Interfaces*, 6(23):1901307, 2019.

[17] Archana Raja, Lutz Waldecker, Jonas Zipfel, Yeongsu Cho, Samuel Brem, Jonas D Ziegler, Marvin Kulig, Takashi Taniguchi, Kenji Watanabe, Ermin Malic, et al. Dielectric disorder in two-dimensional materials. *Nature Nanotechnology*, 14(9):832–837, 2019.

[18] Der-Hsien Lien, Shiekh Zia Uddin, Matthew Yeh, Matin Amani, Hyungjin Kim, Joel W Ager, Eli Yablonovitch, and Ali Javey. Electrical suppression of all nonradiative recombination pathways in monolayer semiconductors. *Science*, 364(6439):468–471, 2019.

[19] Branimir Radisavljevic, Aleksandra Radenovic, Jacopo Brivio, Valentina Giacometti, and Andras Kis. Single-layer MoS_2 transistors. *Nature Nanotechnology*, 6(3):147–150, 2011.

[20] Matin Amani, Der-Hsien Lien, Daisuke Kiriya, Jun Xiao, Angelica Azcatl, Jiyoung Noh, Surabhi R Madhvapathy, Rafik Addou, KC Santosh, Madan Dubey, et al. Near-unity photoluminescence quantum yield in MoS_2. *Science*, 350(6264):1065–1068, 2015.

[21] Praket P Jha and Philippe Guyot-Sionnest. Trion decay in colloidal quantum dots. *ACS Nano*, 3(4):1011–1015, 2009.

[22] Matin Amani, Peyman Taheri, Rafik Addou, Geun Ho Ahn, Daisuke Kiriya, Der-Hsien Lien, Joel W Ager III, Robert M Wallace, and Ali Javey. Recombination kinetics and effects of superacid treatment in sulfur-and selenium-based transition metal dichalcogenides. *Nano Letters*, 16(4):2786–2791, 2016.

[23] Luis A Jauregui, Andrew Y Joe, Kateryna Pistunova, Dominik S Wild, Alexander A High, You Zhou, Giovanni Scuri, Kristiaan De Greve, Andrey Sushko, Che-Hang Yu, et al. Electrical control of interlayer exciton dynamics in atomically thin heterostructures. *Science*, 366(6467):870–875, 2019.

[24] John Crank. *The Mathematics of Diffusion*. Oxford University Press, 1979.

[25] Richard Ghez. *A primer of diffusion problems*. Wiley Online Library, 1988.

[26] Darwin F Cordovilla Leon, Zidong Li, Sung Woon Jang, and Parag B Deotare. Hot exciton transport in WSe_2 monolayers. *Physical Review B*, 100(24):241401, 2019.

[27] Roberto Rosati, Raül Perea-Causín, Samuel Brem, and Ermin Malic. Negative effective excitonic diffusion in monolayer transition metal dichalcogenides. *Nanoscale*, 12(1):356–363, 2020.

[28] David AB Miller, DS Chemla, TC Damen, AC Gossard, W Wiegmann, TH Wood, and CA Burrus. Electric field dependence of optical absorption near the band gap of quantum-well structures. *Physical Review B*, 32(2):1043, 1985.

[29] T Lundstrom, W Schoenfeld, H Lee, and PM Petroff. Exciton storage in semiconductor self-assembled quantum dots. *Science*, 286(5448):2312–2314, 1999.

[30] M Hagn, A Zrenner, G Böhm, and G Weimann. Electric-field-induced exciton transport in coupled quantum well structures. *Applied Physics Letters*, 67(2):232–234, 1995.

[31] AA High, AT Hammack, LV Butov, M Hanson, and AC Gossard. Exciton optoelectronic transistor. *Optics Letters*, 32(17):2466–2468, 2007.

[32] Alex A High, Ekaterina E Novitskaya, Leonid V Butov, Micah Hanson, and Arthur C Gossard. Control of exciton fluxes in an excitonic integrated circuit. *Science*, 321(5886):229–231, 2008.

[33] Oleksandr V Mikhnenko, Paul WM Blom, and Thuc-Quyen Nguyen. Exciton diffusion in organic semiconductors. *Energy & Environmental Science*, 8(7):1867–1888, 2015.

[34] S Moritsubo, T Murai, T Shimada, Y Murakami, S Chiashi, S Maruyama, and YK Kato. Exciton diffusion in air-suspended single-walled carbon nanotubes. *Physical Review Letters*, 104(24):247402, 2010.

[35] Laurent Cognet, Dmitri A Tsyboulski, John-David R Rocha, Condell D Doyle, James M Tour, and R Bruce Weisman. Stepwise quenching of exciton fluorescence in carbon nanotubes by single-molecule reactions. *Science*, 316(5830):1465–1468, 2007.

[36] Tobias Hertel, Sabine Himmelein, Thomas Ackermann, Dominik Stich, and Jared Crochet. Diffusion limited photoluminescence quantum yields in 1-D semiconductors: Single-wall carbon nanotubes. *ACS Nano*, 4(12):7161–7168, 2010.

[37] Y Wu, HR Wu, YC Zhou, YQ Zhan, J Zhou, XM Ding, and XY Hou. Excitation energy transfer between tris-(8-hydroxyquinoline) aluminum and a red dye. *Applied Physics Letters*, 88(12):123512, 2006.

[38] Denis E Markov, Emiel Amsterdam, Paul WM Blom, Alexander B Sieval, and Jan C Hummelen. Accurate measurement of the exciton diffusion length in a conjugated polymer using a heterostructure with a side-chain cross-linked fullerene layer. *The Journal of Physical Chemistry A*, 109(24):5266–5274, 2005.

[39] Elizabeth MY Lee and William A Tisdale. Determination of exciton diffusion length by transient photoluminescence quenching and its application to quantum dot films. *The Journal of Physical Chemistry C*, 119(17):9005–9015, 2015.

[40] Erika Penzo, Anna Loiudice, Edward S Barnard, Nicholas J Borys, Matthew J Jurow, Monica Lorenzon, Igor Rajzbaum, Edward K Wong, Yi Liu, Adam M Schwartzberg, et al. Long-range exciton diffusion in two-dimensional assemblies of cesium lead bromide perovskite nanocrystals. *ACS Nano*, 14(6):6999–7007, 2020.

[41] Y Nagamune, H Watabe, F Sogawa, and Y Arakawa. One-dimensional exciton diffusion in GaAs quantum wires. *Applied Physics Letters*, 67(11):1535–1537, 1995.

[42] G Grosso, J Graves, AT Hammack, AA High, LV Butov, M Hanson, and AC Gossard. Excitonic switches operating at around 100 k. *Nature Photonics*, 3(10):577–580, 2009.

[43] Long Yuan and Libai Huang. Exciton dynamics and annihilation in WS_2 2D semiconductors. *Nanoscale*, 7(16):7402–7408, 2015.

[44] Nardeep Kumar, Qiannan Cui, Frank Ceballos, Dawei He, Yongsheng Wang, and Hui Zhao. Exciton diffusion in monolayer and bulk $MoSe_2$. *Nanoscale*, 6(9):4915–4919, 2014.

[45] Shibin Deng, Enzheng Shi, Long Yuan, Linrui Jin, Letian Dou, and Libai Huang. Long-range exciton transport and slow annihilation in two-dimensional hybrid perovskites. *Nature Communications*, 11(1):1–8, 2020.

[46] MA Tamor and JP Wolfe. Drift and diffusion of free excitons in Si. *Physical Review Letters*, 44(25):1703, 1980.

[47] YH Chen and SA Lyon. Photoluminescence and diffusivity of free excitons in doped silicon. *IEEE Journal of Quantum Electronics*, 25(5):1053–1055, 1989.

[48] Toshi Sanada, Tyuzi Ohyama, and E Otsuka. Diffusion of excitons and electron-hole drops in germanium. *Solid State Communications*, 17(8):999–1001, 1975.

[49] DP Trauernicht, JP Wolfe, and A Mysyrowicz. Highly mobile paraexcitons in Cuprous Oxide. *Physical Review Letters*, 52(10):855, 1984.

[50] Shiekh Zia Uddin, Eran Rabani, and Ali Javey. Universal inverse scaling of exciton–exciton annihilation coefficient with exciton lifetime. *Nano Letters*, 21(1):424–429, 2020.

[51] Hyungjin Kim, Shiekh Zia Uddin, Naoki Higashitarumizu, Eran Rabani, and Ali Javey. Inhibited nonradiative decay at all exciton densities in monolayer semiconductors. *Science*, 373(6553):448–452, 2021.

[52] Shiekh Zia Uddin, Hyungjin Kim, Monica Lorenzon, Matthew Yeh, Der-Hsien Lien, Edward S Barnard, Han Htoon, Alexander Weber-Bargioni, and Ali Javey. Neutral exciton diffusion in monolayer MoS_2. *ACS Nano*, 14(10):13433–13440, 2020.

[53] ZZ Bandić, PM Bridger, EC Piquette, and TC McGill. Minority carrier diffusion length and lifetime in GaN. *Applied Physics Letters*, 72(24):3166–3168, 1998.

[54] Feng Wang, Yang Wu, Mark S Hybertsen, and Tony F Heinz. Auger recombination of excitons in one-dimensional systems. *Physical Review B*, 73(24):245424, 2006.

[55] KE O'hara, JR Gullingsrud, and JP Wolfe. Auger decay of excitons in Cu_2O. *Physical Review B*, 60(15):10872, 1999.

[56] Vivek Pareek, Julien Madéo, and Keshav M Dani. Ultrafast control of the dimensionality of exciton-exciton annihilation in atomically thin black phosphorus. *Physical Review Letters*, 124(5):057403, 2020.

[57] Gleb M Akselrod, Parag B Deotare, Nicholas J Thompson, Jiye Lee, William A Tisdale, Marc A Baldo, Vinod M Menon, and Vladimir Bulović. Visualization of exciton transport in ordered and disordered molecular solids. *Nature communications*, 5(1):1–8, 2014.

[58] Yiling Yu, Yifei Yu, Guoqing Li, Alexander A Puretzky, David B Geohegan, and Linyou Cao. Giant enhancement of exciton diffusivity in two-dimensional semiconductors. *Science Advances*, 6(51):eabb4823, 2020.

[59] Shinichiro Mouri, Yuhei Miyauchi, Minglin Toh, Weijie Zhao, Goki Eda, and Kazunari Matsuda. Nonlinear photoluminescence in atomically thin layered WSe_2 arising from diffusion-assisted exciton-exciton annihilation. *Physical Review B*, 90(15):155449, 2014.

[60] Roberto Rosati, Samuel Brem, Raül Perea-Causín, Robert Schmidt, Iris Niehues, Steffen Michaelis de Vasconcellos, Rudolf Bratschitsch, and Ermin Malic. Strain-dependent exciton diffusion in transition metal dichalcogenides. *2D Materials*, 8(1):015030, 2020.

[61] David W Snoke. The quantum boltzmann equation in semiconductor physics. *Annalen der Physik*, 523(1-2):87–100, 2011.

[62] Raül Perea-Causín, Samuel Brem, and Ermin Malic. Phonon-assisted exciton dissociation in transition metal dichalcogenides. *Nanoscale*, 13(3):1884–1892, 2021.

[63] J Erland, BS Razbirin, K-H Pantke, VG Lyssenko, and JM Hvam. Exciton diffusion in CdSe. *Physical Review B*, 47(7):3582, 1993.

[64] Koloman Wagner, Jonas Zipfel, Roberto Rosati, Edith Wietek, Jonas D Ziegler, Samuel Brem, Raül Perea-Causín, Takashi Taniguchi, Kenji Watanabe, Mikhail M Glazov, et al. Nonclassical exciton diffusion in monolayer WSe_2. *Physical Review Letters*, 127(7):076801, 2021.

[65] Namphung Peimyoo, Jingzhi Shang, Weihuang Yang, Yanlong Wang, Chunxiao Cong, and Ting Yu. Thermal conductivity determination of suspended mono-and bilayer WS_2 by raman spectroscopy. *Nano Research*, 8(4):1210–1221, 2015.

[66] Sujay B Desai, Gyungseon Seol, Jeong Seuk Kang, Hui Fang, Corsin Battaglia, Rehan Kapadia, Joel W Ager, Jing Guo, and Ali Javey. Strain-induced indirect to direct bandgap transition in multilayer WSe_2. *Nano Letters*, 14(8):4592–4597, 2014.

Chapter 5

Efficiency Roll-off Free Electroluminescence from Monolayer WSe_2

5.1 Introduction

Exciton-exciton annihilation (EEA) is a nonradiative process commonly observed in excitonic materials at high exciton densities. Like Auger recombination in conventional semiconductors, EEA degrades luminescence efficiency at high exciton densities and causes efficiency roll-off in light-emitting devices. Transition metal dichalcogenides (TMDCs), such as WSe_2 monolayer, have been demonstrated to exhibit a near-unity photoluminescence (PL) quantum yield (QY) even at the high exciton densities when the band structure is optimally modified by mechanical strain. Although the recombination pathways in TMDCs are well understood, practical application of light-emitting devices however has been challenging. Here, we demonstrate roll-off free electroluminescence (EL) device composed of TMDC monolayers tunable by strain. We show two order of magnitude EL enhancement from WSe_2 monolayer by applying a relatively small strain of 0.5%. We attain internal quantum efficiency of 8% at all injection rates. Finally, we demonstrate transient EL turn-on voltages as small as the bandgap. Our approach will contribute to practical applications of roll-off free optoelectronic devices based on excitonic materials.

5.2 Strained Electroluminescence from Monolayer Semiconductor

Monolayer transition-metal dichalcogenides (TMDCs) have attracted tremendous attention toward optoelectronic applications at the ultimate scale thickness. Although as-exfoliated or as-grown monolayer TMDCs typically show low photoluminescence (PL) quan-

tum yield (QY) of $0.1 - 1\%$, their PL QY can approach near-unity at the low generation rates when non-radiative trion recombination is suppressed by electrostatic or chemical counterdoping [1, 2]. At the high generation rates, however PL QY in TMDC monolayer significantly drops due to exciton-exciton annihilation (EEA). EEA is generally observed in all excitonic materials including organic and some inorganic semiconductors [3, 4]. EEA is primarily responsible for the efficiency roll-off and limits the performance of light-emitting and light-harvesting device applications at high brightness. Recently we reported that EEA is enhanced when van Hove singularity (VHS) resonance occurs at twice of exciton transition energy in the joint density of states (JDOS) [5]. A relatively small strain $\sim 0.4\%$ can move VHS resonance away from resonance and suppress EEA, leading to near-unity PL QY at all exciton densities. However, the roll-off free light-emitting devices based on TMDC monolayers have been still challenging.

A lot of electroluminescence (EL) devices based on TMDC monolayers have been reported in the literature, such as p-n junction [6–14], quantum well [15–17], thermal emission [18, 19], and metal-insulator-semiconductor (MIS) structures [20, 21]. The external quantum efficiency (QE) is lower than 1% in most cases, [22, 23] and efficiency roll-off has been observed in WS_2 EL devices with MIS structure [21]. Although a relatively high external QE of around $1 - 10\%$ has been reported with using a complex quantum well structure of graphene/h-BN/TMDC/h-BN/graphene, bipolar ohmic contact is still challenging. A transient-mode EL device, which consists of a simple capacitor structure with a single source contact, can achieve a large band bending enabling a high injection current rate during the gate voltage transient regardless of the Schottky barrier height [24–28]. Here, we demonstrate a roll-off free transient-mode EL device based on TMDC monolayers. PL QY of WSe_2 monolayers reaches near-unity even at the high exciton density by applying external tensile strain together with gate modulation due to the inhibition of VHS resonance. With applying a small strain of 0.5%, notably, the WSe_2 monolayer shows EL enhancement by two orders of magnitude and its internal QE reaches 8% at maximum, without efficiency roll-off. We also demonstrate turn-on voltages in the order of optical bandgap in our transient EL devices. Our approach will contribute to practical applications of high-efficiency, high-brightness optoelectronic devices based on excitonic materials.

To control electrostatic counter doping and mechanical strain, we utilized a conventional gate oxide on thermally stable polymer substrate, which is more process friendly and can be enlarged to a wafer-scale compared to two-dimensional heterostructure with graphene and h-BN flakes fabricated on plastic substrates. We first explore the PL QY of TMDC monolayers with optimizing background carrier concentration, generation rate, and band structure. Figure 1A shows schematic of the strain tunable device used in PL measurements. Ti (10 nm)/Au (100 nm)/Ti (10 nm) was deposited on a 1.5 mm thick polyimide substrate (Kapton, Dupont) as a gate electrode, followed by an atomic layer deposition (ALD) of 50 nm Al_2O_3 at 200°C as a gate insulator. 50 nm thick Au source electrodes were patterned on ALD oxide adjacent to gate electrodes. Monolayer WSe_2 was grown on SiO_2/Si substrate via chemical vapor deposition (CVD) [25], then dry-transferred onto the ALD oxide using poly(methyl methacrylate) (PMMA) as a transfer medium. Exfoliated few-layer graphene

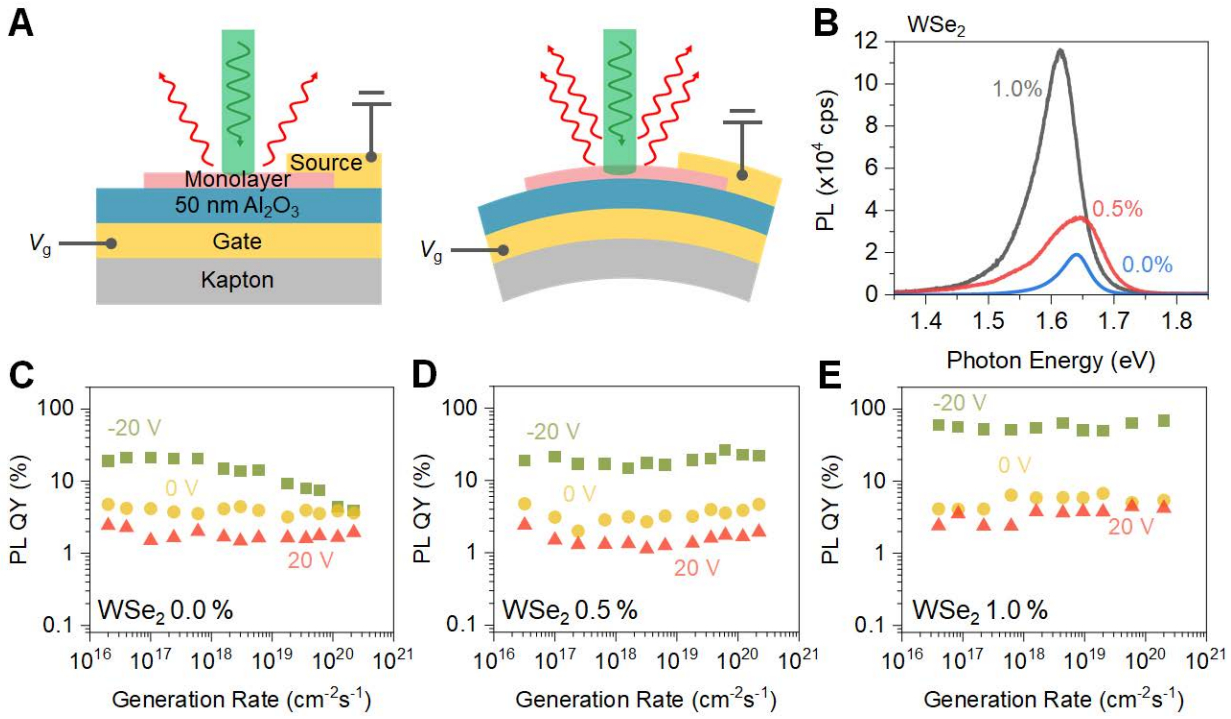

Figure 5.1: **Near-unity PL QY in WSe_2 at all generation rates.** (A) Schematic of the device used to explore photoluminescence from monolayers. (B) Typical PL spectra of monolayer WSe_2 under different uniaxial strains of ϵ = 0%,0.5% and 1.0%, at a high generation rate of G = 2.2×1020 cm-2s-1 and gate voltage of Vg = -20 V. (C, D, E) PL QY in monolayer WSe_2 at different generation rates, gate voltages, and strain.

(Graphenium, NGS Naturgraphit) was transferred by PMMA, bridging the monolayers and source electrodes. A tensile strain was applied in monolayer by a linear actuator. The nominal applied strain was calculated using the equation $\epsilon = t/R$, where $2t$ and R are the substrate thickness and curvature radius. Micro PL measurements were performed at room temperature with using 514.5 nm excitation laser. Figure 1B shows PL spectra of monolayer WSe_2 under different applied strains at a high generation rate and negative gate voltage of $G = 2.2 \times 10^{20}$ cm^{-2}s^{-1} and $V_g = -20$ V, respectively. PL peak position red-shifted with increasing the applied strain. (Similar spectrum change obtained for WS_2 is shown in Figure S1), confirming that the external strain is transferred into the monolayer effectively in this structure.

PL QY of TMDC monolayers generally decrease at the high generation rates because of EEA. Figure 5.1C, D, E shows PL QY in monolayer WSe_2 at different generation rates and electrostatic counterdoping under different applied strain of $\epsilon = 0.0, 0.5$, and 1.0%. As exfoliated monolayer WSe_2 is naturally electron doped because of sulfur vacancies, thus

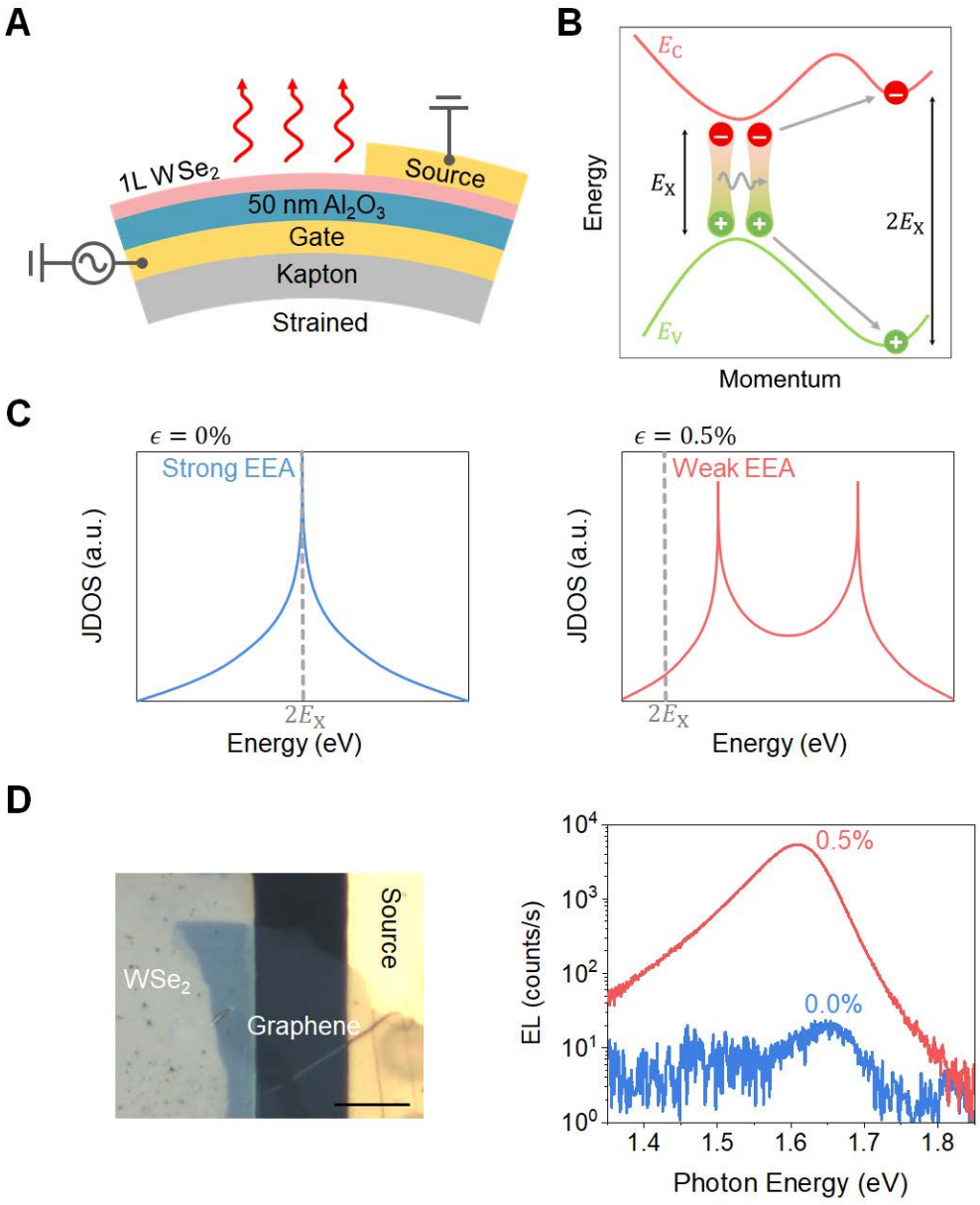

Figure 5.2: **Tunable electroluminescence from monolayer WSe_2.** (A) Schematics of strain tunable transient mode EL device based on monolayer WSe_2. (B) Schematic diagram of EEA process: nonradiatively transferring energy and momentum between two excitons. (C) Schematic diagram of the joint density of states at twice the exciton transition energy $2E_X$ which determines the EEA rate. By applying moderate strain, $2E_X$ have no overlap with VHS resonance, resulting in EEA suppression. (D) Optical image of strain tunable device and typical EL spectra from monolayer WSe_2 at different strain of $\epsilon = 0\%,0.5\%$. The scale bar is 5 μm. Gate voltage and operating frequency were fixed at $V_g = 22.5$ V and $f = 100$ kHz, respectively.

negative gate voltage is required to make it neutral. Without applied strain, PL QY increases by order of magnitude at low generation rates when the negative gate voltage of $V_g = -20$ V is applied, suppressing non-radiative recombination of negatively charged trions by making Fermi level neutral. At higher generation rates above $G = 1 \times 10^{18}$ $cm^{-2}s^{-1}$, PLQY drops due to the EEA. With increasing applied strain, PL QY for neutral excitons ($V_g = -20$ V) increases and approaches near-unity at all generation rates, as shown in Figure 5.1D,E. Similar with WSe_2, roll-off free PL QY was achieved in monolayer WS_2 (Figure 5.6). These enhancements are comparable to the strained TMDC monolayers gate-modulated with h-BN and graphene heterostructures, indicating a successful strain transfer and gate modulation into the emitting layers in the present device structure.

In order to evaluate EL performance with changing strain systematically, transient mode EL [24] were measured using a bipolar sine wave applied to the gate electrode while the source electrode is grounded (Figure 5.2A). The flexible device used in EL measurement was the same structure as that for PL measurement. Monolayer WSe_2 EL devices were measured under nitrogen flow to prevent degradation. By applying moderate strain, VHS resonance is inhibited at the twice of exciton transition energy E_X in the JDOS, suppressing EEA (Figure 5.2B,C). Figure 5.2D shows typical EL spectra with the applied strain of $\epsilon = 0\%$, 0.5%, under the fixed gate voltage and operating frequency at $V_g = 22.5$ V and 100 kHz, respectively. With no strain, EL peak was observed at 1.66 eV, which is consistent with the PL peak position (Figure 5.1B). By applying 0.5% strain, EL peak red-shifted to 1.61 eV and its intensity enhanced by over two orders of magnitude. To further investigate, calibrated EL internal efficiency was measured [26] as a function of gate voltage, injected average carrier rate, and applied strain. Although an accurate measurement of carrier injection is difficult because of the small device size around $50 - 100$ μ m, the external QE can be approximately estimated as a ratio of number of output EL photons to number of injected carriers. In the present capacitor structure, the total injected carrier density when the gate voltage is swept from $-V_g$ to $+V_g$ is given by:

$$n_0 + p_0 = C_{ox}(2V_g - E_g)/q \tag{5.1}$$

where n_0 and p_0 are the steady-state electron and hole concentrations corresponding to a positive and negative V_g, respectively, C_{ox} is the areal gate capacitance, and q is the elementary charge. When an alternating current is applied at the frequency of f, the carrier injection rate Q can be written as

$$Q = f(n_0 + p_0). \tag{5.2}$$

The external QE can be extracted by dividing the emitted EL photons per unit by carrier injection rate, and then converted to internal QE by dividing by the light extraction efficiency of $1/4n^2$, where n is the refractive index of the medium. Fig. 5.3A shows EL internal QE of monolayer WSe_2 with no strain. EL efficiency monotonically increases from 5.0 to 10.0 V and then saturated at over 12.5 V, which is consistent with the previous report on monolayer WS_2 and WSe_2 EL devices. The maximum EL efficiency was around $\sim 3\%$ at

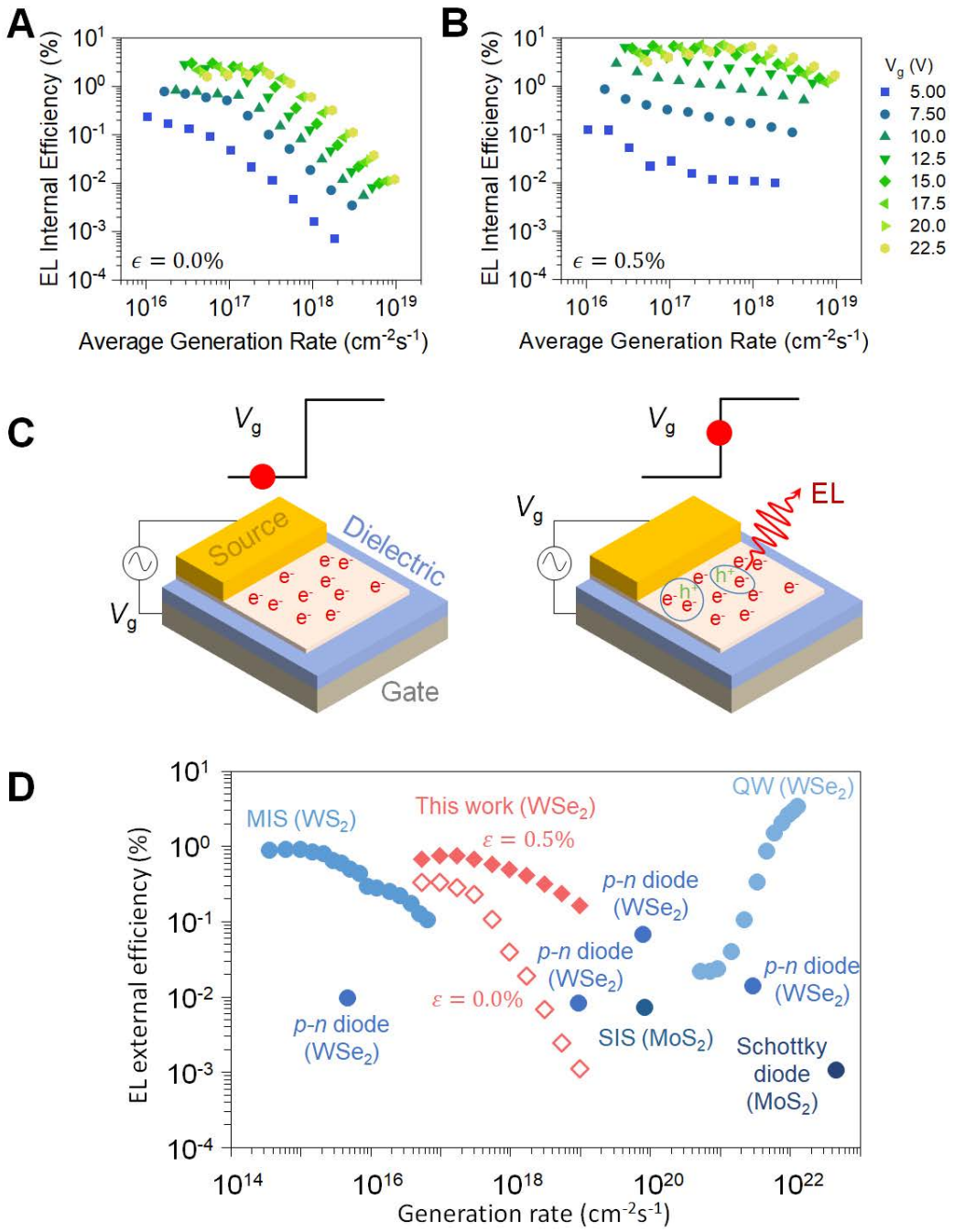

Figure 5.3: **EL internal efficiency in monolayer WSe_2.** (A,B) EL internal efficiency in monolayer WSe_2 as a function of injected average carrier density and gate voltage dependence, under different tensile strain of 0.0% and 0.5%, respectively. (C) Fundamental limits of transient electroluminescence. (D) Benchmark of EL external efficiency for TMDC monolayers: a comparison with p-n diode [6, 7, 9, 13], Schottky diode [23], SIS [22], MIS [21], and QW [16, 15] structures.

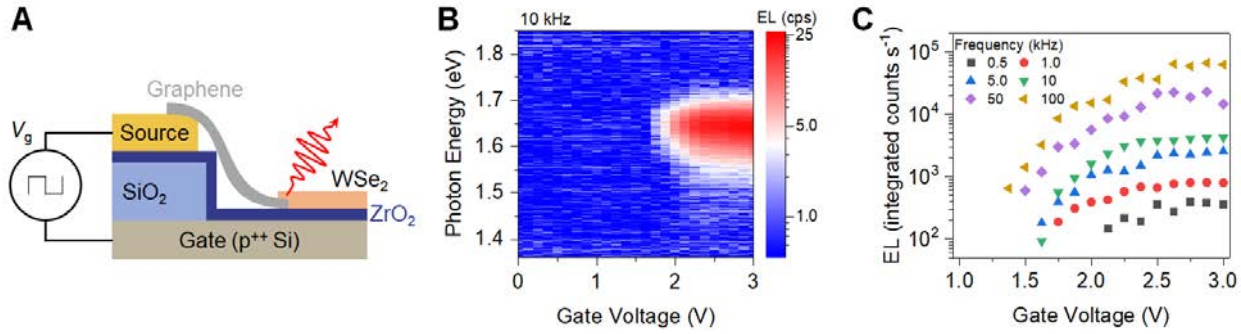

Figure 5.4: **Low voltage transient EL from WSe_2.** (A) Cross-sectional schematic, and (B) EL mapping as a function of photon energy and gate voltage. (C) Integrated EL counts showing device turn-on near the gate voltages comparable with bandgap photon energy of monolayer WSe_2.

the low carrier injection rate. At higher carrier injection rate over mid-10^{17} $cm^{-2}s^{-1}$, the EL QE dramatically decreases by two orders of magnitudes, like as PL QY as a function of generation rate (Figure 5.1C). The typical EL internal QE was at the order of 0.01%, which is comparable to the reported internal QE of as exfoliated WSe_2 monolayer [24]. By applying a small strain of $\epsilon = 0.5\%$, the saturated EL QE reached $\sim 8\%$ at maximum, which exceeds the previously reported transient mode EL device based on chemically counterdoped monolayer TMDC ($\sim 1\%$) (Figure 5.3B) [24]. Unlike as no strain device, the EL QE was maintained even at the high carrier injection rates. This efficiency roll-off free performance is attributed to the suppression of EEA by the strain. The reason why EL efficiency is not as high as PL QY is possibly related to the transient electroluminescence mechanism (Figure 5.3C). When the device reaches steady state, the semiconductor is charged with one polarity of carriers. During the voltage transition, the opposite polarity of carrier is injected. The two types of carriers create both neutral excitons and charged trions. The exciton and trion concentrations are space and time dependent. As trions recombine nonradiatively, not all carrier recombination result in light emission. This fundamentally limits the highest achievable EL efficiency in transient injection. Fig. 5.6D shows a benchmark of EL external efficiency for TMDC monolayers. The external efficiency of transient mode in this work is superior to p-n diodes, Schottky diodes, and semiconductor-insulator-semiconductor (SIS)structures, and comparable to MIS device based on monolayer WS_2 even at the higher generation rates [6, 7, 9, 13, 23, 22, 21, 16, 15]. Here note that the EL QE is underestimated because of parasitic capacitances and resistances in the device. To further improvement of EL QE, it will be helpful to treat TMDC monolayers by chemical counterdoping such as Nafion and TFSI together with the strain engineering. Although the present EL device has a limited lateral size in several tens of micrometer due to the limitation of dry transfer process, it can be enlarged to a centimeter-scale with improving the transfer process. Toward a wafer-scale

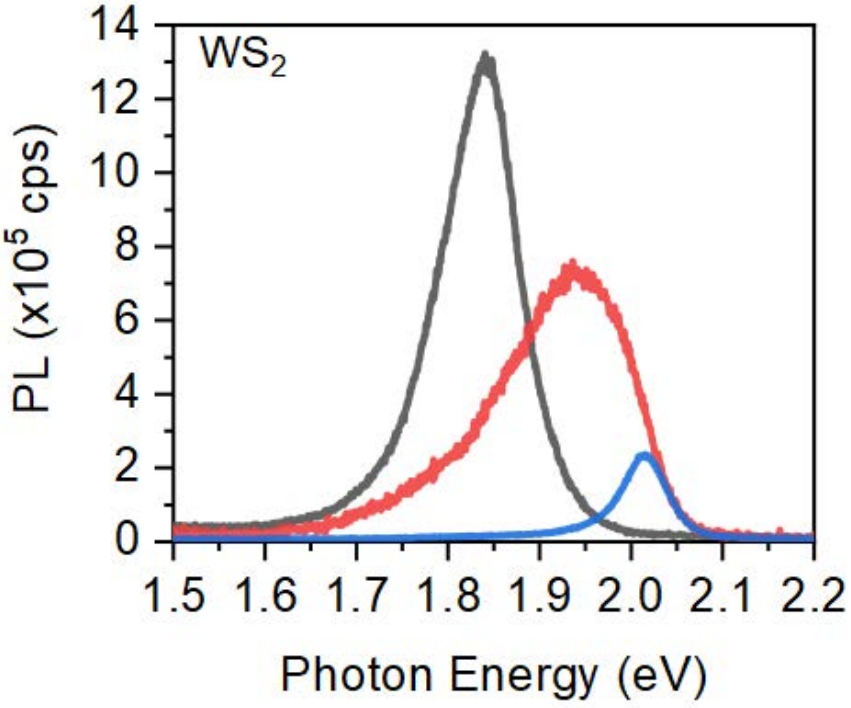

Figure 5.5: **Gated PL from WS_2.** Typical PL spectra of monolayer WS_2 under different uniaxial strains of $\epsilon = 0\%$, 0.5% and 1.0%, at a high generation rate of $G = 2.2 \times 10^{20}$ $cm^{-2}s^{-1}$ and gate voltage of $V_g = -20$ V.

EL device on a solid substrate, strain injection in TMDC monolayer during CVD growth will be useful, with using an appropriate growth substrate due to the difference of thermal expansion coefficient between monolayer and substrate [29].

5.3 Summary

In conclusion, dynamically strain tunable flexible device was fabricated with the conventional gate oxide and TMDC monolayers of WS_2 and WSe_2. Although the transient-mode EL device of monolayer WSe_2 under no strain reveals an efficiency roll-off at the high injection carrier density, an efficiency roll-off free EL device was achieved by applying a small tensile strain, which suppresses the EEA. The present results will be useful for the practical optoelectrical devices such as light sources, photodetectors, and energy harvesting platforms.

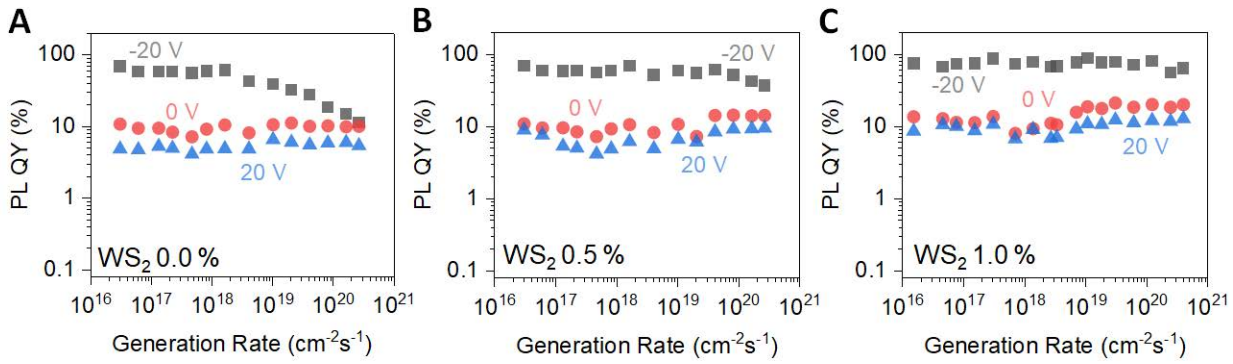

Figure 5.6: **Near-unity PL QY in WS_2 at all generation rates.** PL QY in monolayer WS_2 at different generation rates, gate voltages, and strain.

5.4 Experimental and Theoretical Details

Device Fabrication

The PL and EL devices for were fabricated on polyimide substrate (Kapton, Dupont, 1.5 mm thick). Ti (10 nm)/Au (100 nm)/Ti (10 nm) were fabricated as back gate electrodes using standard photolithography and thermal evaporation. As a gate insulator, 50 nm Al_2O_3 was deposited via ALD at 200°C. 50 nm thick Au source electrodes were patterned on ALD oxide adjacent to gate electrodes. WS_2 and WSe_2 monolayers (HQ Graphene) were grown on SiO_2/Si substrate via CVD. The detailed growth processes for WS_2 and WSe_2 are described in the previously reported papers [25, 29]. Monolayer films were picked up with poly(methyl methacrylate) (PMMA) and transferred onto the ALD oxide, followed by a post baking at 180°C for 5 minutes and dichloromethane treatment to remove PMMA. As a source contact, mechanically exfoliated few layers of graphene (Graphenium, NGS Naturgraphit) was dry-transferred with PMMA to mediate between Au electrode pad and monolayer. Another post baking (180°C, 5 min) was performed to improve the adhesion between the interfaces of TMDC/Al_2O_3 and graphene/TMDC.

Electrical and Optical Characterization

Devices were charged from a Keithley 2410 Source Meter applied to the gate electrode while the Au source was grounded. The PL QY was measured using a home-built micro-PL instrument described in detail in the previous study. A 514.5 nm line was used as the excitation source. A uniaxial tensile strain was applied in the monolayer by a two-point linear actuator. The nominal applied strain was calculated using the equation $\epsilon = t/R$, where $2t$ and R are the substrate thickness and curvature radius measured through the cross-section

optical image. All measurements reported in this paper are taken at room temperature in an ambient lab condition under nitrogen flow.

5.5 References

[1] Matin Amani, Der-Hsien Lien, Daisuke Kiriya, Jun Xiao, Angelica Azcatl, Jiyoung Noh, Surabhi R Madhvapathy, Rafik Addou, KC Santosh, Madan Dubey, et al. Near-unity photoluminescence quantum yield in MoS_2. *Science*, 350(6264):1065–1068, 2015.

[2] Der-Hsien Lien, Shiekh Zia Uddin, Matthew Yeh, Matin Amani, Hyungjin Kim, Joel W Ager, Eli Yablonovitch, and Ali Javey. Electrical suppression of all nonradiative recombination pathways in monolayer semiconductors. *Science*, 364(6439):468–471, 2019.

[3] Caroline Murawski, Karl Leo, and Malte C Gather. Efficiency roll-off in organic light-emitting diodes. *Advanced Materials*, 25(47):6801–6827, 2013.

[4] Wan Ki Bae, Young-Shin Park, Jaehoon Lim, Donggu Lee, Lazaro A Padilha, Hunter McDaniel, Istvan Robel, Changhee Lee, Jeffrey M Pietryga, and Victor I Klimov. Controlling the influence of auger recombination on the performance of quantum-dot light-emitting diodes. *Nature Communications*, 4(1):1–8, 2013.

[5] Hyungjin Kim, Shiekh Zia Uddin, Naoki Higashitarumizu, Eran Rabani, and Ali Javey. Inhibited nonradiative decay at all exciton densities in monolayer semiconductors. *Science*, 373(6553):448–452, 2021.

[6] YJ Zhang, T Oka, Ryo Suzuki, JT Ye, and Y Iwasa. Electrically switchable chiral light-emitting transistor. *Science*, 344(6185):725–728, 2014.

[7] Britton WH Baugher, Hugh OH Churchill, Yafang Yang, and Pablo Jarillo-Herrero. Optoelectronic devices based on electrically tunable p–n diodes in a monolayer dichalcogenide. *Nature Nanotechnology*, 9(4):262–267, 2014.

[8] Sanghyun Jo, Nicolas Ubrig, Helmuth Berger, Alexey B Kuzmenko, and Alberto F Morpurgo. Mono-and bilayer WS_2 light-emitting transistors. *Nano Letters*, 14(4):2019–2025, 2014.

[9] Jason S Ross, Philip Klement, Aaron M Jones, Nirmal J Ghimire, Jiaqiang Yan, DG Mandrus, Takashi Taniguchi, Kenji Watanabe, Kenji Kitamura, Wang Yao, et al. Electrically tunable excitonic light-emitting diodes based on monolayer WSe_2 p–n junctions. *Nature Nanotechnology*, 9(4):268–272, 2014.

[10] Oriol Lopez-Sanchez, Esther Alarcon Llado, Volodymyr Koman, Anna Fontcuberta i Morral, Aleksandra Radenovic, and Andras Kis. Light generation and harvesting in a van der Waals heterostructure. *ACS Nano*, 8(3):3042–3048, 2014.

[11] Yu Ye, Ziliang Ye, Majid Gharghi, Hanyu Zhu, Mervin Zhao, Yuan Wang, Xiaobo Yin, and Xiang Zhang. Exciton-dominant electroluminescence from a diode of monolayer MoS_2. *Applied Physics Letters*, 104(19):193508, 2014.

[12] Rui Cheng, Dehui Li, Hailong Zhou, Chen Wang, Anxiang Yin, Shan Jiang, Yuan Liu, Yu Chen, Yu Huang, and Xiangfeng Duan. Electroluminescence and photocurrent generation from atomically sharp WSe_2/MoS_2 heterojunction p–n diodes. *Nano Letters*, 14(10):5590–5597, 2014.

[13] Andreas Pospischil, Marco M Furchi, and Thomas Mueller. Solar-energy conversion and light emission in an atomic monolayer p–n diode. *Nature Nanotechnology*, 9(4):257–261, 2014.

[14] Weihuang Yang, Jingzhi Shang, Jianpu Wang, Xiaonan Shen, Bingchen Cao, Namphung Peimyoo, Chenji Zou, Yu Chen, Yanlong Wang, Chunxiao Cong, et al. Electrically tunable valley-light emitting diode (vled) based on CVD-grown monolayer WS_2. *Nano Letters*, 16(3):1560–1567, 2016.

[15] F Withers, O Del Pozo-Zamudio, S Schwarz, S Dufferwiel, PM Walker, T Godde, AP Rooney, A Gholinia, CR Woods, P Blake, et al. WSe_2 light-emitting tunneling transistors with enhanced brightness at room temperature. *Nano Letters*, 15(12):8223–8228, 2015.

[16] Freddie Withers, O Del Pozo-Zamudio, A Mishchenko, AP Rooney, Ali Gholinia, K Watanabe, T Taniguchi, Sarah J Haigh, AK Geim, AI Tartakovskii, et al. Light-emitting diodes by band-structure engineering in van der Waals heterostructures. *Nature Materials*, 14(3):301–306, 2015.

[17] Chang-Hua Liu, Genevieve Clark, Taylor Fryett, Sanfeng Wu, Jiajiu Zheng, Fariba Hatami, Xiaodong Xu, and Arka Majumdar. Nanocavity integrated van der Waals heterostructure light-emitting tunneling diode. *Nano Letters*, 17(1):200–205, 2017.

[18] Young Duck Kim, Hakseong Kim, Yujin Cho, Ji Hoon Ryoo, Cheol-Hwan Park, Pilkwang Kim, Yong Seung Kim, Sunwoo Lee, Yilei Li, Seung-Nam Park, et al. Bright visible light emission from graphene. *Nature Nanotechnology*, 10(8):676–681, 2015.

[19] Young Duck Kim, Yuanda Gao, Ren-Jye Shiue, Lei Wang, Ozgur Burak Aslan, Myung-Ho Bae, Hyungsik Kim, Dongjea Seo, Heon-Jin Choi, Suk Hyun Kim, et al. Ultrafast graphene light emitters. *Nano Letters*, 18(2):934–940, 2018.

[20] Carmen Palacios-Berraquero. Atomically-thin quantum light emitting diodes. In *Quantum confined excitons in 2-dimensional materials*, pages 71–89. Springer, 2018.

[21] Shunfeng Wang, Junyong Wang, Weijie Zhao, Francesco Giustiniano, Leiqiang Chu, Ivan Verzhbitskiy, Justin Zhou Yong, and Goki Eda. Efficient carrier-to-exciton conversion in field emission tunnel diodes based on mis-type van der Waals heterostack. *Nano Letters*, 17(8):5156–5162, 2017.

[22] Dehui Li, Rui Cheng, Hailong Zhou, Chen Wang, Anxiang Yin, Yu Chen, Nathan O Weiss, Yu Huang, and Xiangfeng Duan. Electric-field-induced strong enhancement of electroluminescence in multilayer molybdenum disulfide. *Nature Communications*, 6(1):1–8, 2015.

[23] RS Sundaram, M Engel, A Lombardo, R Krupke, AC Ferrari, Ph Avouris, and M Steiner. Electroluminescence in single layer MoS_2. *Nano Letters*, 13(4):1416–1421, 2013.

[24] Der-Hsien Lien, Matin Amani, Sujay B Desai, Geun Ho Ahn, Kevin Han, Jr-Hau He, Joel W Ager, Ming C Wu, and Ali Javey. Large-area and bright pulsed electroluminescence in monolayer semiconductors. *Nature Communications*, 9(1):1–7, 2018.

[25] Joy Cho, Matin Amani, Der-Hsien Lien, Hyungjin Kim, Matthew Yeh, Vivian Wang, Chaoliang Tan, and Ali Javey. Centimeter-scale and visible wavelength monolayer light-emitting devices. *Advanced Functional Materials*, 30(6):1907941, 2020.

[26] Vivian Wang, Yingbo Zhao, and Ali Javey. Performance limits of an alternating current electroluminescent device. *Advanced Materials*, 33(2):2005635, 2021.

[27] Yingbo Zhao, Vivian Wang, Der-Hsien Lien, and Ali Javey. A generic electroluminescent device for emission from infrared to ultraviolet wavelengths. *Nature Electronics*, 3(10):612–621, 2020.

[28] Shiekh Zia Uddin, Naoki Higashitarumizu, Hyungjin Kim, Eran Rabani, and Ali Javey. Engineering exciton recombination pathways in bilayer WSe_2 for bright luminescence. *ACS Nano*, 2022.

[29] Geun Ho Ahn, Matin Amani, Haider Rasool, Der-Hsien Lien, James P Mastandrea, Joel W Ager III, Madan Dubey, Daryl C Chrzan, Andrew M Minor, and Ali Javey. Strain-engineered growth of two-dimensional materials. *Nature Communications*, 8(1):1–8, 2017.

Chapter 6

Exciton Recombination Pathways in Bilayer WSe_2

6.1 Introduction

[1] Exciton-exciton annihilation (EEA) in counterdoped monolayer transition metal dichalcogenides (TMDCs) can be suppressed by favorably changing the band structure with strain. The photoluminescence (PL) quantum yield (QY) monotonously approaches unity with strain at all generation rates. In contrast, here in bilayers (2L) of tungsten diselenide (WSe_2) we observe a nonmonotonic change in EEA rate at high generation rates accompanied by a drastic enhancement in their PL QY at low generation rates. EEA is suppressed both at 0% and 1% strain, but activated at intermediate strains. We explain our observation through the indirect to direct transition in 2L WSe_2 under uniaxial tensile strain. By strain and electrostatic counterdoping, we attain $\sim$ 50% PL QY at all generation rates in 2L WSe_2, originally an indirect semiconductor. We demonstrate transient electroluminescence from 2L WSe_2 with $\sim$ 1.5% internal quantum efficiency for a broad range of carrier densities by applying strain, which is $\sim$50 times higher than without strain. The present results elucidate the complete optoelectronic photophysics where indirect and direct excitons are simultaneously present and provide an insight into exciton engineering in TMDCs multilayer beyond indirect-direct bandgap transition.

6.2 Indirect and Direct Excitons in Bilayer WSe_2

Recombination in monolayers of transition-metal dichalcogenides (TMDCs) is generally dominated by direct transitions, therefore they have received much more attention than their indirect-band gapped multilayer counterparts [1–5]. Near-unity photoluminescence (PL)

[1] The following section was published in a similar form in ACS Nano. (Uddin, S.Z.*, Higashitarumizu, N.*, Kim, H., Rabani, E. and Javey, A., Engineering Exciton Recombination Pathways in Bilayer WSe_2 for Bright Luminescence, ACS Nano, 364(6439), pp.468-471, 2022.

quantum yield (QY) can be achieved in monolayer TMDCs at all generation rates by moving their Fermi level in the middle of the bandgap by electrostatic or chemical counterdoping, and changing the band structure favorably by applying strain [6]. Exciton-exciton annihilation (EEA) is the dominant nonradiative recombination mechanism at high generation rates and is enhanced by van Hove singularities (VHS) in the density of states (DOS). Application of strain moves the process away from VHS and monotonically suppresses EEA [6]. It is desirable to have direct-bandgap thicker TMDCs due to their higher absorptivity and better process stability, but the indirect nature of the multilayer TMDCs limits much of their practical applications in light-emitting devices, photodetectors, and photovoltaics. In contrast to their monolayer counterpart, the photophysics of bilayer TMDCs have not been fully explored quantitatively. Here, first we explore the PL QY of bilayer (2L) WSe_2 as a function of background carrier concentration, generation rate, and band structure. Although the PL QY increases monotonically with strain at low generation rates, we found that the EEA rate changes nonmonotonically at high generation rates. Unlike monolayers, EEA is suppressed both at 0% and 1% strain but activated at intermediate moderate strains. This unique photophysics is due to an indirect to direct transition that bilayer (2L) WSe_2 undergoes with moderate uniaxial tensile strain due to a relatively small difference between the direct and indirect bandgap ($\sim$ 40 meV) [7–9].

Three central elements steer the direct exciton recombination mechanism in TMDC monolayers: exciton generation rate, background carrier concentration, and electronic band structure [6, 10]. In bilayer WSe_2, an additional factor: the coexistence of direct and indirect excitons significantly alters their behavior. With optimum electrostatic doping and tensile strain, we achieved $\sim$ 50% PL QY independent of pump intensity in 2L WSe_2, originally an indirect semiconductor. Finally, we demonstrate transient-mode electroluminescence (EL) devices based on 2L WSe_2 with $\sim$ 1.5% quantum efficiency (QE), which is $\sim$ 50 times higher than without strain. Our results outline the complete optoelectronic photophysics where indirect and direct excitons coexist and instigate exciton engineering in TMDCs multilayer beyond indirect-direct bandgap transition.

Photogenerated carriers in TMDC bilayers form excitons due to strong Coulomb interaction. These excitons can turn into trions in the presence of background carriers leading to nonradiative recombination. We tune the background carrier concentration (electron and hole population densities) of a 2L WSe_2 by varying the back-gate voltage (V_g) in a capacitor structure and alter the generation rate (G) by varying the pump laser intensity. Gate electrodes (Ti/Au/Ti) were fabricated on top of a polyimide substrate, used as the strain platform because of its flexibility and process compatibility. A 50 nm thick Al_2O_3 gate oxide was deposited via an atomic layer deposition (ALD), followed by fabrication of source electrode on top of Al_2O_3 (Figure 1A). As-exfoliated WSe_2 flake was dry-transferred onto the Al_2O_3 gate oxide and contacted with source electrode through few-layer graphene intermediation. The applied strain in 2L WSe_2 was estimated from a cross-section optical image, assuming the strain is transferred entirely from a flexible substrate to WSe_2. Figure 1B shows PL spectra under different uniaxial tensile strains at a medium generation rate of $G = 10^{17}$ $cm^{-2}s^{-1}$ and gate voltage of $V_g = 0$ V. Unstrained 2L WSe_2 shows indirect valley transition

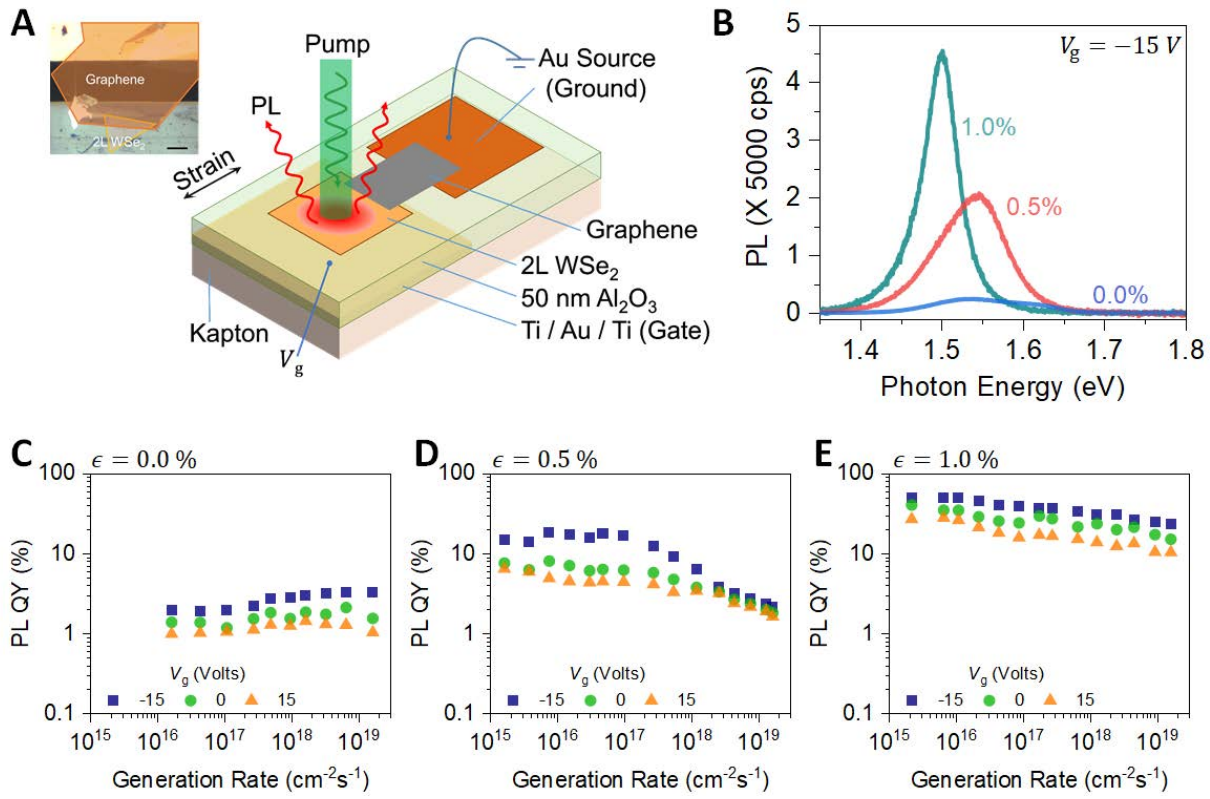

Figure 6.1: **PL QY in 2L WSe_2 at various generation rates and gate voltages.** (A) Schematic and optical micrograph (scale bar 5 μm) of the device used to explore the photophysics of 2L WSe_2. (B) PL spectra of the WSe_2 bilayer device under different uniaxial strains of $\epsilon = 0\%$,0.5% and 1.0% at a medium generation rate of $G = 10^{17}$ cm^{-2}s^{-1} and gate voltage of $V_g = 0$ V, showing the indirect to direct transition. (C-E) PL QY of bilayer WSe_2 as a function of gate voltage, generation rate and strain. At $\epsilon = 1.0\%$ strain, 50% PL QY is achieved.

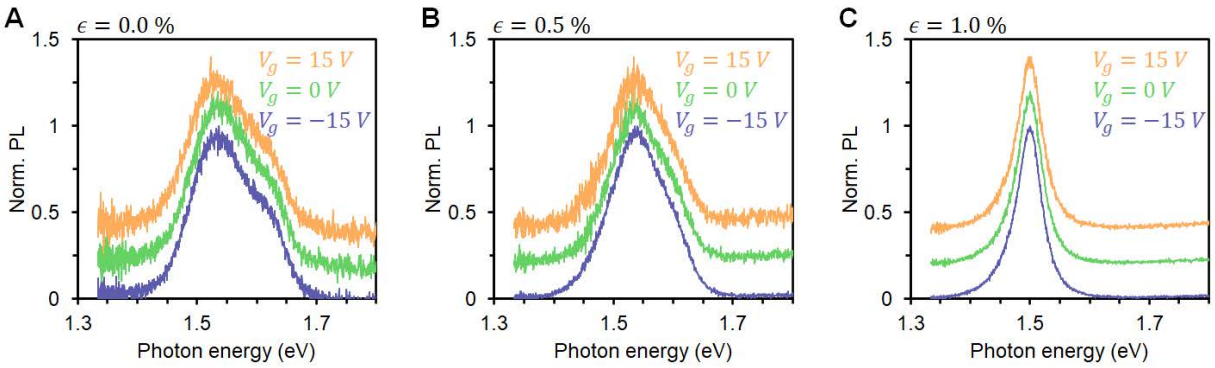

Figure 6.2: **PL Spectra of 2L WSe_2.** (A, B, C) PL Spectra of 2L WSe_2 at different gate voltages and strains.

at lower energy ($\Gamma_C - K_V$) with a shoulder peak at the higher energy corresponding to direct valley transition ($K_C - K_V$) [7, 11]. Under a moderate strain of $\epsilon = 0.5\%$, a single peak is observed with a smaller full-width half-maximum (FWHM) compared to 0% strain. The FWHM further decreases and a redshift is observed at a strain of $\epsilon = 1.0\%$, the maximum strain without a brittle fracture of ALD oxide. These results are attributed to the indirect to direct bandgap transition with increasing tensile strain.

To further understand the photophysics in WSe_2 bilayer, calibrated PL measurements were performed, extracting the QY quantitively as a function of ϵ, V_g, and G (Figures 6.1C-E). Figure 1C shows V_g and G dependence of PL QY in unstrained 2L WSe_2. At zero and positive gate voltages, the nonradiative negative trion recombination is dominant because of the large background electron concentration resulting in a low PL QY of $\sim 1\%$. At negative gate voltage, radiative recombination of neutral excitons becomes dominant leading to PL QY enhancement. We note that, at 0% strain, PL QY does not show a significant dependence on generation rate. PL QY increases by one order of magnitude at low pump with an application of 0.5% tensile strain due to the indirect-direct transition, whereas PL QY drastically droops at the high generation rate (Figure 1D). In excitonic semiconductors, this droop is caused by exciton-exciton annihilation (EEA) [12]. With a tensile strain of 1.0%, PL QY droop is effectively suppressed again at the high generation rate (Figure 1E). With optimum electrostatic doping and tensile strain, we achieved $\sim$ 50% PL QY in 2L WSe_2 at all generation rates. The EEA suppression observed here is markedly different from that of monolayer WSe_2 under strain, where strain monotonically changes EEA.

The observed spectra and the EEA suppression can be explained from the strain dependent band-structure of 2L WSe_2. The qualitative change in the band-structure with strain is illustrated in the schematic of Figure 6.3A. In an unstrained bilayer, the minimum and maximum energy of the conduction and valance band is at the Γ and K point, respectively, resulting in the lowest energy transition being indirect and of low PL QY. With a sufficient

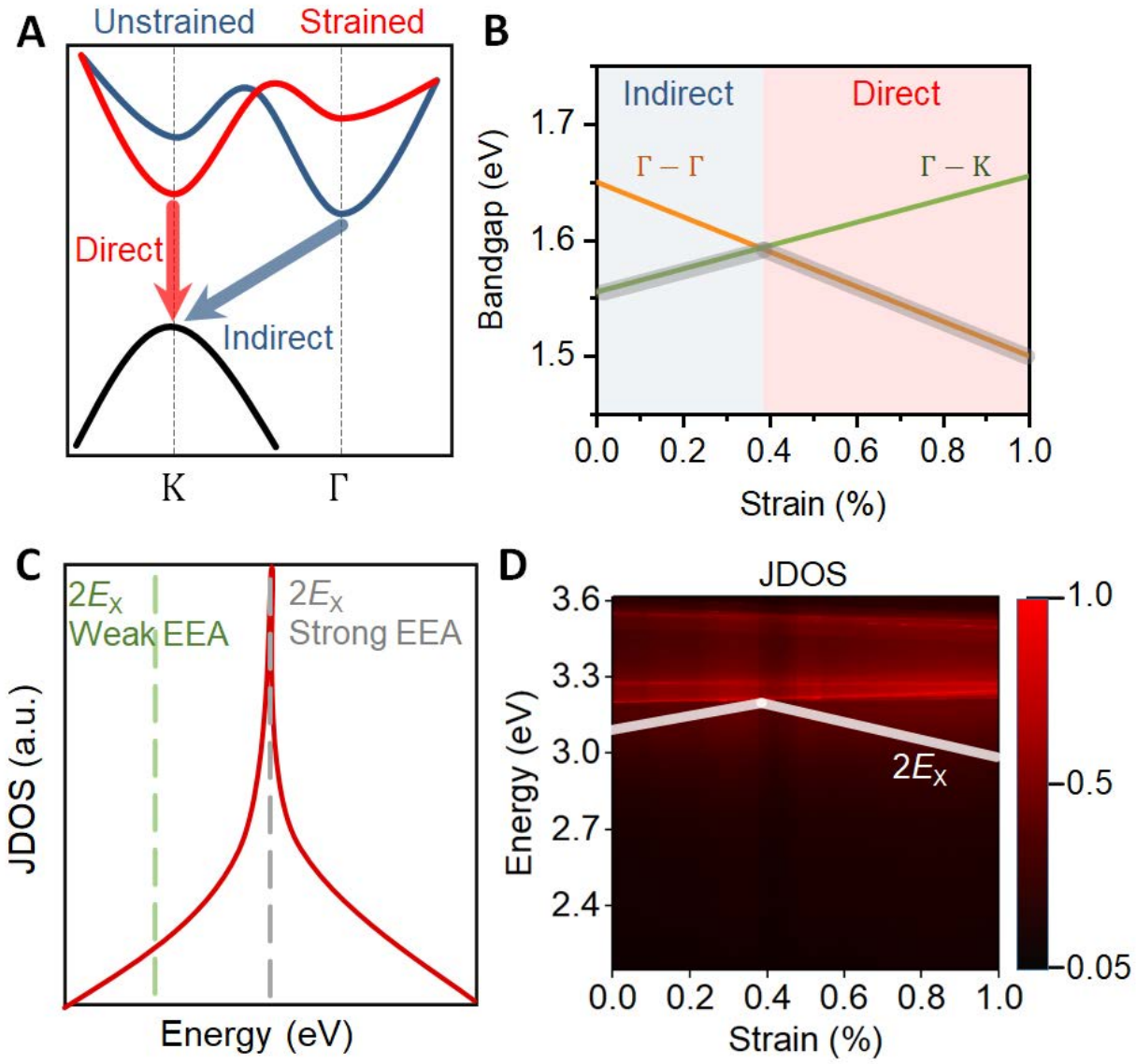

Figure 6.3: **Band structure evaluation of 2L WSe_2 under strain.** (A) Schematic band structure, qualitatively showing direct to indirect transition of 2L WSe_2 with different strain conditions and under illumination. (B) Calculated energy difference for different transitions of bilayer WSe_2. (C) Schematic illustrating how JDOS at twice the exciton transition energy E_X determines the EEA rate. (D) EEA final energy cusping VHS on the JDOS of bilayer WSe_2.

tensile strain, the minimum and maximum energy of the conduction and valance band both reside in the K point, making the lowest energy optical transition being direct, thus increasing PL QY. Strain dependent energy differences of conduction and valance band between Γ points and $\Gamma - K$ points calculated with density functional theory (DFT) are shown in Figure 6.3B. We observe the crossover from indirect to direct bandgap at $\epsilon \sim 0.4\%$. Due to the increasing and decreasing nature of direct and indirect energy gaps with strain, respectively, the minimum energy of optical transition E_X, highlighted in grey in Figure 6.3B, shows a peak at the transition strain. The indirect to direct transition explains the change in PL QY with strain at low generation rate, however we have to look at the joint density of states (JDOS) to understand the change in EEA with strain at high generation rate.. During EEA one exciton nonradiatively transfers its energy to another exciton. Momentum and energy conservation dictates that the electron from the energized exciton ends up with a wavevector in which the energy difference between the conduction and valence bands is equal to twice the exciton transition energy $2E_X$. For a direct bandgap excitonic semiconductor, the joint density of state (JDOS) at the twice exciton transition energy determines the strength of EEA [13]. Because the Coulomb potential in 2D is inversely proportional to the wavevector of the interacting particles, maximum interaction occurs when they have opposing crystal momentum. Therefore, even in indirect semiconductors, the joint density of state (JDOS) at the twice exciton transition energy determines the strength of EEA. If there is a naturally occurring van Hove Singularity (VHS) in 2D JDOS at twice the exciton transition energy $2E_X$, strong EEA is observed. On the other case, if the JDOS is low at $2E_X$, weak EEA is observed (Figure 6.3C). Figure 6.3D shows calculated JDOS of 2L WSe_2 as a function of strain. At around 0.4% tensile strain, the solid curve representing $E = 2E_X$ has a peak maximum touching on a sharply enhanced JDOS of VHSs arising from saddle points in the energy dispersion, which strongly enhances EEA. This explains why no EEA is observed at unstrained bilayers and ϵ=1.0% strain, but EEA is observed at ϵ=0.5% strain. The strain dependence of PL QY and EEA in 2L WSe_2 (Figure 6.1C-E) is well explained by the unique interplay of lowest dominant transition and VHS in 2L WSe_2 under strain, both indirect-direct bandgap transition and EEA enhancement by VHS at the intermediate strains. The movement of the direct exciton transition energy away from the VHS at the maximum strain of 1.0% enables PL QY enhancement with no droop at the high generation rate.

Figure 6.4 summarizes the recombination pathways present in 2L WSe_2. Both indirect and direct excitons can turn into trions, which can be controlled by gate voltage. Strain controls both the ratio of indirect and direct excitons, and their EEA rate. The interplay of these factors give rise to the complex photophysics observed in 2L WSe_2.

Time-resolved (TR) PL measurements were performed with changing gate voltage, pump fluence, and strain. At a low initial carrier concentration of 3.3×10^{10} cm^{-2}, unstrained 2L WSe_2 has the longest lifetime of $\sim$ 0.4 ns at the positive voltage of V_g = 15 V, and a shorter lifetime of $\sim$ 0.3 and $\sim$ 0.07 ns at V_g = 0 and -15 V, respectively (Figure 6.5A). This gate dependence is consistent with the aforementioned PL QY evolution, indicating that trion nonradiative recombination, whose lifetime is much shorter than trion and exciton radiative lifetimes, is predominant at zero and negative voltage. At the highest initial carrier

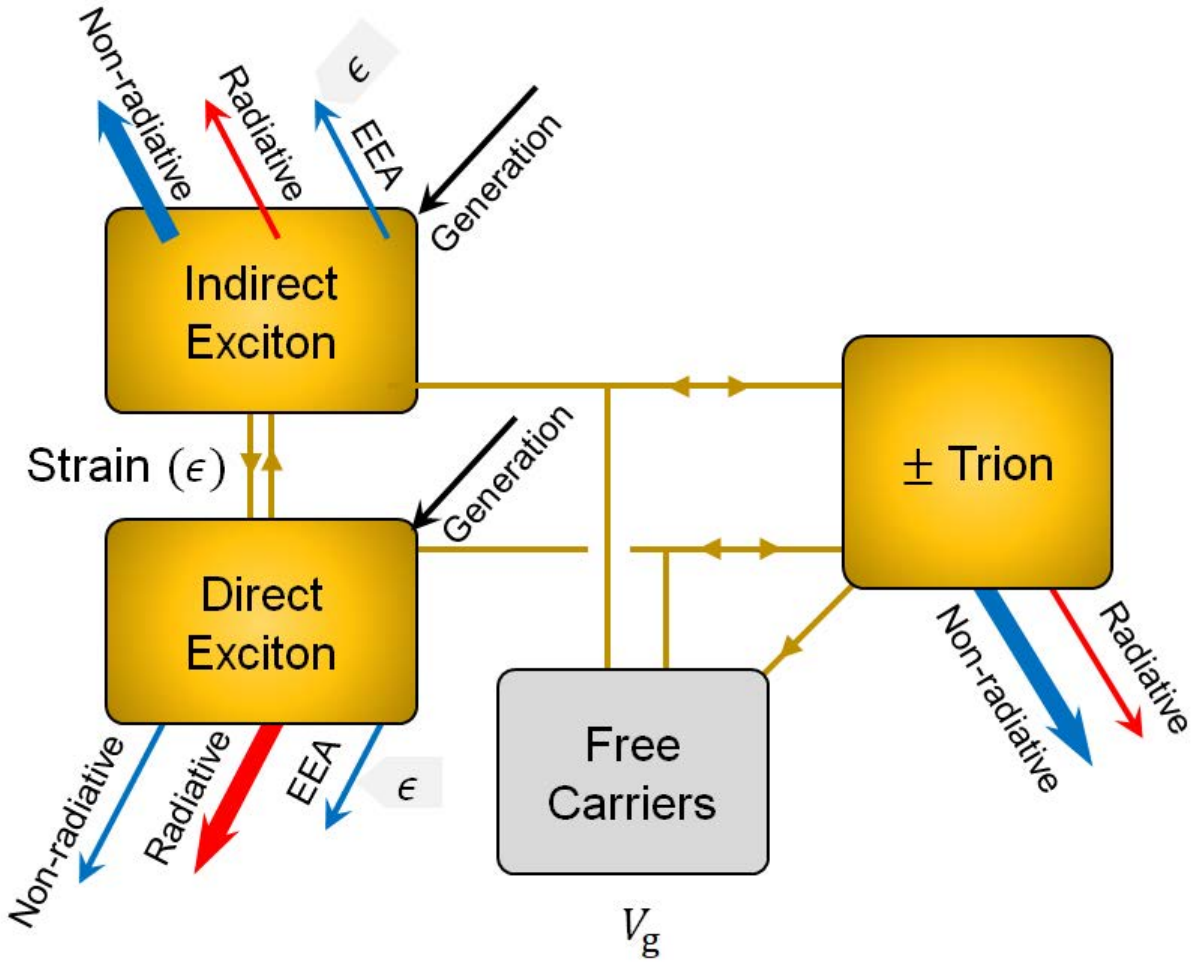

Figure 6.4: **Recombination pathways in 2L WSe_2.** Interaction of direct and indirect excitons, trions, and free carriers and their subsequent recombination channels in bilayer WSe_2.

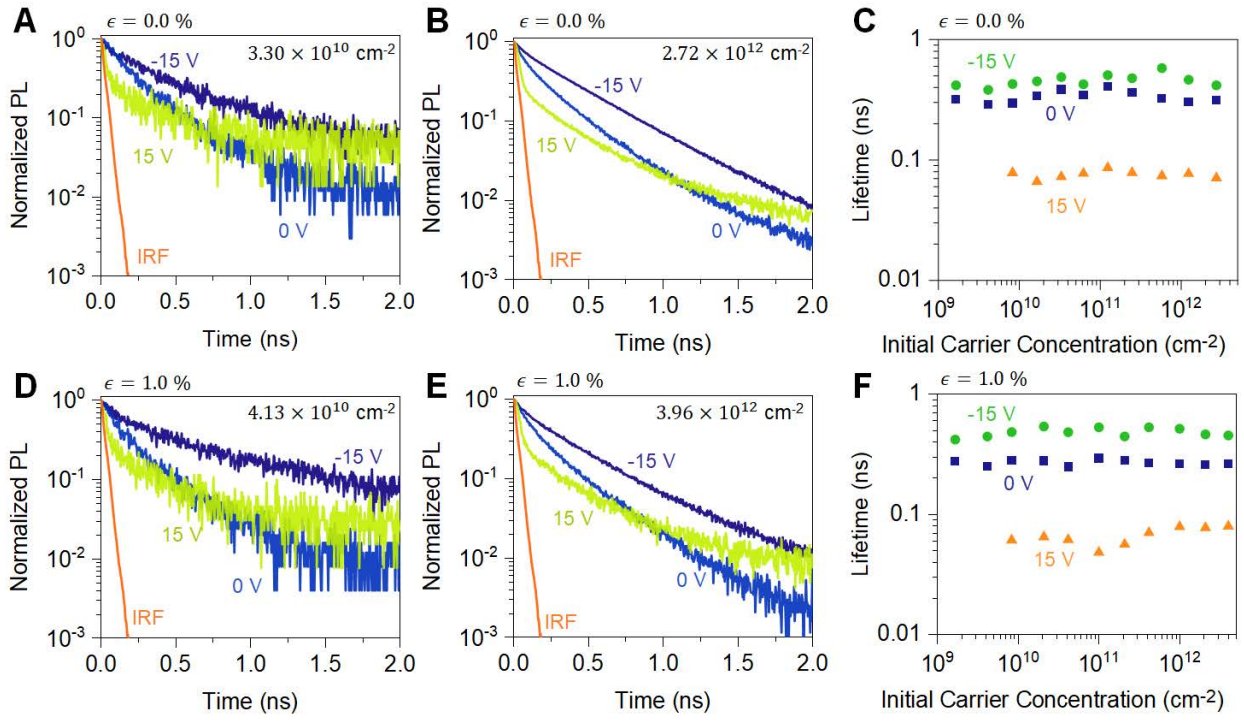

Figure 6.5: **Time-resolved PL of 2L WSe_2.** (A, B) Time-resolved PL of 2L WSe_2 as a function of gate at high and low pump fluence at no strain. (C) Extracted initial lifetime at no strain. (D, E) Time-resolved PL of 2L WSe_2 as a function of gate at high and low pump fluence at 1% applied strain. (F) Extracted initial lifetime at 1% applied strain.

concentration of 2.7×10^{12} cm^{-2}, TR PL decays shows the same gate dependence as that of low carrier concentration (Figure 6.5B), and extracted lifetime is almost constant over three orders of magnitude variation in the pump fluence (Figure 6.5C), indicating the absence of EEA. Figures 4D-F show TR PL and extracted lifetime as a function of gate voltage and initial carrier concentration when a tensile strain of 1.0% is applied [14, 15]. No significant change in the lifetime with strain has been observed.

Exciton diffusion length is important for understanding the energy transport physics in excitonic semiconductors and a key design consideration in many optoelectronic applications [16–18]. PL images of 2L WSe_2 excited by a diffraction-limited laser at different generation rates and strain are shown in Figure 6.6A. Diffusion length is calculated by deconvolving the PL map with laser spot shape and then determining the width of the exciton density profile, as shown in Figure 6.6B. Unstrained 2L WSe_2 shows larger diffusion length $D_{ex}(0\%) \approx 420$ nm, compared to $D_{ex}(1\%) \approx 200$ nm observed in 1% strained bilayer, indicating that indirect exciton diffuses faster than the direct exciton. This is possibly due to fast radiative lifetime of direct excitons and further studies are necessary to understand the pump dependence of

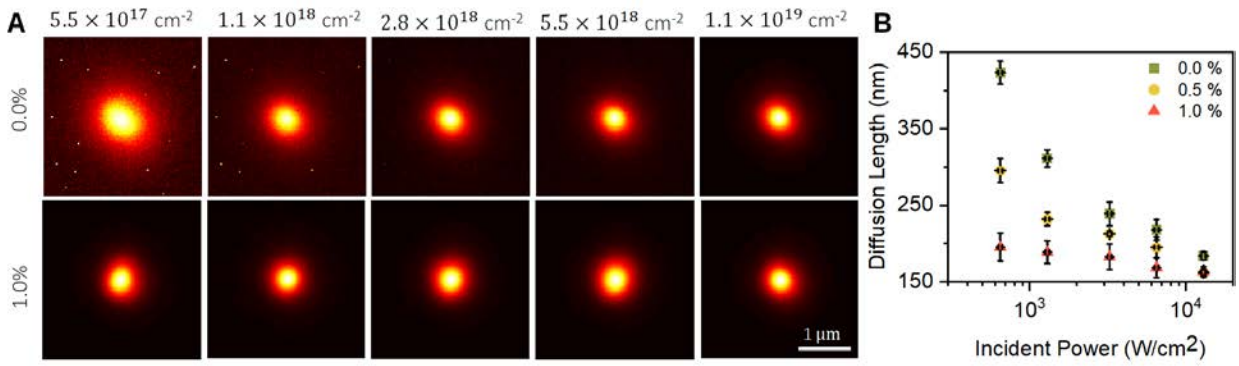

Figure 6.6: **Exciton transport in 2L WSe_2.** (A) Spatial map of emission intensity as a function of pump intensity and strain. (B) Extracted diffusion length at different generation rates and strains.

the diffusion length.

To demonstrate a potential impact of WSe_2 bilayer in the application of light-emitting devices, a transient-mode EL was measured using a bipolar sine wave applied to the gate electrode while the source electrode is grounded (Figure 6.7A). Figure 6.7B shows EL spectra from 2L WSe_2 with and without applying strain at a frequency of $f = 1.0$ MHz and gate voltage of $V_g = 25$ V. A broad peak is observed with applied 0% strain, while EL peak intensity 1% tensile strain is an order of magnitude higher than that of unstrained. Like PL spectrum from unstrained 2L WSe_2 (Figure 6.1B), strained EL device has two emission peaks at lower and higher energy corresponding to the indirect and direct bandgap transitions, respectively. The discrepancy of the spectrum shapes between PL and EL under the specific strain is probably due to a different built-in strain from device to device via PMMA transfer or post-baking process. As a function of operating frequency, the EL intensity monotonically increased with no spectral shape change. The gate voltage dependence was measured with and without applying strain at $f = 1$ MHz (Figure 6.7C). The turn-on voltage Von was approximately 5.0 and 7.5 V for unstrained and 1.0% strained devices, respectively, which depends on the bandgap of materials, gate capacitance, and parasitic resistances [19, 20]. An order of magnitude EL enhancement was confirmed after applying once the device turned on over $V_g = 10$ V. To further quantitatively compare the brightness of 2L WSe_2 with previously reported TMDC EL devices, we extracted QE from EL measurement under various measurement conditions of gate voltage, frequency, and strain. The total number of carriers injected $(n_0 + p_0)$ in a field-effect transistor when the gate voltage is swept from $-V_g$ to $+V_g$ is given by

$$n_0 + p_0 = C_{ox}(2V_g - E_g)/q \tag{6.1}$$

Where n_0 and p_0 are the steady-state electron and hole concentrations corresponding to a positive and negative V_g, respectively, C_{ox} is the areal gate capacitance and q is the

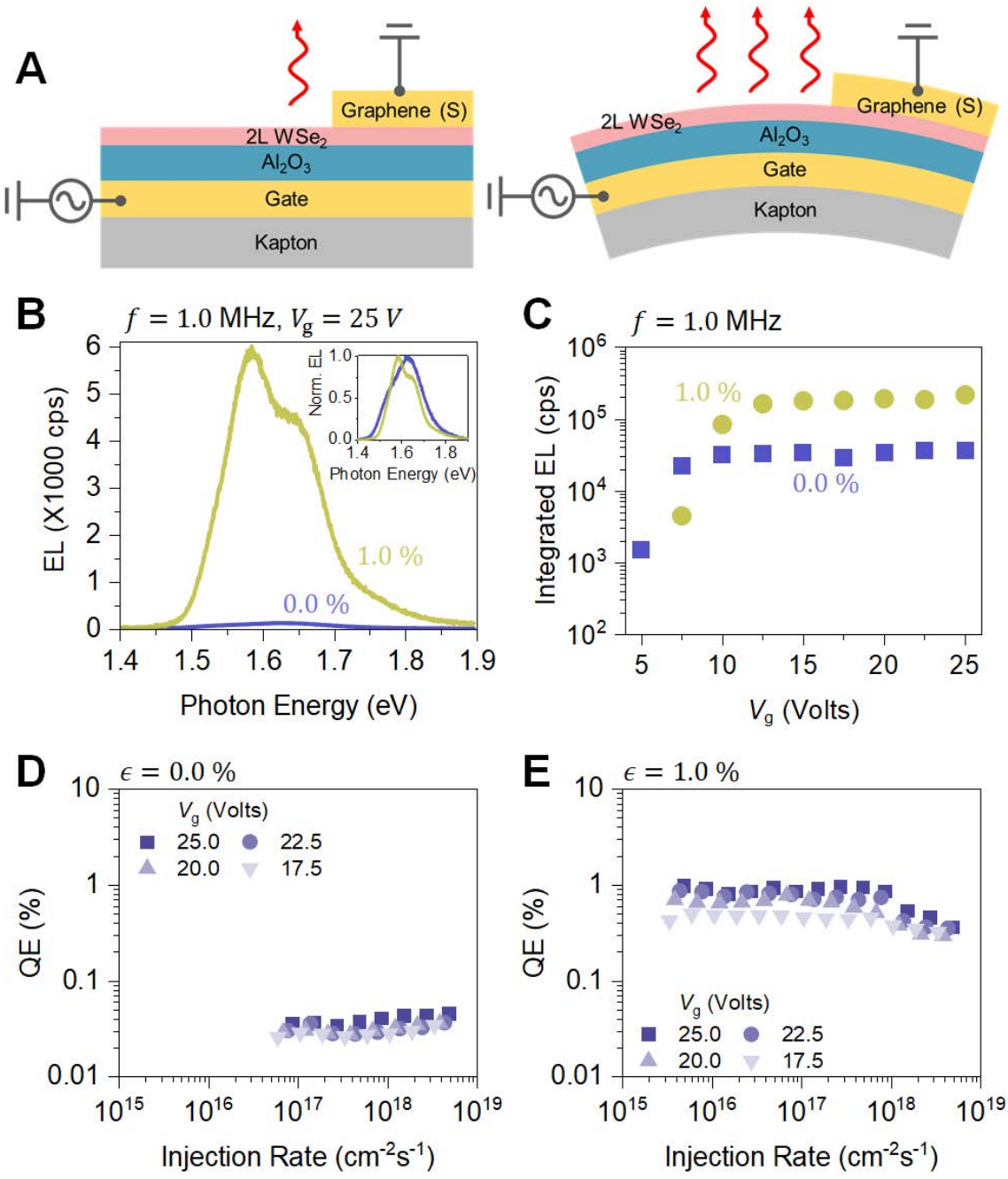

Figure 6.7: **Electroluminescence from 2L WSe_2.** (A) Schematics of strain tunable transit mode EL device. (B) EL spectra of ACEL device with and without strain. (C) Integrated EL intensity as a function of V_g at $f = 1.0$ MHz shows device turn on. (D, E) Internal QE of EL device as a function of injected carrier density under different ϵ and V_g.

elementary charge. When a periodic signal of frequency f is applied across the device, this transition takes place at f times per second. Therefore, the injection rate Q can be written as

$$Q = f(n_0 + p_0) \tag{6.2}$$

Taking the ratio between the output EL photons per unit seconds to the injection rate gives us the quantum efficiency (QE). Figures 6.7D,E shows the dependence of EL QE for unstrained 2L WSe_2 on injected carrier density at different V_g and strain. With increasing the carrier density, EL intensity monotonically enhances. The unstrained device exhibits EL QE of approximately 0.03% at maximum, which is comparable to the reported EL QE of $\sim$ 0.06% in as-exfoliated monolayer WSe_2 [19]. With applying a tensile strain of 1.0%, the EL QE drastically increases by over ten times compared to no strain device. Notably, the efficiency roll-off was effectively suppressed at the high carrier density, indicating reduced nonradiative recombination. The highest EL QE of 2L WSe_2 reached 1.5%, which is $\sim$ 50-fold enhancement compared to the unstrained device. Here, we note that the EL QE is underestimated because the parasitic capacitances are predominant in the current measurement of micrometer-scale devices. Furthermore, the top sub-layer in 2L WSe_2 feels a smaller electric field than the bottom layer because of the single gate structure, leaving room for further improvement of EL performance with utilizing such as dual gate device structure [21]. Further improvement of EL QE is possible by improving the applied strain on the emitting bilayer. Although a WSe_2 thicker film can show similar EL enhancement by strain, trilayer showed poor enhancement compared to bilayer (Figure S1), probably because of the larger energy difference between direct and indirect bandgap [22], and the experimental limitation in ALD oxide with applicable strain up to 1.0%. Further strain engineering in multilayer beyond bilayer can be achievable by using two-dimensional heterostructures such as with graphene and h-BN.

6.3 Summary

In conclusion, we have demonstrated high PL QY in bilayer WSe_2 at all generation rates with modulating background carrier concentration and electronic band structure via strain. Unlike other monolayer and bilayer TMDCs, bilayer WSe_2 experiences the indirect-direct transition and enhanced EEA by VHS resonance at the intermediate tensile strain making it direct bandgap and free from EEA above intermediate strain values, resulting in the highest PL QY of 50% at all exciton densities with applying 1.0% tensile strain. The observed photophysics is corroborated by DFT calculation of band structure correlating the change in the band structure and VHS on the PL QY. Finally, we showed that the transit mode EL device based on 2L WSe_2 and gate with $\sim$ 1.5% QE, as bright as monolayer EL devices, thus enabling bilayer to be a promising candidate for light-emitting materials. Our results resolves the complete optoelectronic photophysics when indirect and direct excitons are coexist and open the way to strain-engineered optoelectronics in multilayered van-der Walls semiconductors.

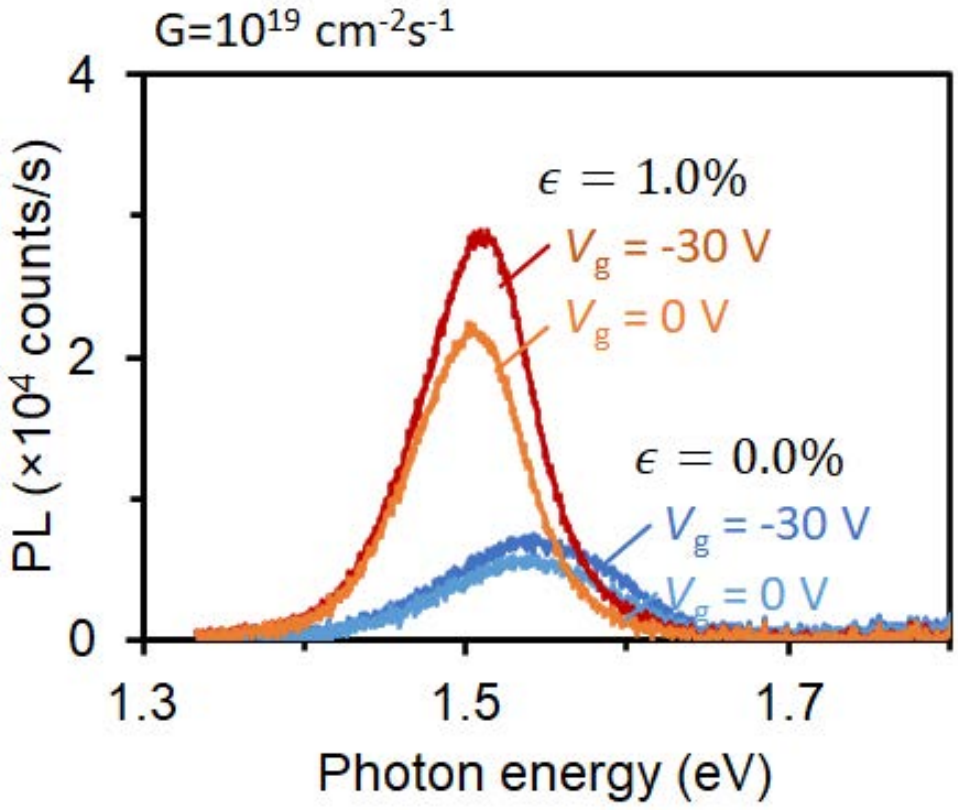

Figure 6.8: **PL Spectra of 3L WSe_2.** PL spectra from WSe_2 trilayer as a function of gate voltage and strain at a generation rate of $G = 10^{19}$ $cm^{-2}s^{-1}$.

6.4 Experimental and Theoretical Details

Device Fabrication

The PL and EL devices for were fabricated on polyimide substrate (Kapton, Dupont, 1.5 mm thick). Ti (10 nm)/Au (100 nm)/Ti (10 nm) were fabricated as back gate electrodes using standard photolithography and thermal evaporation. As a gate insulator, 50 nm Al_2O_3 was deposited via ALD at 200°C. 50 nm thick Au source electrodes were patterned on ALD oxide adjacent to gate electrodes. WSe_2 (HQ Graphene) was mechanically exfoliated on 50 nm SiO_2/Si substrate. Bilayers were identified by optical contrast and AFM height profile. 2L WSe_2 flakes were picked up with poly(methyl methacrylate) (PMMA) and transferred onto the ALD oxide, followed by a post baking at 180°C for 5 minutes and dichloromethane treatment to remove PMMA. As a source contact, mechanically exfoliated few layers of graphene (Graphenium, NGS Naturgraphit) was dry-transferred with PMMA to mediate

between Au electrode pad and 2L WSe_2. Another post baking (180°C, 5 min) was performed to improve the adhesion between the interfaces of WSe_2/Al_2O_3 and graphene/WSe_2.

Electrical and Optical Characterization

Devices were charged from a Keithley 2410 Source Meter applied to the gate electrode while the Au source was grounded. The PL QY was measured using a home-built micro-PL instrument described in detail in the previous study.10 A 514.5 nm line was used as the excitation source. A uniaxial tensile strain was applied in the 2L WSe_2 by a two-point linear actuator.7 The nominal applied strain was calculated using the equation $\epsilon = t/R$, where 2t and R are the substrate thickness and curvature radius measured through the cross-section optical image. TR PL spectra were collected using a time-correlated single photon counting (TCSPC) module. A monochromated line of 514 nm from a supercontinuum laser was used as an excitation source. PL spatial images were measured with taken in a fluorescence microscopy setup using the green laser same as the excitation source for PL measurement, acquiring images by a CCD detector (Andor Luca).17 The samples were excited by a green laser, same as PL measurement, focused to a diffraction-limited spot. EL devices were pumped using a bipolar sine wave from an Agilent 33522A arbitrary waveform generator applied to the gate electrode while the source contact was grounded. All measurements reported in this paper are taken at room temperature in an ambient lab condition under nitrogen flow.

6.5 References

[1] Kin Fai Mak, Changgu Lee, James Hone, Jie Shan, and Tony F Heinz. Atomically thin MoS_2: a new direct-gap semiconductor. *Physical Review Letters*, 105(13):136805, 2010.

[2] Andrea Splendiani, Liang Sun, Yuanbo Zhang, Tianshu Li, Jonghwan Kim, Chi-Yung Chim, Giulia Galli, and Feng Wang. Emerging photoluminescence in monolayer MoS_2. *Nano Letters*, 10(4):1271–1275, 2010.

[3] Branimir Radisavljevic, Aleksandra Radenovic, Jacopo Brivio, Valentina Giacometti, and Andras Kis. Single-layer MoS_2 transistors. *Nature Nanotechnology*, 6(3):147–150, 2011.

[4] Qing Hua Wang, Kourosh Kalantar-Zadeh, Andras Kis, Jonathan N Coleman, and Michael S Strano. Electronics and optoelectronics of two-dimensional transition metal dichalcogenides. *Nature Nanotechnology*, 7(11):699–712, 2012.

[5] Oriol Lopez-Sanchez, Dominik Lembke, Metin Kayci, Aleksandra Radenovic, and Andras Kis. Ultrasensitive photodetectors based on monolayer MoS_2. *Nature Nanotechnology*, 8(7):497–501, 2013.

[6] Hyungjin Kim, Shiekh Zia Uddin, Naoki Higashitarumizu, Eran Rabani, and Ali Javey. Inhibited nonradiative decay at all exciton densities in monolayer semiconductors. *Science*, 373(6553):448–452, 2021.

[7] Sujay B Desai, Gyungseon Seol, Jeong Seuk Kang, Hui Fang, Corsin Battaglia, Rehan Kapadia, Joel W Ager, Jing Guo, and Ali Javey. Strain-induced indirect to direct bandgap transition in multilayer WSe_2. *Nano Letters*, 14(8):4592–4597, 2014.

[8] Geun Ho Ahn, Matin Amani, Haider Rasool, Der-Hsien Lien, James P Mastandrea, Joel W Ager III, Madan Dubey, Daryl C Chrzan, Andrew M Minor, and Ali Javey. Strain-engineered growth of two-dimensional materials. *Nature Communications*, 8(1):1–8, 2017.

[9] H Sahin, Sefaattin Tongay, S Horzum, W Fan, J Zhou, J Li, J Wu, and FM Peeters. Anomalous raman spectra and thickness-dependent electronic properties of WSe_2. *Physical Review B*, 87(16):165409, 2013.

[10] Der-Hsien Lien, Shiekh Zia Uddin, Matthew Yeh, Matin Amani, Hyungjin Kim, Joel W Ager, Eli Yablonovitch, and Ali Javey. Electrical suppression of all nonradiative recombination pathways in monolayer semiconductors. *Science*, 364(6439):468–471, 2019.

[11] Philipp Tonndorf, Robert Schmidt, Philipp Böttger, Xiao Zhang, Janna Börner, Andreas Liebig, Manfred Albrecht, Christian Kloc, Ovidiu Gordan, Dietrich RT Zahn, et al. Photoluminescence emission and raman response of monolayer MoS_2, $MoSe_2$, and WSe_2. *Optics Express*, 21(4):4908–4916, 2013.

[12] Shiekh Zia Uddin, Eran Rabani, and Ali Javey. Universal inverse scaling of exciton–exciton annihilation coefficient with exciton lifetime. *Nano Letters*, 21(1):424–429, 2020.

[13] VN Abakumov, Vladimir Idelevich Perel, and IN Yassievich. *Nonradiative Recombination in Semiconductors*. Elsevier, 1991.

[14] G Wang, Xavier Marie, L Bouet, M Vidal, Andrea Balocchi, Thierry Amand, D Lagarde, and B Urbaszek. Exciton dynamics in WSe_2 bilayers. *Applied Physics Letters*, 105(18):182105, 2014.

[15] Santosh Kumar, Artur Kaczmarczyk, and Brian D Gerardot. Strain-induced spatial and spectral isolation of quantum emitters in mono-and bilayer WSe_2. *Nano Letters*, 15(11):7567–7573, 2015.

[16] Marvin Kulig, Jonas Zipfel, Philipp Nagler, Sofia Blanter, Christian Schüller, Tobias Korn, Nicola Paradiso, Mikhail M Glazov, and Alexey Chernikov. Exciton diffusion and halo effects in monolayer semiconductors. *Physical Review Letters*, 120(20):207401, 2018.

[17] Darwin F Cordovilla Leon, Zidong Li, Sung Woon Jang, Che-Hsuan Cheng, and Parag B Deotare. Exciton transport in strained monolayer WSe_2. *Applied Physics Letters*, 113(25):252101, 2018.

[18] Shiekh Zia Uddin, Hyungjin Kim, Monica Lorenzon, Matthew Yeh, Der-Hsien Lien, Edward S Barnard, Han Htoon, Alexander Weber-Bargioni, and Ali Javey. Neutral exciton diffusion in monolayer MoS_2. *ACS Nano*, 14(10):13433–13440, 2020.

[19] Der-Hsien Lien, Matin Amani, Sujay B Desai, Geun Ho Ahn, Kevin Han, Jr-Hau He, Joel W Ager, Ming C Wu, and Ali Javey. Large-area and bright pulsed electroluminescence in monolayer semiconductors. *Nature Communications*, 9(1):1–7, 2018.

[20] Joy Cho, Matin Amani, Der-Hsien Lien, Hyungjin Kim, Matthew Yeh, Vivian Wang, Chaoliang Tan, and Ali Javey. Centimeter-scale and visible wavelength monolayer light-emitting devices. *Advanced Functional Materials*, 30(6):1907941, 2020.

[21] Freddie Withers, O Del Pozo-Zamudio, A Mishchenko, AP Rooney, Ali Gholinia, K Watanabe, T Taniguchi, Sarah J Haigh, AK Geim, AI Tartakovskii, et al. Light-emitting diodes by band-structure engineering in van der Waals heterostructures. *Nature Materials*, 14(3):301–306, 2015.

[22] Yajing Sun, Dong Wang, and Zhigang Shuai. Indirect-to-direct band gap crossover in few-layer transition metal dichalcogenides: a theoretical prediction. *The Journal of Physical Chemistry C*, 120(38):21866–21870, 2016.

Chapter 7

Excitonic and Free Carrier Recombination in Black Phosphorus

7.1 Introduction

Carrier recombination in a van der Waals (vdW) semiconductor is expected to transition from excitonic to free-carrier in nature as the number of layers is increased. However, in most vdW semiconductors this transition is obscured by the lack of direct bandgap in the bulk state. Black phosphorus (BP) in an exception which maintains a direct bandgap at all thicknesses. While exploring the excitonic to free-carrier transition in BP across a wide range of thicknesses, we find a dramatic and nonmonotonic change in photoluminescence (PL) quantum yield (QY) with thickness. In the excitonic regime the PL QY decreases with thickness and shows the highest PL QY of $\sim 20\%$ when it is completely excitonic at the monolayer limit. On the other hand, when recombination is dominated by free carriers PL QY increases with thickness, and we observe the surface recombination velocity in BP to be two orders of magnitude lower than in passivated silicon: the most electrically inactive surface known to the modern semiconductor industry. The rich excitonic photophysics of monolayer vdW semiconductors have already garnered enormous amount of research interest. Our results, supported by first-principle calculations, emphasize that even in thick vdW semiconductors where excitonic effects are absent, the recombination can be strikingly different from covalently bonded bulk semiconductors.

7.2 Excitonic to Free Carrier Transition

Carrier recombination in very thin layers of van der Waals (vdW) semiconductors such as monolayers of transition metal dichalcogenides (TMDC) are excitonic due to reduced Coulomb screening and have been extensively studied [1, 2]. However, exciton to free-carrier transition in these semiconductors is difficult to study as they become indirect with increasing thickness [3]. In contrast, the dominant optical transition in black phosphorus (BP) remains

direct at all thicknesses due to the strong interlayer electronic state coupling [4, 5]. Moreover, BP has shown tremendous technological potential in mid-infrared detection and emission [6–10]. BP therefore provides an ideal platform to explore how the recombination mechanism evolves from excitonic to free-carrier nature in a semiconductor. Here we explore the room temperature photoluminescence (PL) quantum yield (QY), a key metric of optoelectronic performance that directly dictates the maximum device efficiency, with BP thickness from monolayer to the bulk limit. We find that, at the same level of defect density, larger exciton binding energy leads to more light emission and monolayer BP has the highest PL QY. This corroborates our finding in monolayer TMDCs, where excitons can recombine completely radiatively [1, 11]. We also observe that surface recombination velocity in black phosphorus is two orders of magnitude lower than passivated silicon; the most electrically inactive surface known to modern semiconductor industry [12]. From density functional theory calculations, we see that oxidation of BP surface does not produce defect levels inside the bandgap, consistent with our finding that the nonradiative surface recombination is independent of the quality of the surface.

Few layers of BP were mechanically exfoliated in nitrogen environment from bulk crystals onto quartz substrates. Optical contrast was used to identify flakes with desired thickness and atomic force microscopy was then used to measure layer thickness [13, 14]. Photoluminescence spectra shown in Fig. 7.1A highlights a thickness-dependent optical bandgap ranging from 1.75 eV for a monolayer to 0.3 eV for bulk BP. Large change in optical bandgap is observed with thickness for up to six layers of BP(Fig. 7.1B), beyond which the bandgap redshifts very slowly with thickness (Fig. 7.1B inset). Similar dichotomy is also present in the exciton binding energy curated from the experimental and theoretical works in the literature (Fig. 7.1C). Up to five layers the exciton binding energy is larger than the average room temperature thermal energy, and the photogenerated carriers will be excitons. Above five layers the binding energy falls below the thermal energy, so photogenerated electron-hole pairs will thermalize and relax as free carriers.

We first explore the radiative excitonic recombination in black phosphorus. PL spectra of monolayer BP is shown in Fig. 7.2A with different generation rates. The PL peak positions for one to five layers of BP do not show any change with generation rate, indicating absence of photodegradation (Fig. 7.2B). Calibrated PL QY of BP measured in nitrogen environment decreases drastically from monolayer to five layers at a generation rate of 3.6×10^{26} $cm^{-3}s^{-1}$ (Fig. 7.2C). PL QY at different generation rates from monolayer to five layers are shown in Fig. 7.2D. We note that the monolayer has the largest PL QY in this range. Large exciton binding energy in monolayers leads to strongly bound, robust excitons in phosphorene which then recombine radiatively. We also do not observe any signature of exciton-exciton annihilation that plagues other excitonic materials [15], as illustrated in Fig. 7.2B. Both facts are reminiscent of monolayers of transition metal dichalcogenides (TMDC), where strongly bound excitons can recombine completely radiatively despite the presence of large native defect density [16]. PL QY drastically decreases at all pump when BP thickness is increased (Fig. 7.2D). Such decrease with thickness is also observed in semiconducting TMDC monolayers and generally has been attributed to the dominance

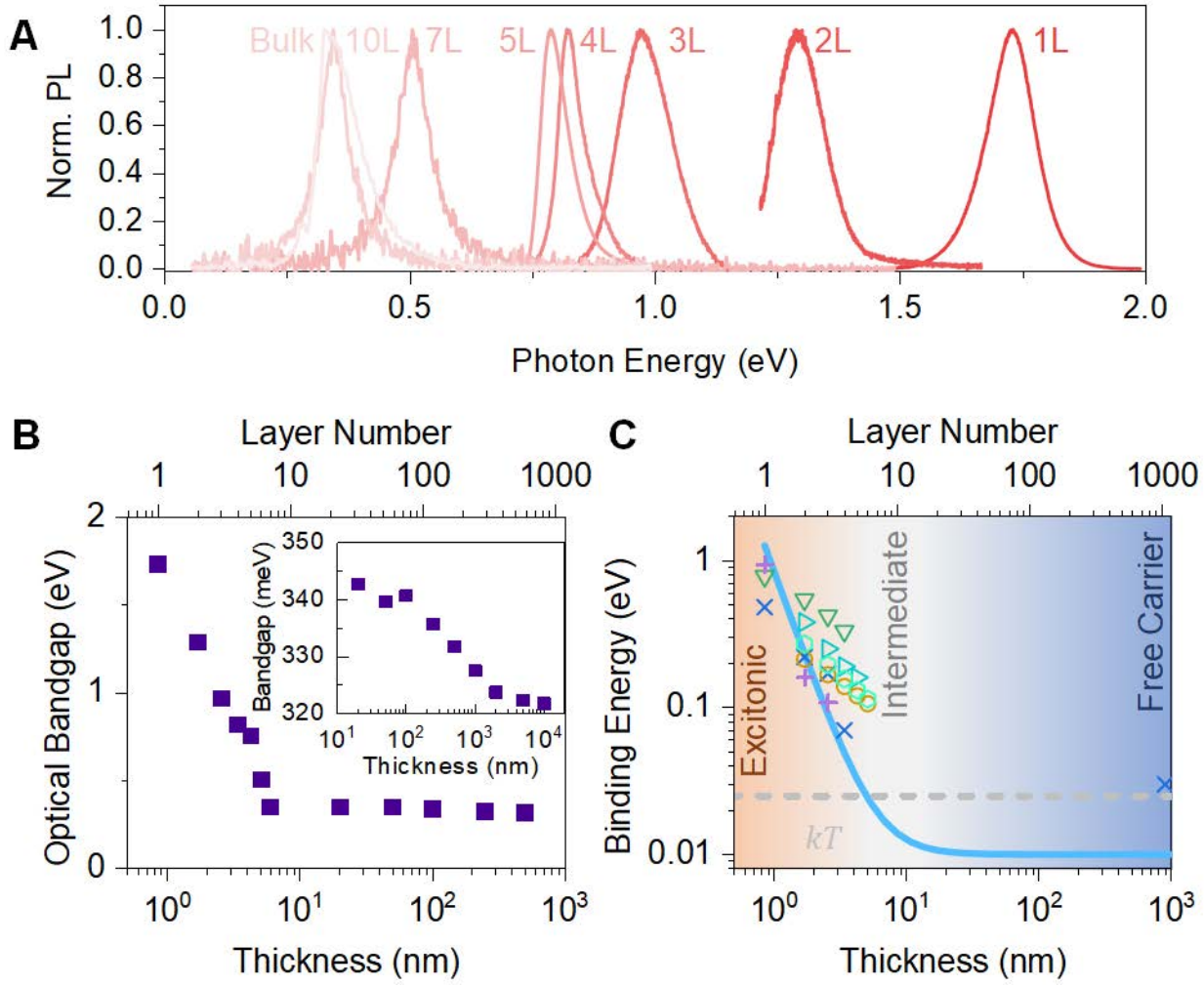

Figure 7.1: **Excitonic to free-carrier transition in black phosphorus.** (A) Normalized photoluminescence spectra of black phosphorus from monolayer to bulk. (B) Optical Bandgap at different thicknesses, PL peak redshifts slightly with increasing thickness at large thicknesses too. (C) Excitonic binding energy at different thicknesses shows excitonic to free-carrier transition. Thermal energy kT at room temperature is shown where k is the Boltzmann's constant and T is the temperature.

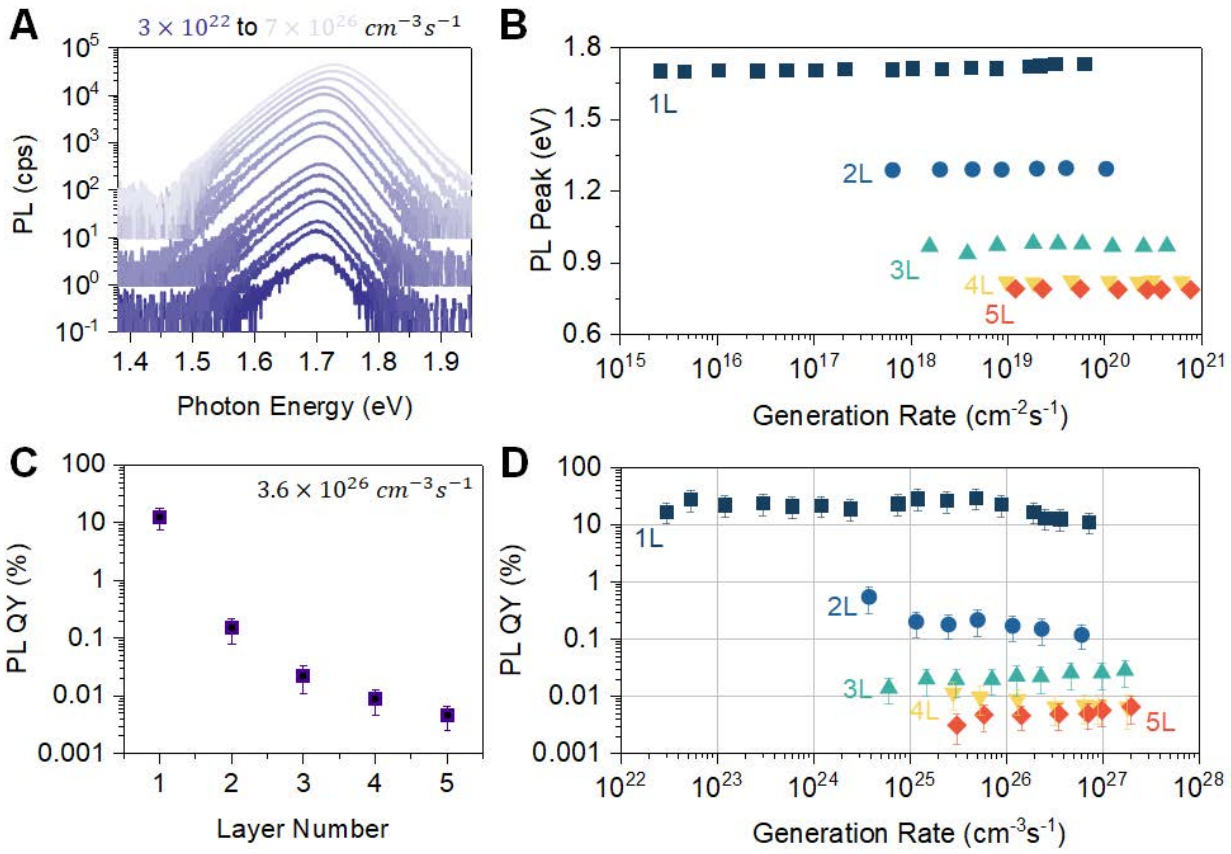

Figure 7.2: **Excitonic recombination in thin black phosphorus.** (A) PL spectra of monolayer black phosphorus at different generation rates. (B) PL peak position as a function of generation rate and thickness. (C) PL QY at a generation rate of $\sim 3.6 \times 10^{26}$ cm^{-3}s^{-1} for different thickness. (D) PL QY as a function of generation rate for different thicknesses.

of the indirect transition when thickness is increased beyond monolayer [17].However, BP remains a direct band gap material when thickness is increased, therefore the observed PL QY decrease with thickness arises from an increase in screening and a decrease in exciton binding energies [18]. As all of these layers are sourced from the same bulk material, our results show that for the same level of defect density, increasing binding energies can lead to increasing radiative recombination.

Before we investigate radiative free-carrier recombination in black phosphorus we first discuss carrier recombination in conventional free-carrier semiconductors. Nonequilibrium population of electron and holes can relax in a conventional semiconductor mainly through four different pathways: Shockley-Read-Hall (SRH) [19, 20], surface [21, 22], bimolecular radiative [23], and Auger recombination [24, 25]. The generation rate G in steady state is

balanced by the rates of all the recombination channels; for the case of a semiconductor with low background doping (that is, where $n = p$)

$$G = (A + 2S/d)(n^2 - n_i^2)/n + B(n^2 - n_i^2) + 2Cn(n^2 - n_i^2) \tag{7.1}$$

where n is the carrier concentration, n_i is the intrinsic carrier concentration, d is the semiconductor thickness, and A, B, C and S are the SRH, radiative and Auger recombination coefficients, and surface recombination velocity (SRV), respectively. Photoluminescence quantum yield (QY) is calculated according to a standard ABC recombination model as:

$$QY = \frac{B(n^2 - n_i^2)}{G} \tag{7.2}$$

Defect-mediated nonradiative SRH recombination, and surface recombination dominate at low generation rates and lowers the QY [26]. Nonradiative Auger recombination dominates and lowers QY at high generation rates [27]. The surface recombination rate depends inversely on the semiconductor thickness [28].

Contrary to the excitonic regime, PL QY of BP increases when thickness is increased in the free-carrier regime (Fig. 7.3A). We do not observe a common QY roll-off at all thicknesses at low generation rates, so the SRH process is negligible ($A \approx 0$) compared to the other processes perceived within our measurement range. We note a thickness dependent QY roll-off at low generation rates, which is indicative of surface recombination ($S \neq 0$). Similar QY roll-off is observed for all thicknesses at high generation rates, therefore the Auger process in thick BP is insensitive to the thickness ($C \neq 0$, $\partial C/\partial d \approx 0$). The radiative bimolecular recombination coefficient B of BP was experimentally measured employing the Shockley-van Roosbroeck relation (details in Supporting Information) and is comparable to other reports in the literature [29]. The surface recombination velocity and Auger coefficient are numerically fitted with the available data using the theoretical expression of QY (Fig. 7.3B, Fig. 7.5). Note that, the experimental data of all thicknesses form an overcomplete system for two thickness-independent parameters: C and S, and no other combination of values leads to a fit (more on Supporting Information).

Now we can summarize carrier recombination in BP (Fig. 7.3C). At the monolayer limit, excitonic recombination leads to bright luminescence. At the intermediate thickness, QY is low due to surface recombination. At large thicknesses, only Auger recombination limits the QY. Our model can be further modified to include excitons. As excitons are formed from and dissociates into electron and holes and no auger recombination in excitons has been observed in the generation rate dependent PL QY, the exciton and carrier concentration are related by

$$n_X/n^2 = K_X e^{E_b/kT} \tag{7.3}$$

where E_b is the exciton binding energy and K_X is the pre-exponential Arrhenius factor [30, 31]. The generation rate can be written as

$$G = (A + \frac{2S}{d})\frac{n^2 - n_i^2}{n} + B(n^2 - n_i^2) + B_X e^(E_b/kT)n^2 + 2Cn(n^2 - n_i^2) \tag{7.4}$$

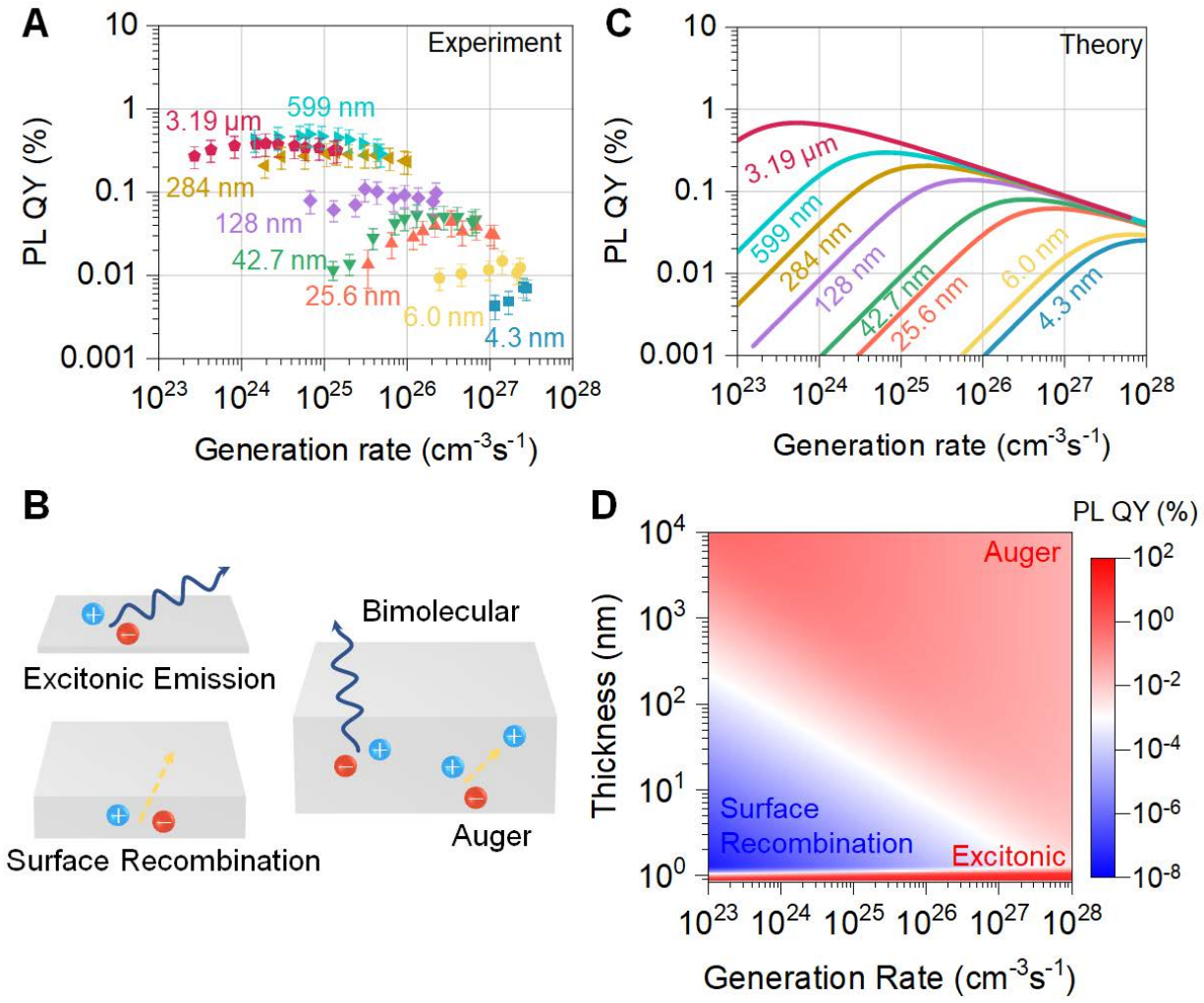

Figure 7.3: **Free-carrier recombination in black phosphorus.** (A) Experimental PL QY vs generation rate for different thickness black phosphorus. (B) Dominant recombination pathways active in black phosphorus with different thickness. (C, D) PL QY as a function of generation rate for select and all thicknesses from theoretical model.

The simulated QY vs. generation rate at all thicknesses are shown in Fig. 7.4D which captures the essential features observed in the experiment (details on Supporting Information) [32].

We observed a surface recombination velocity of $(7 \pm 2) \times 10^{-3}$ cm/s and an Auger coefficient of $(6 \pm 1) \times 10^{-43}$ cm^6/s for BP. The Auger coefficient is consistent with other reports on the literature [29], although no work has reported the surface recombination velocity. The observed SRV is two orders of magnitude lower than passivated silicon: the most electrically inactive surface known to modern semiconductor industry (Fig. 7.4A). Such extraordinarily low SRV indicates that BP surface is naturally passivated as far as nonradiative recombination is concerned and could originate from the BP oxide that forms on the BP surface or its van Der Waals nature. Generally, in covalently bonded semiconductors dangling bonds at the surface introduce electronic energy levels inside the normally forbidden gap, referred to as surface or interface states [33]. Such states greatly enhance nonradiative electron–hole recombination at the surface by acting as steppingstones for transitions between the conduction and valence bands. Since each recombination event at the surface requires precisely one electron and one hole, as well as an interface state, surface passivation in conventional semiconductors have two fundamental avenues: either reduce the number of surface states or reduce the concentration of one or other carrier at the surface [34–36].

In BP, the surface is self-terminated because of the layered structure. Thus, there are no dangling bonds and SRV is expected to be significantly lower. However, defects and native oxides exist. In layered materials bonds are self-satisfied inherent to the crystal structure. In this regard, there are no dangling bonds in an ideal layered material, although defects and native oxides exist. Thus, surface recombination is expected to be low in BP as compared to conventional three-dimensional semiconductors where the surface is entirely filled with dangling bonds. BP surface is easily oxidized in air due to the lone pair electrons [37]. Previous studies have reported that oxidation of BP occurs layer-by-layer. oxide (POx) is possibly formed layer-by-layer, enabling that an steep interface between POx and intact underneath BP layers. POx layer can be formed in a layer-by-layer fashion and is self-limiting, a fact that has been employed previously for controlled exfoliation [38]. Even with the localized POx formation at the interface, the dangling bonds are only at the POx edge, whose density will be much lower than that of covalently bonded semiconductors surface. Furthermore the energy level created by POx is not within bandgap. Such a process restricts the amount of dangling bonds on the interface. BP oxide is also shown to have minimal charge transfer with BP and is suitable for passivation or as an interface layer for further dielectric deposition [39–41]. Even if BP layers underneath the oxide is partially oxidized, ab initio density functional theory (DFT) calculations support the conclusion that the BP surface is naturally passivated and resistant to the formation of in-gap defect states from surface oxidation. Our calculations examine bridging and terminal oxygen defects on the surface of few-layer black phosphorous (Fig. 7.4B), which past work has shown to be the thermodynamically stable oxygen defects in phosphorene. The calculated densities of states show, consistent with other studies [42, 43], that these defects do not form electronic states within the bandgap and that a slight opening of the bandgap occurs with oxidation (Fig.

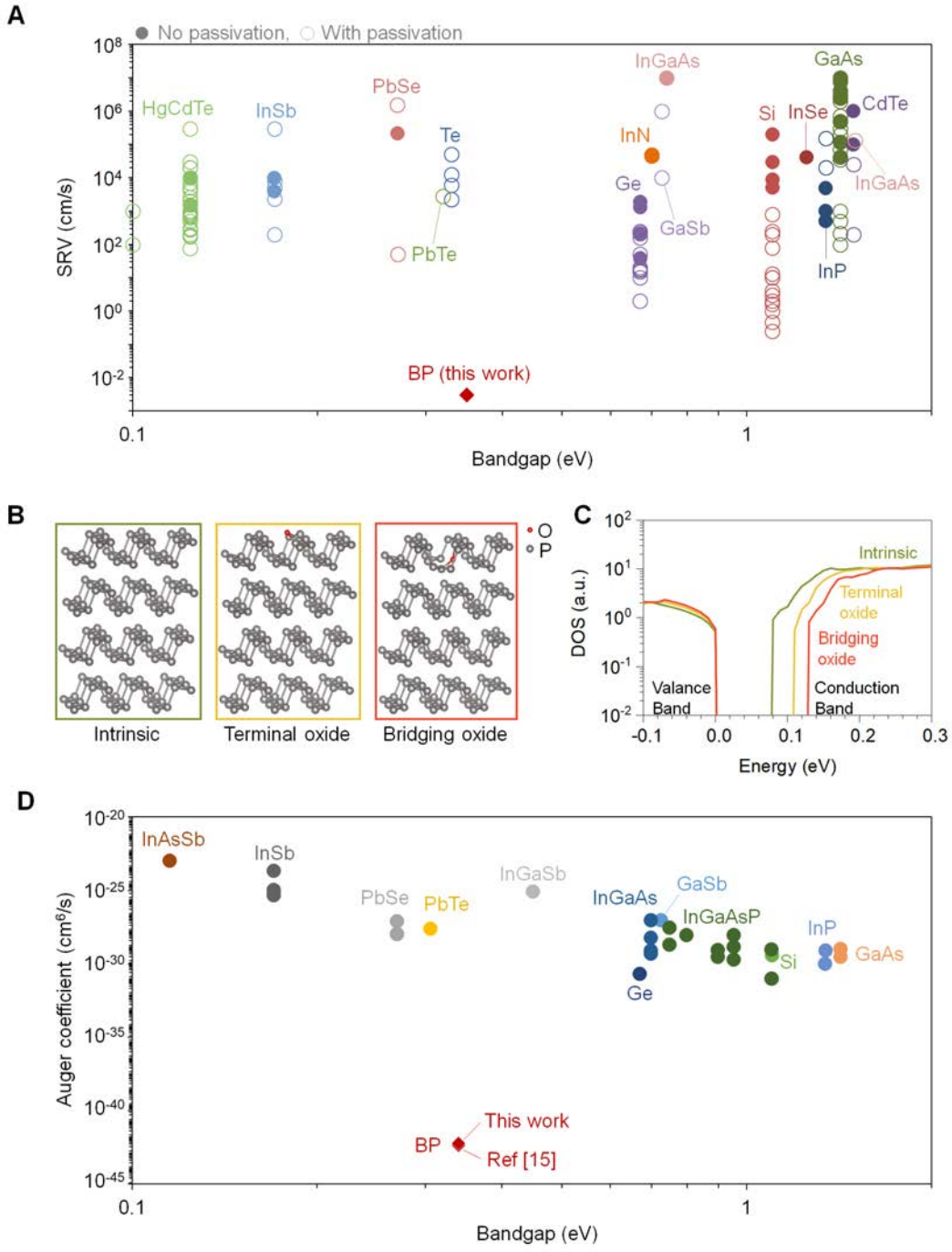

Figure 7.4: **Comparison of surface recombination velocity.** (A) Surface recombination velocities (SRV) of different semiconductors with bandgap. (B, C) Schematic crystal structure and DOS for four layer BP: intrinsic, and with a terminal oxide and bridging oxide atom. (D) Auger coefficient of different semiconductors with bandgap. Full lists of reported SRV and Auger coefficient are shown in Table 7.1.

7.4C). This increase of the bandgap is seen to decrease with the number of layers, and is lower than the thermal energy. This fact, and that the oxide layer is spatially much thinner than the electron Bohr radius, lead us to conclude that the primary reason of low SRV must be from the lack of surface electronic states.

Auger recombination is typically pronounced in small bandgap semiconductors, however in BP the observed Auger coefficient is also low compared to other semiconductors (Fig. 7.4D) [44, 45]. This originates from the relationship between the empirical ratio of the Auger lifetime (τ_a) to the radiative lifetime (τ_r) and the bandgap (E_g), which is given by:

$$\frac{\tau_a}{\tau_r} \propto \exp\left(\frac{m_e^*/m_h^*}{\left(1+\frac{m_e^*}{m_h^*}\right)\frac{E_g}{kT}}\right) \tag{7.5}$$

where m_e^* and m_h^* are the effective masses of electrons and holes, respectively [46]. As electrons and holes have similar effective masses in BP, the effective mass ratio is much higher than that of other small-bandgap semiconductors and results in suppressed Auger recombination [47]. The effect of low Auger recombination is readily observed experimentally comparing electroluminescence and photoluminescence of BP with that of other small-bandgap semiconductors in the high-injection regime [48]. Note that, the expression for Auger lifetime above is overly simplistic and further calculations that consider the total band structures are necessary [49].

7.3 Summary

In conclusion, we have explored radiative recombination in BP when the nature of recombination varies from excitonic to free carrier. We found that at similar defect density excitonic BP has the highest luminescence efficiency. We also observed lowest surface recombination velocity in BP due to oxidation not creating defect levels inside the bandgap. In the future, photonic patterning of BP surface to enhance light outcoupling and integration with photonic circuits becomes possible as surface quality does not determine optoelectronic quality. By expanding upon our approach, surface recombination in other van der Waals system could also be explored.

7.4 Experimental and Theoretical Details

Device Fabrication

BP (HQ graphene) was mechanically exfoliated by Scotch tape and polydimethylsiloxane (PDMS, Gel-pak). BP flakes were transferred on quartz or silicon substrate, then the number of layers was identified with optical contrast and atomic force microscopy. To minimize the formation of natural oxide, both mechanical exfoliations and thickness measurements were

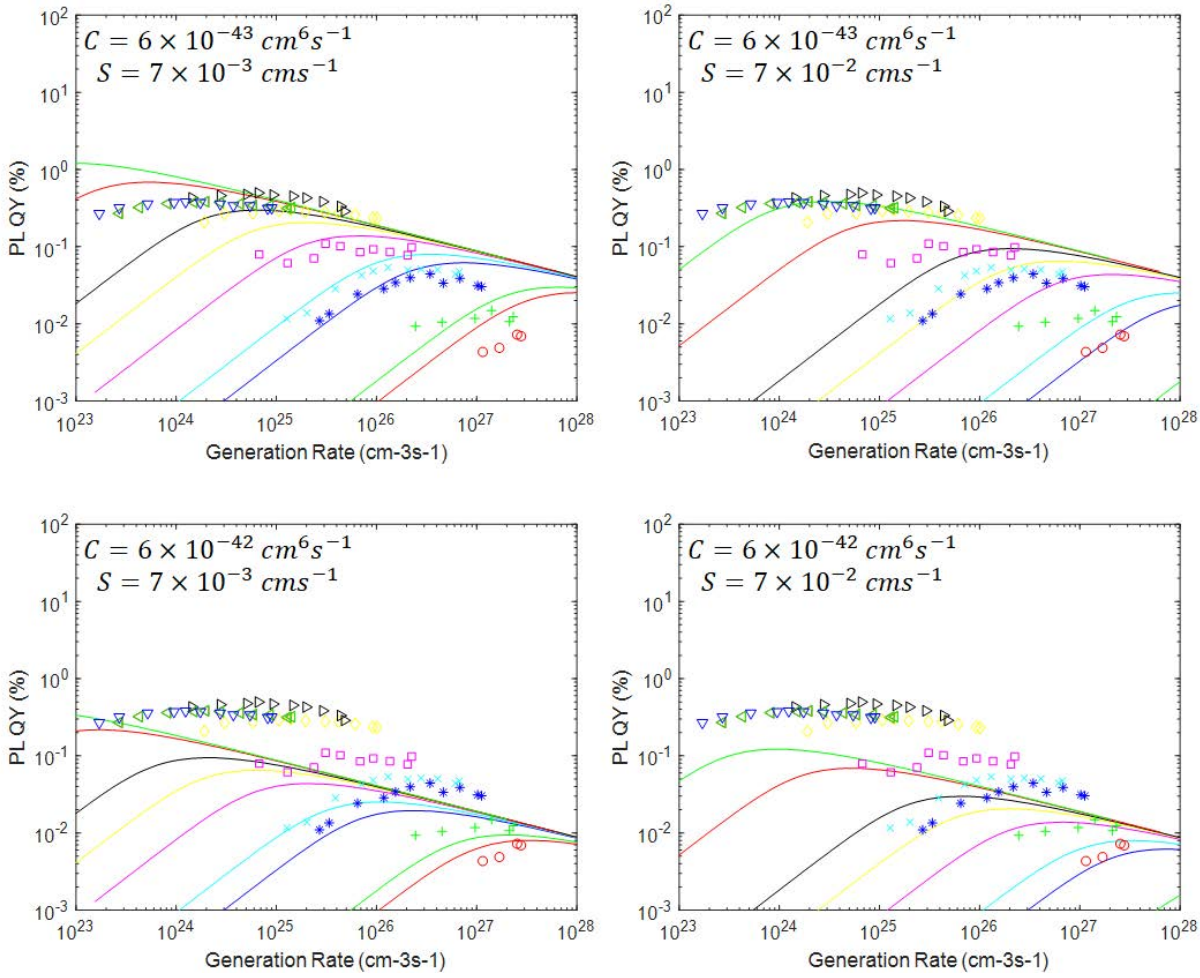

Figure 7.5: **Data and model results for different values of parameters.** Results of model fitting at different parameters.

performed in the nitrogen environment. After the flake isolation, the samples were sealed in nitrogen and transferred to the optical measurement setup.

Optical Characterization

The calibrated PL QY was measured using PL instruments described in detail in the previous study.1,6 Different spectrometers were used depending on the measurement wavelength range. For visible to near-infrared measurements, home-built μ-PL instrument was used with Si-CCD and InGaAs detectors. A 514.5 nm line was used as the excitation source. For longer wavelength, Fourier transform infrared (FT-IR) spectrometer (iS50, Thermo Fisher)

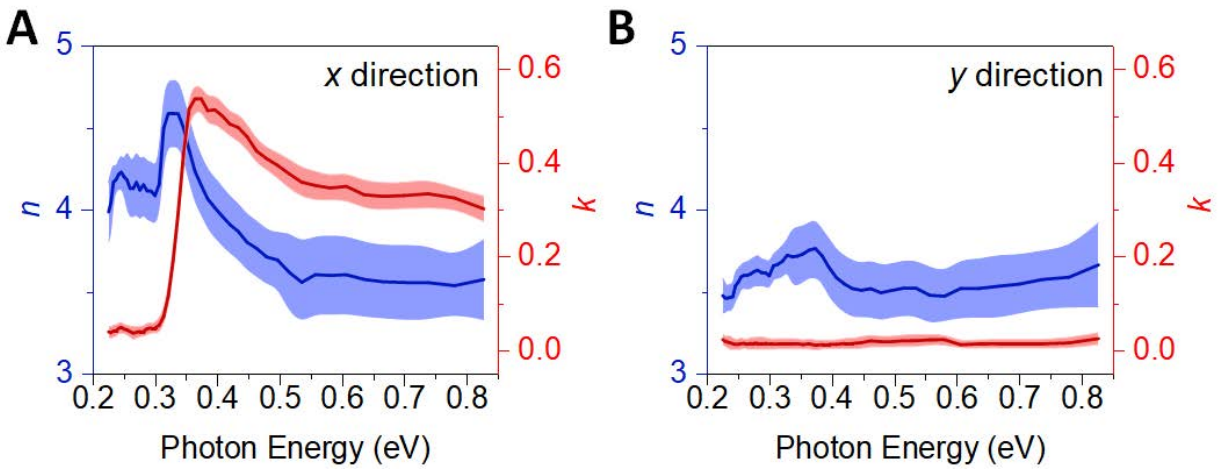

Figure 7.6: **Extracted complex refractive index of bP in the x- and y-direction.** BP refractive index.

was used with a liquid N2-cooled HgCdTe detector. A 638 nm laser was used as the excitation source. All measurements were taken at room temperature in an ambient lab condition under nitrogen flow.

DFT calculations

Density functional theory calculations were carried out using the Quantum Espresso package [50–52]. Optimized geometries for pristine black phosphorous as well as black phosphorous with bridging and terminal oxygen defects were obtained for monolayer through 4 layer systems consisting of a $3 \times 3 \times 1$ supercell with over 2 nm of vacuum in the out-of-plane direction to avoid interactions with periodic replicas. We used the PBE form of the general gradient approximation of the exchange-correlation energy with Grimme-D2 [53, 54] dispersion corrections which have been shown to sufficiently describe oxygen defects in black phosphorous systems. Using these geometries, band structures and densities of states were calculated at the same level of theory. Further details of the calculations and resulting band structures may be found in the Supporting Information.

Shockley-van Roosbroeck relation

The well-known Shockley-van Roosbroeck detailed balance equation (named after W. van Roosbroeck and W. Shockley) relates the spontaneous emission rate of a semiconductor to its absorption coefficient [55]. The photon emission rate $R(h\nu)$ from a body in equilibrium with background thermal radiation would be equal to the absorption rate $\alpha(h\nu)$ of thermal photons. Applying the principle of detailed balance we can describe the spectral distribution

of the rate of photon generation for the photon-radiative recombination of electrons and holes in a semiconductor as:

$$R(hv) = \frac{8\pi n^2 v^2}{c^2}\alpha(hv)\frac{1}{\exp\left(hv/k_B T\right) - 1} \tag{7.6}$$

Where h is the Planck's constant, v is the frequency of the light, n is the refractive index of the semiconductor, c is the speed of light, k_B is the Boltzmann's constant, and T is the lattice temperature. However, the radiative recombination should be proportional to the np product, Bnp, where B is called the radiative recombination co-efficient, as electrons must meet up with holes to radiate. The np product is given by the Law of Mass Action

$$np = N_C N_V \exp\left(-\frac{E_g}{k_B T}\right) \tag{7.7}$$

Where E_g is the bandgap. The radiative recombination co-efficient B can then be written as

$$B = \frac{1}{N_C N_V}\int \frac{8\pi n^2 v^2}{c^2}\alpha(hv)\exp\left(-\frac{hv - E_g}{k_B T}\right)dv \tag{7.8}$$

sometimes called the Shockley-van Roosbroeck relation which connects the absolute absorption spectrum to the absolute emission spectrum. This is a generalization of Einstein's connection between absorption and spontaneous emission. The radiative recombination co-efficient B for the black phosphorus in the direction of emission has been calculated using the extracted complex refractive index of bP shown in Fig. 7.6.

Recombination model with detailed balance between excitons and free carriers

The rate equations for electron-hole and exciton recombination can be written as

$$\frac{dn}{dt} = G - R(n) - G_X \tag{7.9}$$

$$\frac{dn_X}{dt} = G_X - n_X/\tau_X \tag{7.10}$$

Where G is the total generation rate, G_X is the exciton generation rate n_X and n are the densities of excitons and free carriers, τ_X is the exciton lifetime and $R(n)$ is the combined free-carrier recombination rate. Following the notations of the main manuscript for the case of a semiconductor with low background doping (that is, where $n = p$)

$$R(n) = (A + 2S/d)(n^2 - n_i^2)/n + B(n^2 - n_i^2) + 2Cn(n^2 - n_i^2) \tag{7.11}$$

where n is the carrier concentration, n_i is the intrinsic carrier concentration, d is the semiconductor thickness, and A, B, C and S are the SRH, radiative and Auger recombination coefficients, and surface recombination velocity (SRV), respectively. In steady state

$(dn/dt = 0, (dn_X)/dt = 0)$ we get

$$G = R(n) + G_X \tag{7.12}$$

$$G_X = \frac{n_X}{\tau_X} \tag{7.13}$$

Saha equation describes the densities of excitons (n_X) and free carriers (n) after statistical equilibration of their chemical potentials in the classical limit [56]. In equilibrium, the detailed balance for a classical three-dimensional gas of free electron-hole pairs and excitons is given as

$$\frac{n^2}{n_X} = AT^{3/2} \exp\left(-\frac{E_b}{kT}\right), A = \left(\frac{\mu k}{2\pi h^2}\right)^{3/2} \tag{7.14}$$

where $\mu = m_e^* m_h^*/(m_e^* + m_h^*)$ and m_e^* and m_h^* are the density-of-state effective masses of electrons and holes, respectively. Therefore, the exciton generation rate can be written as

$$G_X = 1/(\tau_X AT^(3/2)) \exp\left(\frac{E_b}{kT}\right) n^2 \tag{7.15}$$

$$= B_X \exp\left(\frac{E_b}{kT}\right) n^2 \tag{7.16}$$

And the total generation/recombination rate becomes

$$G = \left(A + \frac{2S}{d}\right) \frac{n^2 - n_i^2}{n} + B(n^2 - n_i^2) + 2Cn(n^2 - n_i^2) + B_X \exp\left(\frac{E_b}{kT}\right))n^2 \tag{7.17}$$

Since both free carriers and excitons emit, the quantum yield can be written as

$$QY = \frac{1}{G}\left(B(n^2 - n_i^2) + B_X \exp\left(\frac{E_b}{kT}\right) n^2\right) \tag{7.18}$$

This is the model used to capture the essential features of both excitonic and free carrier regimes and the intermediate transition in black phosphorus. A value of $B_X = 10^{-30}$ cm^{3}s^{-1} has been used to create Fig. 7.3B in the main manuscript. Note that such combined models have also been reported before [30] but has not been compared to full range of excitonic and free-carrier recombination in a single material system.

Material	E_g (eV)	C (cm^6/s)	S (cm/s)	P
BP	0.34	6×10^{-43} (This work) 4.1×10^{-43} [29] $< 10^{-32}$ [57]	7×10^{-3} (This work)	N N N
$Hg_{1-x}Cd_xTe$	0.100– 0.124		$(1.5 - 10) \times 10^3$ [58] $7.5 - 3 \times 10^5$ [58–70]	N Y
InAsSb	0.115	1.1×10^{-23} [71]		N
InSb	0.17	$(.049 - 2.2) \times 10^{-24}$ [71]	$(4.0 - 10) \times 10^3$ [72, 73] $0.002 - 3 \times 10^5$ [73]	N Y
PbSe	0.27	$(1.1 - 8) \times 10^{-28}$ [49, 75–77]	2.2×10^5 [74] $(0.5 - 1.5) \times 10^6$ [74, 78]	N Y
PbTe	0.306	2.5×10^{-28} [76]	2.8×10^3 [79]	N
Te	0.33		$(0.22 - 5) \times 10^4$ [80–82]	Y
InGaSb	0.45	8.2×10^{-26} [71]		
Ge	0.67	2×10^{-31} [83]	$3.8 - 1.9 \times 10^3$ [84–87] $2 - 2.5 \times 10^2$ [84, 87, 12, 88–93]	N Y
$In_{1-x}Ga_xAs$	$0.7 - 1.5$	$(.5 - 9.8) \times 10^{-29}$ [95–101]	10^7 [94] 1.3×10^5 [102]	N Y
InN	0.7		$(4.6 - 4.9) \times 10^4$ [103]	N
GaSb	0.726	9.3×10^{-28} [104, 105]	$10^4 - 10^6$ [106, 107]	Y
$In_{1-x}Ga_xAs_yP_{1-y}$	$0.75 - 1.1$	$10^{-32} - 3 \times 10^{-28}$ [55]		N
Si	1.1	$(0.1 - 4) \times 10^{-30}$ [83]	$(0.05 - 2) \times 10^5$ [85, 108–110] $0.25 - 8 \times 10^2$ [12, 108–120]	N Y
InSe	1.25		4.1×10^4 [121]	N
InP	1.344	$(1 - 8) \times 10^{-30}$ [55]	$500 - 10^6$ [122–124] $(0.2 - 1.5) \times 10^5$ [125]	N Y
GaAs	1.42	$(0.3 - 1) \times 10^{-29}$ [55]	$4.2 \times 10^4 - 10^7$ [123, 126–129] $10^2 - 3 \times 10^6$ [128, 130–133]	N Y
CdTe	1.49		$(0.1 - 1) \times 10^6$ [134] $(0.02 - 2.5) \times 10^4$ [134, 135]	N Y

Table 7.1: **SRV and Auger Coefficient in different materials.** Auger recombination coefficients C, and surface recombination velocities S in different materials. Rightmost column indicates whether the sample was passivated or not (Y = Yes, N = No).

7.5 References

[1] Der-Hsien Lien, Shiekh Zia Uddin, Matthew Yeh, Matin Amani, Hyungjin Kim, Joel W Ager, Eli Yablonovitch, and Ali Javey. Electrical suppression of all nonradiative recombination pathways in monolayer semiconductors. *Science*, 364(6439):468–471, 2019.

[2] Haining Wang, Changjian Zhang, and Farhan Rana. Ultrafast dynamics of defect-assisted electron–hole recombination in monolayer MoS_2. *Nano Letters*, 15(1):339–345, 2015.

[3] Andrea Splendiani, Liang Sun, Yuanbo Zhang, Tianshu Li, Jonghwan Kim, Chi-Yung Chim, Giulia Galli, and Feng Wang. Emerging photoluminescence in monolayer MoS_2. *Nano Letters*, 10(4):1271–1275, 2010.

[4] Jingsi Qiao, Xianghua Kong, Zhi-Xin Hu, Feng Yang, and Wei Ji. High-mobility transport anisotropy and linear dichroism in few-layer black phosphorus. *Nature Communications*, 5(1):1–7, 2014.

[5] Vy Tran, Ryan Soklaski, Yufeng Liang, and Li Yang. Layer-controlled band gap and anisotropic excitons in few-layer black phosphorus. *Physical Review B*, 89(23):235319, 2014.

[6] Hyungjin Kim, Shiekh Zia Uddin, Der-Hsien Lien, Matthew Yeh, Nima Sefidmooye Azar, Sivacarendran Balendhran, Taehun Kim, Niharika Gupta, Yoonsoo Rho, Costas P Grigoropoulos, et al. Actively variable-spectrum optoelectronics with black phosphorus. *Nature*, 596(7871):232–237, 2021.

[7] Michael Engel, Mathias Steiner, and Phaedon Avouris. Black phosphorus photodetector for multispectral, high-resolution imaging. *Nano Letters*, 14(11):6414–6417, 2014.

[8] Nathan Youngblood, Che Chen, Steven J Koester, and Mo Li. Waveguide-integrated black phosphorus photodetector with high responsivity and low dark current. *Nature Photonics*, 9(4):247–252, 2015.

[9] Xiaolong Chen, Xiaobo Lu, Bingchen Deng, Ofer Sinai, Yuchuan Shao, Cheng Li, Shaofan Yuan, Vy Tran, Kenji Watanabe, Takashi Taniguchi, et al. Widely tunable black phosphorus mid-infrared photodetector. *Nature Communications*, 8(1):1–7, 2017.

[10] Hongtao Yuan, Xiaoge Liu, Farzaneh Afshinmanesh, Wei Li, Gang Xu, Jie Sun, Biao Lian, Alberto G Curto, Guojun Ye, Yasuyuki Hikita, et al. Polarization-sensitive broadband photodetector using a black phosphorus vertical p–n junction. *Nature Nanotechnology*, 10(8):707–713, 2015.

[11] Hyungjin Kim, Shiekh Zia Uddin, Naoki Higashitarumizu, Eran Rabani, and Ali Javey. Inhibited nonradiative decay at all exciton densities in monolayer semiconductors. *Science*, 373(6553):448–452, 2021.

[12] E Yablonovitch, DL Allara, CC Chang, T Gmitter, and TB Bright. Unusually low surface-recombination velocity on silicon and germanium surfaces. *Physical Review Letters*, 57(2):249, 1986.

[13] Hongye Chen, Wenwen Fei, Jianxin Zhou, Chunyang Miao, and Wanlin Guo. Layer identification of colorful black phosphorus. *Small*, 13(5):1602336, 2017.

[14] Jiong Yang, Renjing Xu, Jiajie Pei, Ye Win Myint, Fan Wang, Zhu Wang, Shuang Zhang, Zongfu Yu, and Yuerui Lu. Optical tuning of exciton and trion emissions in monolayer phosphorene. *Light: Science & Applications*, 4(7):e312–e312, 2015.

[15] Shiekh Zia Uddin, Eran Rabani, and Ali Javey. Universal inverse scaling of exciton–exciton annihilation coefficient with exciton lifetime. *Nano Letters*, 21(1):424–429, 2020.

[16] Bumho Kim, Yue Luo, Daniel Rhodes, Yusong Bai, Jue Wang, Song Liu, Abraham Jordan, Baili Huang, Zhaochen Li, Takashi Taniguchi, et al. Free trions with near-unity quantum yield in monolayer $MoSe_2$. *ACS Nano*, 2021.

[17] Kin Fai Mak, Changgu Lee, James Hone, Jie Shan, and Tony F Heinz. Atomically thin MoS_2: a new direct-gap semiconductor. *Physical Review Letters*, 105(13):136805, 2010.

[18] Diana Y Qiu, Felipe H da Jornada, and Steven G Louie. Environmental screening effects in 2D materials: Renormalization of the bandgap, electronic structure, and optical spectra of few-layer black phosphorus. *Nano Letters*, 17(8):4706–4712, 2017.

[19] Re N Hall. Electron-hole recombination in germanium. *Physical Review*, 87(2):387, 1952.

[20] WTRW Shockley and WT Read Jr. Statistics of the recombinations of holes and electrons. *Physical Review*, 87(5):835, 1952.

[21] DJ Fitzgerald and AS Grove. Surface recombination in semiconductors. *Surface Science*, 9(2):347–369, 1968.

[22] Keith R McIntosh and Lachlan E Black. On effective surface recombination parameters. *Journal of Applied Physics*, 116(1):014503, 2014.

[23] William P Dumke. Spontaneous radiative recombination in semiconductors. *Physical Review*, 105(1):139, 1957.

[24] AR Beattie and PT Landsberg. Auger effect in semiconductors. *Proceedings of the Royal Society of London. Series A. Mathematical and Physical Sciences*, 249(1256):16–29, 1959.

[25] A Haug. Auger recombination in direct-gap semiconductors: band-structure effects. *Journal of Physics C: Solid State Physics*, 16(21):4159, 1983.

[26] G Bemski. Recombination in semiconductors. *Proceedings of the IRE*, 46(6):990–1004, 1958.

[27] VN Abakumov, Vladimir Idelevich Perel, and IN Yassievich. *Nonradiative Recombination in Semiconductors*. Elsevier, 1991.

[28] DE Aspnes. Recombination at semiconductor surfaces and interfaces. *Surface Science*, 132(1-3):406–421, 1983.

[29] Shaofeng Ge, Chaokai Li, Zhiming Zhang, Chenglong Zhang, Yudao Zhang, Jun Qiu, Qinsheng Wang, Junku Liu, Shuang Jia, Ji Feng, et al. Dynamical evolution of anisotropic response in black phosphorus under ultrafast photoexcitation. *Nano Letters*, 15(7):4650–4656, 2015.

[30] Thomas Kirchartz, Julian Mattheis, and Uwe Rau. Detailed balance theory of excitonic and bulk heterojunction solar cells. *Physical Review B*, 78(23):235320, 2008.

[31] R Cingolani, L Calcagnile, G Coli, R Rinaldi, M Lomoscolo, M DiDio, A Franciosi, L Vanzetti, GC LaRocca, and D Campi. Radiative recombination processes in wide-band-gap ii–vi quantum wells: the interplay between excitons and free carriers. *JOSA B*, 13(6):1268–1277, 1996.

[32] Samuel D Stranks, Victor M Burlakov, Tomas Leijtens, James M Ball, Alain Goriely, and Henry J Snaith. Recombination kinetics in organic-inorganic perovskites: excitons, free charge, and subgap states. *Physical Review Applied*, 2(3):034007, 2014.

[33] John Bardeen. Surface states and rectification at a metal semi-conductor contact. *Physical Review*, 71(10):717, 1947.

[34] Armin G Aberle. Surface passivation of crystalline silicon solar cells: a review. *Progress in Photovoltaics: Research and Applications*, 8(5):473–487, 2000.

[35] Qi Jiang, Yang Zhao, Xingwang Zhang, Xiaolei Yang, Yong Chen, Zema Chu, Qiufeng Ye, Xingxing Li, Zhigang Yin, and Jingbi You. Surface passivation of perovskite film for efficient solar cells. *Nature Photonics*, 13(7):460–466, 2019.

[36] Xiangyang Huang, Eric Lindgren, and James R Chelikowsky. Surface passivation method for semiconductor nanostructures. *Physical Review B*, 71(16):165328, 2005.

[37] Joshua D Wood, Spencer A Wells, Deep Jariwala, Kan-Sheng Chen, EunKyung Cho, Vinod K Sangwan, Xiaolong Liu, Lincoln J Lauhon, Tobin J Marks, and Mark C Hersam. Effective passivation of exfoliated black phosphorus transistors against ambient degradation. *Nano Letters*, 14(12):6964–6970, 2014.

[38] Alexandre Favron, Etienne Gaufres, F Fossard, PL Lévesque, AL Phaneuf-L'Heureux, N Tang, A Loiseau, R Leonelli, S Francoeur, and R Martel. Exfoliating pristine black phosphorus down to the monolayer: photo-oxidation and electronic confinement effects. *arXiv preprint arXiv:1408.0345*, 2014.

[39] Mark Thomas Edmonds, Anton Tadich, Alexandra Carvalho, Angelo Ziletti, Kane Michael O'Donnell, Steven P Koenig, David F Coker, Barbaros Ozyilmaz, AH Castro Neto, and MS Fuhrer. Creating a stable oxide at the surface of black phosphorus. *ACS applied materials & interfaces*, 7(27):14557–14562, 2015.

[40] Qionghua Zhou, Qian Chen, Yilong Tong, and Jinlan Wang. Light-induced ambient degradation of few-layer black phosphorus: mechanism and protection. *Angewandte Chemie International Edition*, 55(38):11437–11441, 2016.

[41] Wei Luo, Dmitry Y Zemlyanov, Cory A Milligan, Yuchen Du, Lingming Yang, Yanqing Wu, and D Ye Peide. Surface chemistry of black phosphorus under a controlled oxidative environment. *Nanotechnology*, 27(43):434002, 2016.

[42] Angelo Ziletti, A Carvalho, David K Campbell, David F Coker, and AH Castro Neto. Oxygen defects in phosphorene. *Physical Review Letters*, 114(4):046801, 2015.

[43] A Ziletti, A Carvalho, PE Trevisanutto, DK Campbell, DF Coker, and AH Castro Neto. Phosphorene oxides: Bandgap engineering of phosphorene by oxidation. *Physical Review B*, 91(8):085407, 2015.

[44] Y Aytac, BV Olson, JK Kim, EA Shaner, SD Hawkins, JF Klem, J Olesberg, ME Flatté, and TF Boggess. Bandgap and temperature dependence of auger recombi-

nation in inas/inassb type-ii superlattices. *Journal of Applied Physics*, 119(21):215705, 2016.

[45] Kris T Delaney, Patrick Rinke, and Chris G Van de Walle. Auger recombination rates in nitrides from first principles. *Applied Physics Letters*, 94(19):191109, 2009.

[46] Monique Combescot and Roland Combescot. Auger recombination in direct-gap semiconductors: effect of anisotropy and warping. *Physical Review B*, 37(15):8781, 1988.

[47] SR Kurtz, RM Biefeld, and LR Dawson. Modification of valence-band symmetry and auger threshold energy in biaxially compressed inas 1- x sb x. *Physical Review B*, 51(11):7310, 1995.

[48] Chen Chen, Feng Chen, Xiaolong Chen, Bingchen Deng, Brendan Eng, Daehwan Jung, Qiushi Guo, Shaofan Yuan, Kenji Watanabe, Takashi Taniguchi, et al. Bright mid-infrared photoluminescence from thin-film black phosphorus. *Nano Letters*, 19(3):1488–1493, 2019.

[49] Xie Zhang, Jimmy-Xuan Shen, and Chris G Van de Walle. Anomalous auger recombination in PbSe. *Physical Review Letters*, 125(3):037401, 2020.

[50] Paolo Giannozzi, Stefano Baroni, Nicola Bonini, Matteo Calandra, Roberto Car, Carlo Cavazzoni, Davide Ceresoli, Guido L Chiarotti, Matteo Cococcioni, Ismaila Dabo, et al. Quantum espresso: a modular and open-source software project for quantum simulations of materials. *Journal of physics: Condensed matter*, 21(39):395502, 2009.

[51] Paolo Giannozzi, Oliviero Andreussi, Thomas Brumme, Oana Bunau, M Buongiorno Nardelli, Matteo Calandra, Roberto Car, Carlo Cavazzoni, Davide Ceresoli, Matteo Cococcioni, et al. Advanced capabilities for materials modelling with quantum espresso. *Journal of physics: Condensed matter*, 29(46):465901, 2017.

[52] Paolo Giannozzi, Oscar Baseggio, Pietro Bonfà, Davide Brunato, Roberto Car, Ivan Carnimeo, Carlo Cavazzoni, Stefano De Gironcoli, Pietro Delugas, Fabrizio Ferrari Ruffino, et al. Quantum espresso toward the exascale. *The Journal of Chemical Physics*, 152(15):154105, 2020.

[53] John P Perdew, Kieron Burke, and Matthias Ernzerhof. Generalized gradient approximation made simple. *Physical Review Letters*, 77(18):3865, 1996.

[54] Stefan Grimme, Andreas Hansen, Jan Gerit Brandenburg, and Christoph Bannwarth. Dispersion-corrected mean-field electronic structure methods. *Chemical reviews*, 116(9):5105–5154, 2016.

[55] Rupak Bhattacharya, Bipul Pal, and Bhavtosh Bansal. On conversion of luminescence into absorption and the van roosbroeck-shockley relation. *Applied Physics Letters*, 100(22):222103, 2012.

[56] T Ichii, Y Hazama, N Naka, and K Tanaka. Study of detailed balance between excitons and free carriers in diamond using broadband terahertz time-domain spectroscopy. *Applied Physics Letters*, 116(23):231102, 2020.

[57] Prashant Bhaskar, Alexander W Achtstein, Martien JW Vermeulen, and Laurens DA Siebbeles. Radiatively dominated charge carrier recombination in black phosphorus. *The Journal of Physical Chemistry C*, 120(25):13836–13842, 2016.

[58] J Zhang, GKO Tsen, Jarek Antoszewski, JM Dell, Lorenzo Faraone, and WD Hu. A study of sidewall effects in hgcdte photoconductors passivated with mbe-grown cdte. *Journal of electronic materials*, 39(7):1019–1022, 2010.

[59] V Kumar, R Pal, PK Chaudhury, BL Sharma, and V Gopal. A CdTe passivation process for long wavelength infrared HgCdTe photo-detectors. *Journal of electronic materials*, 34(9):1225–1229, 2005.

[60] Eustace L Dereniak and Robert T Sampson. Infrared detectors, focal plane arrays, and imaging sensors. *SPIE*, 1107, 1989.

[61] E Finkman and SE Schacham. Surface recombination velocity of anodic sulfide and ZnS coated p-HgCdTe. *Journal of Vacuum Science & Technology A: Vacuum, Surfaces, and Films*, 7(2):464–468, 1989.

[62] MA Kinch, MJ Brau, and A Simmons. Recombination mechanisms in 8–14-μ HgCdTe. *Journal of Applied Physics*, 44(4):1649–1663, 1973.

[63] Jong-Hwa Choi Chul Lee. Characterization of the surface recombination velocity of HgCdTe using a gate-controlled diode. *Japanese Journal of Applied Physics*, 39(2B):L152, 2000.

[64] Ronald D Graft, Frederick F Carlson, John H Dinan, Phillip R Boyd, and Randolph E Longshore. Surface and interface recombination in thin film HgCdTe photoconductors. *Journal of Vacuum Science & Technology A: Vacuum, Surfaces, and Films*, 1(3):1696–1699, 1983.

[65] Robert Sporken, R Kiran, T Casselman, F Aqariden, S Velicu, Yong Chang, and Sivalingam Sivananthan. The effect of wet etching on surface properties of HgCdTe. *Journal of electronic materials*, 38(8):1781–1789, 2009.

[66] VC Lopes, WH Wright, and AJ Syllaios. Characterization of (hg, cd) te by the photoconductive decay technique. *Journal of Vacuum Science & Technology A: Vacuum, Surfaces, and Films*, 8(2):1167–1170, 1990.

[67] G Sarusi, A Zemel, D Eger, S Ron, and Yoram Shapira. Investigation of the bulk and surface electronic properties of HgCdTe epitaxial layers using photoelectromagnetic, hall, and photoconductivity measurements. *Journal of Applied Physics*, 72(6):2312–2321, 1992.

[68] JP Rosbeck, RE Starr, SL Price, and KJ Riley. Background and temperature dependent current-voltage characteristics of HgCdTe photodiodes. *Journal of Applied Physics*, 53(9):6430–6440, 1982.

[69] MB Reine, KR Maschhoff, SP Tobin, PW Norton, JA Mroczkowski, and EE Krueger. The impact of characterization techniques on HgCdTe infrared detector technology. *Semiconductor Science and Technology*, 8(6S):788, 1993.

[70] A Rogalski. HgCdTe photodetectors. In *Mid-infrared Optoelectronics*, pages 235–335. Elsevier, 2020.

[71] Pallab Bhattacharya. *Semiconductor optoelectronic devices*. Prentice-Hall, Inc., 1997.

[72] SW Kurnick and RN Zitter. Photoconductive and photoelectromagnetic effects in InSb. *Journal of Applied Physics*, 27(3):278–285, 1956.

[73] W Schneider, H Groh, and K Hübner. Recombination coefficients in extrinsicn-InSb. *Zeitschrift für Physik B Condensed Matter*, 25(1):29–35, 1976.

[74] DG Coates, WD Lawson, and AC Prior. Single crystal photoconductive detectors in lead selenide. *Journal of The Electrochemical Society*, 108(11):1038, 1961.

[75] The intrinsic carrier concentration in $Pb_{1-x}Sn_xTe$, $Pb_{1-x}Sn_xSe$, and $PbS_{1-x}Se_x$, author=Rogalski, A and Jóźwikowski, K, journal=Physica Status Solidi (a), volume=111, number=2, pages=559–565, year=1989, publisher=Wiley Online Library.

[76] Robert Klann, Thomas Höfer, Rainer Buhleier, Thomas Elsaesser, and Jens W Tomm. Fast recombination processes in lead chalcogenide semiconductors studied via transient optical nonlinearities. *Journal of Applied Physics*, 77(1):277–286, 1995.

[77] PC Findlay, CR Pidgeon, R Kotitschke, A Hollingworth, BN Murdin, CJGM Langerak, AFG van Der Meer, CM Ciesla, Josef Oswald, Alois Homer, et al. Auger recombination dynamics of lead salts under picosecond free-electron-laser excitation. *Physical Review B*, 58(19):12908, 1998.

[78] P Collot, F Nguyen-Van-Dau, and V Mathet. Monolithic integration of PbSe ir photodiodes on si substrates for near ambient temperature operation. *Semiconductor science and technology*, 9(5):1133, 1994.

[79] A Pinto Neto, H Vargas, NF Leite, and LCM Miranda. Photoacoustic investigation of semiconductors: influence of carrier diffusion and recombination in pbte and si. *Physical Review B*, 40(6):3924, 1989.

[80] NG Shyamprasad, CH Champness, and I Shih. Thickness dependence of photoconductivity in tellurium. *Infrared Physics*, 21(1):45–52, 1981.

[81] Vasudevan Iyer, Mauricio Segovia, Yixiu Wang, Wenzhuo Wu, Peide Ye, and Xianfan Xu. Infrared ultrafast spectroscopy of solution-grown thin film tellurium. *Physical Review B*, 100(7):075436, 2019.

[82] James N Heyman, Ayaskanta Sahu, Nelson E Coates, Brittany Ehmann, and Jeffery J Urban. Carrier lifetime enhancement in a tellurium nanowire/PEDOT:PSS nanocomposite by sulfur passivation. *MRS Online Proceedings Library (OPL)*, 1742, 2015.

[83] NG Nilsson. Band-to-band auger recombination in silicon and germanium. *Physica Scripta*, 8(4):165, 1973.

[84] Bibhu P Swain, Hidetaka Takato, and Isao Sakata. Wet chemical surface passivation of germanium wafers by quinhydrone–methanol treatment for minority carrier lifetime measurements. *Applied Physics Express*, 2(10):105501, 2009.

[85] N Derhacobian, P Fine, JT Walton, YK Wong, CS Rossington, and PN Luke. Determination of surface recombination velocity and bulk lifetime in detector grade silicon and germanium crystals. *IEEE transactions on nuclear science*, 41(4):1026–1030, 1994.

[86] P Balk and EL Peterson. Properties of HF-H_2O_2 treated germanium surfaces. *Journal of The Electrochemical Society*, 110(12):1245, 1963.

[87] NJ Harrick. Use of infrared absorption to determine carrier distribution in germanium and surface recombination velocity. *Physical Review*, 101(1):491, 1956.

[88] JP McKelvey and RL Longini. Volume and surface recombination rates for injected carriers in germanium. *Journal of Applied Physics*, 25(5):634–641, 1954.

[89] TM Buck and WH Brattain. Investigations of surface recombination velocities on germanium by the photoelectromagnetic method. *Journal of The Electrochemical Society*, 102(11):636, 1955.

[90] Walter H Brattain and John Bardeen. Surface properties of germanium. *The Bell System Technical Journal*, 32(1):1–41, 1953.

[91] NE Posthuma, G Flamand, W Geens, and J Poortmans. Surface passivation for germanium photovoltaic cells. *Solar energy materials and solar cells*, 88(1):37–45, 2005.

[92] RH Kingston. Review of germanium surface phenomena. *Journal of Applied Physics*, 27(2):101–114, 1956.

[93] SG Ellis. Surface studies on single-crystal germanium. *Journal of Applied Physics*, 28(11):1262–1269, 1957.

[94] RK Jain. Suitability of InP window layers for InGaAs solar cells. In *3rd World Conference onPhotovoltaic Energy Conversion, 2003. Proceedings of*, volume 1, pages 75–78. IEEE, 2003.

[95] ALBRECHT Mozer, K Romanek, OLAF Hildebrand, WOLFGANG Schmid, and M Pilkuhn. Losses in GaInAs (P)/InP and GaAlSb (As)/GaSb lasers-the influence of the split-off valence band. *IEEE Journal of Quantum Electronics*, 19(6):913–916, 1983.

[96] B Sermage, HJ Eichler, JP Heritage, RJ Nelson, and NK Dutta. Photoexcited carrier lifetime and auger recombination in 1.3-μm InGaAsP. *Applied Physics Letters*, 42(3):259–261, 1983.

[97] C Henry, B Levine, R Logan, and C Bethea. Minority carrier lifetime and luminescence efficiency of 1.3 μm InGaAsP-InP double heterostructure layers. *IEEE Journal of Quantum Electronics*, 19(6):905–912, 1983.

[98] Robert Olshansky, C Su, J Manning, and William Powazinik. Measurement of radiative and nonradiative recombination rates in InGaAsP and AlGaAs light sources. *IEEE journal of quantum electronics*, 20(8):838–854, 1984.

[99] CB Su, J Schlafer, J Manning, and R Olshansky. Measurement of radiative recombination coefficient and carrier leakage in 1.3 μm InGaAsP lasers with lightly doped active layers. *Electronics Letters*, 18(25):1108–1110, 1982.

[100] T Uji, K Iwamoto, and R Lang. Dominance of auger recombination in InGaAsP light emitting diode current-power characteristics. *IEEE Transactions on Electron Devices*, 30(4):316–320, 1983.

[101] E Wintner and EP Ippen. Nonlinear carrier dynamics in $Ga_xIn_{1-x}As_yP_{1-y}$ compounds. *Applied Physics Letters*, 44(10):999–1001, 1984.

[102] Guy Brammertz, Marc Heyns, Marc Meuris, Matty Caymax, Dehuai Jiang, Yves Mols, Stefan Degroote, Maarten Leys, and Gustaaf Borghs. Surface recombination velocity in GaAs and $In_{0.15}Ga_{0.85}As$ thin films. *Applied Physics Letters*, 90(13):134102, 2007.

[103] Ramon Cuscó, Jordi Ibáñez, Esther Alarcón-Lladó, Luis Artús, Tomohiro Yamaguchi, and Yasushi Nanishi. Photoexcited carriers and surface recombination velocity in InN epilayers: A raman scattering study. *Physical Review B*, 80(15):155204, 2009.

[104] S Marchetti, M Martinelli, and R Simili. The auger recombination coefficient in InAs and GaSb derived from the infrared dynamical plasma reflectivity. *Journal of Physics: Condensed Matter*, 14(13):3653, 2002.

[105] YP Varshni. Band-to-band radiative recombination in groups IV, VI, and III-V semiconductors (I). *Physica Status Solidi (b)*, 19(2):459–514, 1967.

[106] AW Bett and OV Sulima. GaSb photovoltaic cells for applications in tpv generators. *Semiconductor science and technology*, 18(5):S184, 2003.

[107] OV Sulima and AW Bett. Fabrication and simulation of GaSb thermophotovoltaic cells. *Solar energy materials and solar cells*, 66(1-4):533–540, 2001.

[108] Andrés Cuevas, Paul A Basore, Gaëlle Giroult-Matlakowski, and Christiane Dubois. Surface recombination velocity of highly doped n-type silicon. *Journal of Applied Physics*, 80(6):3370–3375, 1996.

[109] D Baek, S Rouvimov, B Kim, T-C Jo, and DK Schroder. Surface recombination velocity of silicon wafers by photoluminescence. *Applied Physics Letters*, 86(11):112110, 2005.

[110] O Palais and A Arcari. Contactless measurement of bulk lifetime and surface recombination velocity in silicon wafers. *Journal of Applied Physics*, 93(8):4686–4690, 2003.

[111] G Agostinelli, A Delabie, P Vitanov, Z Alexieva, HFW Dekkers, Stefaan De Wolf, and G Beaucarne. Very low surface recombination velocities on p-type silicon wafers passivated with a dielectric with fixed negative charge. *Solar energy materials and solar cells*, 90(18-19):3438–3443, 2006.

[112] Martin Otto, Matthias Kroll, Thomas Käsebier, Roland Salzer, Andreas Tünnermann, and Ralf B Wehrspohn. Extremely low surface recombination velocities in black silicon passivated by atomic layer deposition. *Applied Physics Letters*, 100(19):191603, 2012.

[113] Thomas Lauinger, Jan Schmidt, Armin G Aberle, and Rudolf Hezel. Record low surface recombination velocities on 1 ω cm p-silicon using remote plasma silicon nitride passivation. *Applied Physics Letters*, 68(9):1232–1234, 1996.

[114] AW Stephens, AG Aberle, and MA Green. Surface recombination velocity measurements at the silicon–silicon dioxide interface by microwave-detected photoconductance decay. *Journal of Applied Physics*, 76(1):363–370, 1994.

[115] Yimao Wan, Keith R McIntosh, Andrew F Thomson, and Andres Cuevas. Low surface recombination velocity by low-absorption silicon nitride on c-Si. In *2012 IEEE 38th Photovoltaic Specialists Conference (PVSC) PART 2*, pages 1–7. IEEE, 2012.

[116] MJ Kerr, J Schmidt, A Cuevas, and JH Bultman. Surface recombination velocity of phosphorus-diffused silicon solar cell emitters passivated with plasma enhanced chemical vapor deposited silicon nitride and thermal silicon oxide. *Journal of Applied Physics*, 89(7):3821–3826, 2001.

[117] Mark J Kerr and Andres Cuevas. Very low bulk and surface recombination in oxidized silicon wafers. *Semiconductor science and technology*, 17(1):35, 2001.

[118] Appu Paduthol, Mattias K Juhl, Gizem Nogay, Philipp Löper, Andrea Ingenito, and Thorsten Trupke. Carrier injection from amorphous silicon into crystalline silicon

determined with photoluminescence. In *2018 Ieee 7Th World Conference On Photovoltaic Energy Conversion (Wcpec)(A Joint Conference Of 45Th Ieee Pvsc, 28Th Pvsec & 34Th Eu Pvsec)*, pages 3746–3750. IEEE, 2018.

[119] Z Chen, SK Pang, K Yasutake, and A Rohatgi. Plasma-enhanced chemical-vapor-deposited oxide for low surface recombination velocity and high effective lifetime in silicon. *Journal of Applied Physics*, 74(4):2856–2859, 1993.

[120] Pierre Saint-Cast, Daniel Kania, Marc Hofmann, Jan Benick, Jochen Rentsch, and Ralf Preu. Very low surface recombination velocity on p-type c-si by high-rate plasma-deposited aluminum oxide. *Applied Physics Letters*, 95(15):151502, 2009.

[121] Chengmei Zhong, Vinod K Sangwan, Joohoon Kang, Jan Luxa, Zdenek Sofer, Mark C Hersam, and Emily A Weiss. Hot carrier and surface recombination dynamics in layered InSe crystals. *The Journal of Physical Chemistry Letters*, 10(3):493–499, 2019.

[122] S Bothra, S Tyagi, SK Ghandhi, and JM Borrego. Surface recombination velocity and lifetime in InP. *Solid-state electronics*, 34(1):47–50, 1991.

[123] HC Casey Jr and E Buehler. Evidence for low surface recombination velocity on n-type InP. *Applied Physics Letters*, 30(5):247–249, 1977.

[124] Y Rosenwaks, Yoram Shapira, and D Huppert. Evidence for low intrinsic surface-recombination velocity on p-type InP. *Physical Review B*, 44(23):13097, 1991.

[125] CA Hoffman, HJ Gerritsen, and AV Nurmikko. Study of surface recombination in GaAs and InP by picosecond optical techniques. *Journal of Applied Physics*, 51(3):1603–1604, 1980.

[126] L Jastrzebski, J Lagowski, and HC Gatos. Application of scanning electron microscopy to determination of surface recombination velocity: GaAs. *Applied Physics Letters*, 27(10):537–539, 1975.

[127] NL Dmitruk, VI Lyashenko, AK Tereshenko, and SA Spektor. Investigation of surface recombination on epitaxial GaAs films. *Physica Status Solidi (a)*, 20(1):53–62, 1973.

[128] RJ Nelson, JS Williams, HJ Leamy, B Miller, HC Casey Jr, BA Parkinson, and A Heller. Reduction of GaAs surface recombination velocity by chemical treatment. *Applied Physics Letters*, 36(1):76–79, 1980.

[129] Hiroshi Ito Hiroshi Ito and Tadao Ishibashi Tadao Ishibashi. Surface recombination velocity in p-type GaAs. *Japanese Journal of Applied Physics*, 33(1R):88, 1994.

[130] Sharon R Lunt, Gail N Ryba, Patrick G Santangelo, and Nathan S Lewis. Chemical studies of the passivation of GaAs surface recombination using sulfides and thiols. *Journal of Applied Physics*, 70(12):7449–7467, 1991.

[131] Sharon R Lunt, Patrick G Santangelo, and Nathan S Lewis. Passivation of GaAs surface recombination with organic thiols. *Journal of Vacuum Science & Technology B: Microelectronics and Nanometer Structures Processing, Measurement, and Phenomena*, 9(4):2333–2336, 1991.

[132] E Yablonovitch, CJ Sandroff, R Bhat, and T Gmitter. Nearly ideal electronic properties of sulfide coated GaAs surfaces. *Applied Physics Letters*, 51(6):439–441, 1987.

[133] JM Olson, RK Ahrenkiel, DJ Dunlavy, Brian Keyes, and AE Kibbler. Ultralow recombination velocity at $Ga_{0.5}In_{0.5}P$/GaAs heterointerfaces. *Applied Physics Letters*, 55(12):1208–1210, 1989.

[134] Matthew O Reese, Craig L Perkins, James M Burst, Stuart Farrell, Teresa M Barnes, Steve W Johnston, Darius Kuciauskas, Timothy A Gessert, and Wyatt K Metzger. Intrinsic surface passivation of CdTe. *Journal of Applied Physics*, 118(15):155305, 2015.

[135] Rachel Cohen, V Lyahovitskaya, E Poles, A Liu, and Y Rosenwaks. Unusually low surface recombination and long bulk lifetime in n-CdTe single crystals. *Applied Physics Letters*, 73(10):1400–1402, 1998.

Chapter 8

Conclusion and Future Prospects

The 20th century ushered the "Big Bang" for the semiconductor field, ushering in the invention of all solid-state electronic and optoelectronic devices that shape our society today. This century is the era to optimize device performance to their limits. Over the last few years, there has been an emerging interest in monolayer semiconductors due to their potential to achieve advanced optoelectronics with higher efficiencies and enhanced functionalities. Following the revolutionary discovery of direct gap monolayer MoS_2, several 2D materials have been identified and their novel optical and electronic properties have been explored. At the same time, various proof-of-concept 2D devices have appeared in the literature. However, while significant recent progress has been made, the deep body of knowledge concerning the material physics, particularly the photophysics with respect to the excitonic nature was lacking. This dissertation as a whole attempts to develop a fundamental understanding of 2D material physics in order to achieve the goal of efficient and practical devices.

In Chapter 2, how background carrier concentration effects recombination in 2D TMDC monolayers have been descried. At low generation rates, near-unity PL QY in MoS_2 and WS_2 has been demonstrated with electrostatic and chemical counterdoping. Excitonic monolayers can be bright even in the presence of native defects.

In Chapter 3, entirely radiative TMDC monolayers at all exciton generation rates have been demonstrated. Because most optoelectronic devices operate at high photocarrier densities, low PL QY at high exciton densities in monolayer semiconductors impeded their utility in practical applications. By applying small mechanical strain, we achieve near-unity PL QY in TMDC monolayers at all exciton densities, which paves the way for developing LEDs that will retain high efficiency at all brightness.

In Chapter 4, we explore the diffusion of pure neutral excitons and trions by electrostatic and chemical counterdoping. We observe that neutral excitons in monolayer MoS_2 diffuse micrometers at room temperature. We show that this long diffusion length is due to EEA enhanced diffusion.

In Chapter 5, we demonstrate efficiency roll-off free electroluminescence from monolayer WSe_2 by applying strain. We show two order of magnitude EL enhancement from WSe_2 monolayer by applying a relatively small strain of 0.5%. We attain internal quantum effi-

ciency of 8% at all injection rates.

In Chapter 6, we explore how EEA evolves during an indirect-to-direct transition in Bilayer WSe_2. EEA is suppressed both at 0% and 1% strain, but activated at intermediate strains. By strain and electrostatic counterdoping, we attain $\sim 50\%$ PL QY at all generation rates in 2L WSe_2, originally an indirect semiconductor. We demonstrate transient electroluminescence from 2L WSe_2 with $\sim 1.5\%$ internal quantum efficiency for a broad range of carrier densities by applying strain, which is ~ 50 times higher than without strain.

In Chapter 7, we explore exciton to free carrier transition in black phosphorus. In the excitonic regime the PL QY decreases with thickness and shows the highest PL QY of $\sim 20\%$ when it is completely excitonic at the monolayer limit. On the other hand, when recombination is dominated by free carriers PL QY increases with thickness, and we observe the surface recombination velocity in BP to be two orders of magnitude lower than in passivated silicon: the most electrically inactive surface known to the modern semiconductor industry.

Understanding and engineering the recombination pathways in excitonic systems in critical for basic science and optoelectronic applications. This work has established various recombination pathways in two dimensional excitonic semiconductors. Specifically, we found that neutral excitons interact weakly with native defects and inherently undergo radiative recombination. On the other hand, charged excitons (trions) strongly interact with defects and undergo nonradiative Auger recombination. Controlling background charge is a key factor in dictating high PLQY in monolayer semiconductors. So far, our understanding of this phenomenon is based on excitonic physics and is not specific to monolayer semiconductors only. Therefore, a fundamental question arises: are neutral excitons bright in all excitonic semiconductors? Looking into other excitonic semiconductors might provide a broader understanding to this questions. In black phosphorus we already see PL QY is maximum at the excitonic limit. Semiconducting quantum dots (QD) are important for a number of practical applications, can be excitonic due to confinement, and another ideal platform for exploring excitonic photophysics in the presence of surface defects and background charge. Ligand chemistry plays a big role in achieving high efficiency in colloidal QDs, but their role is not well understood. Often the improvement by ligands is attributed to the passivation of the surface dangling bonds, however ligands has also been shown to dope the semiconductor nanocrystals by surface charge transfer. To fully understand and deconvolute the effect to surface passivation to charge transfer, in the future it is desirable to quantitatively measure PL QY of QD with electrostatically counterdoping. It might be possible to interchanging Lewis acid or base ligands and then electrostatically attempt to recover their PL intensity. As the confinement energy depends on the quantum dot's size, excitonic to free-carrier transition can also be explored. Preliminary measurements show electrostatic counterdoping can improve PL intensity of QD. Once a proper device structure is developed for QD measurement, same framework might be applicable to luminescent molecular systems and C60.

Another aspect of this work is also exploring the effect of band structure modulation on the exciton-exciton annihilation or reduced QY at high generation rates. The dielectric environment also strongly influences the multiparticle interactions in monolayer TMDCs. It

has been shown that EEA rate can be suppressed by orders of magnitude by using a high-k dielectric substrate, such as $SrTiO_3$. This is due to an increase of screening strength in the semiconductor monolayers by high-k substrates. In the future combined effect of dielectric screening and band structure tuning can be explored by measuring PL on different substrates with strain. EEA suppression found in this dissertation along with the understanding can be extended to the shorter wavelength regime where, EEA is the primary reason for rapid organic device degradation.

Looking forward, it is also important to first build up an accessible monolayer library to accelerate the development and understanding of the entire space of 2D materials, and then explore excitonic photophysics in other material systems such as quantum dots and molecular crystals. It is also important to find materials whose bandgap span the most important and yet inaccessible blue-to-UV wavelength regime. This range is particularly important for applications in medical uses, displays and lighting. In the United States, 6% of total electricity consumption, or about 91 billion kWh, goes to lighting alone. Lighting takes up an even greater share globally, accounting for $15 - 20\%$ of worldwide electricity consumption and 5% of greenhouse gas emissions. As such, while much work has been done to improve the efficiency of light-emitting devices—for example, phasing out incandescent bulbs for LEDs—it is still of great environmental interest to develop devices that perform at the limit of energy efficiency, especially at shorter wavelengths and higher brightnesses. It is also essential to explore the new physics of vdW heterostructures and develop corresponding devices to fully unlock the potential of 2D materials, including the capability to actively tune heterojunction band alignment electrically, as well as various optical phenomena arising from the twist-angle degree of freedom. Moreover, it is important to explore the potential of 2D/bulk semiconductor heterostructures to develop new types of light-emitting devices. The simultaneous development of growth and transfer technologies for 2D materials targeting high optoelectronic performance will give a higher freedom to the design of the next-generation 2D light-emitting devices. With enabled monolayer-enabled functionality such as high quantum efficiency and color tunability, the future could be bright indeed.